UC Santa Barbara

UC Santa Barbara Electronic Theses and Dissertations

Title

Part 1. Investigations of Reaction Pathways for Catalytic Biomass Conversion Part 2. Mechanistic Study of Hydrogen Peroxide Triggered Carbon Monoxide Release from a Manganese Tricarbonyl Complex

Permalink

Author

Barrett, Jacob Alexander

Publication Date

2019

UNIVERSITY OF CALIFORNIA

Santa Barbara

Part 1. Investigations of Reaction Pathways for Catalytic Biomass Conversion

Part 2. Mechanistic Study of Hydrogen Peroxide Triggered Carbon Monoxide Release from

a Manganese Tricarbonyl Complex

A dissertation submitted in partial satisfaction of the

requirements for the degree Doctor of Philosophy

in Chemistry

by

Jacob Alexander Barrett

Committee in charge:

Professor Peter C. Ford, Chair

Professor Gabriel Meńard

Professor Javier Read de Alaniz

Professor Lior Sepunaru

June 2019

The dissertation of Jacob Alexander Barrett is approved.

_____

Gabriel Meńard

_____

Javier Read de Alaniz

_____

Lior Sepunaru

_____

Peter C. Ford, Committee Chair

June 2019

Part 1. Investigations of Reaction Pathways for Catalytic Biomass Conversion

Part 2. Mechanistic Study of Hydrogen Peroxide Triggered Carbon Monoxide Release from

a Manganese Tricarbonyl Complex

DEDICATION

This dissertation is dedicated to my parents, Barry R. Katz and Tranita L. Barrett, without

whom I could not be here today. I appreciate their love and support during this process.

ACKNOWLEDGEMENTS

were vital to my well-being and I could not imagine a better group of people to live with in Isla Vista. Some of the happiest moments in my life came from sharing a home with them and I look forward to our lifelong relationships. I am eternally grateful to Samuel Boldissar for being the most kind, helpful, and intelligent human being I've had the pleasure to know. He may be gone from this world, but he is not forgotten. I am extremely appreciative of my roommate and future brother-in-law, Owen R. Liu, for welcoming me into his home and family. I'd also like to thank Austin Barnes for his friendship and specifically pushing me to maintain my physical health while in graduate school. I'd like to express my gratitude to the "psych girls" who gave me the opportunity to expand my small science graduate circle. I am thankful to all the members of the Black Graduate Student Association for allowing me to be a part of a black graduate community. I'd also like to acknowledge Meredith Merchant and Mario Barfield for your support through the Black Graduate Student Support Space. I'd also like to thank Keanu Birkelbach for his friendship and infectious smile.

I would also like to generally express my appreciation for the Ford Group specifically Christopher Bernt, Po-Ju Huang, Zhi Li, and Qin Jiang who greatly helped me in much of my research. The department staff keep us functioning daily. I am grateful for both current and former staff in helping with my technical and administrative needs. I'd like to thank the Louis Stokes Alliance for Minority Participation Program for helping fund my undergraduate education and research. I'd like to express my sincerest gratitude to the NSF Graduate Research Fellowship program for funding three years of my graduate career. I would also like to acknowledge the National Science Foundation and the UC Santa Barbara Academic Senate Committee on Faculty Grants for funding the research.

Finally, I want to thank my partner, Sabrina R. Liu. You have continually been there to lift me up at my lowest and highest points. I could not have completed this dissertation

without your love, support, and companionship these past 5 years. Your work ethic, empathy, and kindness have inspired me to be the best version of myself. My heart is at home in your hands and I'm extremely fortunate to share my life with you. Sabrina, her brother Owen, and her parents, Penny and Leo, have given me a second family that I am ecstatic to be part of.

VITA OF JACOB ALEXANDER BARRETT

August 2019

EDUCATION

Doctor of Philosophy in Chemistry, University of California, Santa Barbara, June 2019 (expected)
Bachelor of Arts in Chemistry, Sonoma State University of California, Rohnert Park, May 2014 (with Distinction)

EMPLOYMENT

2016-2019: Graduate Student Researcher, Department of Chemistry, University of California, Santa Barbara (as an NSF Graduate Research Fellow)
2014-2016: Teaching Assistant, Department of Chemistry, University of California, Santa Barbara
2011-2014: Student Research Assistant, Department of Chemistry, Sonoma State University, Rohnert Park
2012: Summer Internship, CSU-LSAMP Project NUTRia, Cabo Blanco Absolute Reserve, Costa Rica

AWARDS/HONORS/FELLOWSHIPS

2016-2019: National Science Foundation Graduate Research Fellowship Recipient, University of California, Santa Barbara
2019: UCSB B.R. Baker Memorial Award
2018: UCSB Robert H. DeWolfe Graduate Teaching Award
2017: UCSB Grad Slam People's Choice Award
2016: American Chemical Society Catalyst Division Travel Award
2015 & 2019: Outstanding Service to the Department Award, University of California, Santa Barbara
2014: California State University Louis Stokes Alliance for Minority Participation Program for Recognition of Undergraduate Distinction Scholar
2013: Department of Chemistry Summer Research Award, Sonoma State University, Rohnert Park

PUBLICATIONS

First Author
[1] **Jacob A. Barrett**, Zachary Jones, Craig Stickelmaier, Nora Schopp, Peter C. Ford, "A Pinch of Salt Improves n-butanol Selectivity in the Guerbet Condensation of Ethanol over Cu-doped Mg/Al Oxides." *ACS Sustainable Chem. Eng.* 2018, 6, 11, 15119-15126.
[2] **Jacob A. Barrett**, Yu Gao, Chris M. Bernt, Megan Chui, Anthony Tran, Marcus Foston, Peter. C. Ford. " Enhancing Aromatic Production from Reductive Lignin Disassembly: in Situ O-Methylation of Phenolic Intermediates", *ACS Sustainable Chem. Eng.*, 2016, 4, 12, 6877-6886.

[3] **Jacob Barrett**, Arianna Spentzos, Carmen Works. "An Advanced Organometallic Lab Experiment with Biological Implications: Synthesis and Characterization of $Fe_2(\mu\text{-}S_2)(CO)_6$" *J. of Chem. Ed.*, 2015, 92 (4), 719–722.

Contributing Author

[4] Yu Gao, Michael Walker, **Jacob A Barrett**, Omid Hosseinaei, David Harper, Peter C Ford, Brent Williams, Marcus Foston, "Analysis of gas chromatography/mass spectrometry data for catalytic lignin depolymerization using positive matrix factorization." *Green Chem.*, 2018, 20, 4366-4377.

[5] Andrew Hunt, **Jacob Barrett**, Meghan McCurry, Carmen Works. "Photochemical Reactivity of a Binuclear Fe(I)-Fe(I) Hydrogenase Model Compound with Cyano Ligands" *Polyhedron*, 2016, 114, 306-312.

[6] Christopher M. Bernt, Giovanni Bottari, **Jacob A. Barrett**, Susannah L. Scott, Katalin Barta, and Peter C. Ford. "Mapping Relative Reactivities for Aromatic Models of Lignin Disassembly Over Cu-doped Porous Metal Oxides" *Catal. Sci. Technol.*, 2016, 6, 2984-2994.

PRESENTATIONS

[1] **Jacob A. Barrett**, Loc Ngo, Peter C. Ford, "Kinetics of Hydrogen Peroxide Facilitated Release of CO from a Manganese Carbonyl." Gordon Research Conference on Nitric Oxide (Poster), February 2019, Ventura

[2] **Jacob A. Barrett**, Peter C. Ford, Chris M. Bernt, Megan A. Chui, Craig Stickelmaier, "An Overview of Lignin Disassembly with Cu-Doped Porous Metal Oxides." 255th National Meeting of the American Chemical Society (Invited Talk for "Challenge and Opportunity in Lignin Valorization" Symposium), March 2018, New Orleans.

[3] **Jacob A. Barrett**, Zachary Jones, Craig Stickelmaier, Nora Schopp, Peter C. Ford, "Guerbet Reaction of Ethanol over Cu Doped Porous Metal Oxides: Effects of Chloride "poisoning." 255th National Meeting of the American Chemical Society (Poster), March 2018, New Orleans.

[4] **Jacob A. Barrett**, Yu Gao, Chris Bernt, Marcus Foston, Peter C. Ford. "Catalytic depolymerization of lignin by Cu-PMO: Preserving aromatic products through O-methylation". 251st American Chemical Society National Meeting (Poster), March 2016, San Diego.

[5] **Jacob Barrett**, Brianna Dearing, Carmen Works. "The Synthesis and Characterization of Iron-Iron Hydrogenase Model Compounds for Their Potential Use as Photo-CORMs". 26th Annual ACS Northern California Undergraduate Research Symposium (Poster), May 2014, University of San Francisco

[6] **Jacob Barrett**, Carmen Works. "The Synthesis and Characterization of Iron-Iron Hydrogenase Model Compounds for use as potential Photo-CORMs" 26th Annual CSU Biotechnology Symposium (Poster), January 2014, Santa Clara

[7] **Jacob Barrett**, Carmen Works. "The Synthesis and Characterization of Iron-Iron Hydrogenase Model Compounds". SSU Chemistry Seminar Series (Oral), September 2013, Sonoma State University

[8] **Jacob Barrett**, Carmen Works. "The Synthesis and Photochemical Properties of a Hydroxyl-Functionalized Diiron Complex as a Potential CO releasing Molecule". 25th

Annual ACS Northern California Undergraduate Research Symposium (Oral), May 2013, Santa Clara University

[9] **Jacob Barrett**, Carmen Works. "Synthesis of a Napthalene Monoimide Dithiolate Diiron Hydrogenase Model Compound", 24th Annual ACS Northern California Undergraduate Research Symposium (Poster), May 2012, Oakland, Ca; Mills College

[10]   **Jacob Barrett**, Nathaniel Bell, Danielle Kuperus, & Kathleen Sowul, "Habitat preference of the intertidal Frillfin Bathygobius (Gobiidae) in Cabo Blanco Absolute Reserve, Costa Rica Pp. 95-107 in Lieberman, D. & Leiker, S. (editors)", Expedition Report, CSU-LSAMP Costa Rica Research Program, Summer 2012.

OTHER MEDIA
- **Barrett, J. A.** (2017, May 19.) Recent work of our fellow GSDS members [Blog post]. Retrieved from http://gsds.mrl.ucsb.edu/?p=932
- **Barrett, J. A.** (2017, March 10.) Santa Barbara's newest museum, the MOXI [Blog post]. Retrieved from http://gsds.mrl.ucsb.edu/?p=903
- **Barrett, J. A.** (2017, February 17.) GSDS Member Spotlight: Emre Discekici [Blog post]. Retrieved from http://gsds.mrl.ucsb.edu/?p=864
- **Barrett, J. A.** (2016, December 9.) Prof. Martin Moskovits: Just how devoid of cultural, racial, gender and national tarnish is Science as an approach to understanding the physical world? [Blog post]. Retrieved from http://gsds.mrl.ucsb.edu/?p=724
- **Barrett, J. A.** (2016, November 11.) Get to know our members: Yvonne Diaz, salsa fiend and polymer whiz kid [Blog post]. Retrieved from http://gsds.mrl.ucsb.edu/?p=631

FIELDS OF STUDY

Major Field: Inorganic Chemistry

Studies on catalytic hydrogenolysis of lignin and lignin model compounds with Professor Peter C. Ford including collaborative work with Professor Susannah L. Scott and Professor Marcus Foston.

Studies on the condensation of ethanol over transition metal doped porous metal oxides with Professor Peter C. Ford

Studies on the reaction of hydrogen peroxide with manganese carbonyl complexes with Professor Peter C. Ford and Professor Lior Sepunaru

ACADEMIC SERVICE AND OUTREACH

Graduate
2019: Gordon Research Seminar on Nitric Oxide
Led and moderated a discussion on mentorship and collaboration as part of the conference schedule.
2016-present: Black Graduate Student Association
Co-founded organization and served as Treasurer for 2 years. Aided in organization of annual Celebrating Black Scholarship event, as well as community building events for graduate students of the African diaspora.

2015-present: Science as a Career Outreach Program Experiment (SCOPE)
Visited multiple high schools in Santa Barbara and Ventura counties (Dos Pueblos, Bishop Diego, Santa Barbara, Buena Vista) to give a presentation about my life path and scientific research I have done. Led tours through the Ford Group lab and gave a short photochemistry demonstration to Ventura HS students.

2014-2017: Graduate Students for Diversity in Science
Served in multiple positions (Marketing, Recruitment, Outreach committees) of the student run organization which engages in outreach to Cal State University undergraduates and arranges seminar speakers to give research and diversity lectures at UCSB. Aided in the organization of recruitment social hours, published articles on the GSDS website, and created surveys for visiting undergraduates.

2015: Center for Sustainable Use of Renewable Feedstocks Zoo Outreach
Led a learning module for children on carbon dioxide and greenhouse gas effects at the Santa Barbara Zoo on behalf of CENSURF.

Undergraduate
2013-2014: Instructional Student Assistant and Tutor for Organic Chemistry
Prepared supplemental worksheets for students and provided help with specific problems

2011-2012: National Chemistry Week Volunteer
Led a learning module about phase transitions and performed a liquid nitrogen demonstration

ABSTRACT

Part 1. Investigations of Reaction Pathways for Catalytic Biomass Conversion

Part 2. Mechanistic Study of Hydrogen Peroxide Triggered Carbon Monoxide Release from

a Manganese Tricarbonyl Complex

by

Jacob Alexander Barrett

Society's dependence on fossil carbon resources encompasses many aspects of modern life. Humankind depends on fossil carbon for much of the energy we consume, the medicine we take, and the clothes we wear. Combustion of carbon fuels in a typical engine produces primarily carbon dioxide (CO_2) and water which are emitted into the atmosphere. The environmental impact of the resulting anthropogenic CO_2 emissions from the combustion of fossil fuels has motivated interest in sustainable technologies to meet our growing energy and manufacturing demands. The selective conversion and upgrading of lignocellulosic biomass and bio-derived chemicals is paramount to creating an environmentally sustainable chemical and fuel industry. This thesis is divided into two parts, where the first part of this work describes efforts to understand the reactivity of Cu-doped porous metal oxide in the conversion of biomass and bioalcohols.

Specifically, lignin conversion into aromatic compounds has the potential to serve as a "green" alternative to the production of petrochemical aromatics. Herein, the use of an earth abundant catalyst, Cu-doped porous metal oxides (CuPMO), for the selective

conversion of lignin into oxygenated aromatics was demonstrated using model compounds and organosolv lignin. The catalyst generates hydrogen from alcohols which is then used in hydrogenolysis of aromatic ether bonds. It was shown that in the presence of a non-toxic methylating agent, dimethyl carbonate, O-methylation of hydroxyaromatic intermediates occurs which greatly decreases hydrogenation of the aromatic ring.

Establishing alternatives to petrochemical aromatics only addresses a fraction of the products we utilize. The upgrading of bio-derived alcohols has the potential to serve as "green" alternatives to petrochemicals commonly used in fuels, solvents, and plasticizers. Modification of CuPMO by the addition of small amounts of a chloride salt result in increased catalytic activity and selectivity in the Guerbet condensation of ethanol to n-butanol, due to marked changes in the catalyst's structural properties.

The second part of this work examines the release of carbon monoxide, a small molecule bioregulator, from manganese carbonyls by photochemical labilization or by the chemical reaction with hydrogen peroxide. Carbon monoxide (CO) and CO releasing molecules have been implicated in several biological applications, including antibacterial and anticancer therapeutics. For example, CO has been shown to negatively affect cellular respiration and thus may be the primary cytotoxic action of manganese carbonyl CORMs against bacterial and tumor cells. On the other hand, manganese carbonyl CORMs that have been depleted of CO also exhibit cytotoxicity. Specifically, it has been proposed that hydrogen peroxide plays a role in the observed cytotoxicity of these manganese carbonyls however, research on the mechanisms of this reaction is currently lacking. Understanding the reaction mechanisms of manganese carbonyls is important in establishing their potential applicability as therapeutics. Herein, the mechanisms of these reactions were probed spectroscopically and electrochemically by kinetic evaluation in aqueous conditions.

LIST OF ABBREVIATIONS

3CCA	3-carboxy-coumarin
4-O-5	diaryl ether lignin linkage
7OH3CCA	7-hydroxycoumarin-3-carboxylic acid
ABE	acetone-butanol-ethanol
ATR-IR	attenuated total reflectance infrared
β-5	phenylcoumaran lignin linkage
β-O-4 and α-O-4	aryl ether lignin linkage
BET	Brunauer-Emmet-Teller
bpCO$_2$H	2,2′-Bipyridine-4,4′-dicarboxylic acid
BPE	benzyl phenyl ether
n-BuOH	n-butanol
CO	carbon monoxide
CORM	carbon monoxide releasing molecule
CuPMO, Cu$_{20}$PMO	copper doped porous metal oxide
CV	cyclic voltammetry
DHBF	dihydrobenzofuran
DMC	dimethyl carbonate
DPE	diphenyl ether
ECN	effective carbon number
EPR	electron paramagnetic resonance
EtOAc	ethyl acetate
EtOH	ethanol
fac	facial isomer
FID	flame ionization detection
FT-IR	Fourier transform infrared
FWHM	full width at half maximum
G	coniferyl alcohol
GC	gas chromatography
GHG	greenhouse gas emissions
GPC	gel permeation chromatography
H	coumaryl alcohol
HDG	hydrogenolysis
HDO	hydrodeoxygenation
HexOH	1-hexanol
HO	heme oxygenase
HSQC	Heteronuclear Single Quantum Coherence
HTC	hydrotalcite
ICP-OES	inductively coupled plasma-optical emission spectroscopy
M$_n$	number average molecular weight
M$_w$	weight average molecular weight
MeCN	acetonitrile
MeOH	methanol
MLCT	metal-ligand charge transfer
MPP	2-methoxy-4-propylphenol
MS	mass spectrometry

NMR	nuclear magnetic resonance
OPL	organosolv poplar lignin
OTf	trifluoromethanesulfonate
PDI	polydispersity index
PMO	porous metal oxide
PPE	2-phenoxy-1-phenylethan-1-ol
rf	response factor
RFS	renewable fuel standard
ROS	reactive oxygen species
S	sinapyl alcohol
sc	supercritical
SCE	saturated calomel electrode
SEM	scanning electron microscopy
SF	stoichiometric factor
SHE	standard hydrogen electrode
TCD	thermal conductivity detection
TEM	transmission electron microscopy
THF	tetrahydrofuran
TMDP	2-chloro-4,4,5,5-tetramethyl-1,3,2-dioxaphospholane
TPD	temperature programed desorption
XRD	x-ray diffraction

TABLE OF CONTENTS

Chapter 1. Thesis Scope

1.1. Research Motivations, Perspectives, and Interests

Over 1 billion tons of combined biomass resources (i.e. forestry, agricultural, and urban food waste) are available annually.[1] When I started in the Ford Research Group, the Center for Sustainable Use of Renewable Feedstocks largely influenced my thoughts on where I could make meaningful contributions in the sustainable chemistry field. From my perspective, a sustainable process is one that maintains balance in the resources it uses and the wastes it produces for the next thousand years without any changes.[2] The continued depletion of natural resources and use of unsustainable technologies by our current generations that adversely affect the ability of our future grandchildren to maintain a good standard of living, deeply trouble me. The aforementioned is what attracted me to the research projects described herein. My original motivation for investigating reaction pathways of lignin was to find a way to obtain a useful high value chemical that is otherwise only currently obtainable from oil. It is my perspective that we will be dependent on oil for as long as it makes up most of our medicines, polymers, and transportation fuel. Much of the publics' attention has been focused on switching to electric light duty vehicles. It is equally crucial to consider where our society will obtain our chemical feedstocks once we discontinue the use of oil as our primary fuel source. In this context, Chapters 2 and 3 describe some of these contributions with the objective of developing alternative chemical processes to meet our needs without the use of nonrenewable resources.

The field of catalytic biomass conversion can stand to learn a lot from the petroleum industry. The petroleum industry is often demonized; however, it is vital to maintain our

current standard of life. What has made oil's use so ubiquitous is how the petroleum industry does not treat any part of a barrel of oil as waste. In contrast, lignin was largely viewed as an obstacle in the path of valorization of the cellulose portion of lignocellulose. Recently the field has changed its perspective to focus on how all biomass components can be applied to society's needs as either materials or feedstock chemicals.

The selective conversion of organosolv poplar lignin into methoxylated alkylbenzenes catalyzed by Cu-doped porous metal oxides (CuPMO) and substrate driven changes in catalyst structure are the subject of Chapter 2. While we were publishing the studies described in Chapter 2, I became interested in life cycle analysis which quantitatively evaluates the environmental impact a specific product has. My literature research into this field cemented two rules in my perspective on catalytic biomass conversion. (1) Edible biomass should not be turned into chemicals or fuels and (2) water and land usage to grow chemical/fuel crops should only be done when it is environmentally, socially, and economically sustainable to do so. In this context, residual forestry, agricultural, and food waste are attractive chemical resources. The creation of a value-added product from waste, which may have zero or even negative value, is a straightforward concept yet difficult in practice. These waste streams are by definition more trouble than they are currently worth and adequately efficient and selective processes are needed to achieve this goal.

The U.S. government has supported the production of ethanol, primarily from corn, as a renewable fuel additive to reduce greenhouse gas (GHG) emissions for decades.[3] Virtually all gasoline we use today is blended with, at minimum, 10% ethanol. However, life-cycle analysis has shown that we cannot just replace gasoline with ethanol to decrease our GHG emissions without increasing our overall environmental impact.[4] Suh et. al showed, through life-cycle analysis, replacing gasoline with corn-derived ethanol results in

shifted environmental impact to increased eutrophication and local water scarcity in place of GHG emissions.[4] Additionally, as our society continues its transition to electric light duty vehicles, gasoline will become obsolete and with it fuel ethanol. In this context, there is current motivation to develop chemical processes that use ethanol as a feedstock and/or create advanced biofuels that may be applicable to heavy duty vehicles. Thus, I was interested in researching a catalytic process to produce value-added chemicals and/or fuels from ethanol. The breakthrough in this project was originally an observation made from reactivity changes of CuPMO during lignin disassembly. Dr. Zach Jones and I had found that chloride, which was unknowingly added with our substrate, significantly changed the structure of the catalyst and was detrimental to its lifetime. While I was initially motivated to understand how CuPMO changes during the disassembly of lignin I was inspired to turn a disadvantage into a benefit. Hence, the effect of chloride driven structural changes of CuPMO on the condensation reaction of ethanol to form n-butanol, a potential advanced biofuel and biochemical, are the subject of Chapter 3.

Much of my research experience in graduate school pertained to heterogenous inorganic chemistry. I wanted to initiate a research project pertaining to mechanistic inorganic chemistry in solutions to expand my perspective. My undergraduate research experience in the Works group pertained to the photochemical and photophysical properties of homogenous iron carbonyl complexes. Metal carbonyls have potential use as bactericidal[4] and tumoricidal[5] medications, however the mechanisms of their reactions under biologically relevant conditions are not well characterized. Specifically, the reaction mechanism of manganese carbonyls with a ubiquitous reactive oxygen species, hydrogen peroxide, is unknown. In this context, I initiated a kinetics investigation of the hydrogen peroxide oxidation of facial tricarbonylbromido-2,2'-bipyridine-4,4'-dicarboxylic acid manganese (I),

fac-Mn(CO)$_3$(Br)(bpCO$_2$H), in buffered pH 7.4 aqueous media. Chapter 4 summarizes these studies and attempts to place them into the broader context of medicinal usage of metal carbonyls. It is my view that the reaction mechanisms and kinetics of the key reactions with the various components of physiological media must be well characterized for both previously known and novel metal carbonyl complexes to realize any potential as medicines.

1.2. References

1. U.S. Department of Energy. 2016. 2016 Billion-Ton Report: Advancing Domestic Resources for a Thriving Bioeconomy, Volume 1: Economic Availability of Feedstocks. M. H. Langholtz, B. J. Stokes, and L. M. Eaton (Leads), ORNL/TM-2016/160. Oak Ridge National Laboratory, Oak Ridge, TN. 448p. doi: 10.2172/1271651. http://energy.gov/eere/bioenergy/2016-billion-ton-report.

2. Horvath, I. T.; Cséfalvay, E.; Mika, L. Sustainability Metrics for Biomass-Based Carbon Chemicals. *ACS Sustain. Chem. Eng.* **2017**, *5*, 2734–2740

3. U.S. Environmental Protection Agency. Partial Grant of Clean Air Act Waiver Application Submitted by Growth Energy To Increase the Allowable Ethanol Content of Gasoline to 15%. *Fed. Regist.* **2011**, 76 (17), 4662−4683

4. Yang, Y.; Bae, J.; Kim, J.; Suh, S. Replacing Gasoline with Corn Ethanol Results in Significant Environmental Problem-Shifting. *Environ. Sci. Technol.* **2012**, *46* (7), 3671–3678

5. Wareham, L. K.; Poole, R. K.; Tinajero-Trejo, M. CO-Releasing Metal Carbonyl Compounds as Antimicrobial Agents in the Post-Antibiotic Era. *J. Biol. Chem.* **2015**, *290* (31), 18999–19007

6. Schatzschneider, U. Novel Lead Structures and Activation Mechanisms for CO-Releasing Molecules (CORMs). *Br. J. Pharmacol.* **2015**, *172*, 1638–1650

Part 1. Investigations of Reaction Pathways for Catalytic Biomass Conversion

Chapter 2. Biomass Conversion using Porous Metal Oxides

2.1. Abstract

The selective conversion of lignin into aromatic compounds has the potential to serve as a renewable source of crucial chemicals traditionally derived from petroleum. Section 1 of this chapter will focus on a method to increase aromatic selectivity and decrease product proliferation in a previously studied biomass conversion system. The addition of dimethyl carbonate (DMC) as a selective *O*-methylation agent to Cu-doped porous metal oxide (Cu$_{20}$PMO) catalyzed lignin disassembly in supercritical methanol (sc-MeOH) was investigated. This material catalyzes C−O hydrogenolysis of the aryl−ether bonds that are key linkages in the polymeric structure of lignin. However, Cu$_{20}$PMO also catalyzes methylation and hydrogenation of the resultant phenolic products. The MeOH/DMC co-solvent system significantly suppresses hydrogenation of the reactive phenolic intermediates responsible for much of the undesirable product proliferation by intercepting these reactive species via *O*-methylation of aryl−OH groups to form more stable aryl-OCH$_3$ species. Consequently, product diversity was greatly reduced, and aromatic yields were greatly enhanced in reactions with the lignin models, 2-methoxy-4-propylphenol (MPP), benzyl

phenyl ether (BPE), and 2-phenoxy-1-phenylethan-1-ol (PPE). A similar result was observed when organosolv poplar lignin (OPL) was examined as a substrate in this MeOH/DMC co-solvent system. In each case, products were characterized by nuclear magnetic resonance spectroscopy (^{31}P, ^{13}C, and 2D ^{1}H$-^{13}$C NMR) and gas chromatography$-$mass spectrometry techniques.

Catalyst stability is crucial to develop new processes to replace petrochemical ones. Section 2 of this chapter focuses on the structural characterization, evolution, and irreversible lignin disassembly activity loss of $Cu_{20}PMO$. The overall activity of $Cu_{20}PMO$ with OPL diminished significantly over three recycles in the MeOH/DMC solvent system. Implementation of a biomass conversion process requires catalysts that have minimal activity loss over hundreds to thousands of recycles or are easily regenerated. We evaluated the structural evolution of $Cu_{20}PMO$ to assess the cause of these structure driven reactivity changes. During the reaction in sc-MeOH, relatively small Cu metal nanoparticles (about 3-5 nm) are formed. These nanoparticles are stable for at least 72 h at 300 °C in the presence of lignin model compounds (anisole, phenol, and benzyl phenyl ether), water, and sc-MeOH under batch conditions. However, the catalytic reaction with OPL led to extensive sintering to give larger (ca. 30 nm) Cu nanoparticles. It appears that chloride impurities in the OPL substrate promote sintering and lead to irreversible reactivity decreases and selectivity changes. Similarly, the addition of chloride containing compounds led to analogous structural and activity changes with model compound reactions using $Cu_{20}PMO$.

2.2. Introduction

2.2.1. Lignin Valorization

Petroleum feedstocks supply more than 90% of organic chemicals used in our society.[1] Development in the utilization of renewable chemical feedstocks is essential to maintain our crucial chemical industries as society transitions from the use of fossil carbon to sustainable and renewable resources. Almost 50 million dry tons of forestry and wood waste were readily available at $60 per dry ton in 2017.[2] This figure includes waste from forestland, timberland, mill residues, and urban use. The current pharmaceutical and polymer industries largely depend upon petrochemical feedstocks.[1] To this end, large-scale biorefineries that efficiently utilize lignocellulosic biomass are being developed to produce renewable fuels and chemicals.[3] Research advances in catalytic biomass conversion has largely focused on the selective conversion of the carbohydrate fractions of biomass, whereas lignin is typically used for low grade heat generation. The complex, amorphous structure of lignins and the low reactivity of the aromatic ethers that serve as the primary linkages of this polymeric material makes lignin very resistant to chemical and biological degradation. Lignin is the largest potential source of renewable aromatic chemicals, therefore the development of economically sustainable processes to harness this potential is of great interest for biorefineries.[4] Thus far its natural recalcitrance to degradation has hindered its industrial scale conversion processes.[5] The development of sustainable technologies for lignin conversion that maximize atom economy would improve the economic feasibility of large-scale biorefineries and facilitate development of a renewable chemical industry.[6]

2.2.2. Lignocellulosic Biomass Composition

Lignocellulose is primarily composed of three biopolymers; cellulose, hemicellulose, and lignin.[7] Cellulose is a carbohydrate polymer composed of linear chains of glucose monomers. Hemicellulose is also a carbohydrate polymer but contains pentoses (i.e. sugars with five carbon atoms) as well as glucose. Lignin is an aromatic polymer made from the radical polymerization of three hydroxycinnamyl alcohols; conniferyl alcohol (G), sinapyl alcohol (S), and coumaryl alcohol (H). Lignin is formed by radical reaction pathways for the hydroxycinnamyl alcohols,[8] so, unlike the carbohydrate polymers, its monomers are linked by a variety of different chemical bonding motifs. The heterogeneity of the polymeric structure imparts natural recalcitrance to biotic and abiotic degradation.[8] Additionally, the techniques employed to extract lignin from lignocellulose often result in formation of C-C crosslinking bonds between benzylic carbons that are considerably harder to break than the C-O bonds.[9] The primary structural motifs characteristic of lignin linkages include aryl ether carbon-oxygen (C-O) bonds. Some of the more common motifs are aryl ether (β-O-4 and α-O-4), phenylcoumaran (β-5), and diaryl ether (4-O-5) linkages (Figure 2.1). Other linkages are present in smaller amounts, the abundances being highly dependent on the plant species, growth conditions, and lignin isolation technique.[10]
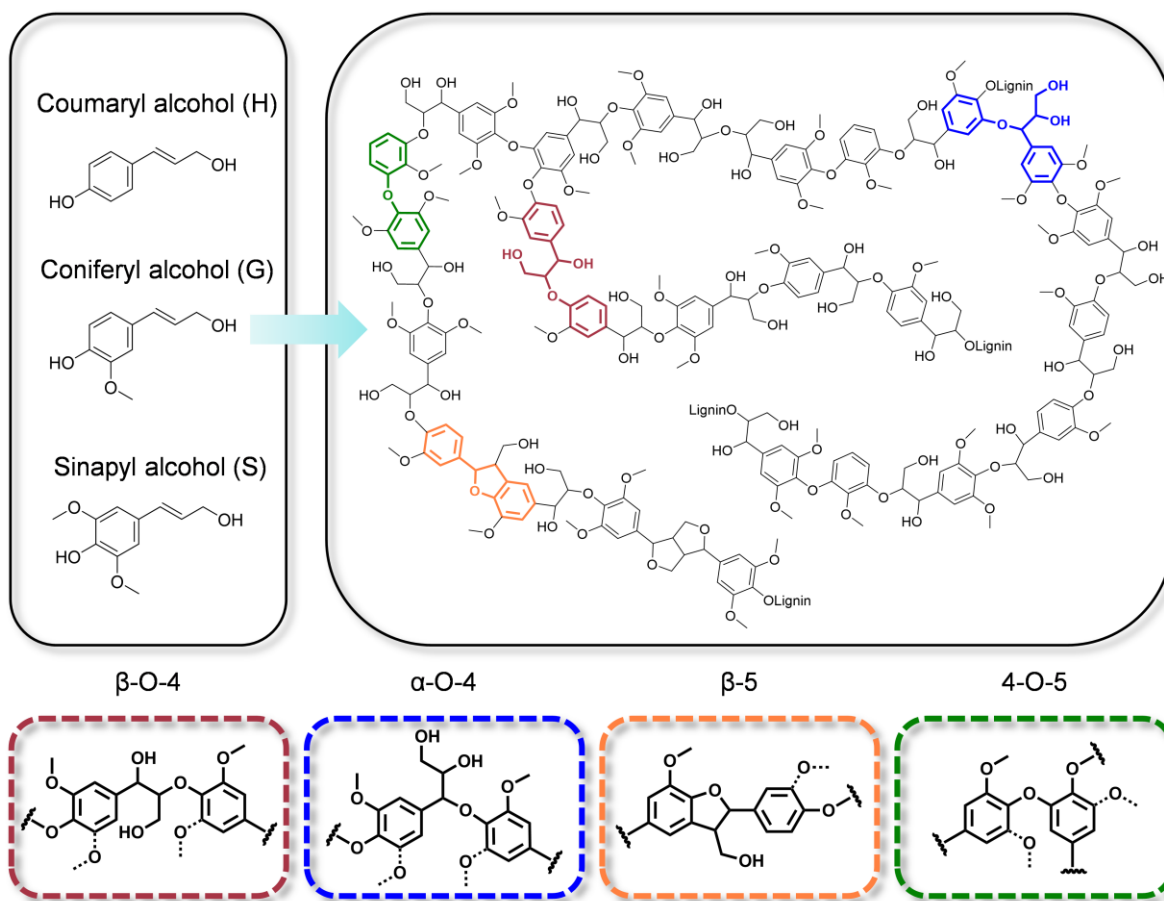
Figure 2.1. Visual depiction of lignin with common linkages highlighted in color based on structural data on poplar wood from Sannigrahi et al.[7] The three hydroxycinnamyl alcohols are shown on the top left with four of the more common aryl−ether linkages depicted along the bottom. Reproduced with permission from *ACS Sustain. Chem. Eng.* **2016**, *4*, 6877–6886. Copyright 2016 American Chemical Society.

Lignocellulosic biomass also contains a small inorganic component in addition to the carbon fractions. Elements such as sodium, potassium, calcium, silicon, phosphorous, and chlorine are all present in lignocellulose to varying degrees.[11] The abundance of these inorganic elements is largely dependent on plant species. While the inorganic component is typically minute, these elements can act as catalysts for char-forming reactions at high temperatures and can affect properties of transition metal catalysts.[12] Char is a solid material that can be formed when carbonaceous materials are subjected to high temperature. Halogen

and sulfur containing feedstocks can accelerate sintering and/or coking based catalyst deactivation on platinum group metal catalysts.[13] Specifically, chloride is a copper catalyst poison which leads to irreversible deactivation.[14] In summary, lignocellulosic biomass is composed of two fairly uniform polymers (cellulose and hemicellulose), a complex macromolecule (lignin), and a small fraction of inorganic elements.

2.2.3. Lignocellulose Conversion using Hydrogenolysis

Various lignin disassembly methods utilizing acids, bases, and transition metal based hetero- and homogeneous catalysis have been described.[15-18] Catalytic hydrogenolysis is a promising method to produce aromatic compounds from several types of lignin.[19,20] Hydrogenolysis (HDG) uses hydrogen (or hydrogen equivalents) to cleave C-X (X= O, S, Cl, and F) bonds.[21] Such reductive cleavage of aryl-ether bonds is a conceivable route towards the production of aromatic chemicals. β-O-4 and α-O-4 linkages generally undergo cleavage by HDG more easily than do other types of bonds linking lignin fragments.[22] However, catalysts effective for C-O bond HDG may also be effective at phenol hydrogenation to give cyclohexyl derivatives.[19] Thus, the desired aromatic compounds are produced and consumed under the same reaction conditions. In this context, one principal objective of the research described in this chapter is the disassembly of lignin through HDG to cleave aryl-ether bonds while minimizing aromatic ring hydrogenation.[20]

Acid-base properties have profound effects on the rates and selectivities of key pathways for lignin disassembly by heterogeneous catalysts. For example, Song et al. observed that the nickel catalyzed HDG of lignosulfonate to organic liquids and the selectivity toward production of propyl guaiacol and 4-ethylguaiacol are dependent on the catalyst support.[23] In another contribution, this group discussed the important role that

methanol (MeOH) can play in lignin solvation and solvolysis. Hence, given the limitation of transport between macromolecular lignin and a heterogeneous catalyst, hydrogenolysis is likely to occur on smaller, soluble lignin fragments generated by solvolysis.[24]

Another catalytic system that was developed in Abu-Omar's group showed remarkable retention of aromatic products using a Zn/Pd/C catalyst.[25] They hypothesized that the Zn is dissolved in solution as Zn(II) ions during the reaction and helps activate the aryl-ether bonds at relatively low reaction temperature (150°C).[25] These more mild reaction conditions allow for lignin to be converted without significantly altering the cellulose.[26]

The Ford Laboratory developed a process to disassemble lignocellulosic solids (i.e. sawdust, poplar wood chips, and cellulose) using supercritical methanol and a Cu-doped porous metal oxide catalyst.[27] The supercritical region is at temperature and pressure above the critical point of the substance where the is no distinction between gas and liquid. The lignin disassembly reaction conditions were above 300°C with an autogenous pressure over 100 bar, which is well past the critical point of methanol (240°C and 81 bar). The porous metal oxides were prepared by calcining synthesized transition metal doped hydrotalcites. Mg-Al carbonate hydrotalcite is a type of layered double hydroxide that contains magnesium (Mg^{2+}) and aluminum (Al^{3+}) metal cations in a 3:1 ratio and include carbonate anions and water molecules in the interlayer space. Synthetic layered double hydroxides are in the hydrotalcite supergroup and have a wide range $Mg^{2+}:Al^{3+}$ ratios. The calcination of a copper-doped layered double hydroxide where 20% of the Mg^{2+} was replaced with Cu^{2+} produced an effective lignin disassembly catalyst ($Cu_{20}PMO$).[28]

The $Cu_{20}PMO$ catalyzed reaction of lignocellulosic solids in supercritical MeOH (sc-MeOH) gave a mixture of cyclohexyl alcohols and small aliphatic alcohols with little or no char formation after reacting for 8 h at 320 °C.[27] Barta et. al determined that the cyclohexyl

alcohols were from catalytic hydrogenolysis and hydrogenation of aromatic ethers of lignin by using ^{1}H and ^{2}H NMR spectroscopic analysis of the products from organosolv lignin when the reaction was carried out in sc-CD$_3$OD.[29] Cu$_{20}$PMO is particularly effective in MeOH, catalyzing not only the hydrogenolysis of aryl ethers, but also MeOH reformation and water gas shift reactions to generate the necessary reducing equivalents of H$_2$ (eqs. 2.1 & 2.2).[30]

$$CH_3OH \rightleftharpoons 2\,H_2 + CO \qquad\qquad \textbf{(2.1)}$$

$$CO + H_2O \rightleftharpoons CO_2 + H_2 \qquad\qquad \textbf{(2.2)}$$
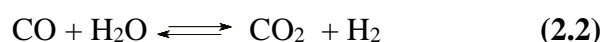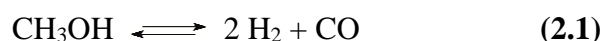
While the Cu$_{20}$PMO utilizes the H$_2$ produced by these reactions to hydrogenolyze C-O bonds, it also catalyzes the hydrogenation of alkenes and various aromatic centers. A key advantage of using this catalyst system with sc-MeOH to disassemble lignin or lignocellulose is that very little char or tar is formed.[30] Subsequent studies showed Cu$_{20}$PMO and related catalysts to be effective in disassembling different types of lignin,[31] producing H$_2$ equivalents from other alcohols,[32,32] and performing selective organic transformations[34] such as the upgrading of furfural derivatives.[35]

2.2.4. Enhancing Aromatic Selectivity Over Porous Metal Oxides

The selectivity of the Cu$_{20}$PMO/sc-MeOH system toward aromatic products is poor owing to the tendency toward aromatic ring hydrogenation activity.[36] This was shown in Bernt et al. who extensively mapped the reaction pathways of various model compounds for lignin fragments. The study clearly showed that phenol is particularly reactive in this system while its *O*-methylated counterpart anisole is much less reactive.[36] To capitalize on Cu$_{20}$PMO's reactivity, we developed a strategy to enhance aromatic production from

organosolv lignin by using a mixed solvent to enhance *O*-methylation of reactive phenolics. This work is one of the two major topics addressed in this chapter.[37]

Although, the fully hydrogenated cyclohexyl alcohol products have value as potential fuels, synthetic precursors, and solvents,[38] product proliferation is a key issue that presents a major limitation for the industrial implementation of $Cu_{20}PMO$ catalyzed lignin disassembly in sc-MeOH. Our model studies showed that these side reactions can largely be attributed to the reactivity of phenolic intermediates.[35] Our premise was phenolic intermediates can be intercepted after HDG by *O*-methylation. Notably, O-methylation of guaiacol, catechol, and phenol by DMC has been reported by Talawar, Jyothi, and coworkers to be catalyzed by calcined Mg-Al hydrotalcite.[39,40]

In section 1 of this chapter, studies on the methodology to trap reactive phenolic intermediates generated during the reductive disassembly of lignin and several relevant models are described. This work evaluated several lignin model compounds including 2-phenoxy-1-phenylethan-1-ol (PPE), which is a model for the β-O-4 linkage that comprises 40-60 % of lignin's linkages,[7] and organosolv poplar lignin (OPL), which is a much more complex model for lignins. These lignocellulosic biomass models each show substantially higher yields of aromatic products in the MeOH/DMC co-solvent system than in the analogous reactions in sc-MeOH).

Section 1. Increasing Aromatic Selectivity

2.3. Results and Discussion

The reactions described herein were performed at 300 °C in a stainless steel mini-autoclave reactor unless otherwise noted. Typically, model compound reactions were

performed with 0.5 to 1 mmol of substrate, 3 mL of solvent, 50 mg of $Cu_{20}PMO$, and 20 µL of n-decane (internal standard) added to the reactor, sealed, and placed into a pre-heated furnace for a set amount of time. The standard ratio of MeOH/DMC used was 2:1 mL. The reactors were quenched in a room temperature water bath to stop the reaction. The reactors were carefully opened, and the gas volumes measured with a water displacement setup. When gas products were characterized it was done by sampling the released gas at atmospheric pressure and injecting onto a gas chromatogram (GC) equipped with a thermal conductivity detector. The liquid products were filtered to remove the solid catalyst, diluted in methanol, and characterized using both mass spectrometry and GC equipped with a flame ionization detector. Details on the quantification methods are shown in Section 2.5 or Appendix A.

2.3.1. Enhancing *O*-Methylation in Model Compound Reactions

In Bernt et. al, we showed that the introduction of the methylating agent dimethyl carbonate (DMC) greatly enhanced the net yield of aromatic products from the α-O-4 lignin model, benzyl phenyl ether.[36] The activities of $Cu_{20}PMO$ with BPE in sc-MeOH and in 2 mL MeOH/1 mL DMC under conditions effective for disassembly of lignin and lignocellulose were previously compared in a study from this laboratory by Bernt et al.[36] In both solvent systems, the benzyl ether bond undergoes rapid HDG to give toluene and phenol. The phenol represents the core chemical moiety of the *p*-hydroxyphenyl (i.e., coumaryl alcohol) monolignol. Phenolic compounds undergo secondary reactions with $Cu_{20}PMO$ in sc-MeOH to generate numerous products, mostly aliphatic alcohols. After 1 h in sc-MeOH with $Cu_{20}PMO$ at 310 °C, 85 % of the BPE was converted. The principal products of aryl-ether bond hydrogenolysis were toluene and phenol. The former was formed in near

15

stoichiometric quantities and remains essentially constant for at least 12 h. After 1 hour 90 %

of the phenol from BPE was observed, however, after 3 h only 24 % remains. After 3 h

phenol is converted to aliphatics, i.e. cyclohexanol and methylcyclohexanol (39 % of initial

BPE) and aromatics, i.e. anisole and cresol (20 % of initial BPE).[36] At 6 h, no phenol

remained, and 72 % combined aliphatic compound yield was observed. These secondary

products are largely attributed to hydrogenation to cyclohexanol, which further reacts to

form methylcyclohexanols. In contrast, the behavior was significantly different in the 2 mL

MeOH/1 mL DMC co-solvent owing to the phenol product being captured by undergoing *O*-

methylation to anisole (i.e., methoxybenzene). After 1 h in 2 mL MeOH/1 mL DMC with

$Cu_{20}PMO$ at 300 °C, 89 % of the BPE was converted. Anisole was found in 28 % yield of

initial BPE with 32 % phenol. After 6 h, no phenol remained, and 61 % anisole yield was

observed.
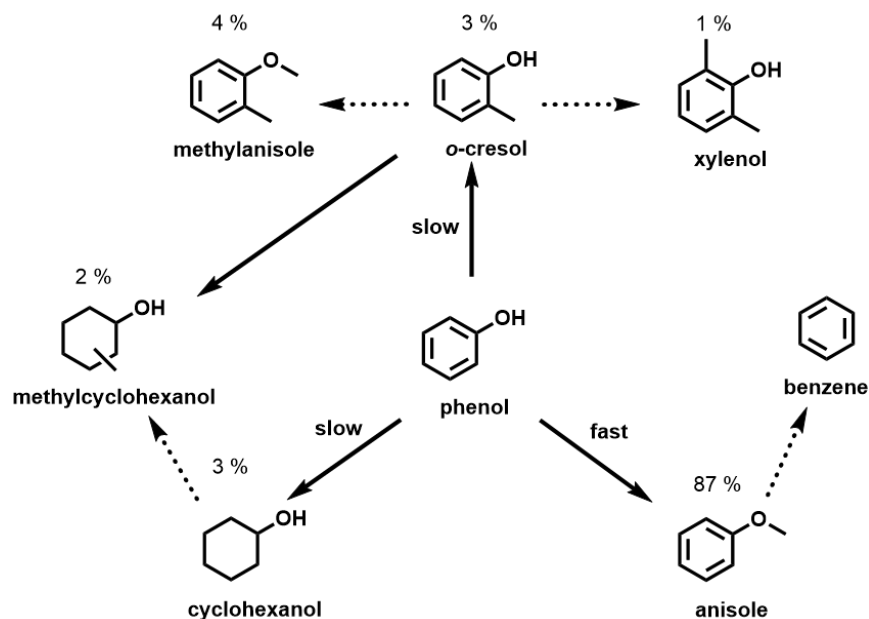
Scheme 2.1. Reactivity network for phenol in 2 mL MeOH/1 mL DMC with $Cu_{20}PMO$ at 300 °C. Values shown are mole % yield. Data for triplicate 6 h runs in Appendix A Table S2.1. Reproduced with permission from *ACS Sustain. Chem. Eng.* **2016**, *4*, 6877–6886. Copyright 2016 American Chemical Society.

The direct *O*-methylation of phenol was confirmed by studying it directly as a substrate in the MeOH/DMC co-solvent under the same reaction conditions. The data from this experiment are presented in Appendix A Table S2.1 and show that 87 % of the phenol is converted to anisole after 6 h reaction at 300 °C. Aliphatic products total only about 5 % (Scheme 2.1), and ring methylated aromatics make up the remainder. In 2 mL MeOH/1 mL DMC at 300 °C anisole undergoes some hydrodeoxygenation (HDO) to benzene, but the reaction is quite slow. While ortho, para, and meta-cresols are all observed, *O*-cresol is the major ring methylation product. This is expected as -OH is an activating ortho-para directing group. The ring-methylation product, *o*-cresol, was previously shown to convert to xylenol, methylcyclohexanol, and methylanisole in sc-MeOH.[36]

One rationale for the high reactivity of phenol compared to anisole is the difference in interactions with the catalyst surface. Porous metal oxides prepared from transition metal hydrotalcites are solid bases as evidenced by their ability to catalyze transesterification reactions of triglyceride.[41] Thus, these catalyst supports should have a greater affinity for an acidic substrate like phenol than for a neutral compound such as anisole. This proposed decrease in substrate adsorption on the catalyst surface may explain why molecules like anisole, toluene, and benzene are relatively slow to react with $Cu_{20}PMO$. Similarly, studies of SiO_2-Al_2O_3 surfaces show a much lower molar adsorptivity for anisole than for phenol at 400 °C.[42]

2-methoxy-4-propylphenol (MPP) is a more complex model for lignin disassembly intermediates than is phenol (Scheme 2.2). Two monolignols, guaiacyl (G, or i.e., coniferyl alcohol) and syringyl (S, or i.e., sinapyl alcohol), contain methoxy (-OCH_3) groups. G monomers have one methoxy while S monomers have two. In both monomers, the -OCH_3 functionalities are *ortho* to the phenolic -OH (Figure 2.1). In this context, we examined MPP

reactivity with Cu_{20}PMO in sc-MeOH and in 2 mL MeOH/1 mL DMC at 300 °C. Reaction

for 6 h in the sc-MeOH system led to ~50 % conversion of MPP to a broad distribution of

products; some were too low in abundance to identify (Appendix A Table S2.2).

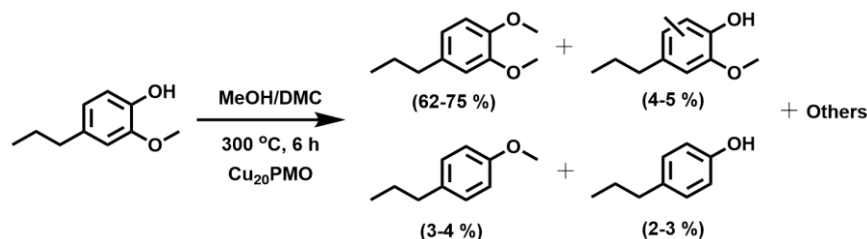**Scheme 2.2.** Observed products from the reaction of MPP in 2 mL MeOH/1 mL DMC with Cu_{20}PMO at 300 °C. Values shown are mole % yield. Data for triplicate 6 h runs in Appendix A Table S2.2. Reproduced with permission from *ACS Sustain. Chem. Eng.* **2016**, *4*, 6877–6886. Copyright 2016 American Chemical Society.

The largest component of the product mixture from the reaction in sc-MeOH was the

O-methylated MPP derivative 1,2-dimethoxy-4-propylbenzene, which represented 21 % of

the products. In the 2 mL MeOH/1 mL DMC co-solvent, there was 95 % conversion to

products and better material balance. Not surprisingly 1,2-dimethoxy-4-propylbenzene (67

% yield) was by far the predominant product; however, small amounts of the two HDO

products 4-propylphenol and 4-propylanisole were also observed (Scheme 2.2). The good

material balances from these GC-FID analyses are consistent with the absence of chars or of

undetected gaseous products with these model compounds.

The reaction of BPE with Cu_{20}PMO in the presence of DMC was reexamined to

provide a more comprehensive picture, and the temporal distribution of products from the

reaction of BPE over Cu_{20}PMO in 2 mL MeOH/1 mL DMC at 300 °C is shown in Figure

2.2. A complete product list is summarized in Appendix A Table S2.3 and the reaction

network in Scheme 2.3. The reaction network was developed from global fitting analysis

performed using DynaFit software.[43] The experimental concentration data for the different

substrates involved in the reaction network are fitted using a non-linear least squares approach. Dynafit concurrently produces growth and decay curves for all compounds in a proposed reaction network using an algorithm defined by a system of first-order ordinary differential equations. The rate constants in the given reaction network are optimized to best fit the experimental temporal data. For example, the ordinary differential equation for BPE in the fit model for Scheme 2.3 was $d[BPE]/dt = -k_1[BPE] - k_{s1}[BPE]$. The rate of BPE disappearance was k_1 (1.7 h^{-1}). The rate constant k_{s1} (~0 h^{-1}) denotes an unknown product sink specifically to evaluate for unaccounted products. In this case all the products from BPE were accounted for by the modeled reaction network.

In Scheme 2.3, hydrogenolysis of BPE produces toluene and phenol. Toluene is unreactive and remains in the reaction solution once produced. There are three known pathways shown for phenol. Aromatic ring hydrogenation produces cyclohexanol and ring methylation produces O-cresol. Under these conditions (2 mL MeOH/1 mL DMC) these are the minor pathways. The product sink (k=0.42 h^{-1}) for O-cresol is primarily 2-methylcyclohexanol. The major pathway in MeOH/DMC is O-methylation to form anisole. The product sink (k=0.04 h^{-1}) for anisole is primarily benzene.
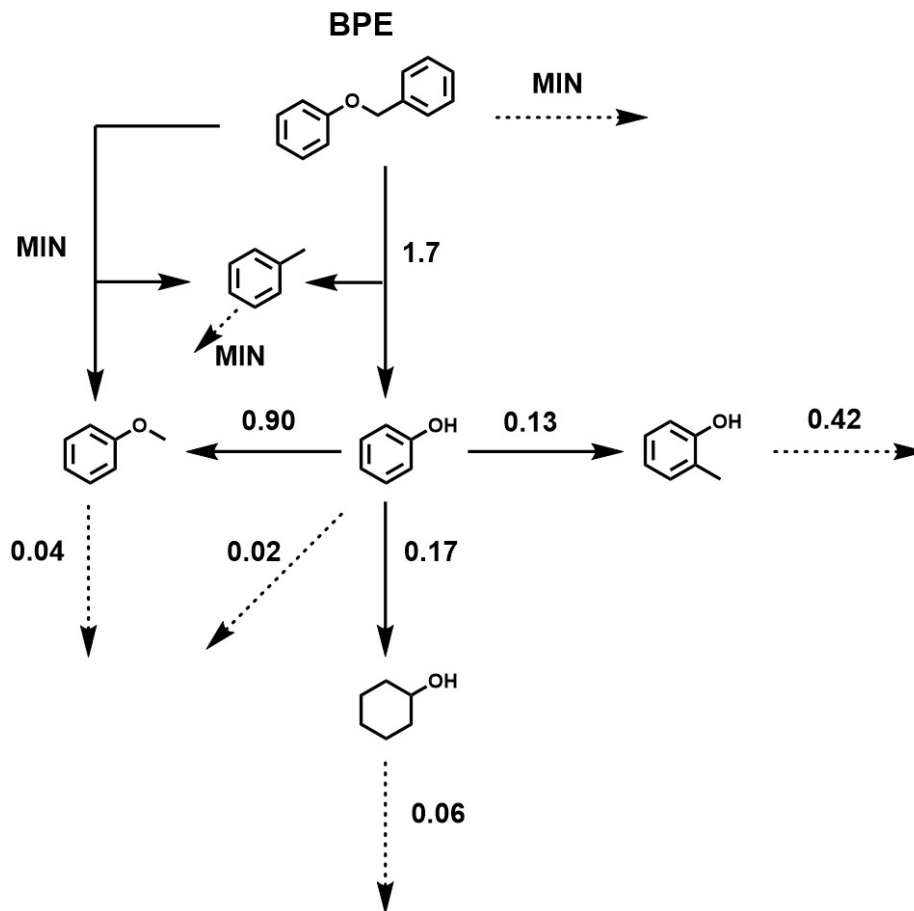
Scheme 2.3. Reactivity network from the reaction of BPE in MeOH/DMC with $Cu_{20}PMO$ at 300 °C. For the observed rate constants (k_{obs}) the units are h^{-1}. MIN refers to k_{obs}=~0. Reproduced with permission from *ACS Sustain. Chem. Eng.* **2016**, *4*, 6877–6886. Copyright 2016 American Chemical Society.

Within 2 h, BPE was entirely converted, and toluene yield from HDG of the $PhCH_2$-OPh bond was quantitative within experimental uncertainty (±5 %). The amount of toluene was essentially constant over the next 4 h. The yield of anisole after 2 h, presumably by *O*-methylation of intermediate phenol was 71 %. Although anisole is relatively unreactive, it underwent a gradual decrease in percent yield over the next 4 h. By contrast when the catalysis was carried out in sc-MeOH alone, the yield of toluene was comparable, but the principal oxygen containing products were methylcyclohexanols (72 % yield, Appendix A Table S2.3). Reducing the DMC used in the co-solvent system (0.5 mL instead of 1 mL to

20

give a 5:1 MeOH/DMC ratio) resulted in a 42 % decrease in yield of anisole and consequently higher yield of aliphatic products (Appendix A Table S2.4). This indicated that the *O*-methylation of phenol is performed by DMC and not MeOH. Bernt and coworkers previously determined hydrogenolysis reactions are first order with respect to the substrate and independent of H_2 pressure between operating temperatures of 280-330°C in sc-MeOH.[44] The authors hypothesized that the fast hydrogen production rate of CuPMO from methanol reforming saturates the catalyst active sites for hydrogenolysis.[44] In the 2 mL MeOH/1 mL DMC cosolvent system, both solvents are in much higher concentration than the substrates and thus the reactions are under pseudo first order conditions.
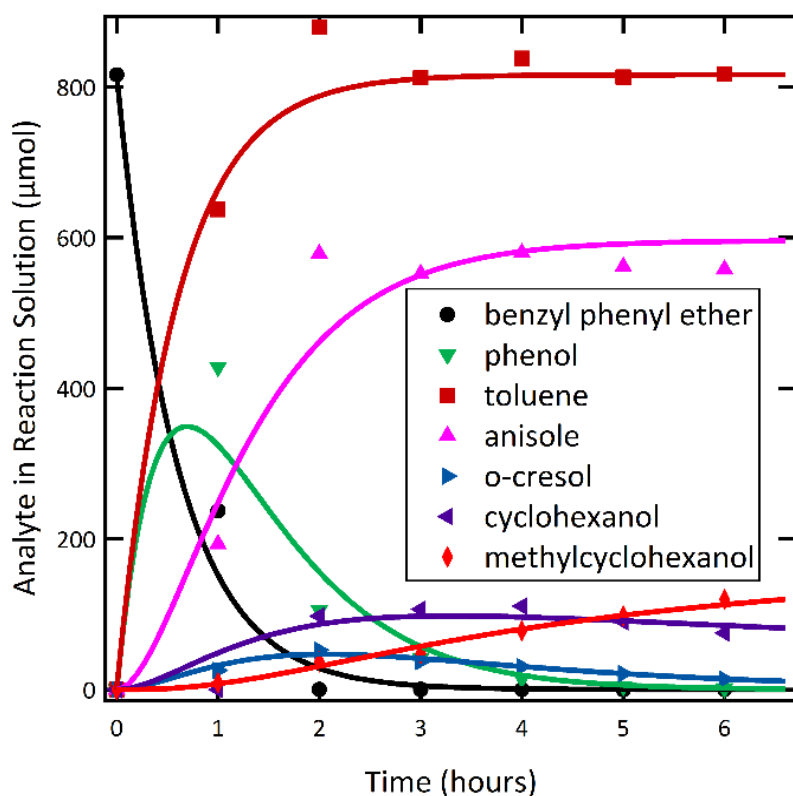
Figure 2.2. Temporal product distribution and progress curve fits from reaction of BPE (~800 µmol) in MeOH/DMC with $Cu_{20}PMO$ (50 mg) at 300 °C. Minor products are listed in Appendix A Table S2.3. The fits were generated from Dynafit. Reproduced with permission from *ACS Sustain. Chem. Eng.* **2016**, *4*, 6877–6886. Copyright 2016 American Chemical Society.

21

O-methylation of phenols by DMC results not only in the formation of the stable PhOCH$_3$ species but also in release of MeOH and CO$_2$. Thus, analysis of the gas phase generated by the reaction of BPE in MeOH/DMC with Cu$_{20}$PMO at 300 °C showed significantly more CO$_2$ production than seen in sc-MeOH alone (Appendix A Tables S2.5 & S2.6, Figure 2.3). Notably, over the course of 6 h, the CO$_2$ initially formed diminishes with a corresponding increase of CO in the gas phase. This is likely the result of reverse water gas shift owing to excess H$_2$ generated by Cu$_{20}$PMO reforming of MeOH.
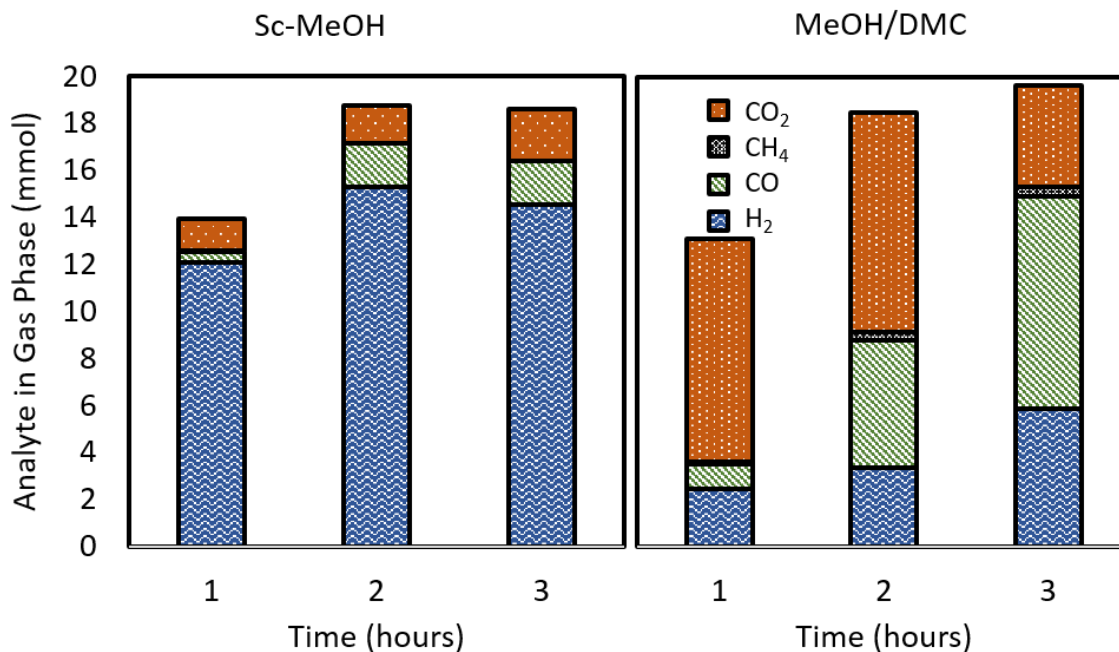
Figure 2.3. Temporal gas product distribution from the reaction of BPE in Sc-MeOH (left) and 2 mL MeOH/1 mL DMC (right) with Cu$_{20}$PMO at 300 °C. Reproduced with permission from *ACS Sustain. Chem. Eng.* **2016**, *4*, 6877–6886. Copyright 2016 American Chemical Society.

As Song et al. noted,[23,24] the medium very likely plays a role in the solvolysis of lignin ether linkages to generate lower molecular weight and soluble fragments. One can easily envision such pathways for the α-O-4 linkage of BPE. To address this question, we

studied BPE reactivity in sc-MeOH and MeOH/DMC absent the $Cu_{20}PMO$ catalyst. In sc-MeOH at 300 °C, BPE underwent about 23% conversion after 3 h and 51% conversion after 6 h with respective material balances of 89 and 79 % (Appendix A Table S2.7). The identifiable products were mostly toluene (49 %) and phenol (38%), although other products, such as benzophenone (12%) and 2-phenylmethylphenol (10%), were identified by gas chromatography-mass spectrometry. The toluene and phenol were possibly formed by an analogous mechanism to BPE acidolysis proposed by Pelzer et. al.[45] Hydrolysis of BPE by residual water in the solvents would result in phenol and benzyl alcohol. Dehydration of benzyl alcohol would give toluene. The material balance progressively worsened as the reaction proceeded owing to formation of insoluble, presumably polymeric, materials which is consistent with the reaction pathways proposed by Pelzer and coworkers.[45] The result without catalyst compares poorly to the 74% conversion after 1 h and ~100% conversion after 3 h under comparable conditions with $Cu_{20}PMO$ present (material balance ~100%). These observations indicate that the role of the catalyst is not only to activate the ether linkage toward HDG, but it also may prevent char formation by intercepting intermediates that can undergo condensation. When the analogous catalyst-free reaction of BPE was carried out in the 2 mL MeOH/1 mL DMC, conversion was only ~43 % after 6 h. Toluene (34 %) and phenol (37 %) were the most prominent products, but, unlike the reaction in sc-MeOH, anisole (24 %) was also observed. Benzophenone (12%) and 2-phenylmethylphenol (10%) were also observed. The material balance was ~90 % (Appendix A Table S2.8). Thus, it appears that the solid base catalyst $Cu_{20}PMO$ serves to activate DMC for the *O*-methylation reactions.

Another question we had was whether the metal oxide support itself would catalyze these transformations. When the BPE reaction was studied in 2 mL MeOH/1 mL DMC at

300 °C with copper-free PMO (50 mg) derived from calcining commercially available 3:1 Mg-Al hydrotalcite, the conversion was 32 % after 6 h. The four most prominent products were toluene (18 %), benzophenone (11 %), phenol (8 %), and anisole (7 %) (Appendix A Table S2.9). The material balance improved somewhat (to ~96 %), compared to the catalyst-free reaction. Although there was some shift in the product distribution, the copper-free PMO was not significantly more active than the catalyst-free systems. The production of anisole was high in relation to phenol, consistent with the work of Talawar, Jyothi, and coworkers.[39,40]
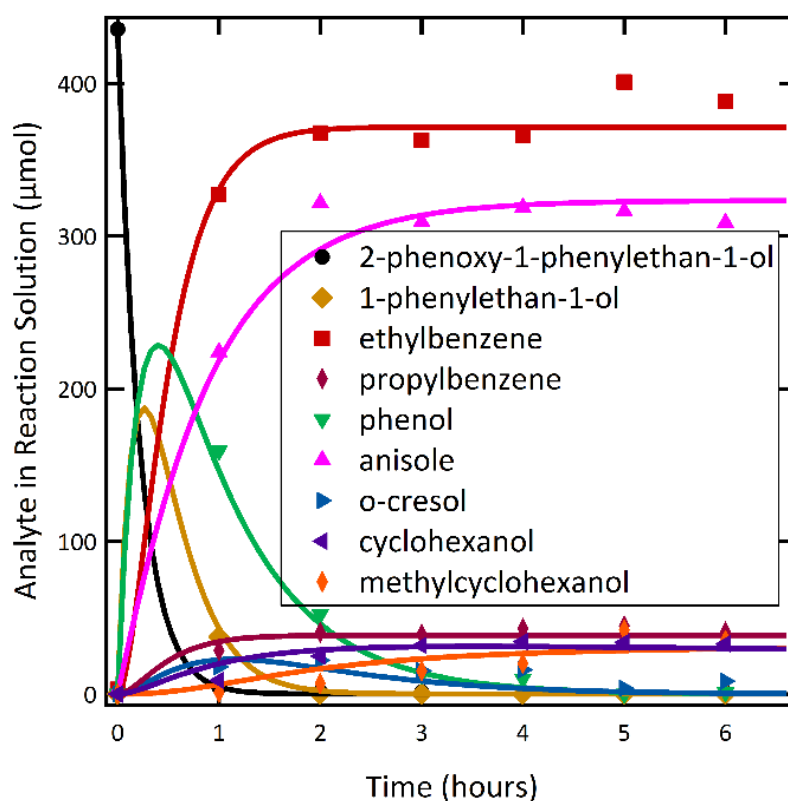
Figure 2.4. Temporal product distribution from the reaction of 2-phenoxy-1-phenylethan-1-ol (~500 µmol) in MeOH/DMC with $Cu_{20}PMO$ (50 mg) at 300 °C. Additional products are listed in Appendix A Table S2.10. Reproduced with permission from *ACS Sustain. Chem. Eng.* **2016**, *4*, 6877–6886. Copyright 2016 American Chemical Society.

Figure 2.4 summarizes the temporal evolution of 2-phenoxy-1-phenylethan-1-ol (PPE) and the products for reaction with $Cu_{20}PMO$ in the MeOH/DMC co-solvent at 300 °C. The β-O-4 bond was cleaved with 98 % conversion in 1 h. A small amount of the expected 1-phenylethanol was observed at 1 h, but this apparently underwent rapid HDO to ethylbenzene (76-92 % yield). Propylbenzene (6-10 % yield, Appendix A Table S2.10) was a lesser product and can be attributed to β-carbon methylation of acetophenone (derived from 1-phenylethanol dehydrogenation) followed by HDO (Scheme 2.4).[35] Anisole was also formed (74 % yield after 2 h) and, as noted above, underwent modest conversion over longer reaction times. After 3 h, aromatic products represented ~91 % of the theoretical yield. At 6 h the aromatic yield was the same, although there was some redistribution of the products. The aliphatics were mostly cyclohexanols; the remainder was cyclohexanes. Of those products originating from the phenol fraction, the aromatic yields were 89 % and 83 % respectively at 3 h and 6 h. Material balance for each time point was ~100%.

Scheme 2.4. Plausible mechanism for the β-carbon methylation of 1-phenylethanol to form propylbenzene. Acetophenone tautomerizes to the enol 1-phenylethen-1-ol. DMC = dimethyl carbonate.

Appendix A Table S2.10 also summarizes products and yields from the analogous PPE reactions catalyzed by $Cu_{20}PMO$ in sc-MeOH at 300 °C. In comparison to the 2 mL MeOH/1 mL DMC system, the total yield of aromatic products after 6 h was only 69 %, mostly ethylbenzene and propylbenzene. Of the products originating with the phenol fraction, the aromatic yield was only 33%. Scheme 2.5 also presents the results of a Dynafit

analysis of the temporal data shown in Appendix A Table S2.10 and Figure 2.4 to estimate rate constants for respective reaction network pathways for PPE in the MeOH/DMC co-solvent. Unlike BPE (Appendix A Scheme S2.1), the results of the kinetics fitting imply a direct pathway from PPE to anisole. Similar fits were reported in our previous studies of reactivities in sc-MeOH.[36] Comparisons of key reactions such as aryl-ether HDG indicate that these rates are essentially the same in the two solvent systems.
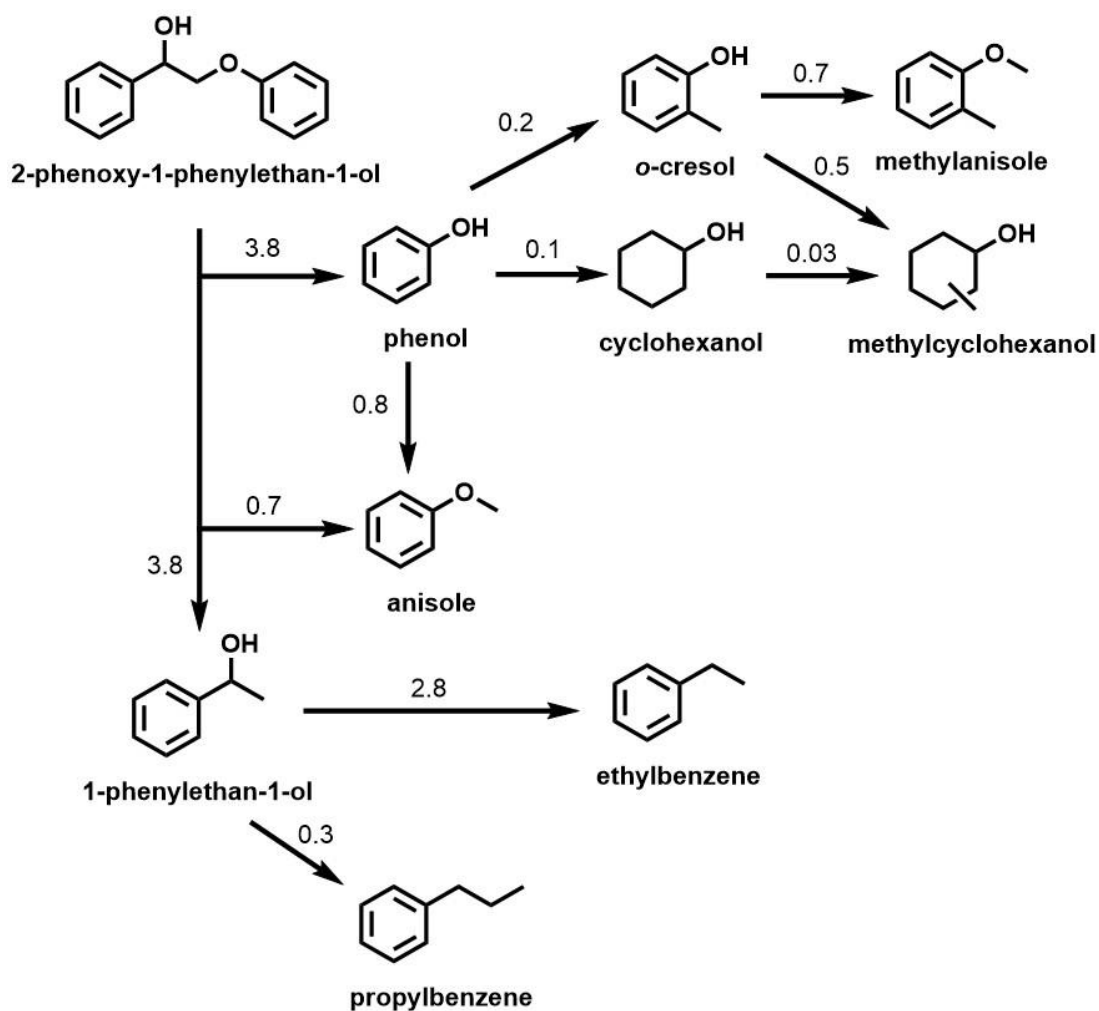
Scheme 2.5. Reactivity network from the reaction of PPE in MeOH/DMC with $Cu_{20}PMO$. The units for the calculated rate constants (k_{obs}) are h^{-1}. Reproduced with permission from *ACS Sustain. Chem. Eng.* **2016**, *4*, 6877–6886. Copyright 2016 American Chemical Society.

Comparisons across the reactivity network provide valuable insight into improving the catalytic selectivity (Table 2.1). Since phenolic derivatives are inevitable outcomes of reductive lignin disassembly, one must address the facile ring hydrogenation and methylation of these species in order to enhance the yield of aromatics. Possible scenarios might include designing an HDO co-catalyst to be very active toward phenols, modifying the catalyst composition to suppress phenolic hydrogenation, or chemically trapping such intermediates.[44] What has been presented thus far is the third approach whereby a 'green' chemical reagent, dimethyl carbonate (DMC) was successfully used to trap reactive intermediates.

Table 2.1. Summary of relative trends in k_{obs} for key reactions with 0.5 mmol substrate, 50 mg Cu$_{20}$PMO, and 3 mL sc-MeOH or MeOH/DMC, at 300 °C.[36] Includes values reported in Bernt et. al.[35]

Reaction	Solvent	k_{obs} (h^{-1})	Qualitative rate
β-O-4/α-O-4 ether hydrogenolysis	Sc-MeOH	>1.0	Fastest
	MeOH/DMC	>1.0	Fastest
Phenol O-methylation	Sc-MeOH	0.05-0.10	Slow
	MeOH/DMC	0.8-1.2	Fast
Phenol Hydrogenation	Sc-MeOH	0.2-0.75	Fast
	MeOH/DMC	0.10	Slow

According to the k_{obs} for phenol hydrogenation versus phenol O-methylation, the MeOH/DMC system can limit aliphatic product formation to between 8 and 13 %. Some plausible future objectives for improving reactive intermediate trapping would be (1)

qualitatively matching *O*-methylation rate with hydrogenolysis or (2) further disfavoring hydrogenation chemistry. Reaction temperature and solvent system provide two controls for achieving these objectives. Alternatively, selective catalyst poisoning could also be a promising avenue towards a more selective system.

Section 2.2.2. of this chapter previously discussed the complicated and variable structural nature of lignin. Most of the focus up to this point has been on the relatively reactive aryl-ether model compounds. Diphenyl ether (DPE) is a model for the 4-O-5 linkage in lignins, while 2,3-dihydrobenzofuran (DHBF) contains β-5 and α-O-4 type linkages (Figure 2.5). The β-5 linkage is common to softwoods (9-12 % occurrence) such as pine but are less prevalent in hardwoods (3-11 % occurrence) such as poplar.[7,10] The 4-O-5 linkage only occurs in about 2 % of linkages in both softwood and hardwood.[9] The 4-O-5 and β-5 linkages are more resistant to cleavage than are the α-O-4 and β-O-4 linkages, and this is consistent with the current results.[22] For example, the reaction of DPE with $Cu_{20}PMO$ in sc-MeOH or in MeOH/DMC at 300 °C for a period of 6 h, led to relatively little conversion (15% and 7%, respectively) in either medium (Table 2.2). The expected products of DPE hydrogenolysis are phenol and benzene. The mass balance for the phenol derived products of DPE at 300 °C was 74 % in MeOH/DMC and 82 % in sc-MeOH. These results indicate that $Cu_{20}PMO$ is ineffective at breaking 4-O-5 lignin linkages. DPE is a very simple model compound, however, theoretical bond dissociation energies for 4-O-5 linkages with $-OCH_3$ substituents are only 3-11 % lower.[46]

dihydrobenzofuran(DHBF)   diphenyl ether (DPE)
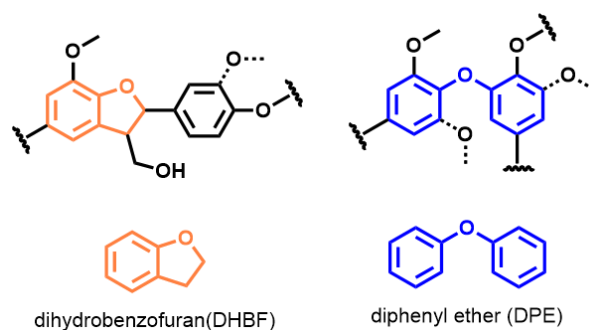
Figure 2.5. Structures of the β-5 model dihydrobenzofuran and the 4-O-5 model diphenyl ether. Reproduced with permission from *ACS Sustain. Chem. Eng.* **2016**, *4*, 6877–6886. Copyright 2016 American Chemical Society.

Table 2.2. Reaction of diphenyl ether with $Cu_{20}PMO$ at 300 °C. [a]MeOH/DMC and [b]sc-MeOH.

Compound (μmol)	0 h	6 h[a]	6 h[b]
anisole	0	1	2
benzene	0	16	34
cyclohexanol	0	0	0
diphenyl ether	266	249	227
methylcyclohexanol	0	8	27
o-cresol	0	1	1
phenol	0	2	2
Phenol-derived mass balance (%)	-	74	82
Benzene mass balance (%)	-	95	88
Total mass balance (%)	-	99	98

DHBF proved to be more reactive than DPE in the presence of $Cu_{20}PMO$ which was previously studied in Macala et. al.[28] After 6 h at 300 °C, DHBF conversion was 57 % in sc-MeOH but only 27 % in MeOH/DMC (Table 2.3). (The respective material balances were 90 % and ~100 %.) The expected β-5 hydrogenolysis product is 2-ethylphenol from DHBF.[28] In 2 mL MeOH/1 mL DMC, a 51 % yield of 2-ethylphenol was observed. The

second most abundant product was 2-ethylcyclohexanol (25 % yield), indicating that DMC is not effective at O-methylation under these conditions. As expected much of the 2-ethylphenol was hydrogenated in sc-MeOH and resulted in only 13 % yield. The most abundant product was 2-ethylcyclohexanol (45 % yield) however methyl-2-ethylphenol (8 % yield) and ethylbenzene (6% yield) were also observed. The 2 mL MeOH/1 mL DMC cosolvent system did not drastically improve the yield of the *O*-methylated product, 2-ethylanisole (3 % yield). Although the reactivity of DHBF was lower in MeOH/DMC, a larger percentage of the products were aromatic (73%) than in sc-MeOH (29 %). However, it is not entirely clear why this was so, since the O-methylated product, 2-ethylanisole, was a relatively minor product in the former. One explanation is there is lower H_2 pressure measured in 2mL MeOH/1 mL DMC (Figure 2.3), making hydrogenation slower.

Table 2.3. Reaction of DHBF with $Cu_{20}PMO$ at 300 °C. [a]MeOH/DMC and [b]sc-MeOH.

Compound (μmol)	0 h	6 h[a]	6 h[b]
anisole	0	0	1
benzofuran	2	2	1
dihydrobenzofuran	229	167	98
dimethyl-ethylcyclohexanol	0	0	1
ethylanisole	0	2	0
ethylbenzene	0	2	8
ethylcyclohexane	0	0	1
ethylcyclohexanol	0	16	60
ethylcyclohexanone	0	1	4
ethylphenol	0	32	17
methyl-dihydrobenzofuran	0	1	1
methyl-ethylphenol	0	6	10
octahydrobenzofuran	0	1	2
Total mass balance (%)	-	101	90

2.3.2. *O*-Methylation in Lignin Reactions

The substrate organosolv poplar lignin (OPL) was examined to assess whether (and how) the conclusions drawn from the above model systems inform our understanding of a more complex model for lignin conversion. Reductive disassembly was performed in a mini-autoclave reactor that contained 100 mg of OPL, 100 mg of $Cu_{20}PMO$, and 3 mL of MeOH kept at 300 °C for either 3 or 6 h. In MeOH/DMC cosolvent at 300 °C, lignin disassembly likely occurs in a step-wise manner, first by solvolysis to give lower molecular weight

fragments,[24] followed by catalytic HDG of the aryl-ether bonds of the fragments (Scheme 2.6).
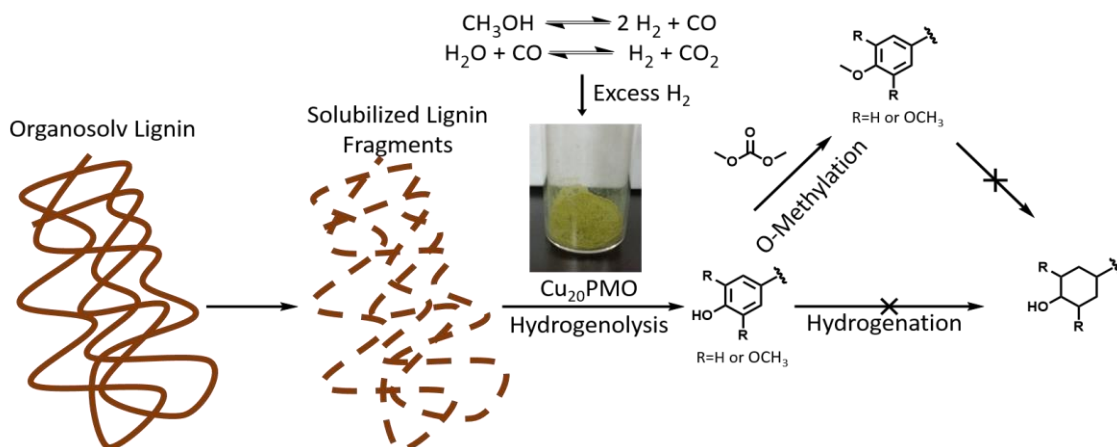
Scheme 2.6. Proposed mechanism of lignin disassembly in MeOH/DMC as catalyzed by $Cu_{20}PMO$. Solvolysis breaks lignin into smaller fragments. Catalytic HDG further disassembles them to phenols. *O*-methylation by DMC yields methoxybenzenes. Reproduced with permission from *ACS Sustain. Chem. Eng.* **2016**, *4*, 6877–6886. Copyright 2016 American Chemical Society.

Henceforth, liquid samples of disassembled lignin are discussed using the terms "unprocessed" and "non-volatile". The "unprocessed" products refers to liquid samples collected from the reaction that have had only $Cu_{20}PMO$ removed by filtration. The "non-volatile" products refer to liquid samples from which the solvent was removed under vacuum at ~-20 °C in addition to catalyst removal. The weight percent of the recovered non-volatile, soluble product from OPL disassembly by $Cu_{20}PMO$ was 45 wt % in sc-MeOH and 64 wt % in MeOH/DMC. In the absence of catalyst, considerable char formation was observed in each medium (35 and 32 wt %, respectively, Appendix A Table S2.11). No char was observed when the catalyst was present. Similar to the reactions with lignin model compounds, more CO_2 and less H_2 were generated for reactions in MeOH/DMC compared to those in sc-MeOH.

GPC analysis was performed on untreated OPL as well as unprocessed and non-volatile products generated in sc-MeOH and in 2 mL MeOH/1 mL DMC with and without $Cu_{20}PMO$ at 3 h. Relative molecular weight values including number average molecular weight (M_n), weight average molecular weight (M_w), and polydispersity index (PDI = M_w/M_n) were determined based on a polystyrene standard calibration curve. All data are summarized in Appendix A Table S2.11. Figure 2.6 shows the data for untreated OPL, unprocessed, and non-volatile products generated in sc-MeOH and in 2 mL MeOH/1 mL DMC with $Cu_{20}PMO$ at 3 h. There was only a modest difference between the chromatographs for the unprocessed and non-volatile products (the latter being slightly higher M_n and M_w), meaning that the product molecular weight distributions were not seriously affected by the solvent removal step. The high PDI for all samples indicates a broad distribution of molecular weights. However, the M_n for each depolymerized sample (~310-390 g/mol) is ~3-4 times lower than that of untreated OPL (~1,290 g/mol). This result indicates the macromolecular structure of lignin is largely disassembled to lower molecular weight monomeric (~200 g/mol), dimeric (~400 g/mol), and trimeric (~600 g/mol) products. The M_w is considerably larger for products from reactions without $Cu_{20}PMO$ (630-720 g/mol) than from reactions with $Cu_{20}PMO$ (400-510 g/mol) (Appendix A Table S2.11 and Figure 2.6). Notably, the M_n and M_w for samples disassembled in 2 mL MeOH/1 mL DMC with $Cu_{20}PMO$ are slightly larger than their sc-MeOH counterparts. A possible explanation is *O*-methylation by DMC contributes to the molecular weight, however the experimental uncertainty of this GPC technique is too large to draw that conclusion.

33
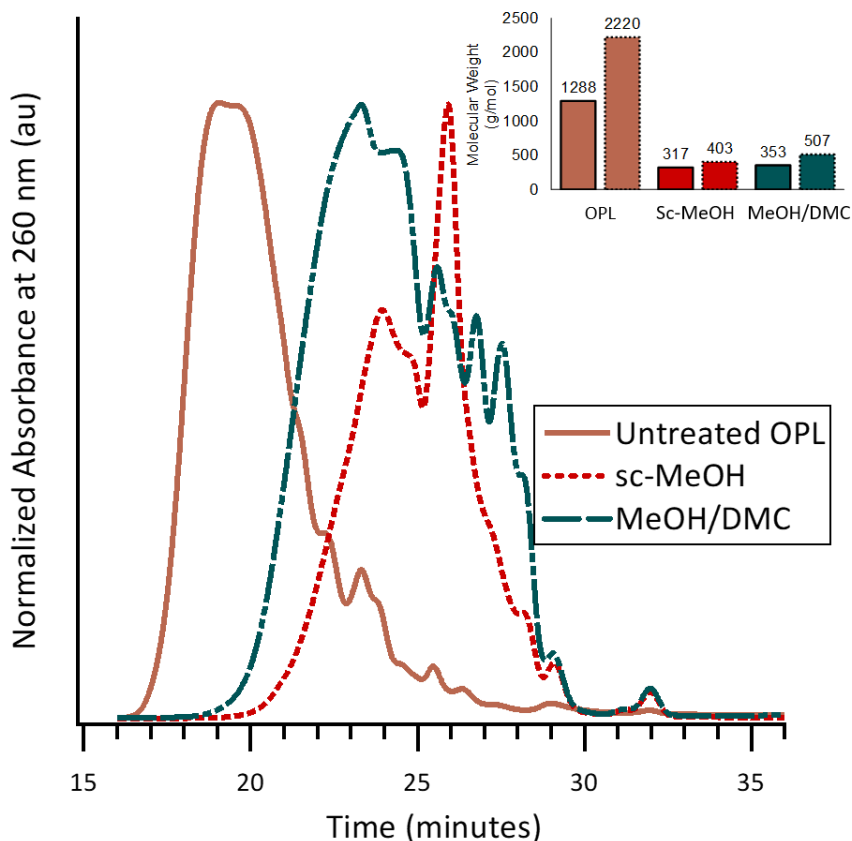
Figure 2.6. GPC chromatograms for untreated OPL and unprocessed liquid samples. Inset: number average (M_n) and weighted average (M_w) molecular weight for each sample shown. Adapted with permission from *ACS Sustain. Chem. Eng.* **2016**, *4*, 6877–6886. Copyright 2016 American Chemical Society.

The decrease in molecular weight can be attributed to solvolytic fragmentation and catalytic HDG of the lignin aryl-ether bonds. This is supported by [1]H (Figures 2.7 & 2.8) and 2D ^{1}H-^{13}C HSQC (Figure 2.9) NMR data on the non-volatile products of lignin disassembly with $Cu_{20}PMO$ in sc-MeOH and MeOH/DMC. These data show a large decrease in the chemical shifts associated with both the β- and γ-carbon of various aryl-ether linkages; coupled with a large increase in alkyl carbons attached to aromatic rings. The ^{1}H NMR spectra confirmed that the vacuum processing removed the MeOH and DMC, but it is also likely that some volatile aliphatic products are removed. Thus, the NMR analyses provides

information only about the molecular products with relatively low volatility (e.g., oligomers or small molecules with a low vapor pressure). GC-MS analysis of the liquid nitrogen-trapped solvent and volatile product components removed from the unprocessed products of the 3 h OPL disassembly indicated the minor presence of unidentified compounds (probably aliphatics). Whereas GC-MS analysis of the unprocessed products will detect almost all small molecule compounds (even dimers), it is not capable of oligomer analysis. Therefore, by combining the results of the unprocessed products GC-MS analysis and non-volatile products NMR analysis, a comprehensive picture can be developed to describe the chemical and compositional profile of OPL disassembly products.
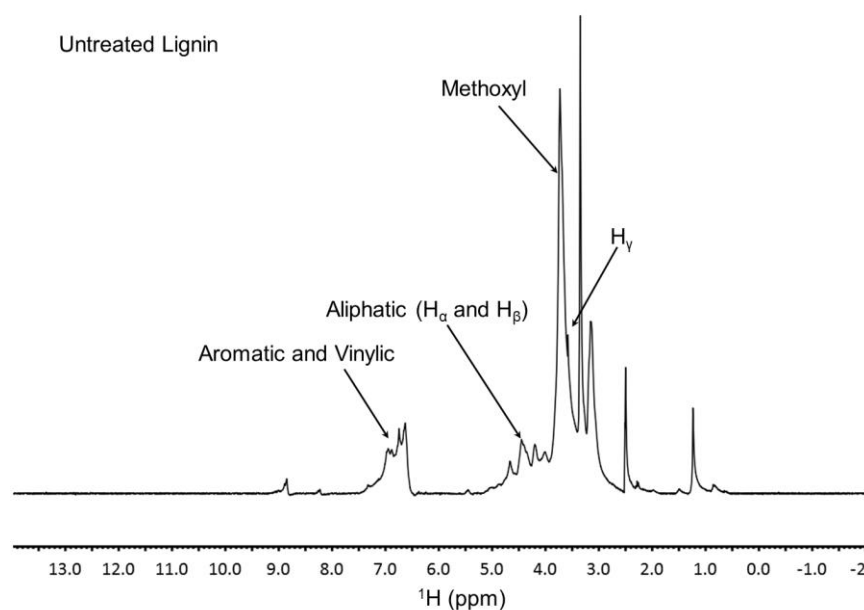
Figure 2.7. ^{1}H NMR spectrum for untreated organosolv poplar lignin (OPL). Reproduced with permission from *ACS Sustain. Chem. Eng.* **2016**, *4*, 6877–6886. Copyright 2016 American Chemical Society.

Barta et. al previously used holistic ^{1}H NMR analysis of OPL and catalytic reaction products to evaluate product distributions. In short, three types of proton environments were examined, aromatic, aliphatic, and oxygenated (O-aliphatic).[28] The extent of OPL

disassembly and deoxygenation can be evaluated by the decrease in integration area of chemical shift range 3.0-5.0 ppm. Hydrogenolysis should result in a concurrent increase in the integration area of chemical shift range 0.3-3.0 ppm (aliphatic). Deoxygenation could result in increase in both aliphatic and aromatic (chemical shift range 5.0-7.2 ppm) proton environments.
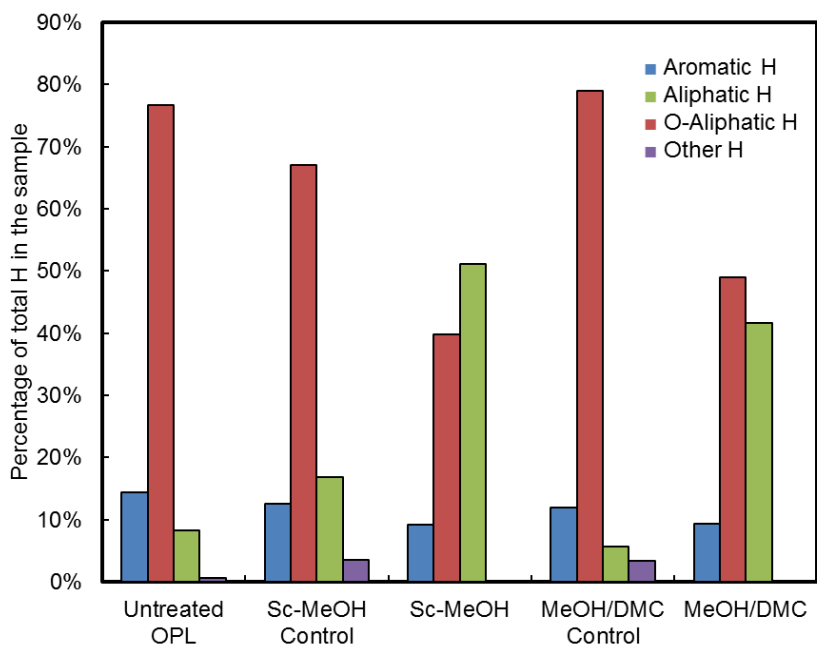
Figure 2.8. Proton percentage (%) distribution for untreated OPL, disassembled lignin in sc-MeOH solvent with/without $Cu_{20}PMO$, and disassembled lignin in sc-MeOH/DMC solvent with/without $Cu_{20}PMO$ in ^1H NMR spectrum. Control = without $Cu_{20}PMO$. Reproduced with permission from *ACS Sustain. Chem. Eng.* **2016**, *4*, 6877–6886. Copyright 2016 American Chemical Society.

Untreated OPL is characterized by 76% O-aliphatic protons, 15% aromatic protons, and 9% aliphatic protons. Substantial decreases in O-aliphatic proton environments was only observed for reactions with $Cu_{20}PMO$. There are more O-aliphatic protons observed in 2 mL MeOH/1 mL DMC presumably due to phenolic *O*-methylation. This is offset by higher aliphatic protons observed in sc-MeOH versus MeOH/DMC. It is not evident that aromatic

products were maintained in MeOH/DMC from this data. Consequently, additionally characterization methods were performed.
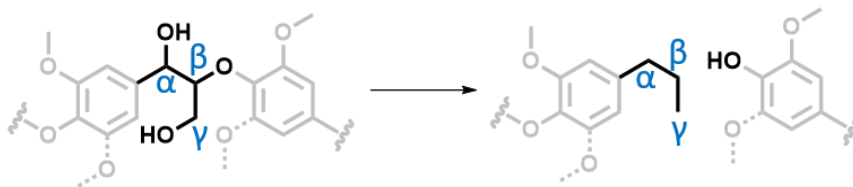
Scheme 2.7. Depiction of hydrogenolysis and hydrodeoxygenation of β-O-4 motif showing the α-,β-, and γ-carbon positions represented in the aryl-ether (left) and the aryl-propyl (right) moieties.

The 2D ^{1}H-^{13}C HSQC NMR spectra for untreated OPL and non-volatile products from disassembly in sc-MeOH or MeOH/DMC at 300 °C for 3 h are shown in Figure 2.9. Chemical shift assignments are presented as '^{1}H/^{13}C ppm'.[47] There are some key differences that indicate lignin is disassembled. The β-carbon of the A-S and A-G linkage (Scheme 2.7) for untreated OPL can be clearly seen at 4.2/85 ppm and 4.4/82 ppm for the threo and erythro diasteromers (non-mirror image non-identical isomers). The non-volatile products show complete disappearance of these peaks. The alkyl-carbons attached to an aromatic ring are labeled F1 through F5. The appearance of ^{1}H/^{13}C environments for F2 (2.1/15 ppm), F3 (2.4/37 ppm and 2.5/40 ppm), and F4 (1.1/30 ppm and 1.5/24 ppm) indicate that the broken A-S and A-G linkages underwent HDO to form propylmethoxybenzene like products (Scheme 2.7). The peak for aliphatics (F5, 0.9/15 ppm) is larger for non-volatile products from reaction in sc-MeOH compared to reaction in DMC. There is however an unassigned region which borders with the propyl-aromatic F4 region that could not assigned based on literature. The recalcitrant resinol linkage represented as motif C is still present after the reaction ($C_α$, 4.7/85 ppm $C_β$, 3.6/55 ppm, and $C_γ$, 3.7/71 ppm and 4.2/71 ppm). For binding motif C, the γ-carbon peak was the only one of the three to decrease, which implies a

carbon-carbon linkage is left. The γ-carbon of the A-S/G linkage also remains after 3 h reaction. These 2D NMR results are consistent with monomeric products as well as larger fragments which was concluded from the GPC results.
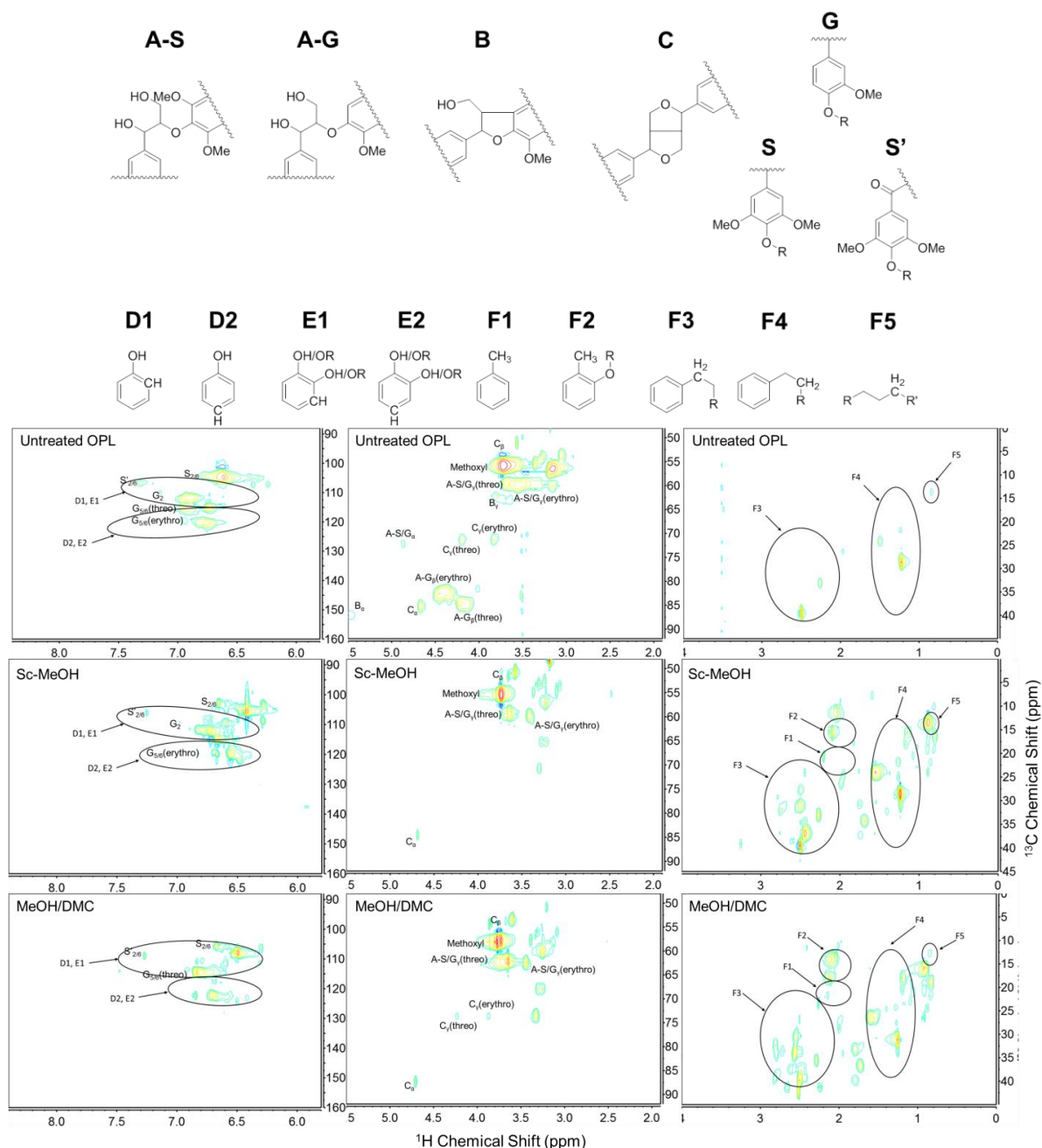
Figure 2.9. HSQC-NMR spectra and the assignments (with key above) for untreated OPL and its depolymerized product. Reproduced with permission from *ACS Sustain. Chem. Eng.* **2016**, *4*, 6877–6886. Copyright 2016 American Chemical Society.

38

A quantitative ^{31}P NMR analytical method was used to evaluate the types of free –OH groups that are present in untreated OPL and in the non-volatile products from the catalyzed reactions in sc-MeOH and in MeOH/DMC. This involved phosphorylating the free –OH groups of the samples with 2-chloro-4,4,5,5-tetramethyl-1,3,2-dioxaphospholane (TMDP). The ^{31}P chemical shifts and integration regions for the phosphorylated aryl/alkyl hydroxyl groups were recorded and analyzed by procedures previously used to analyze the hydroxyl functional groups present in lignins and in pyrolysis oils (Appendix A Table S2.12).[48,49] This quantitative method determines the amounts (mmol) of different types of -OH functional groups per gram of sample. The results of such experiments with untreated OPL and with the non-volatile products from the catalytic disassembly of OPL in sc-MeOH and in MeOH/DMC after 3 h reaction are shown in Figure 2.10. These data indicate the removal and disruption of the primary and secondary aliphatic alcohols of the alkyl chains linking the aromatic units of lignin. This may result from HDO occurring in conjunction with the HDG disassembly reactions.

Hydrogenolysis of lignin aryl-ether linkages generates phenols, principally the syringyl and guaiacyl terminated fragments (Figure 2.1). The relatively high content of syringyl units seen in Figure 2.10 for the disassembly products is consistent with the higher degree of oxygenation in hardwoods such as poplar.[7] For OPL disassembly in 2 mL MeOH/1 mL DMC co-solvent, lower quantities of syringyl (~142.7 ppm) and guaiacyl (140.2-139.0 ppm) –OH are seen relative to disassembly in sc-MeOH, reflecting partial O-methylation of these species in the co-solvent system. Notably, increased carboxylic acid (136-133.6 ppm) –OH content is seen in the products of catalytically disassembled lignin. The ^{31}P NMR spectra of the products from OPL disassembly in sc-MeOH or MeOH/DMC show no

evidence of substitution at the 5-Carbon position or condensed phenolic alcohols, which are formed by recombination of HDG products. This absence further confirms that $Cu_{20}PMO$ suppresses condensation of reactive intermediates, thus preventing char formation.
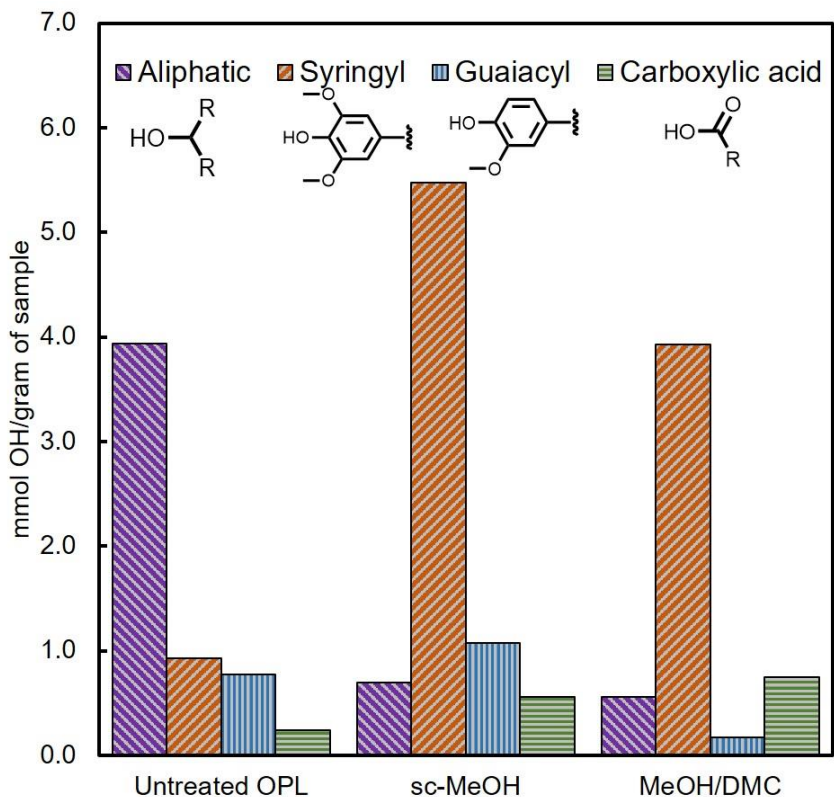
Figure 2.10. Quantification of the OH functional group content (mmol/g) using the ^{31}P NMR technique with organosolv poplar lignin, and products of OPL disassembly in sc-MeOH, and in MeOH/DMC after 3 h reaction at 300 °C. The bars for each experiment are presented in the order shown at the top. Reproduced with permission from *ACS Sustain. Chem. Eng.* **2016**, *4*, 6877–6886. Copyright 2016 American Chemical Society.

^{13}C NMR analyses were also performed on DMSO-d$_6$ solutions of untreated OPL (Figure 2.11) and the non-volatile product mixtures from the OPL disassembly in sc-MeOH and in MeOH/DMC (Figure 2.12). This method relies upon the chemical shifts determined by Ben et al.[49] (Table 2.4) to characterize functional group carbons of lignin and pyrolysis oil products. For the non-volatile products, the ^{13}C NMR spectra (Figure 2.12) displayed a

number of peaks in the 90-0 ppm region indicating the presence of aliphatic carbons. These peaks may indicate the presence of non-volatile aliphatic products as well as alkyl substituents on aromatic lignin fragments. Based on integration of the aliphatic region (excluding DMSO) and of the region assigned to aromatic carbons (160-100 ppm), one can evaluate changes in the nature of the products relative to untreated OPL. There was a marked reduction in the number of aliphatic carbons adjacent to an oxygen atom (95.8-60.8 ppm) from about 13% to ~ 1% (excluding aromatic methoxide groups) for non-volatile products generated by OPL disassembly with Cu$_{20}$PMO in sc-MeOH or MeOH/DMC. This observation is consistent with the hydrogenolysis of β-O-4 and α-O-4 ether linkages as well as the HDO of aliphatic alcohols seen in the 2D ^{1}H-^{13}C NMR (Figures 2.9).

Table 2.4. ^{13}C NMR chemical shift assignment range of untreated lignin and its depolymerized products according to literature methods in a ^{13}C NMR spectrum.[49]

Functional Group		Integration Region (δ ppm)
Carbonyl or Carboxyl C		215.0-166.5
Aromatic C-O		166.5-142.0
Aromatic C-C		142.0-125.0
Aromatic C-H		125.0-95.8
Aliphatic C-O		95.8-60.8
CH$_3$O-Aromatic C		60.8-55.2
Aliphatic C-C	General	55.2-0
	CH$_3$O-Aromatic	21.6-19.1
	Methyl-Aromatic ortho to a hydroxyl or methoxyl group	16.1-15.4
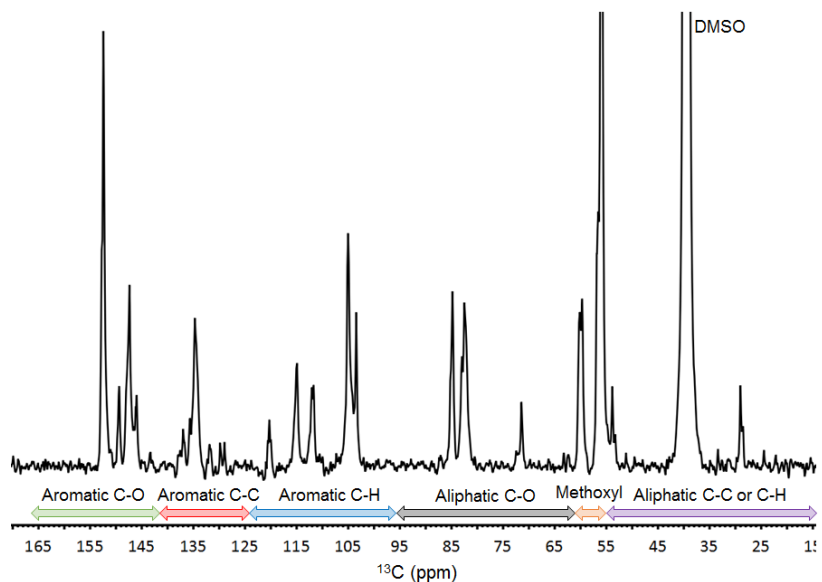
Figure 2.11. ^{13}C NMR spectrum in DMSO-d[6] of untreated organosolv poplar lignin with peak assignments. Reproduced with permission from *ACS Sustain. Chem. Eng.* **2016**, *4*, 6877–6886. Copyright 2016 American Chemical Society.
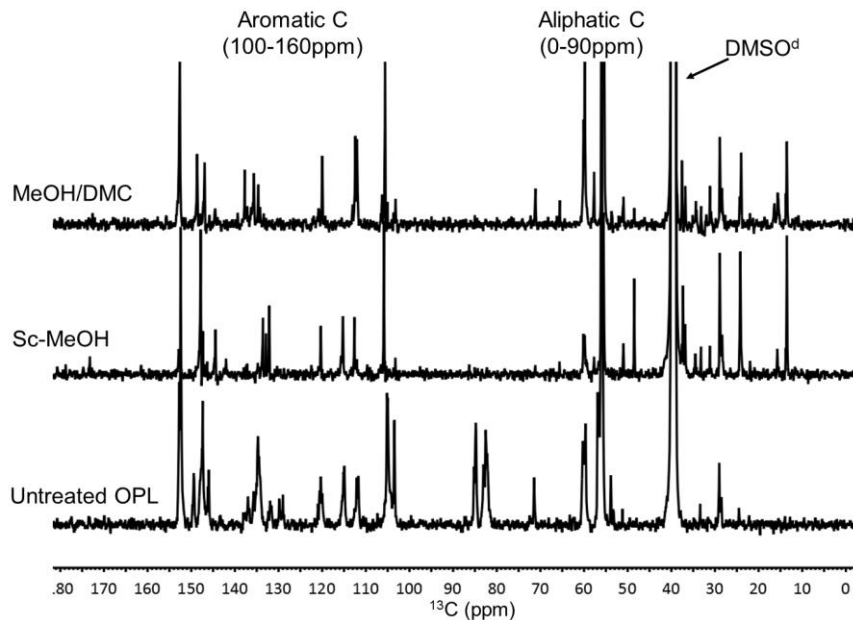
Figure 2.12. Quantitative ^{13}C NMR spectrum of untreated OPL, disassembled lignin in sc-MeOH solvent with Cu[20]PMO, and disassembled lignin in DMC/MeOH cosolvent with Cu[20]PMO. Reproduced with permission from *ACS Sustain. Chem. Eng.* **2016**, *4*, 6877–6886. Copyright 2016 American Chemical Society.
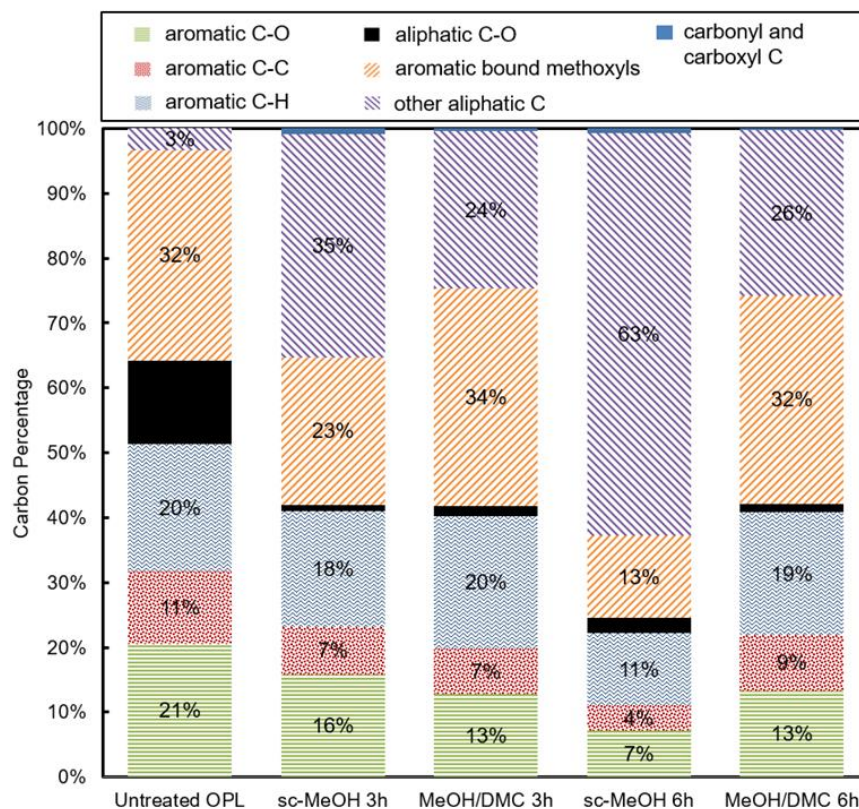
Figure 2.13. Distribution of carbons (in percent) based on ^{13}C NMR data for untreated OPL and for the products of disassembled OPL in sc-MeOH, and in MeOH/DMC. Reproduced with permission from *ACS Sustain. Chem. Eng.* **2016**, *4*, 6877–6886. Copyright 2016 American Chemical Society.

In concurrence with the decrease in aliphatic C-O carbons, the percentages of aliphatic carbons jumped from 3% in OPL to 32% after 3 h and 63% after 6 h reaction in sc-MeOH (Figure 2.13). In 2 mL MeOH/1 mL DMC aliphatic carbons increased from 3% to 24% after 3 h but this only increased to 26% after 6 h in the reactor. Another key feature is the reduction in aromatic carbons (C-O at 166.5-142.0 ppm, C-H at 125.0-95.8 ppm and other carbons at 142.0-125.0 ppm) from 51% in OPL to ~42% in the two product mixtures after 3 h reaction. In sc-MeOH this continued to decrease to ~23% in the 6 h product, but there was little difference between the compositions of the 3 h and 6 h products in MeOH/DMC. Thus, the reductive disassembly process in both cases is accompanied by

some arene hydrogenation. However, the presence of DMC increases the percentage of methoxyl carbons relative to the products generated in sc-MeOH, and such *O*-methylation stabilizes those products against further hydrogenation. From the model substrate studies and the fact that the aromatic methoxyls (60.8-55.2 ppm) correspond to a much larger percentage of the carbons in the latter product after 3 h, it seems likely that the protective effect involves the *O*-methylation of phenolate oxygen on OPL hydrogenolysis products.

GC-MS analysis of the unprocessed products from the four lignin disassembly experiments (with/without $Cu_{20}PMO$ and with/without DMC, each for 3 h and 6 h at 300 ºC) is summarized in Appendix A Table S2.13 where all the major and identified products (>80 % match to the MS database) are listed. Heating OPL in either media without catalyst at 300 ºC gave liquid fractions with much broader product distributions, in addition to considerable char, than did the $Cu_{20}PMO$ catalyzed disassembly. The 3 h reaction in sc-MeOH with $Cu_{20}PMO$ showed largely phenolic products, whereas analogous methoxybenzene compounds were the principal products in MeOH/DMC (Figure 2.14). The difference between lignin disassembly with $Cu_{20}PMO$ in sc-MeOH for 6 h (B1) and in MeOH/DMC for 6 h (B2) illustrates the decrease in product proliferation facilitated by in-situ *O*-methylation. There are five major peaks in B1 and more than 30 minor ones. The largest peak corresponds to 2-methoxy-4-propylphenol, the expected HDG product of conniferyl alcohol (G) type β-O-4 linkages. The second highest peak matched to a complex aliphatic compound which was assigned but may be a result of the MS database limitations. Nonetheless it is likely an aliphatic complex based upon factor analysis mass spectrometric techniques later used in Gao et. al.[50]
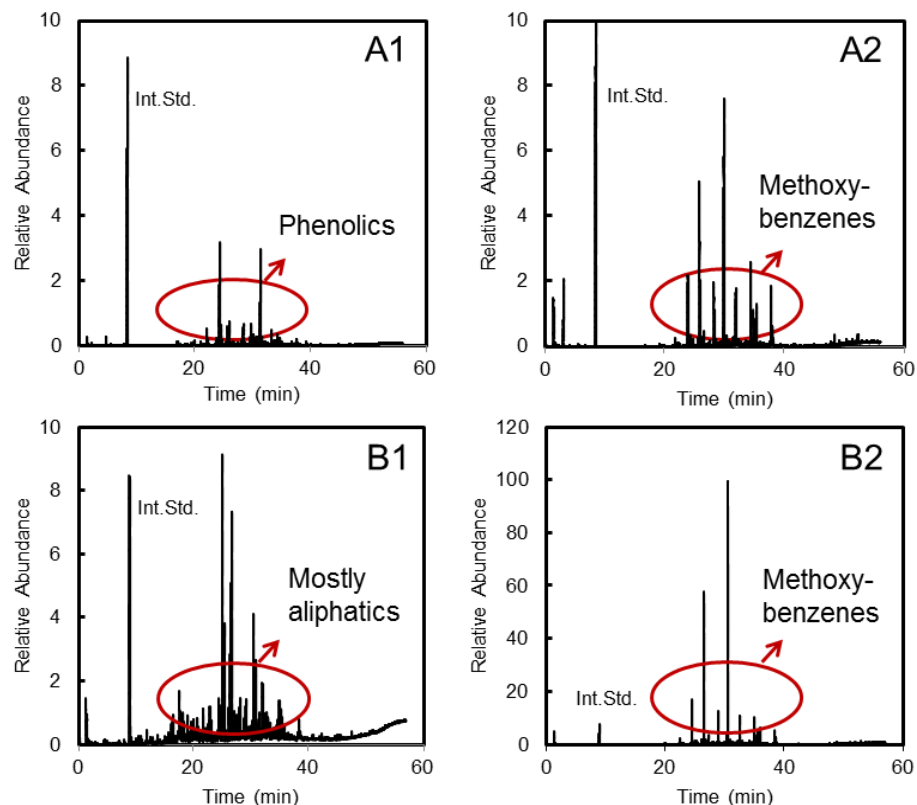
Figure 2.14. GC chromatograms of crude products from disassembled lignin with $Cu_{20}PMO$ catalyst in sc-MeOH and in MeOH/DMC for 3 h and 6 h: A1) sc-MeOH 3h, A2) MeOH/DMC 3 h; B1) sc-MeOH 6 h, B2) MeOH/DMC 6 h. Reproduced with permission from *ACS Sustain. Chem. Eng.* **2016**, *4*, 6877–6886. Copyright 2016 American Chemical Society.

In contrast, there are 2 major peaks in B2 (MeOH/DMC) with 10 minor ones. The largest peak corresponds to 1,2,3-trimethoxy-5-propylbenzene and the second largest peak is 1,2-dimethoxy-4-propylbenzene. The minor peaks were other various methoxybenzenes and methoxyphenols and are shown on the GC chromatogram in Figure 2.15. In conclusion, after a longer reaction time (6 h), the products generated in $Cu_{20}PMO$ catalyzed disassembly in sc-MeOH are more susceptible to secondary reactions like hydrogenation to aliphatic compounds which caused significant product proliferation, evident in the GC-MS data. In contrast, a narrower product distribution from the reaction in MeOH/DMC, can be largely

attributed to the methoxybenzene products remaining intact (Figures 2.14 & 2.15) and not undergoing further ring hydrogenation and subsequent reactions.
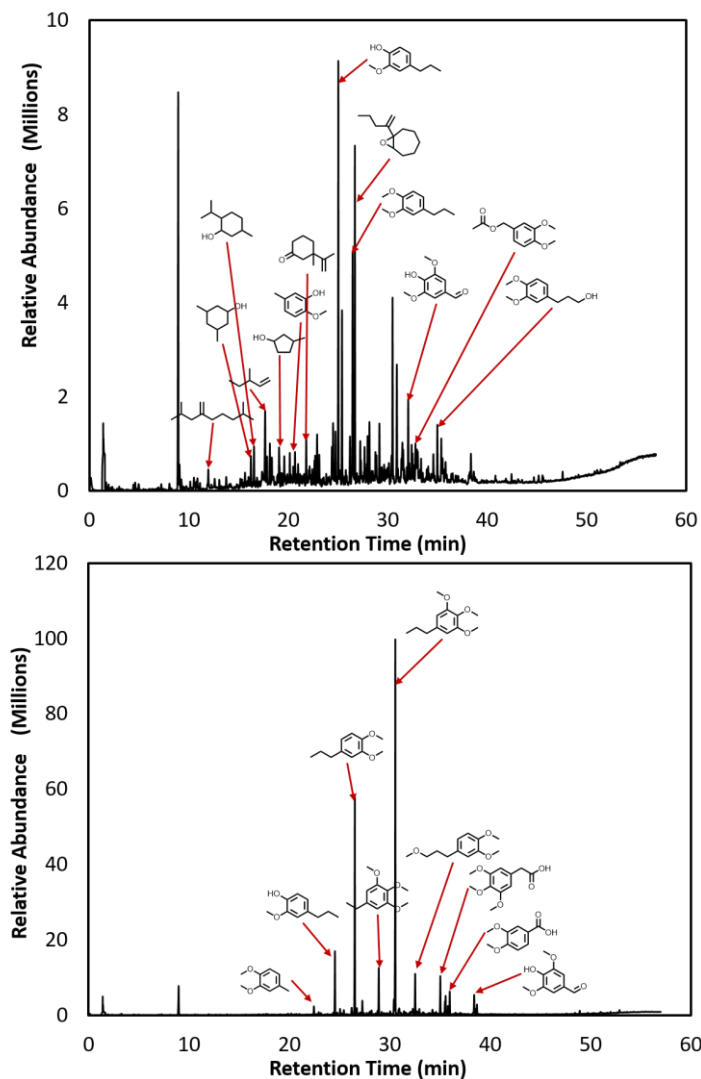
Figure 2.15. GC-MS chromatograms of liquid products from OPL disassembled by a 6 h reaction with $Cu_{20}PMO$ in sc-MeOH (top) and in MeOH/DMC (bottom). The more abundant components are labeled to illustrate the differences. Reproduced with permission from *ACS Sustain. Chem. Eng.* **2016**, *4*, 6877–6886. Copyright 2016 American Chemical Society.

In order to study the recyclability of $Cu_{20}PMO$, 100 mg of catalyst was used for five consecutive reactions (each with 100 mg of OPL) at 300°C for 3 h in MeOH/DMC. The catalyst was recycled without any regeneration procedure. GC-MS analyses of the

unprocessed product solutions showed nearly the same yields and compositions for the first

three runs (Figure 2.16). GPC results indicate the product molecular weights are unchanged

over all 5 runs (Appendix A Table S2.14). However, a significant drop in $Cu_{20}PMO$ activity

was observed on the fourth reaction cycle. In collaboration with the Ford group, Dr. Zachary

Jones, was studying $Cu_{20}PMO$ structural evolution.[51] We initiated studies to understand how

structural changes affect activity and why they occur to understand $Cu_{20}PMO$ deactivation.
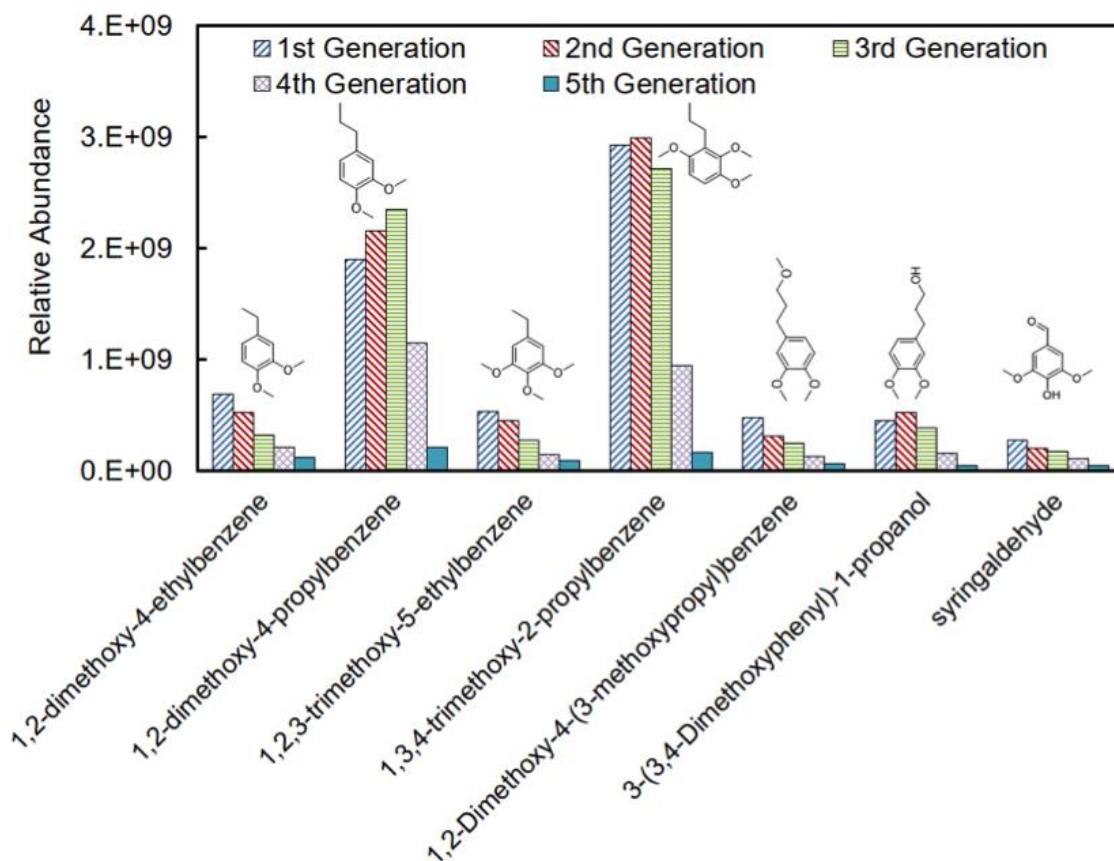
Figure 2.16. GC-MS results for the seven most abundant products from consecutive 3 h runs with organosolv poplar lignin as substrate and the same $Cu_{20}PMO$ catalyst in MeOH/DMC at 300 °C. Reproduced with permission from *ACS Sustain. Chem. Eng.* **2016**, *4*, 6877–6886. Copyright 2016 American Chemical Society.

Section 2. Understanding Catalyst Evolution and Stability.

2.4. Results and Discussion

2.4.1 Considerations for Catalyst Stability in Biomass Conversion

Catalyst stability is vital for biomass based chemical processes to be both environmentally and economically sustainable alternatives to petrochemical processes. In this context, the nature of $Cu_{20}PMO$ changes and deactivation studies are described in this section. The overarching goal of these studies was to identify methods for improving recyclability or regenerating the catalyst.

There are three generally accepted pathways to deactivated heterogeneous metal catalysts; sintering of metal atoms to form large metal nanoparticles, buildup of carbon materials as either coke or tar, and poisoning of sites by impurities in the feedstock that form strongly bound species resulting in reduced active site accessibility.[13] Alternative preparation methods and supports can be used to limit sintering and carbonaceous materials can often be removed simply by calcination. However, some catalyst poisons are difficult to remove making regeneration impractical or impossible.[13] In many cases, feedstocks are treated to remove potential poisons before being introduced to a catalyst. For instance, sulfur is a common trace component in hydrocarbon feedstocks and hydrodesulfurization of naptha feeds is required to prevent sulfur from poisoning noble metal catalysts.[52] Therefore feedstock impurities that may act as catalyst poisons are a crucial variable which must be controlled in catalytic biomass conversion systems.[12]

Naturally, ensuring that feed impurities in biomass will not poison catalysts is critical to creating a successful bio-based chemical industry. There are a multitude of impurities in

48

biomass feedstocks that can threaten the long-term stability of catalysts. Biomass contains more oxygen in its chemical structure but will also contribute oxygen in the form of water in hydrogenolysis based catalytic systems. Additionally, trace elements in woody biomass include K, Mg, Na, Ca, Fe, Mo, Mn, Cu, Zn, B, N, P, S, and Cl.[53] Chlorine is a known copper catalyst poison that's been shown to decrease soybean hydrogenation rates of copper chromite catalyst at less than 100 ppm Cl.[14] Chlorine content is generally low for poplar (0.02 wt% or 200 ppm) but can be much larger for wheat straw (0.26 wt% or 2600 ppm) and fescues/grasses (0.34 wt% or 3400 ppm).[54] Woody biomass can have Cl content ranging from 0.003 wt % (30 ppm) to 0.19 wt% (1900 ppm).[11,53,54] The abundance of Cl in biomass is a substantial deactivation pathway for many transition metal and noble metal based heterogeneous catalysts that has limited avenues for regeneration.[13]

A study on Cu distributed on ZnO(0001)–Zn speculated that adsorbed Cl atoms increase the mobility of Cu, thereby enabling its transition to thermodynamically favored large spherical particles.[55] Finding the most active catalyst for selective conversion of lignocellulosic biomass is equally as important as understanding how feedstock impurities influence selectivity and recyclability. While there are similarities in the processes between valorization of petroleum and lignocellulosic feedstocks,[52] the impurities and catalyst poisons that must be overcome are different and should be critically examined. The effects of Cl$^-$, as low as 10 ppm Cl$^-$ (added as $MgCl_2 \cdot 6H_2O$), on the activity of $Cu_{20}PMO$ are discussed in the following section.

2.4.2. Catalyst Structural Evolution and Activity Changes

The theoretical molecular formula for $Cu_{20}HTC$ is $Cu_{1.2}Mg_{4.8}Al_2CO_3(OH)_{16} \cdot 4(H_2O)$. The Mg-Al carbonate hydrotalcite structure is maintained as evidenced by powder XRD

(Figure 2.17). The observed mass ratios of Cu, Mg, and Al normalized to aluminum were 1.45, 2.23, and 1.0 as measured by inductively coupled plasma-optical emission spectroscopy (ICP-OES). This is consistent with the theoretical molecular formula of Cu = 0.6 mol, Mg = 2.5 mol, Al = 1.0 mol. A Brunauer–Emmett–Teller (BET) Surface Area of 158 m^2/g was found for $Cu_{20}PMO$, which is consistent with previous reports. The XRD pattern of $Cu_{20}PMO$ shows features for MgO which has been previously observed and documented in recent literature.[33,37]

The Cu, Mg, and Al content for $Cu_{20}PMO$ catalysts reacted with sc-MeOH or MeOH/DMC for 3 h were no different than calcined catalyst (Table 2.5). However, the XRD patterns of matured $Cu_{20}PMO$ exhibit features consistent with the formation of metallic Cu(0) (Figure 2.17). The reflection at 44° 2Θ was assigned as a Mg-Al spinel phase.[51,56] The ATR-IR spectra of the catalysts shown in Figure 2.17 can be found in Figure 2.18. The HTC and $Cu_{20}HTC$ exhibit large peaks for water and carbonate bending frequencies around 1550 and 1450 cm^{-1} respectively. After calcination at 460 °C the interstitial water and carbonate are largely removed. Calcined PMOs absorb CO_2 from air, so a small peak at 1450 cm^{-1} is still apparent.[57] The $Cu_{20}PMO$ catalyst after reaction in sc-MeOH and MeOH/DMC show some weak broad stretching frequencies between 1400 and 1600 cm^{-1}. These peaks may correspond to organics with C=C and/or C-H bonds, however, they are not distinct enough to identify.

Table 2.5. ICP-OES data for various $Cu_{20}PMO$ samples. The ppm quantities were determined by standard calibration curves for each element analyzed. ppm = 1 mg/L *=3 h reaction at 300 °C

$Cu_{20}PMO$	2 mL MeOH/1 mL DMC*			MeOH*			Stored at 110 °C		
Element	ppm	mM	Ratio (to Al)	ppm	mM	Ratio (to Al)	ppm	mM	Ratio (to Al)
Al	19.7	0.73	1.00	17.9	0.66	1.00	26.2	0.97	1.00
Cu	28.0	0.44	0.60	25.3	0.40	0.60	37.8	0.60	0.61
Mg	43.9	1.81	2.47	39.9	1.64	2.48	58.2	2.39	2.46
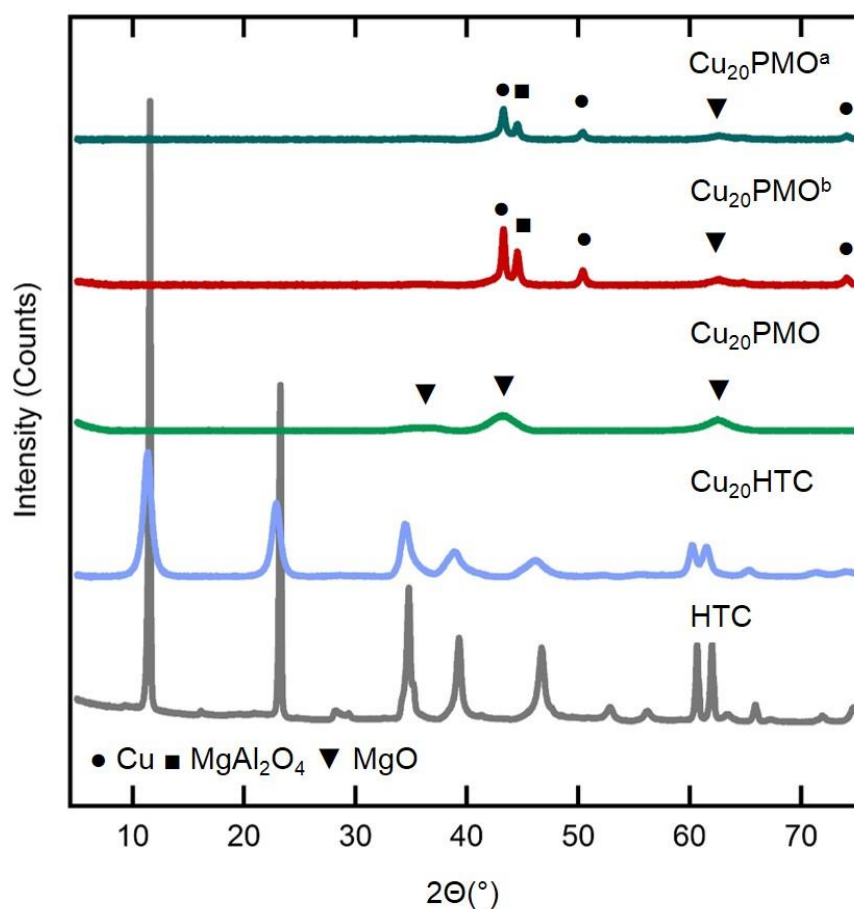
Figure 2.17. XRD patterns for catalysts used. [a]reacted with MeOH/DMC and [b]reacted with sc-MeOH at 300 °C for 6 h. HTC = hydrotalcite. Assignments were made based on database references.[56]
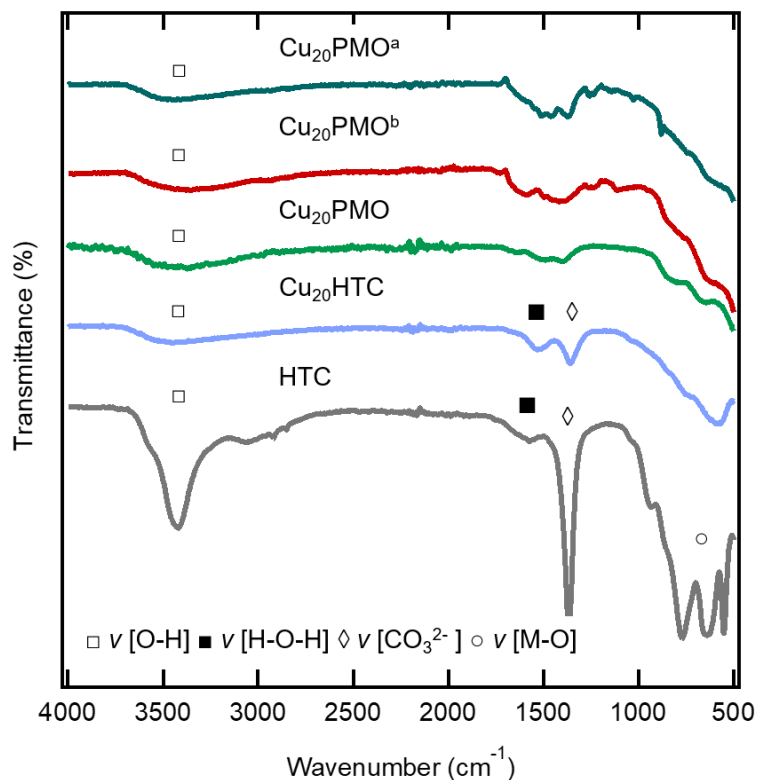
Figure 2.18. ATR-IR spectra for catalysts used. [a]reacted with MeOH/DMC and [b]reacted with sc-MeOH. HTC = hydrotalcite.

In agreement with the XRD data, spherical particles (in the 10 nm range) were observed by scanning electron microscopy (SEM) images which are likely Cu nanoclusters (Figure 2.19). The formation of copper nanoclusters on $Cu_{20}PMO$ under hydrogen at 260 °C or sc-MeOH at 300 °C was previously observed by Dr. Zachary Jones.[51] The SEM images in Figure 2.20 show the texture of $Cu_{20}HTC$. Comparison of these images indicate the destruction of long-range order in the $Cu_{20}HTC$ (Figure 2.20) after calcination and reacting with sc-MeOH or MeOH/DMC to form amorphous $Cu_{20}PMO$ (Figure 2.19). These micrographs are corroborated by the observed XRD patterns which showed loss of characteristic hydrotalcite reflections after calcination and appearance of Cu metal reflections.
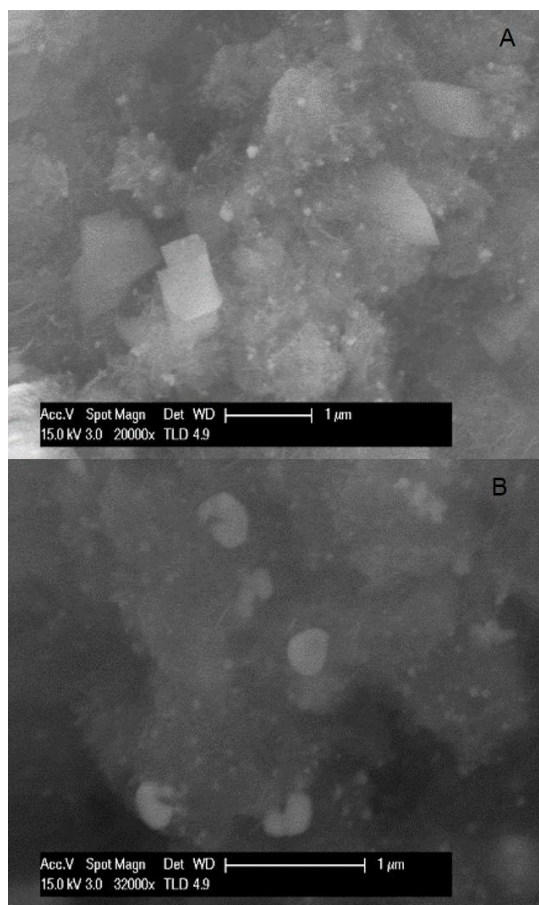
Figure 2.19. SEM Images for $Cu_{20}PMO$ after being subjected to substrate in sc-MeOH (A) and MeOH/DMC (B).
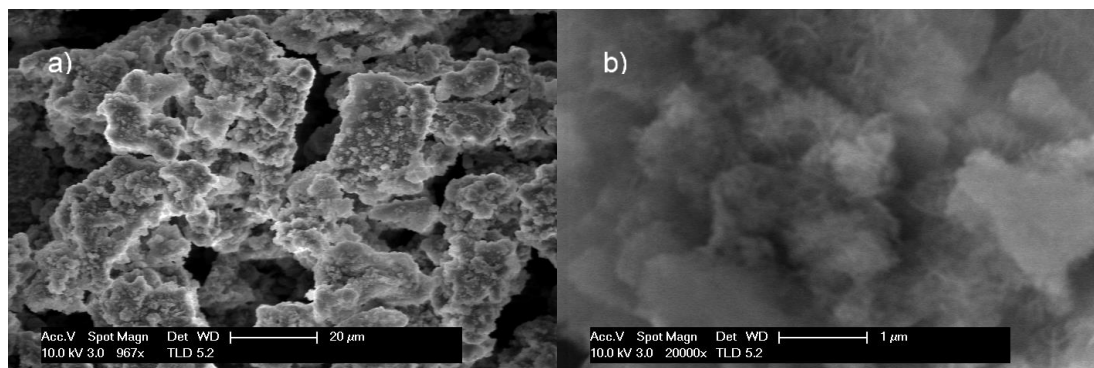
Figure 2.20. Scanning electron micrographs of the $Cu_{20}HTC$ at 967x (a) and 20000x (b) magnification.

The solvent treated $Cu_{20}PMO$ exhibits ~5 nm spheres which we propose serve as the sites for MeOH reforming, HDG, and hydrogenation. Methylation by DMC likely occurs

53

over the acid-base pairs of the support and has been previously proposed with calcined

hydrotalcite and guaiacol.[39] A proposed mechanism for the reaction of PPE with the solvent

treated $Cu_{20}PMO$ is shown in Scheme 2.8.
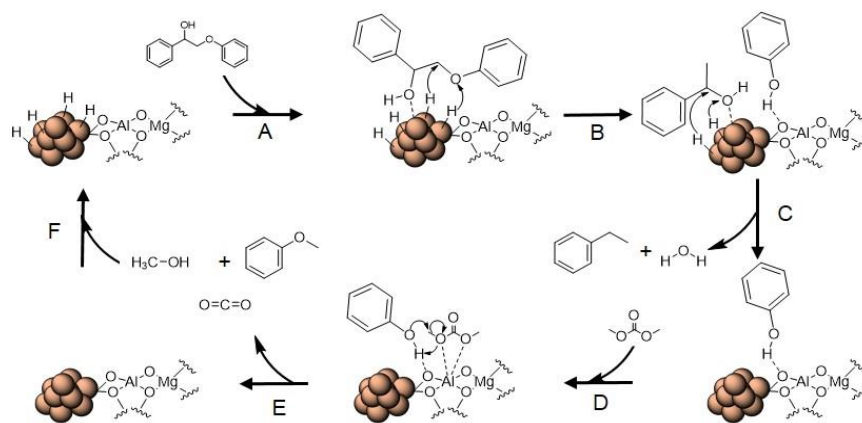
Scheme 2.8. Proposed mechanism of PPE breakdown in MeOH/DMC with Cu metal nanoparticle and acid-base pair active sites. Methanol reforming, hydrogenolysis, and hydrodeoxyenation occur over the Cu nanoparticles (shown as spheres) while *O*-methylation occurs on the M-O pair. Note: not all O atoms are shown on the Al or Mg.

It has been previously proposed that metal nanoparticles are the active site for

HDG.[51] An activation period of about 15 minutes is required for $Cu_{20}PMO$ to reach a large

enough hydrogen surface coverage and the reactor to reach a high enough pressure.[44] It is

likely that during this activation period Cu(0) nanoparticles begin forming on the catalyst.

The first step of the reaction for model compounds would be adsorption onto the metal

active site (Scheme 2.8, A). As a reminder, we are assuming that for lignin the solubilization

of large fragments is likely to occur first and that any interaction with the catalyst surface

would be limited by mass transport based on Song et al.[24] Hydrogen transfer would result in

the cleavage of the C-O bond (Scheme 2.8, B). The resulting phenol is likely to be stabilized

through hydrogen bonding to a lattice O atom. Methyl transfer from DMC to phenol occurs

with the help of the adjacent Lewis base.[58] Finally the products desorb from the catalyst. The active reduced catalyst is regenerated by methanol reforming (Scheme 2.8 F).

The facile hydrogenation of phenol and relative unreactivity of anisole is not explained by resonance stability or electrophilic aromatic directing groups. Both methoxyl and hydroxyl groups are electron donating groups making the aromatic ring more susceptible to electrophilic addition and hydrogenation. Considering a hydroxyl substituent, the phenoxide anion is stabilized through resonance, making the ortho- and para- carbons more reactive to electrophiles. In addition, phenol may undergo tautomerization, the keto form being more susceptible to hydrogen transfer from a reduced Cu(0) nanoparticle on Cu$_{20}$PMO. Furthermore, studies on the hydrogenation of phenol by noble metal supported catalysts implicate that more basic catalyst supports result in specific binding of phenoxide and therefore higher conversions to cyclohexanone.[59] A nonplanar conformation of the aromatic ring was implied which promotes hydrogenation to cyclohexanone.[59] Unlike anisole, phenol may bind to acid sites (as phenoxide) or basic sites. Seeing as the hydrogenation of phenol over transition metal catalysts likely proceeds via a Langmuir-Hinshelwood mechanism, the difference in anisole reactivity may be partially explained simply by hinderance to binding. The methyl group of anisole would sterically hinder chemisorption onto the catalyst surface and result in a substantially decreased conversion of anisole as compared to phenol. Furthermore, anisole lacks the ability to bind to basic sites on the catalyst surface through hydrogen bonding.

The Cu$_{20}$PMO catalyst has been shown in Figure 2.16 to deactivate after three consecutive 3 h reactions with organosolv lignin (OPL) in 2 mL MeOH/ 1 mL DMC at 300 °C. We hypothesized that a component in the biomass was accelerating the deactivation of the catalyst based on the minimal changes in physical properties of Cu$_{20}$PMO after 24 h

reaction with BPE (Table 2.6). After testing other plausible substrate components, like water, we found that chloride causes rapid growth of Cu(0) nanoparticles, reduces hydrogen production, and increases condensation reactions.[51]

Table 2.6. Physical properties of Cu-doped HTC derived catalysts from N_2 physisorption

Material	Surface Area BET (m^2/g)	Pore Vol. (cm^3/g)	Pore Diameter (nm)
$Cu_{20}HTC$	130(2)	0.9	20.0
Calcined at 460 °C	168(1)	0.6	11.2
Calcined at 600 °C	166(1)	0.6	12.7
BPE reaction for 24 h	162(1)	0.4	10.4

The BET surface area of $Cu_{20}HTC$ is lower than that of $Cu_{20}PMO$, because calcination of hydrotalcites removes the interstitial ions and increases porosity.[57] Curiously, the pore volume and diameter are slightly higher for $Cu_{20}HTC$ than for $Cu_{20}PMO$. After $Cu_{20}PMO$ was reacted with BPE for 24 h in the batch reactor there were very minimal changes in BET surface area, pore volume, and diameter (Table 2.6). These results indicate that after 24 h in supercritical conditions with a simple substrate and MeOH there is no evidence of significant change in the physical characteristics of $Cu_{20}PMO$.

Lignocellulose pretreatments to obtain organosolv lignin often employ acids such as HCl, which is what was used to obtain OPL in this case.[60] Chloride and chlorine are known to hinder hydrogenation in supported copper metal catalysts.[61] If the $Cu_{20}PMO$ were exposed to enough Cl/Cl^-, methanol may no longer completely dehydrogenate to carbon monoxide, and formaldehyde could potentially be formed. The reaction of formaldehyde with phenol to form resins is well known.[62] Therefore, we hypothesized that chloride/chlorine in the OPL is accelerating the growth of Cu(0) nanoparticles, hindering methanol reforming, and

56

ultimately causing the deposition of phenolic resin like structures on the catalyst surface. To provide evidence for the deposition of phenolic resins on the catalyst surfaces we obtained ATR-IR spectra of the catalyst (Figure 2.21) and substrate (Figure 2.22).
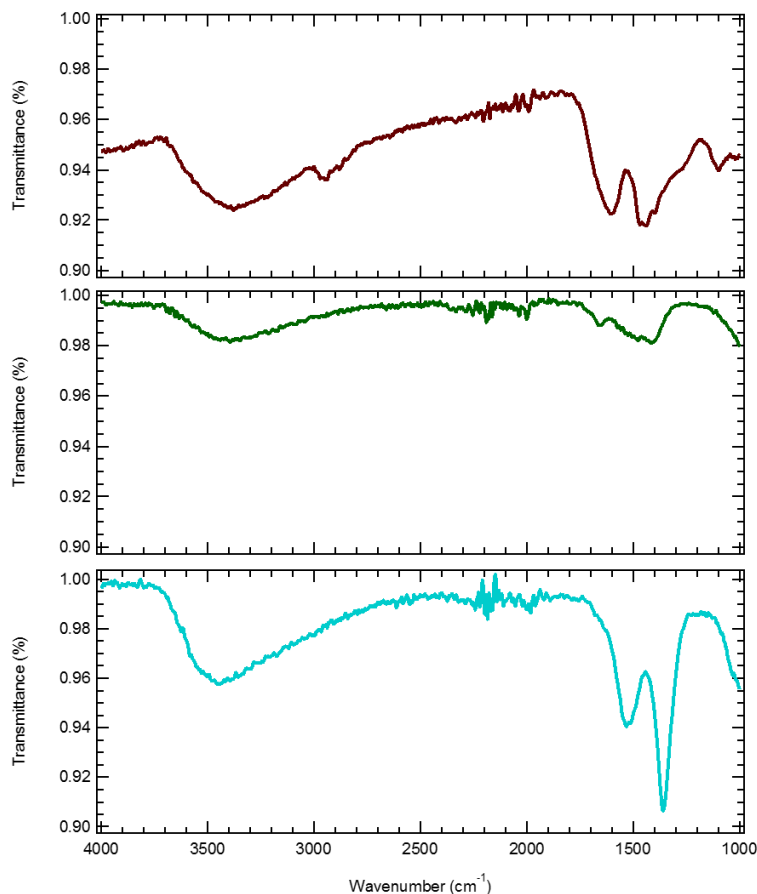
Figure 2.21. ATR-IR spectra of $Cu_{20}PMO$ after third consecutive 6 hr reaction with OPL in sc-MeOH (top), $Cu_{20}PMO$ calcined at 600 °C (middle), and $Cu_{20}HTC$ stored at 110°C.

For $Cu_{20}HTC$ the absorbance between 1400-1600 cm^{-1} is from the interstitial carbonate in the metal hydroxide layers. The broad absorbance from 2800-3800 cm^{-1} is from water. After calcining the HTC at 600 °C the carbonate and water peaks substantially decrease. Small peaks are observed from water and carbon dioxide absorption from the atmosphere. $Cu_{20}PMO$ which has been reacted with OPL three times at 300 °C shows new peaks around 1100, 1400, 1600 and 2900 cm^{-1}.
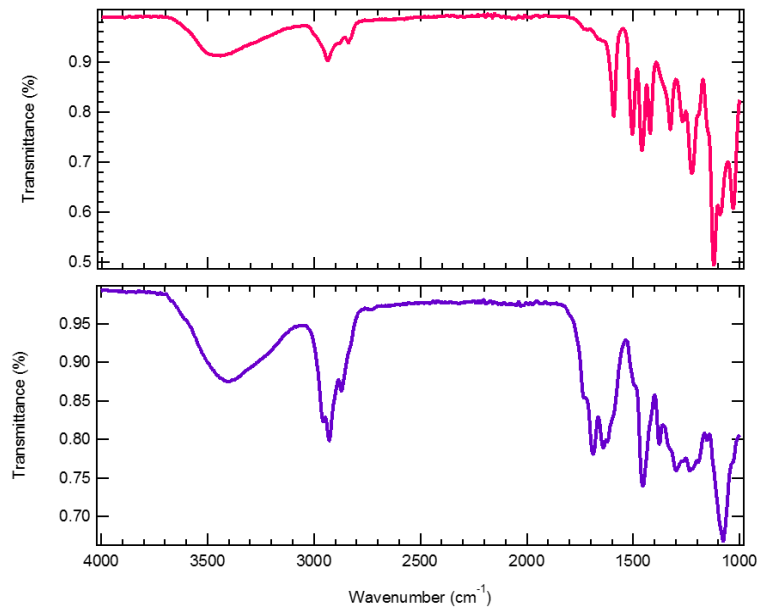
Figure 2.22. ATR-IR spectra of OPL (top) and reaction mixture after third consecutive 6 hr reaction of OPL in sc-MeOH with $Cu_{20}PMO$ (bottom).

These peaks likely correspond to methylene diphenol structures, which have absorbances at 2900 cm^{-1} and between 1000-1700 cm^{-1}.[63] For comparison, the ATR-IR spectra of OPL also contained absorbances at 2900 cm^{-1} and between 1000-1700 cm^{-1}. These IR spectra suggest that $Cu_{20}PMO$ catalyst activity loss after several reactions with OPL, are due to the formation of condensed products with methylene diphenol type structures on the catalyst surface. To further examine this premise, samples of the post-use $Cu_{20}PMO$ catalyst were prepared by consecutive 6 h batch reactor runs with OPL in sc-MeOH at 300 °C. The experimental procedure gave catalyst samples that had been used one, two, and three times with the OPL substrate. After the first use, the Cu(0) nanoparticles underwent significant sintering to give nanoparticles with calculated diameters of ~29 nm (Table 2.7); however, further reuse only led to modest increases in average size to ~32 nm. This result is also consistent with TEM images from $Cu_{20}PMO$ reactions with sugar fractions of bio-oil.[64]

58

The larger nanoparticle size is also consistent with the crystalline Bragg reflections observed in the XRD patterns for the samples reacted with OPL substrate (Figure 2.23). Furthermore, the CuPMO recovered after reaction in sc-MeOH at 300 °C with OPL, shows Bragg reflections at 51° and 75° for Cu metal in the powder XRD pattern (Figure 2.23). Identical reflections were seen when $Cu_{20}PMO$ was reacted in sc-MeOH with added chloride but not in sc-MeOH alone (Figure 2.23) in addition to reflections corresponding to a CuCl phase (111, 200 and 220). A sample of the OPL used in these studies was submitted for analysis to ALS Global (Tucson, AZ), and it was found to contain 998 mg chloride per kg of OPL (~0.1%). For a typical run utilizing 100 mg of this substrate, this would give a chloride concentration of ~33 ppm in the solvent, assuming it is all solubilized in the reaction media.

Table 2.7. Characteristics of the Cu species in $Cu_{20}PMO$ determined by N_2O temperature programed desorption (TPD)[51] after various operations with the catalyst.[a] Procedure for N_2O TPD is described in Appendix A.

Substrate	Rxn time (h)	Cu surface area ($m^2\ g_{Cu}^{-1}$)	Diameter (nm)	Dispersion (%)
Hydrogen[b]	2	225	3.0	35
sc-MeOH only	3	156	4.2	25
sc-MeOH only	72	154	4.4	24
anisole	3	222	3.0	34
anisole (1 mmol H_2O)	3	302	2.2	47
anisole (100 ppm Cl)[c]	3	76	8.8	12
phenol	3	139	4.8	22
OPL	6	23	29.2	4
OPL	12	21	32.0	3
OPL	18	21	32.1	3

[a] A typical run involved reaction of the $Cu_{20}PMO$ catalyst (100 mg), substrate (120 mg) and MeOH (3.0 mL) at 300 ºC for the designated time period in a sealed mini-autoclave (10 mL total volume). [b]2 h reduction in 10% H_2 at 260 ºC. [c]Concentration of chloride in the MeOH solvent with $MgCl_2 \cdot 6H_2O$ as the chloride source. Values presented are known to have a relative ± 7% uncertainty based on three $Cu_{20}PMO$ measurements.

We expected water to enhance sintering as more polar media typically results in increased ion mobility in heterogenous catalysts; however, this was not observed (Table 2.7). In addition to water content (Appendix A Table S2.15), we evaluated Mg^{2+}/Na^+ nitrates (Appendix A Table S2.16), phosphate (Appendix A Table S2.17), and a more reactive substrate i.e. phenol (Appendix A Table S2.18) which did not result in the same catalyst modifications as seen with chloride.
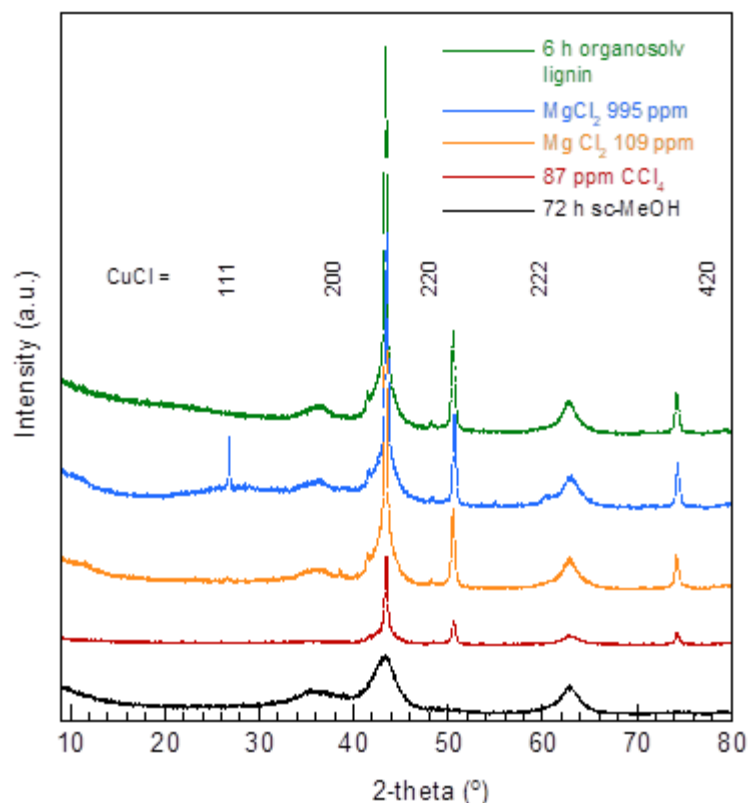
Figure 2.23. Powder X-ray diffraction patterns of various Cu$_{20}$PMO samples recorded after different treatments as listed from the bottom pattern: *Black*: Heated for 72 h in sc-MeOH alone. *Red:* Reaction with anisole as the substrate for 3 h in sc-MeOH containing 87 ppm Cl (CCl$_4$). *Yellow:* Reaction with anisole for 3 h in sc-MeOH containing 109 ppm Cl⁻ (MgCl$_2$). *Blue:* Reaction with anisole for 3 h in sc-MeOH containing 995 ppm Cl⁻ (MgCl$_2$), *Green:* Reaction with 120 mg OPL in sc-MeOH for 6 h (green). In each case the reaction temperature was 300 °C.

Figure 2.24 illustrates the effect of adding small quantities of chloride from various sources on catalysis runs using the relatively unreactive substrate anisole. Anisole is more reactive over Cu$_{20}$PMO calcined at 600 °C versus 460 °C due to an increase in catalyst base strength at the higher calcination temperature.[58] Reaction under standard conditions (100 mg substrate, 100 mg Cu$_{20}$PMO, 3.0 mL MeOH, 300 °C in sealed 10 mL mini-autoclave) led to 21% conversion after 3 h. The material balance was good, the principal products being

61

benzene (~63% based on amount converted) and methyl anisole (~14%) with cyclohexanol, methylcyclohexanol and cyclohexane as lesser products. Introducing chloride as $MgCl_2 \cdot 6H_2O$ resulted in marked decreases in this catalytic activity. For examples, 16 ppm Cl (relative to MeOH) cut the conversion rate by > 50%, but gave a similar product distribution, while higher amounts of Cl^- further suppressed the conversion (Figure 2.24 & Appendix A Tables S2.19.1-2.19.3). Similar activity decreases were observed with the addition of NaCl (10 ppm Cl^-) or CCl_4 (16 ppm Cl); thus, we can conclude that it is the chloride, not the cations or the small amount of water in the added salt, that is modifying the catalyst. Recalcination of the catalyst at 600 °C after reactions with added chloride did not restore the activity toward anisole conversion (Appendix A Table S2.19.1).
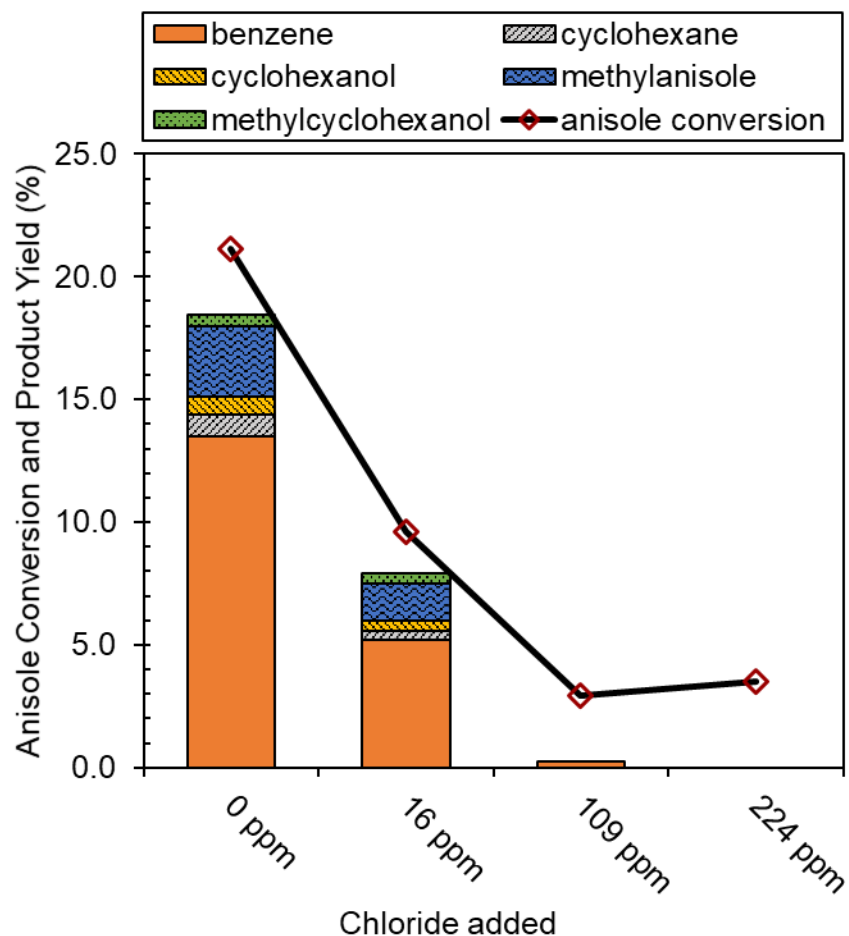
Figure 2.24. Product yields, mass balance, and conversion for the reaction of anisole in the presence of ppm quantities of chloride. All reactions were done for 3 h at 300 °C with $Cu_{20}PMO$ calcined at 600 °C. The Cl- was added as $MgCl_2 \cdot 6H_2O$ in the anisole stock solution. The bars correspond to the yield of products and the lines w/ markers correspond to the mass balance and substrate conversion. Full data is shown in Appendix A Table S2.19.1.

After the anisole reaction with added chloride (100 ppm), analysis of the catalyst indicated significant decreases in Cu surface area and a corresponding increase in the calculated Cu nanoparticle diameter to 8.8 nm (Table 2.7). Thus, the chloride-induced suppression of the catalytic activity correlates to key structural changes. Given that the $Cu_{20}PMO$ catalysts used with deliberately added ppm quantities of chloride showed crystalline Bragg reflections similar to those that had reacted with OPL (Figure 2.23), this provides circumstantial evidence that catalyst deactivation upon repeated reactions of the

63

OPL substrate is related to the chloride content of that OPL. Notably, after the reaction with anisole and 109 ppm chloride, the catalyst displayed Bragg reflections that can be indexed to CuCl (Figure 2.23, yellow/blue), however, in that case the chloride content was higher than normally is present using OPL.

The effect of chloride restructuring the reactive catalyst sites was also examined using benzyl phenyl ether (BPE) as the substrate and $Cu_{20}PMO$ catalysts that had been pretreated in sc-MeOH for 3 or 72 h containing different amounts of added $MgCl_2 \cdot 6H_2O$ (15, 111 & 1022 ppm Cl^-). The reaction catalyzed by chloride-free $Cu_{20}PMO$ illustrates that BPE is a very reactive substrate in sc-MeOH and undergoes complete hydrogenolysis of the $PhCH_2$-OPh bond to toluene and phenol within 2 h at 300 °C. As previously observed, toluene is relatively unreactive under these conditions, while phenol undergoes secondary reactions such as hydrogenation, *O*-methylation, ring-methylation, and condensation.[36,37] As a result, once formed, the phenol typically is rapidly converted and leads to a plethora of aromatic and aliphatic products (Figure 2.25). For example, the BPE reaction for 2 h in 300 °C with $Cu_{20}PMO$ that had been pretreated by heating in sc-MeOH for 72 h, gives ~100 % conversion. However, besides toluene, the principal products were phenol derived aliphatics (51%) such as cyclohexanol and methylated/deoxygenated derivatives of cyclohexanol with much smaller yields of phenol derived aromatics, such as anisole, cresol, and xylenol, (17%) and phenol (5%) itself. When the pretreatment sc-MeOH medium contained 15 ppm chloride, conversion remained near 100%, but the selectivity changed dramatically with the major products now being phenol (59%) and phenol derived aromatics (18%) while formation of phenol-derived aliphatics (5%) was severely depressed. The presence of small amounts of chloride appears to suppress the phenol hydrogenation, the major cause of product proliferation. The enhanced selectivity toward aromatic products continued for

reactions with $Cu_{20}PMO$ pretreated with higher chloride concentrations, but BPE conversion rates drop (Figure 2.25). In addition, a greater percentage of the products are dimers and unidentified oligomers (M/z >180 in the mass spectra) possibly formed by condensation of phenol derivatives (Appendix A Tables S2.20.1-2.20.3). Discrepancies between conversion and material balance may be due to formation of oligomers not sufficiently volatile to be analyzed by GC techniques. When $Cu_{20}PMO$ was reacted with OPL in sc-MeOH for 6 h and then either calcined at 600 °C or washed with methanol there was still significant loss in activity toward BPE conversion as well as low mass balance (Appendix A Table S2.21).
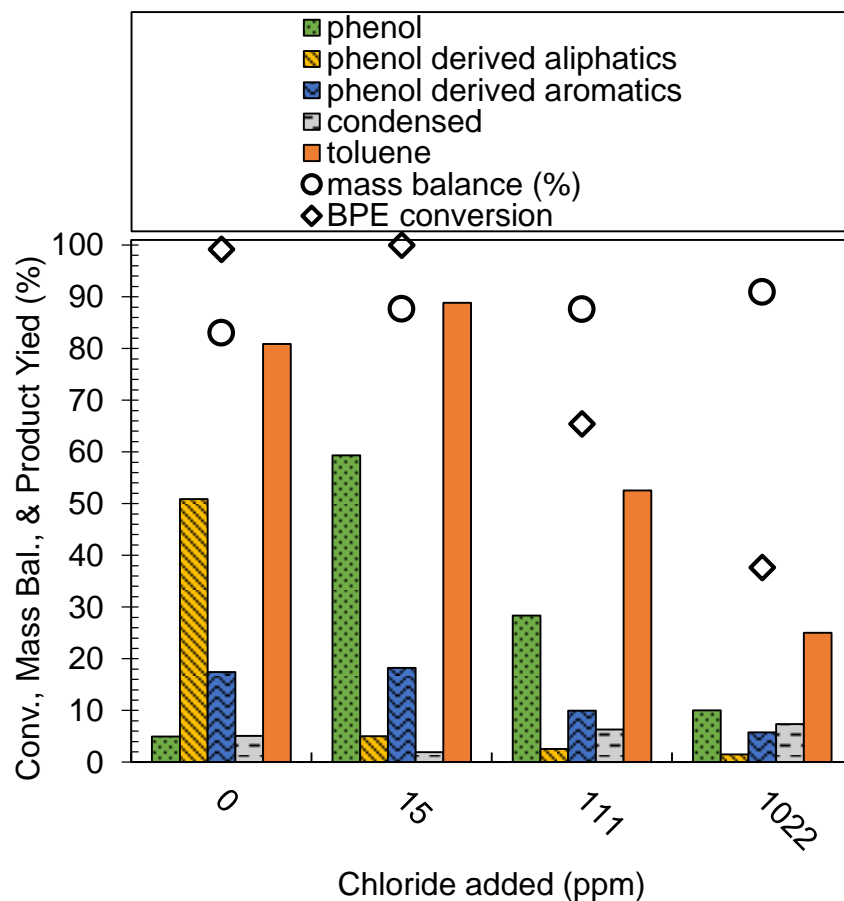
Figure 2.25. Select products, material balance, and conversion for the reaction of benzyl phenyl ether with 72 h sc-MeOH pretreated catalyst. All reactions were done for 2 h at 300°C with CuPMO calcined at 600°C and pretreated with methanol at 300°C for 72 h. The Cl- was added as $MgCl_2 \cdot 6H_2O$ in the 72 h sc-MeOH pretreatment. The bars correspond to the yield of products and the lines w/ markers correspond to the mass balance and substrate conversion. The label 'condensed' corresponds to compounds which could not be identified but showed m/z over 180. Full data is shown in Appendix A Tables S2.20.1-2.20.3.

Notably after 72 hours in sc-MeOH at 300 °C in the absence of substrate we observed <5 nm Cu(0) nanoparticles on $Cu_{20}PMO$ by N_2O TPD. This result indicates that high operating temperature and/or high temperature MeOH are not responsible for the extensive formation of large nanoparticles or catalyst deactivation. Jeong et. al obtained XRD data of CuPMO after reacting with concentrated strong acid hydrolysis lignin (ash content of 6.8 wt%) which had Cu Bragg reflections consistent with our data.[65] An

explanation or mechanism for sintering is not given. Our characterization of $Cu_{20}PMO$ after reactions has identified chloride as one source of catalyst deactivation.

Twigg and Spencer noted that chloride poisoning of supported copper metal catalysts occurs by concurrent mechanisms, where Cl atoms block or modify active sites and create mobile species that increase sintering.[61] In biomass, chloride is most likely in the form of an alkali/alkaline salt.[53] In many biomass pretreatment methods inorganic components like chloride, sulphates, and alkaline are utilized.[60,66,67] Our model studies with anisole and benzyl phenyl ether show that chloride has a large impact on the structure of the catalyst and overall reactivity. Formation of a copper chloride phase increases surface mobility creating larger nanoparticles. Decreased Cu surface area also decreases H_2 production, which is seen in anisole reactions where $Cu_{20}PMO$ was first pretreated with OPL (Appendix A Table S2.22). The Cl atoms could also be blocking active sites for hydrogenolysis and hydrogenation. The Cu to Cl mole ratio at low chlorine content (10 ppm) is about 435:1 so a small amount of chlorine relative to copper results in a disproportionately large drop in activity. The highest chlorine content (1000 ppm) tested has a Cu:Cl mole ratio 4:1.

2.5. Conclusions

Using select model compounds as a testing platform, these studies indicate that the solvent system can be used to manipulate product distribution. The yield of aromatic products from the $Cu_{20}PMO$ catalyzed reductive disassembly of lignin models and of organosolv poplar lignin was substantially increased by the addition of dimethyl carbonate. This strategy exploits the high catalytic activity of copper for hydrogenolysis of aromatic ethers and solid base properties of the PMO support to catalyze *O*-methylation of phenolic intermediates. Reactive alkylphenols undergo selective *O*-methylation to form

alkylmethoxybenzenes, which are markedly less reactive toward arene hydrogenation, thereby preserving aromaticity and reducing undesirable product proliferation.

While lignin is increasingly used for production of thermoplastics,[68] crosslinkers[69] and carbon materials;[70] its use as an aromatic commodity chemical feedstock is minimal apart from vanillin production. The present chapter presents a clear example of how a green reagent, dimethyl carbonate,[71] can be used as a reactive co-solvent to intercept reactive intermediates generated during the reductive disassembly of lignin to give aromatic monomers. The resulting alkylmethoxybenzenes can be used as chemical precursors or can undergo further hydrodeoxygenation to simpler aromatics. Investigations on optimizing the application of such reactive co-solvent systems have potential to greatly impact how we utilize lignin in future biorefineries.

Additionally, this chapter identifies a key issue that will need to be overcome to develop sustainable biomass based chemical processes. It was initially proposed that the high operating temperature and residual water content of biomass would promote copper migration and thus contribute to catalyst deactivation. In this chapter we have shown that Cu-doped porous metal oxides are robust to polar high temperature environments and that the small inorganic component of biomass will play a larger role in irreversible catalyst deactivation. Curiously, there seems to be an amount of chloride which results in a beneficial decrease in certain activity, specifically phenol hydrogenation at 15 ppm Cl. It would be difficult to exploit this in biomass conversion, however, poisoning porous metal oxides may be useful for increased selectivity in other organic transformations. For examples, condensation and alkylation reactions of biomass derived substrates like furfurals or ethanol may be more selective over partially deactivated PMO catalysts.

2.6. Experimental Methods for Lignin and Model Compound Conversion

2.6.1. Materials

Methanol was purchased from Fischer Scientific and dried using molecular sieves (type 3 Å 8-12 mesh beads). Acetone, K_2CO_3, and ethanol were used as purchased from Fischer Scientific. Dimethyl carbonate, synthetic hydrotalcite, n-decane, phenol, 2-bromoacetophenone, and 2-methoxy-4-propylphenol (MPP) were used as purchased from Sigma Aldrich. Benzyl phenyl ether (BPE) was used as purchased from Acros Organics. Diphenyl ether (DPE) and dihydrobenzofuran (DHBF) were purchased from Oakwood Chemicals and used as received. 2-Phenoxy-1-phenylethan-1-ol (PPE) was synthesized according to a known procedure.[72] Phenol and 2-Bromoacetophenone were refluxed in acetone in the presence of potassium carbonate. The resulting brown yellow solution was filtered over Celite and dried in vacuo to afford a yellow solid. After dissolution in ethanol followed by cooling the product precipitated as a white solid. ^{1}H NMR (500 MHz, CDCl$_3$) δ 8.02 (d, 2H), 7.62 (t, 1H), 7.50 (t, 2H), 7.31 (t, 2H), 6.99 (t, 1H), 6.96 (d, 2H), 5.27 (s, 2H). The white precipitate was isolated and subsequently washed with cold ethanol. 2-phenoxy-1-phenylethan-1-one was reduced in a THF/H_2O mixture using NaBH$_4$ to afford 2-phenoxy-1-phenylethan-1-ol as a yellow oil. Drying under vacuum at 70 °C afforded a white powder. ^{1}H NMR (500 MHz, CDCl$_3$) δ 7.46 (d, 2H), 7.40 (t, 2H), 7.34 (t, 1H), 7.31 (t, 2H), 6.98 (t, 1H), 6.94 (d, 2H), 5.14 (d, 1H), 4.12 (dd, 1H), 4.02 (t, 1H), 2.74 (bs, 1H). Proton NMR data are consistent with previous reports.

Poplar Organosolv Extraction. Organosolv poplar lignin (OPL) was obtained by treatment of poplar wood chips using an adaptation of a previous procedure.[73] In a typical procedure, poplar wood chips were treated with 1:1 ethanol/toluene, filtered, and dried

overnight. To 4.5 L of methanol, 600 g of treated Poplar wood chips and 12 mL of concentrated HCl were added. Care was taken to add the wood chips portion-wise as a thick suspension can halt stirring. The mixture was heated to reflux and stirred for 12 days. Over the course of the reaction the methanol turns deep brown. The solution is separated from residual solids by filtration and the solution volume reduced. One liter of ice was added whereupon a beige solid precipitates. The solid was collected by filtration and washed with cold water until the pH of the filtrate was 7. The resulting organosolv lignin was then dried in vacuo overnight, yielding 21.6 g of material. All reactions performed used organosolv lignin isolated from a single batch.

2.6.2. Preparation of Porous Metal Oxide Catalysts

Copper-doped hydrotalcite ($Cu_{20}HTC$) was prepared by the standard co-precipitation method[27] and analyzed by inductively coupled plasma optical emission spectroscopy (ICP-OES), powder-x-ray diffraction (XRD) and attenuated total reflectance IR spectroscopy and shows typical XRD patterns and IR spectra. To a solution of 250 mL deionized water containing $Mg(NO_3)_2 \cdot 6H_2O$ (30.8 g, 0.12 mol), $Cu(NO_3)_2 \cdot 3H_2O$ (7.25 g, 0.03 mol), and $Al(NO_3)_3 \cdot 9H_2O$ (18.76 g, 0.05 mol), a Na_2CO_3 solution (5.3 g, 0.05 mol in 375 mL) was slowly added at 65 °C with vigorous stirring. The pH of the mixture was maintained at approximately 10 by alternating aliquots of 1M NaOH to the reaction mixture. After the addition of the metal solution was complete, the reaction slurry was stirred overnight. The light blue precipitate was isolated by filtration and washed with a sodium carbonate solution (0.05 mol in 1 L distilled water) for a minimum of four hours, then filtered and washed with deionized water. The precipitate was dried overnight at 110 °C resulting in $Cu_{20}HTC$.

All ICP-OES measurements were obtained using a ThermoiCAP 6300 ICP equipped with a 6000 K Ar plasma. Powder XRD patterns were collected under ambient temperature using a Panalytical Empyrean Diffractometer, with Cu Kα radiation (λ= 1.5405980 Å) in a stainless-steel sample holder, scanned from 5-75° (2θ). Structures were assigned using a reference or crystal structure database.[56] ATR-IR spectra were collected on a Bruker ALPHA FT-IR instrument. The standard solutions were prepared by dissolving a known amount of $Mg(NO_3)_2 \cdot 6H_2O$, $Cu(NO_3)_2 \cdot 3H_2O$, and $Al(NO_3)_3 \cdot 9H_2O$ in 18.2 MΩ deionized water with 5% HNO_3. The catalyst samples were prepared by digesting a known mass in nitric acid for 24 hours and diluted using 18.2 MΩ deionized water. Reference emission lines were monitored at 1267.079 nm, 308.215 nm, 309.271 nm, 396.152 nm, 219.958 nm, 224.700 nm, 324.754 nm, 327.396 nm, 202. 582 nm, 280.270 nm, and 285.213 nm. Each measurement is the average of three replicates. Observed samples amount of Cu, Mg, Al were 24.0, 36.8, and 14.5 respectively leading to a Cu/Mg/Al mole ratio of 0.6:2.5:1 with the ideal being 0.6:2.4:1 which is consistent with the molecular formula $Cu_{1.2}Mg_{4.8}Al_2CO_3(OH)_{16} \cdot 4(H_2O)$. $Cu_{20}HTC$ was calcined at 460 °C or 600 °C for 15 h to obtain $Cu_{20}PMO$, which was shown to have a BET surface area of 158-166 m^2/g consistent with previous reports.

2.6.3. Reaction Procedures

Small-scale reactions were conducted using custom built, high-pressure stainless-steel reactors. The mini-autoclave reactors consisted of a 3/4 Swagelok union with two 3/4-inch Swagelok plugs and have an internal volume of ~10 mL. These are described in detail in Matson et al.[27] A typical catalysis run consisted of a set of mini-reactors charged identically with a substrate, catalyst, methanol (2-3 mL), dimethyl carbonate (0-1 mL), and

an internal standard n-decane (20 µL). With model compounds, the substrate sample was 0.25 to 1 mmol, and a 50 mg portion of catalyst was used. For studies with OPL, the sample size was 100 mg and a 100 mg portion of catalyst was used. Temporal product distribution studies were conducted by adding identical quantities of substrate, catalyst, and solvent to a set of mini reactors. These reactors were sealed and placed in an aluminum heating block in a preheated oven set at a specified temperature (typically 300 °C). Individual reactors were removed after a given time interval (1-6 hours) and quenched via rapid cooling in a water bath. The volume of the gas phase was measured with a water displacement apparatus containing a 1/4-inch brass Swagelock pipe tee fitted with a septum for gas analysis samples. (WARNING: High pressures are produced from the reactions and appropriate precautions should be taken when handling and opening.) The reactors were washed with methanol and the combined liquids were filtered using a 10 mL syringe fitted with a 0.2 µm Acrodisc nylon membrane filter. As these reactors become older the Swagelock fittings can seize therefore it is beneficial to use Nickel anti-seize grease on the threading.

2.6.4. Product Analysis

Product identification and quantification was largely done by gas chromatography with thermal conductivity, flame ionization, and mass spectrometry detection (GC-TCD, GC-FID, and GC-MS, respectively). Liquid products were analyzed using the aforementioned Agilent 6890N (G1530N) gas chromatograph equipped with a flame ionization detector (FID) and 30 m × 0.25 mm Agilent DB-5 Column (0.25 µm (5%-phenyl)-methylpolysiloxane lining). The inlet temperature was 200 °C with a split ratio of 200:1 and helium carrier gas at 27 mL/min flow rate. One µL of the filtered liquid mixture was injected. The column temperature was held at 70 °C for 2 minutes, then ramped to 300

°C at 12 °C/min where it was held for 2 minutes. The FID was set at 250 °C with a 30 mL/min H_2 flow rate and 350 mL/min air flow rate. Peaks in the FID chromatogram were identified using standards or GC-MS. For GC-MS, a Hewlett Packard 5890 GC-MS-FID equipped with a 60×0.25 mm $\times 0.25$ μm Restek RTX-1701 film capillary column was used. The injector temperature was set at 250 °C with a split ratio of 1:1, MS to FID. The temperature was held at 40 °C for 10 minutes and increased at 10 °C/min to 280°C. The MS detector is kept at 285 °C and turned on 2 minutes after the injection start time. Generally, the elution order was identical between GC-FID and GC-MS.

Gaseous products were analyzed by Agilent 6890N (G1530N) gas chromatograph equipped with a thermal conductivity detector (GC-TCD) and 30 m $\times$ 0.53 mm Fused Silica Capillary Column. Samples were obtained using a gas tight syringe and injected into the inlet at 225 °C. The carrier gas, helium, was set at a constant flow rate of 7 mL/min. The column temperature was held at 35 °C for 7 minutes, then ramped to 225°C at 24 °C/min where it was held for 10 minutes. The GC-TCD was set at 250 °C with a 40 mL/min H_2 flow rate and 450 mL/min air flow rate. Gas phase products (H_2, CO, CH_4, and CO_2) were quantified by comparison to calibration curves generated using a standardized syngas mixture. Liquid products were quantified using response factors (rf) for all analytes that were approximated using the effective carbon number (ECN) technique described previously,[36] based upon work by Scanlon and Willis (see Appendix A).[74] Reactions kinetics were assumed to be first order with respect to the substrate at each step. Global fitting was performed using DynaFit version 4.05.087 software on a desktop computer (BioKin Ltd.) as described previously.[43] The experimental concentration data for the different substrates involved in the reaction network are fitted using a non-linear least squares approach. Dynafit concurrently produces growth and decay curves for all compounds in a proposed reaction

network using an algorithm defined by a system of first-order ordinary differential equations. The rate constants in the given reaction network are optimized to best fit the experimental temporal data.

Compounds were identified by comparing their mass spectra with those from the system database (NIST10). The weight average molecular weight (M_w), number average molecular weight (M_n), and molecular weight polydispersity of the disassembled and starting lignin were determined by GPC. Unprocessed products were directly injected into the GC-MS and GPC for characterization.

Quantification of Products from Model Reactions. Response factors (rfs) for analytes were determined using the rf for the internal standard, n-decane (experimentally derived), as well as the ECN of n-decane and the analyte (see eq. 1). The rf$_{analyte}$ was then used with the peak area from the GC-FID chromatogram to calculate the concentration of the analyte (see eq. 2). The change in the amount of decane (20 µL, 103 µmol) is insignificant over the course of the reaction. In order to account for changes in solvent volume and losses in handling of GC samples eq. 3 is used to correlate the theoretical amount of decane added (103 µmol) to the amount found in a sample.

$$rf_{analyte} = (rf_{decane})\left(\frac{ECN_{analyte}}{ECN_{decane}}\right) \qquad (1)$$

$$[Analyte] = \left(\frac{A_{analyte}}{rf_{analyte}}\right) \qquad (2)$$

$$\mu mol_{analyte} = [Analyte]\left(\frac{Decane_{theoretical}}{Decane_{measured}}\right) \qquad (3)$$

GC-MS/GPC Analysis of Disassembled Lignin. The column used was RTX-50 column (film thickness 0.5um, length 30m, ID 0.25 mm). 1µL of filtered reaction raw product solution was injected in to the GC inlet (250 °C). The carrier gas was He at 1mL/min with a split ratio of 10:1. The column temperature was programmed to hold at 35 ˚C for 2 min. Then, the oven temperature was increased to 300 ˚C with a heating ramp of 5 ˚C/min. Finally, the oven temperature was held for 5 mins. Decane was used as internal standard for GC-MS analysis. GPC analysis was performed in a Waters e2695 system with a 2489 UV detector (260 nm) on a three-column sequence of WatersTM Styragel columns (HR0.5, HR1, and HR3). Tetrahydrofuran (THF) was used as eluent, and the flow rate was 1.0 ml/min. 200uL of raw product (~5mg) solution (two product samples and 1 standard of 2:1 ratio MeOH & DMC solution) was then dissolved in 1mL of tetrahydrofuran (THF) and filtered through a 0.45-µm nylon membrane filter with an injection volume of 50µL. Molecular weights (M_n and M_w) were calibrated against a polystyrene calibration curve. A calibration curve was constructed by fitting a third-order polynomial equation to the retention volumes obtained from six narrow polystyrene standards and two small molecules (diphenylmethane and toluene) ranging in molecular weight from 92 to 3.4×10^4 g/mol. The curve fit had an R^2 value of 0.99.

NMR Analysis of Disassembled Lignin. Quantitative ^{13}C NMR was performed in a Varian Inova 500 MHz spectrometer at 40°C employing an inverse gated decoupling pulse sequence, 90º pulse angle, 11s pulse delay and ~8,000 scans. For ^{31}P NMR analysis of lignin depolymerization, we employed a mixture of anhydrous pyridine and deuterated chloroform ($Py/CDCl_3$, 1.6/1.0, v/v) containing a relaxation agent, chromium(III) acetylacetonate, and an internal standard, N-hydroxy-5-norbornene-2,3-dicarboximide. Pyridine was used as the base to capture the hydrogen chloride liberated during phosphorylation. The mixture was

prepared as following: An internal standard (21.5 mg) and relaxation agent (5.76 mg) were dissolved in Py/CDCl3 (1.16 g) solvent mixture. The concentration of the internal standard was calculated to be 1.81%. For depolymerized products, the nonvolatile product distribution from lignin depolymerization was obtained in the same way as ^{13}C NMR. A sample (~40 mg) was dissolved in 1.0 mL Py/CDCl$_3$ in a small vial containing a small stir bar, then an accurately weighed relaxation agent/ internal standard solvent mixture (~100 µL) was added and the mixture was stirred for 30 min at room temperature. Phosphorylating agent (~200 µL), 2-chloro-4,4,5,5-tetramethyl-1,3,2-dioxaphospholane (TMDP) was added and the mixture was stirred for another 30 min. The reaction mixture was then transferred into a NMR tube for ^{31}P NMR analysis. Since the phosphorous reagent is moisture sensitive, all the operations were carried out under protection of argon. Quantitative ^{31}P NMR analysis was carried out on a 300 MHz Varian Unity Plus spectrometer. We employed an inverse gated decoupling pulse to eliminate the nuclear Overhauser effects for quantitative purpose; using a 90° pulse, 15s pulse delay, and 256 acquisitions at room temperature. The TMDP hydrolysis product signal (132.2 ppm) was chosen as a reference.

2.6.5. *Analyses for Catalyst Evolution Studies*

Catalyst Sample Preperations: Reactions were run in duplicate for each set of specific conditions. The mini-reactors were custom built stainless-steel pressure vessels with an internal volume of approximately 10 mL. The sc-MeOH pretreatment method was performed by loading the mini-reactor with 120 mg of freshly calcined Cu$_{20}$PMO and 3 mL of MeOH. The reactor was sealed and placed into a preheated furnace at 300°C for 3 or 72 h, then quenched in a room temperature water bath. The reactor was placed in a vauum desiccator to remove the solvent. Where noted impurities in the form of inorganic salts were

added to the MeOH in ppm quantities. The OPL pretreatment method was performed by loading the mini-reactor with 120 mg of OPL, 120 mg of $Cu_{20}PMO$, and 3 mL of MeOH. The reactor was placed in a preheated furnace at 300 °C for 6 h. After the reactor was cooled to room temeprature it was carefully opened to minimize catalyst loss. The gas product volume was measured by a water displacement apparatus, and its composition analyzed by GC-TCD. The solvent was removed in a vacuum desiccator. Consecutive 6 h OPL reactions were performed by removing liquid products, washing the catalyst with 20 mL MeOH (4 mL five times), and removing resiudal solvent under vacuum. After the catalyst was dried, more OPL (120 mg) and MeOH (3 mL) were added, the reactor resealed, and placed into the 300 °C furnace for another 6 h. $Cu_{20}PMO$ catalyst samples that had undergone 6, 12, and 18 h reactions with OPL were obtained from this procedure.

Model compound reactions with OPL pretreated catalysts were performed by first "cleaning" the catalyst as much as possible. After the OPL pretreatment, the reactor's contents were washed into a Falcon 40 mL conical centrifuge tube and diluted with MeOH. The suspension was centrifuged (8000 RPM for 15 minutes) and the supernatant was removed. The catalyst pellet was washed with MeOH and centrifuged three times to remove as much OPL disassembly products as possible. The dry "pretreated" $Cu_{20}PMO$ was added back into the reactor as well as the model compound stock solution. After reaction at 300 °C for the specified time period, the reactor contents were analyzed by liquid and solid analysis techniques described above.

For consecutive catalysis reactions, the reactor contents were thoroughly rinsed with MeOH into a 40 mL conical centrifuge tube. A syringe filter was used to ensure no solids remained in liquid samples for GC analysis. This syringe filter was cut open and rinsed with methanol to minimize catalyst mass loss. The tube containing solids was centrifuged at 8000

77

RPM for 15 min and the supernatant removed in a vacuum desiccator. The solid was resuspended in ~25 mL of methanol and centrifuged again. This procedure was performed three times, after which the solid was dried in a vacuum dessicator.

Conversion and Mass Balance Calculations. Conversion was calculated by eq. 4. $Mol_{initial}$ was the amount of analyte observed in the stock solution and $mol_{unreacted}$ was the amount of analyte observed after after the reaction. Mass balance was calculated by eq. 5. The total moles of products observed was $\sum mol_{products}$. A stoichiometric factor (SF) was required for the reaction of BPE where 1 mole of toluene and 1 mole of phenol (2 mole of total products) per mole of BPE are produced in hydrogenolysis.

$$conversion\ (\%) = \frac{mol_{initial} - mol_{unreacted}}{mol_{initial}} \times 100$$

(4)

$$mass\ balance\ (\%) = \frac{SF \cdot \sum(mol_{products}) + mol_{unreacted}}{mol_{initial}} \times 100$$

(5)

The sample standard deviation (s) was used and denoted as "±#", where an average value of multiple experiments was given for a data entry in a table or plot. The excel function STDEV.S uses the below formula where x = sample value, $\bar{x}$ = mean value, and n = number of samples.

$$s = \sqrt{\frac{\sum(x - \bar{x})^2}{n - 1}}$$

N_2O TPD Analysis. Cu metal surface area, nanoparticle diameter, and dispersion were determined by selective oxidation of surface Cu atoms with N_2O (9.99 vol%), and subsequent titration with H_2.[75] These experiments were performed in a U-shaped quartz reactor. The reactor was packed with quartz wool to support a 110 mg catalyst bed. A

thermocouple was attached on the outside of the reactor in such a way that it was at the mid level of the catalyst bed. The $Cu_{20}PMO$ sample was subjected to flowing O_2 (20 vol% in Ar) while the temperature was increased from room temperature to 300 °C at 10 °C min^{-1}. The temperature was held at 300 °C for 1 h, before cooling back to room temperature using flowing Ar. The $Cu_{20}PMO$ sample was then heated in H_2 (10 vol% in Ar) to 300 °C and held for 1 h, then cooled to room temperature using flowing He. This results in a reduced $Cu_{20}PMO$ sample. The sample was then subjected to flowing N_2O at 60 °C for 45 min to oxidize surface Cu to Cu_2O as shown in eq 6. The Cu surface area was determined from the H_2 consumption during a second temperature programmed reduction, which served as a back-titration, as shown by eq 7.

$$2\ Cu(0) + N_2O\ \rightarrow\ Cu_2O\ +\ N_2 \qquad \textbf{(6)}$$

$$Cu_2O\ +\ H_2\ \rightarrow\ 2\ Cu(0)\ +\ H_2O \qquad \textbf{(7)}$$
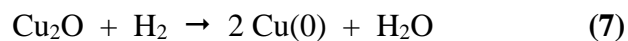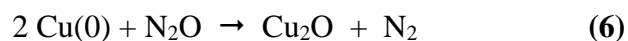
Cu metal surface area, SA_{Cu} (m^2 g$_{Cu}$$^{-1}$), was calculated according to eq. 8. The estimated nanoparticle size, d_{Cu} (nm), was calcualted according to eq. 9. The Cu dispersion, D_{Cu} (%), was calculated accoridng to eq. 10. These calculations assume a spherical model for the supported Cu nanoparticles. In eq. 8, the product of the mole amount of H_2 consumed (n), Avogadro's constant (N_A, 6.022 x 10^{23} mol^{-1}), and the stoichiometry factor (SF) from eq. 7 was divided by the product of the mass of catalyst (m_{cat}) used in the chemisorption experiment, the weight fraction of Cu (W_{Cu}) determined by ICP (0.196 Cu), and the surface copper coverage (A_{Cu}) of 1.46 x 10^{19} Cu atoms m^{-2}. In eq. 9, ρ_{Cu} is the Cu density 8.92 g cm^{-3}. The d_{Cu} can also be calculated by 104/D_{Cu} as previously shown in Evans et al.[75] In eq. 10,

the product of moles of H_2 consumed (n), the molar mass of Cu (M_{Cu}, 63.546 g mol^{-1}) and the SF are divided by the product of the weight fraction of Cu (W_{Cu}) and the mass of catalyst (m_{cat}) used in the experiment.

$$SA_{Cu}(m^2 \ g_{Cu}^{-1}) = \frac{n_{H_2} \cdot N_A \cdot SF}{m_{cat} \cdot W_{Cu} \cdot A_{Cu}}$$

(8)

$$d_{Cu}(nm) = \frac{6 \cdot 10^3}{SA_{Cu} \cdot \rho_{Cu}}$$

(9)

$$D_{Cu}(\%) = \frac{n_{H_2} \cdot M_{Cu} \cdot SF}{W_{Cu} \cdot m_{cat}} \cdot 10^2$$

(10)

2.7. Acknowledgements

Lisa Stamper for ATR-FTIR usage. I would like to express my immense appreciation for Dr. Zachary Jones of Professor Susannah Scott's group who was an essential collaborator in understanding catalyst structural evolution.

2.8. References

1. Wittcoff, H. A.; Reuben, B. G.; Plotkin, J. S. Chapter 4. Chemicals from Natural Gas and Petroleum. In *Industrial Organic Chemicals*; John Wiley & Sons, Inc.: New York, **2013**; pp 93–138.

2. U.S. Department of Energy. 2016. 2016 Billion-Ton Report: Advancing Domestic Resources for a Thriving Bioeconomy, Volume 1: Economic Availability of Feedstocks. M. H. Langholtz, B. J. Stokes, and L. M. Eaton (Leads), ORNL/TM-2016/160. Oak Ridge National Laboratory, Oak Ridge, TN. 448p. doi: 10.2172/1271651. http://energy.gov/eere/bioenergy/2016-billion-ton-report.

3. Pu, Y. Q.; Zhang, D. C.; Singh, P. M.; Ragauskas, A. J. The New Forestry Biofuels Sector. *Biofuels Bioprod. Bioref.* **2008**, *2* (1), 58–73

4. Sun, Z.; Santi, A. De; Elangovan, S.; Barta, K. Bright Side of Lignin Depolymerization : Toward New Platform Chemicals. *Chem. Rev.* **2018**, *118*, 614–618.

5. Tuck, C. O.; Perez, E.; Horvath, I. T.; Sheldon, R. a.; Poliakoff, M. Valorization of Biomass: Deriving More Value from Waste. *Science* **2012**, *337* (6095), 695–699

6. Ragauskas, A. J.; Williams, C. K.; Davison, B. H.; Britovsek, G.; Cairney, J.; Eckert, C. A.; Frederick Jr., W. J.; Hallett, J. P.; Leak, D. J.; Liotta, C. L.; Mielenz, J. R.; Murphy, R.; Templer, R.; Tschaplinski, T. The Path Forward for Biofuels and Biomaterials. *Science* **2006**, *311* (5760), 484–489.

7. Sannigrahi, P.; Ragauskas, A. J.; Tuskan, G. A. Poplar as a Feedstock for Biofuels: A Review of Compositional Characteristics. *Biofuels, Bioprod. Biorefining* **2010**, *4* (2), 209–226

8. Ragauskas, A. J.; Beckham, G. T.; Biddy, M. J.; Chandra, R.; Chen, F.; Davis, M. F.; Davison, B. H.; Dixon, R. A.; Gilna, P.; Keller, M.; Langan, P: Naskar, A. K; Saddler, J. N.; Tschaplinski, T. J.; Tuskan, G. A.; Wyman, C. E. Lignin valorization: improving lignin processing in the biorefinery. *Science* **2014**, *344*, 1246843-1-1246843-10

9. Rinaldi, R.; Jastrzebski, R.; Clough, M. T.; Ralph, J.; Kennema, M.; Bruijnincx, P. C. A.; Weckhuysen, B. M. Paving the Way for Lignin Valorisation: Recent Advances in Bioengineering, Biorefining and Catalysis. *Angew. Chemie - Int. Ed.* **2016**, *55* (29), 8164–8215

10. Argyropoulos, D. S.; Jurasek, L.; Krištofová, L.; Xia, Z.; Sun, Y.; Paluš, E. Abundance and reactivity of dibenzodioxocins in softwood lignin. *J. Agric. Food Chem.* **2002**, *50*, 658–666.

11. Thy, P.; Yu, C.; Jenkins, B. M.; Lesher, C. E. Inorganic Composition and Environmental Impact of Biomass Feedstock. *Energy and Fuels* **2013**, *27* (7), 3969–3987

12. Likun, P. K. W.; Zhang, H.; Vitidsant, T.; Reubroycharoen, P.; Xiao, R. Influence of Inorganic Matter in Biomass on the Catalytic Production of Aromatics and Olefins in a Fluidized-Bed Reactor. *Energy & Fuels* **2017**, *31* (6), 6120–6131.

13. Argyle, M.; Bartholomew, C. Heterogeneous Catalyst Deactivation and Regeneration: A Review. *Catalysts* **2015**, *5* (1), 145–269.

14. Heldal, J. A.; Mørk, P. C. Chlorine-Containing Compounds as Copper Catalyst Poisons. *J. Am. Oil Chem. Soc.* **1982**, *59* (9), 396–398

15. Zakzeski, J.; Bruijnincx, P. C. A.; Jongerius, A. L.; Weckhuysen, B. M. The catalytic valorization of lignin for the production of renewable chemicals. *Chem. Rev.* **2010**, *110*, 3552–3599.

16. Zakzeski, J.; Jongerius, A. L.; Bruijnincx, P. C. A.; Weckhuysen, B. M. Catalytic Lignin Valorization Process for the Production of Aromatic Chemicals and Hydrogen. *ChemSusChem* **2012**, *5*, 1602–1609.

17. Wang, X.; Rinaldi, R. A Route for Lignin and Bio-Oil Conversion: Dehydroxylation of Phenols into Arenes by Catalytic Tandem Reactions, *Angew. Chem.- Int. Ed.* **2013**, *52*, 11499 –11503

18. Deuss, P. J.; Barta, K. From models to lignin: Transition metal catalysis for selective bond cleavage reactions. *Coord. Chem. Rev.* **2015**, *306*, 510-532.

19. Zaheer, M.; Kempe, R. Catalytic Hydrogenolysis of Aryl Ethers: A Key Step in Lignin Valorization to Valuable Chemicals. *ACS Catal.* **2015**, *5*, 1675−1684.

20. Cheng, C.; Shen, D.; Gu, S.; Luo, K. H. State-of-the-Art Catalytic Hydrogenolysis of Lignin for the Production of Aromatic Chemicals. *Catal. Sci. Technol.* **2018**, *8*, 6275–6296.

21. Sinfelt, J. H. Catalytic hydrogenolysis on metals. *Catal. Letters* **1991**, 9, 159–172.

22. Kim, S.; Chmely, S. C.; Nimlos, M. R.; Bomble, Y. J.; Foust, T. D.; Paton, R. S.; Beckham, G. T. Computational study of bond dissociation enthalpies for a large range of native and modified Lignins. *J. Phys. Chem. Lett.* **2011**, *2*, 2846–2852.

23. Song, Q.; Wang, F.; Xu, J. Hydrogenolysis of lignosulfonate into phenols over heterogeneous nickel catalysts. *Chem. Commun.* **2012**, *48*, 7019–7021

24. Song, Q.; Wang, F.; Cai, J.; Wang, Y.; Zhang, J.; Yu, W.; Xu, J. Lignin depolymerization (LDP) in alcohol over nickel-based catalysts via a fragmentation-hydrogenolysis process. *Energy Environ. Sci.* **2013**, *6*, 994–1007

25. Parsell, T. H.; Owen, B. C.; Klein, I.; Jarrell, T. M.; Marcum, C. L.; Haupert, L. J.; Amundson, L. M.; Kenttämaa, H. I.; Ribeiro, F.; Miller, J. T.; Abu-Omar, M. M. Cleavage and hydrodeoxygenation (HDO) of C–O bonds relevant to lignin conversion using Pd/Zn synergistic catalysis. *Chem. Sci.* **2013**, *4*, 806-813

26. Parsell, T.; Yohe, S.; Degenstein, J.; Jarrell, T.; Klein, I.; Gencer, E.; Hewetson, B.; Hurt, M.; Kim, J. I.; Choudhari, H.; Saha, B.; Meilan, R.; Mosier, N.; Ribeiro, F.; Delgass, W. N.; Chapple, C.; Kenttämaa, H.I.; Agrawal, R.; Abu-Omar, M. M. A synergistic biorefinery based on catalytic conversion of lignin prior to cellulose starting from lignocellulosic biomass. *Green Chem.* **2015**, *17*, 1492–1499.

27. Matson, T. D.; Barta, K.; Iretskii, A. V; Ford, P. C. One-Pot Catalytic Conversion of Cellulose and of Woody Biomass Solids to Liquid Fuels. *J. Am. Chem. Soc.* **2011**, *133* (35), 14090–14097

28. Macala, G. S.; Matson, T. D.; Johnson, C. L.; Lewis, R. S.; Iretskii, A. V.; Ford, P. C. Hydrogen Transfer from Supercritical Methanol over a Solid Base Catalyst: A Model for Lignin Depolymerization. *ChemSusChem* **2009**, *2* (3), 215–217

29. Barta, K.; Matson, T. D.; Fettig, M. L.; Scott, S. L.; Iretskii, A. V.; Ford, P. C. Catalytic Disassembly of an Organosolv Lignin via Hydrogen Transfer from Supercritical Methanol. *Green Chem.* **2010**, *12* (9), 1640

30. Barta, K.; Ford, P. C. Catalytic conversion of nonfood woody biomass solids to organic liquids. *Acc. Chem. Res.* **2014**, 47, 1503–1512.

31. Barta, K.; Warner, G. R.; Beach, E. S.; Anastas, P. T. Depolymerization of organosolv lignin to aromatic compounds over Cu-doped porous metal oxides. *Green Chem.* **2014**, *16*, 191–196.

32. Huang, X.; Korányi, T. I.; Boot, M. D.; Hensen, E. J. M. Catalytic depolymerization of lignin in supercritical ethanol. *ChemSusChem* **2014**, *7*, 2276–2288.

33. Huang, X.; Atay, C.; Korányi, T. I.; Boot, M. D.; Hensen, E. J. M. Role of Cu–Mg–Al Mixed Oxide Catalysts in Lignin Depolymerization in Supercritical Ethanol. *ACS Catal.* **2015**, *5*, 7359–7370.

34. Sun, Z.; Bottari, G.; Barta, K. Supercritical methanol as solvent and carbon source in the catalytic conversion of 1,2-diaminobenzenes and 2-nitroanilines to benzimidazoles. *Green Chem.* **2015**, *17*, 5172-5181.

35. Hansen, T. S.; Barta, K.; Anastas, P. T.; Ford, P. C.; Riisager, A. One-pot reduction of 5-hydroxymethylfurfural via hydrogen transfer from supercritical methanol. *Green Chem.* **2012**, *14*, 2457–2461.

36. Bernt, C. M.; Bottari, G.; Barrett, J. A.; Scott, S. L.; Barta, K. Mapping Reactivities of Aromatic Models with a Lignin Disassembly Catalyst. Steps toward Controlling Product Selectivity. *Catal. Sci. Technol.* **2016**, *6*, 2984–2994

37. Barrett, J. A.; Gao, Y.; Bernt, C. M.; Chui, M.; Tran, A. T.; Foston, M. B.; Ford, P. C. Enhancing Aromatic Production from Reductive Lignin Disassembly: In Situ O - Methylation of Phenolic Intermediates. *ACS Sustainable Chem. Eng.* **2016**, *4*, 6877–6886.

38. Musser, M. T. Cyclohexanol and Cyclohexanone. *Ullmann's Encycl. Ind. Chem.* **2011**, *11*, 49–58

39. Talawar, M. B.; Jyothi, T. M.; Raja, T.; Rao, B. S.; Sawant, P. D. Calcined Mg–Al hydrotalcite as an efficient catalyst for the synthesis of guaiacol. *Green Chem.* **2000**, *2*, 266–268.

40. Jyothi, T. M.; Raja, T.; Talawar, M. B.; Sugunan, S.; Rao, B. S.; Energy, H. Selective Methylation of Phenol, Aniline and Catechol with Dimethyl Carbonate Over Calcined Mg-Al Hydrotalcites. *Synth. Commun.* **2000**, *30*, 3929–3934.

41. Macala, G. S.; Robertson, A. W.; Johnson, C. L.; Day, Z. B.; Lewis, R. S.; White, M. G.; Iretskii, A. V.; Ford, P. C. Transesterification Catalysts from Iron Doped Hydrotalcite-like Precursors: Solid Bases for Biodiesel Production. *Catal. Letters* **2008**, *122* (3–4), 205–209

42. Popov, A.; Kondratieva, E.; Goupil, J. M.; Mariey, L.; Bazin, P.; Gilson, J. P.; Travert, A.; Maugé, F. Bio-oils hydrodeoxygenation: Adsorption of phenolic molecules on oxidic catalyst supports. *J. Phys. Chem. C* **2010**, *114*, 15661−15670

43. Kuzmic, P. Program DYNAFIT for the analysis of enzyme kinetic data: application to HIV proteinase. *Anal. Biochem.* **1996**, *237*, 260–273.

44. Bernt, C. M.; Manesewan, H.; Chui, M.; Boscolo, M.; Ford, P. C. Temperature Tuning the Catalytic Reactivity of Cu-Doped Porous Metal Oxides with Lignin Models. *ACS Sustainable Chem. Eng.* **2018**, *6*, 2501–2516

45. Pelzer, A. W.; Sturgeon, M. R.; Yanez, A. J.; Chupka, G.; O'Brien, M. H.; Katahira, R.; Cortright, R. D.; Woods, L.; Beckham, G. T.; Broadbelt, L. J. Acidolysis of the α-O-4 Aryl- Ether Bonds in Lignin Model Compounds: A Modeling and Experimental Study, *ACS Sustain. Chem. Eng.,* **2015**, 3, 1339–1347

46. Jin-bao, H.; Shu-bin, W. U.; Hao, C.; Ming, L. E. I.; Jia-jin, L.; Hong, T. Theoretical Study of Bond Dissociation Energies for Lignin Model Compounds. *J. Fuel Chem. Technol.* **2015**, *43* (4), 429–436

47. Yuan, T.; Sun, S.; Xu, F.; Sun, R. Characterization of Lignin Structures and Lignin À Carbohydrate Complex (LCC) Linkages by Quantitative ^{13}C and 2D HSQC NMR Spectroscopy. *J. Agric. Food Chem.* **2011**, *59*, 10604–10614

48. Pu, Y.; Cao, S.; Ragauskas, A. J. Application of quantitative 31P NMR in biomass lignin and biofuel precursors characterization. *Energy Environ. Sci.* **2011**, *4*, 3154-3166

49. Ben, H.; Ragauskas, A. J. NMR characterization of pyrolysis oils from kraft lignin. *Energy and Fuels* **2011**, *25*, 2322–2332

50. Gao, Y.; Walker, M. J.; Barrett, J. A.; Hosseinaei, O.; Harper, D. P.; Ford, P. C.; Williams, B. J.; Foston, M. B. Analysis of Gas Chromatography / Mass Spectrometry Data for Catalytic Lignin Depolymerization Using Positive Matrix. *Green Chem.* **2018**, *20*, 4366–4377

51. Jones, Z. R., "Elucidating Structure-Activity Relationships through X-ray Absorption Fine Structure Analyses: from Site-Isolated Systems, to Nanoclusters, and to Supported Nanoparticle Catalysts", Doctoral Dissertation, **2019**

52. Huber, G. W.; Corma, A. Synergies between bio- and oil refineries for the production of fuels from biomass. *Angew. Chemie - Int. Ed.* **2007**, *46* (38), 7184–7201

53. Vassilev, S. V.; Baxter, D.; Andersen, L. K.; Vassileva, C. G., An overview of the composition and application of biomass ash. Part 1. Phase-mineral and chemical composition and classification. *Fuel* **2013,** *105*, 40-76

54. Da Silva Perez, D.; Dupont, C.; Guillemain, A.; Jacob, S.; Labalette, F.; Briand, S.; Marsac, S.; Guerrini, O.; Broust, F.; Commandre, J. M. Characterisation of the most

representative agricultural and forestry biomasses in France for gasification. *Waste and Biomass Valorization* **2015**, *6* (4), 515–526

55. Grant, A.; Ranney, J.; Campbell, C. The influence of chlorine on the dispersion of Cu particles on Cu/ZnO (0001) model catalysts. *Catal. Letters* **2000**, *65*, 159–168

56. Downs, R. T.; Hall-Wallace, M. The American Mineralogist crystal structure database. *Am. Mineral.* **2003**, *88*, 247−250

57. Yavuz, C. T.; Shinall, B. D.; Iretskii, A. V.; White, M. G.; Golden, T.; Atilhan, M.; Ford, P. C.; Stucky, G. D. Markedly Improved CO_2 Capture Efficiency and Stability of Gallium Substituted Hydrotalcites at Elevated Temperatures. *Chem. Mater.* **2009**, *21* (15), 3473–3475

58. Debecker, D. P.; Gaigneaux, E. M.; Busca, G. Exploring, Tuning, and Exploiting the Basicity of Hydrotalcites for Applications in Heterogeneous Catalysis. *Chem. - A Eur. J.* **2009**, *15* (16), 3920–3935

59. Zhong, J.; Chen, J.; Chen, L. Selective Hydrogenation of Phenol and Related Derivatives. *Catal. Sci. Technol.* **2014**, *4*, 3555–3569

60. Ta, Y. L.; Wu, Y.; Jahim, J. Typical conversion of lignocellulosic biomass into reducing sugars using dilute acid hydrolysis and alkaline pretreatment. *Cellulose* **2016**, *23* (3), 1491–1520

61. Twigg, M. V.; Spencer, M. S. Deactivation of supported copper metal catalysts for hydrogenation reactions. *Appl. Catal. A Gen.* **2001**, *212* (1–2), 161–174

62. Franz, A. W.; Kronemayer, H.; Pfeiffer, D.; Pilz, R. D.; Reuss, G.; Disteldorf, W.; Gamer, A. O.; Hilt, A. Formaldehyde. *Ullmann's Encycl. Ind. Chem.* **2016**, 1–33

63. SDBS Web : https://sdbs.db.aist.go.jp (National Institute of Advanced Industrial Science and Technology, accessed April, 6, 2018)

64. Yin, W.; Venderbosch, R. H.; Bottari, G.; Krawzcyk, K. K.; Barta, K.; Heeres, H. J. Catalytic Upgrading of Sugar Fractions from Pyrolysis Oils in Supercritical Mono-Alcohols over Cu Doped Porous Metal Oxide. *Appl. Catal. B Environ.* **2015**, *166–167*, 56–65

65. Jeong, S.; Hun, G.; Do, J.; Kim, H. Decomposition of Lignin Using MO – MgAlO$_y$ Mixed Oxide Catalysts (M = Co , Ni and Cu) in Supercritical Ethanol. *Top. Catal.* **2017**, *60* (9), 637–643

66. Henrique, M.; Silveira, L.; Morais, R. C.; Costa, M. Current Pretreatment Technologies for the Development of Cellulosic Ethanol and Biorefineries. *ChemSusChem* **2015**, 3366–3390

67. Putro, J. N.; Soetaredjo, F. E.; Lin, S.; Ju, Y.; Ismadji, S. Pretreatment and conversion of lignocellulose biomass into valuable chemicals. *RSC Adv.* **2016**, *6*, 46834–46852

68. Sadeghifar, H.; Cui, C.; Argyropoulos, D. S. Toward Thermoplastic Lignin Polymers. Part 1. Selective Masking of Phenolic Hydroxyl Groups in Kraft Lignins via Methylation and Oxypropylation Chemistries. *Ind. Eng. Chem. Res.* **2012**, *51*, 16713–16720

69. Zhao, S.; Abu-omar, M. M. Renewable Epoxy Networks Derived from Lignin-Based Monomers: Effect of Cross-Linking Density. *ACS Sustainable Chem. Eng.* **2016**, *4*, 6082–6089

70. Oroumei, A.; Fox, B.; Naebe, M. Thermal and Rheological Characteristics of Biobased Carbon Fiber Precursor Derived from Low Molecular Weight Organosolv Lignin. *ACS Sustainable Chem. Eng.* **2015**, *3*, 758–769

71. Selva, M.; Perosa, A.; Fiorani, G. Dimethyl Carbonate: A Versatile Reagent for a Sustainable Valorization of Renewables. *Green Chem.* **2017**, *20* (2), 288–322

72. Nichols, J. M.; Bishop, L. M.; Bergman, R. G.; Ellman, J. A. Catalytic C - O Bond Cleavage of 2-Aryloxy-1-arylethanols and Its Application to the Depolymerization of Lignin-Related Polymers. *J. Am. Chem. Soc.* **2010**, *132*, 12554–12555.

73. Kleineri, T. N. Organosolv Pulping and Recovery Process. US 3,585,104, **1971**.

74. Scanlon, J. T.; Willis, D. E. Calculation of Flame Ionization Detector Relative Response Factors Using the Effective Carbon Number Concept. *J. Chromatogr. Sci.* **1985**, *23*, 333–340.

75. Evans, J. W.; Mainwright, M. S.; Bridgwater, A. J.; Young, D. J., On the determination of copper surface area by reaction with nitrous oxide. *Appl. Catal.* **1983**, *7* (1), 75-83

2.9. Appendix A. Supporting Information for Chapter 2

Table S2.1. Reaction of phenol in MeOH/DMC with $Cu_{20}PMO$ at 300 °C.

Compound (µmol)	0 h	6 h	6 h	6 h	Mean±SE
anisole	0	488	533	479	500±24
benzene	0	3	2	2	2±0.3
cyclohexane	0	1	1	1	1±0.2
cyclohexanol	0	13	20	24	19±5
xylenol	0	3	7	9	6±3
methyl anisole	0	23	26	23	24±2
methylcyclohexanols	0	8	12	14	11±2
o-cresol	0	3	18	23	15±9
p/m-cresol	0	1	1	1	1±0.1
phenol	577	0	7	8	5±4
toluene	0	0	2	1	1±0.7
Total mass balance (%)	-	94	109	102	102±6

Table S2.2. Reaction of 2-methoxy-4-propylphenol with $Cu_{20}PMO$ at 300 °C: [a]in MeOH/DMC, [b]in sc-MeOH. Three independent experiments are reported for each.

Compound (µmol)	0 h	6 h[a]	6 h[a]	6 h[a]	6 h[b]	6 h[b]	6 h[b]	Mean±SE[a]	Mean±SE[b]
2-methoxy-4-propylphenol	892	39	48	53	414	413	496	47±6	441±39
1,2-dimethoxy-4-propylbenzene	0	549	672	579	89	90	107	600±53	95±8
dimethyl methoxypropylphenol	0	17	18	16	5	7	8	17±1	7±1
methoxybutylbenzene	0	3	4	3	0	0	0	3±0.5	-
methoxypropylbenzene	0	30	33	29	4	5	6	31±2	5±1
methyl-dimethoxypropylbenzene	0	13	17	16	5	5	5	15±2	5±0.3
methyl methoxypropylbenzene	0	2	3	2	1	1	1	2±0.2	1±0.2
methyl-methoxypropylphenol	0	37	48	42	31	35	40	42±4	35±4
methylpropylphenol	0	17	20	14	43	53	69	17±2	55±11
propylcyclohexane	0	2	2	1	1	1	1	2±0.3	1±0.1
propylcyclohexanol	0	12	12	8	24	30	38	11±2	31±6
propylphenol	0	22	28	23	59	71	88	25±3	73±12
Unidentified (average Calc. r.f.)	0	23	26	20	17	20	24	23±2	21±3
Total mass balance (%)	-	86	104	90	78	82	99	94±8	86±9

Table S2.3. Reaction of benzyl phenyl ether in MeOH/DMC with $Cu_{20}PMO$ at 300 °C.

Compound (µmol)	0 h	1 h	2 h	3 h	4 h	5 h	6 h	6 h[a]
anisole	0	193	579	552	580	561	558	109
benzene	0	0	3	4	8	13	14	6
benzyl phenyl ether	816	238	0	0	0	0	0	1
cyclohexane	0	0	3	6	11	9	14	8
cyclohexanol	0	0	97	107	111	90	75	0
dimethylanisole	0	0	0	1	1	1	2	1
dimethylcyclohexanol	0	0	3	3	5	6	8	42
methylanisole	0	0	25	24	28	29	30	15
methylcyclohexane	0	0	0	1	3	5	6	5
methylcyclohexanol	0	9	37	48	78	98	120	584
o-cresol	0	25	51	37	31	21	14	9
p/m-cresol	0	1	2	1	0	0	0	0
phenol	1	428	105	42	14	4	1	8
toluene	0	637	880	812	838	813	817	845
xylenol	0	0	8	7	10	10	10	17
Phenol mass balance (%)	0	113	112	102	108	104	104	99
Toluene mass balance (%)	0	110	108	100	103	100	100	104
Total mass balance (%)	100	108	110	101	105	102	102	101

[a] reaction in sc-MeOH

Table S2.4. Reaction of benzyl phenyl ether in MeOH/DMC (5:1 ratio) with $Cu_{20}PMO$ at 300°C.

Compound (µmol)	0 h	1 h	2 h	3 h	4 h	5 h	6 h
anisole	0	345	342	416	367	383	337
benzene	0	0	2	5	5	14	8
benzyl phenyl ether	846	126	1	1	1	0	2
cyclohexane	0	0	1	3	8	12	11
cyclohexanol	0	25	130	186	245	154	195
dimethylanisole	0	1	1	2	2	3	2
dimethylcyclohexanol	0	2	2	2	2	10	5
methylanisole	0	10	11	19	15	21	17
methylcyclohexane	0	0	0	1	1	7	3
methylcyclohexanol	0	7	32	83	103	202	142
o-cresol	0	64	71	72	54	13	26
p/m-cresol	0	2	1	1	0	0	0
phenol	1	405	296	86	38	1	5
toluene	0	803	832	844	836	815	750
xylenol	0	6	6	14	12	15	13
Phenol mass balance (%)	-	120	106	106	101	99	90
Toluene mass balance (%)	-	111	99	100	99	96	90
Total mass balance (%)	-	114	102	103	100	98	90

Table S2.5. Gaseous products from the reaction of benzyl phenyl ether in MeOH/DMC at 300 °C with Cu_{20}PMO.

mmol	1 h	2 h	3 h	4 h	5 h	6 h
H_2	1	3	6	6	6	6
CO	2	5	9	8	7	7
CH_4	0	1	0	0	0	0
CO_2	19	9	4	3	4	3
total	22	18	18	17	18	17

Table S2.6. Gaseous products from the reaction of benzyl phenyl ether in sc-MeOH at 300 °C with Cu_{20}PMO.

mmol	1 h	2 h	3 h	6 h
H_2	12	15	14	12
CO	0	2	1	0
CH_4	0	0	0	0
CO_2	1	1	2	0
total	13	18	18	12

Table S2.7. Reaction of benzyl phenyl ether in sc-MeOH without catalyst at 300 °C.

Compound (µmol)	0 h	1 h	2 h	3 h	4 h	5 h	6 h
2-(phenylmethyl)-phenol	5	2	13	22	30	42	47
2,2-diphenylpropan-1-ol	0	0	1	2	2	2	2
2-hydroxy-1-phenyl-ethanone	0	3	2	3	3	3	3
acetophenone	0	0	0	0	1	1	1
benzaldehyde	0	2	3	4	5	6	5
benzene	0	0	1	2	3	5	7
benzophenone	0	1	11	22	31	48	52
benzyl alcohol	0	1	1	3	4	5	6
benzyl phenyl ether	843	747	733	650	616	490	417
bibenzyl	0	0	1	2	3	5	6
diphenylmethane	0	0	0	0	0	0	1
o-cresol	0	0	0	0	0	1	1
phenol	0	9	36	71	98	149	164
toluene	0	2	31	68	100	167	208
Total Mass Balance (%)	-	90	93	89	90	84	79

Table S2.8. Reaction of benzyl phenyl ether in MeOH/DMC without catalyst at 300 °C.

Compound (µmol)	0 h	6 h
1-methoxy-2-[(4-methoxyphenyl)methyl]-benzene	0	3
1-methoxy-4-(phenylmethyl)-benzene	0	10
2-(phenylmethyl)-phenol	0	38
3-methoxydiphenylmethane	0	17
anisole	0	92
benzaldehyde	0	11
benzene	0	18
benzophenone	0	46
benzyl alcohol	0	10
benzyl phenyl ether	883	499
bibenzyl	0	8
diphenylmethane	0	1
methyl diphenylmethyl ether	0	46
methyl ester benzoic acid	0	5
o-cresol	0	2
phenol	7	143
phenylethyl alcohol	0	3
toluene	3	131
Total Mass Balance (%)	-	90

Table S2.9. Reaction of benzyl phenyl ether in MeOH/DMC (2/1) with copper-free calcined HTC at 300 °C.

Compound (μmol)	0 h	6 h
1-methoxy-4-(phenylmethyl)-benzene	0	9
2-(phenylmethyl)-phenol	0	17
anisole	0	73
benzene	0	22
benzophenone	0	106
benzyl alcohol	0	27
benzyl phenyl ether	1000	683
bibenzyl	0	11
diphenylmethane	0	3
o-cresol	0	15
phenol	7	79
toluene	4	181
Total Mass Balance (%)	-	96

Table S2.10. Reaction of 2-phenoxy-1-phenylethan-1-ol in MeOH/DMC with $Cu_{20}PMO$ at 300 °C. [a] reaction in sc-MeOH.

Compound (µmol)	0	1 h	2 h	3 h	4 h	5 h	6 h	6 h[a]
1-phenylethanol	0	37	0	0	0	0	0	0
2-phenoxy-1-phenylethanol	435	5	1	1	1	0	1	0
anisole	3	224	322	309	319	316	309	40
benzene	1	1	0	3	2	12	6	2
cyclohexane	0	0	1	3	4	8	7	3
cyclohexanol	0	9	25	32	34	34	33	234
dimethylcyclohexanol	0	1	1	1	1	3	3	2
ethylbenzene	3	327	368	363	366	401	388	427
methylanisole	0	28	47	39	34	19	22	6
methylcyclohexane	0	0	0	0	0	3	1	0
methylcyclohexanol	0	1	7	15	20	42	35	65
o-cresol	0	18	22	15	16	4	8	46
phenol	0	159	52	13	10	0	1	39
propyl benzene	0	28	40	39	43	45	41	28
toluene	0	2	4	4	5	5	6	4
xylenol	0	1	3	4	4	4	6	7
Phenol mass balance (%)	0	102	110	100	102	102	99	102
1-phenylethan-1-ol mass balance (%)	0	91	94	93	94	102	99	105
Total mass balance (%)	101	97	103	97	99	103	100	104

Table S2.11. Char amounts and GPC data for raw liquid and non-volatile products from the reaction of organosolv poplar lignin (OPL) with/without $Cu_{20}PMO$ at 300 °C for 3 h in MeOH/DMC and in sc-MeOH.

GPC parameters	OPL	No catalyst	No catalyst	$Cu_{20}PMO$	$Cu_{20}PMO$
		MeOH/DMC	sc-MeOH	MeOH/DMC	sc-MeOH
Raw product M_n (g/mol)	1290	360	430	350 (320)[a]	320 (310)
Raw product M_w (g/mol)	2220	720	630	510(460)	400 (430)
Raw product PDI	1.72	2.01	1.47	1.44(1.41)	1.27 (1.35)
Non-volatile product (wt %)		59	37	50 (64±2)[b]	24[c] (45±2)[b]
Non-volatile product M_n (g/mol)		390	480	390	360
Non-volatile product M_w (g/mol)		880	720	550	480
Non-volatile product PDI		2.28	1.52	1.40	1.52
Char (wt %)		32	35	-	-

[a] values in parentheses represent a second run under analogous conditions. [b] average of two independent experiments. Doubling the drying time gave similar recovery values (66 % and 47% for experiments in MeOH/DMC and sc-MeOH, respectively) The weight percentages obtained from catalytic runs of 6 h duration were the same within experimental uncertainties (44 ± 4 % and 62 ± 2 %, respectively) [c]We have discounted this value as likely due to an experimental error

Table S2.12. Chemical shifts and integration regions for lignin and its depolymerized products in a ^{31}P NMR spectrum.
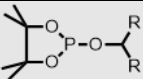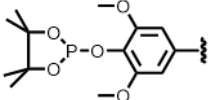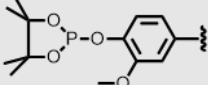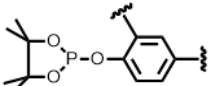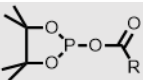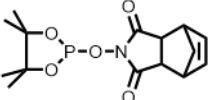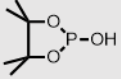
Identification	Chemical Structure	δ (ppm)
Aliphatic OH		150.0-145.4
Syringyl Phenolic OH		~142.7
Guaiacyl Phenolic OH		140.2-139.0
Condensed Phenolic OH (β-5, 5-5, 4-0-5)		144.7-140.2
Carboxylic Acid OH		136.0-133.6
Internal Standard (N-hydroxy-5-norbornene-2,3-dicarboximide)		152.8-151.0
TMDP Hydrolysis product		~132.2

Table S2.13. GC-MS detected peak assignments for depolymerized products from lignin disassembly with/without $Cu_{20}PMO$ and with/without DMC for 3 h; and with $Cu_{20}PMO$ and with/without DMC for 6 h.

Ret. Time (min)	Compound	Normalized Area					
		sc-MeOH Control 3h	MeOH/DMC Control 3h	sc-MeOH 3h	MeOH/DMC 3h	sc-MeOH 6h	MeOH/DMC 6h
17.2	2-methoxyphenol	0.12	0	0.009	0	0	0
20.0	2-methoxy-4-methylphenol	0	0	0.009	0	0.036	0
22.2	4-ethyl-2-methoxyphenol	0	0	0.046	0	0.14	0
23.8	4-ethyl-1,2-di-methoxybenzene	0	0	0.014	0.11	0	0.99
24.1	2-methoxy-4-ethyl-6-methylphenol	0	0	0.012	0	0	0
24.4	2-methoxyl-4-propylphenol	0	0	0.26	0	0	0
25.8	1,2-dimethoxy-4-propylbenzene	0	0	0.094	0.29	0	3.6
28.1	4-methyl-syringol (2,6-di-methoxy-4-methyl-phenol)	0	0	0.010	0	0	0
28.5	1-(4-hydroxyl-3,5-dimethoxyphenyl)-ethan-1-one	0	0	0.046	0	0	0
29.7	4-ethyl-2,6-dimethoxy phenol	0	0	0.018	0	0	0
29.8	3-propyl-1,2,4-trimethoxy-benzene	0	0	0.043	0.41	0	5.7
30.8	benzeneacetic acid, alpha-	0	0	0.023	0	0	0

102

	hydroxy-3-methoxy, methyl ester						
31.4	2,6-dimethoxy-4-propylphenol	0	0	0.19	0	0	0
31.7	4-propionyl-syringol	0	0	0.017	0	0.091	0
33.4	dihydro coniferyl alcohol	0	0	0.029	0	0	0
33.9	4-(ethoxymethyl)-2-methoxyphenol	0	0	0.013	0	0	0
34.3	3-(3,5-dimethoxy-phenyl)-1-propanol	0	0	0.029	0	0	0
34.7	3-(3,4-dimethoxy-phenyl)-1-propanol	0	0	0.012	0	0.16	0
37.7	4-methyl-dibenzofuran	0	0	0.016	0	0	0
21.7	3,4-dimethoxy-toluene	0	0	0	0.013	0.026	0.13
24.3	2-methyoxy-4-propylphenol	0	0	0	0.018	0	0.11
25.5	1-(2,4-dihydroxy-3-propylphenyl)-ethanone	0	0	0	0.021	0	0.18
26.5	1,2,3-trimethyoxy-5-methylbenzene	0	0	0	0.022	0	0.25
28.2	5-ethyl-1,2,3-trimethoxy-benzene	0	0	0	0.11	0.060	0.78
29.7	2-ethoxy-3,4,6,7,8,9-hexahydro-8,8-dimethyl-6-oxo-2H-chromene	0	0	0	0.032	0	0.28

31.8	1,2-dimethoxy-4-(3-methoxypropyl)-benzene	0	0	0	0.094	0	0.71
34.3	3-(3,4-dimethoxy-phenyl)-propan-1-ol	0	0	0	0.15	0	0.60
34.8	methyl 3,4-dimethoxyphenyl propanoic acid	0	0	0	0.061	0	0.22
34.9	3-(3,4-di-methoxy-phenyl)propanoic acid	0	0	0	0.048	0	0.31
35.1	methyl 3,4,5-trimethoxy benzoic acid	0	0	0	0.030	0	0.20
35.3	3,4-dimethoxy benzoic acid	0	0	0	0.073	0	0.39
37.7	syringaldehyde	0.17	0	0	0.13	0	0.42
37.9	2-methyl-4-(methoxycarbonyl)-1H-benzo[ij](2,7)-naphthyridine	0	0	0	0.035	0	0.099
38.0	2,3-dihydro-1,3-methano-1H-cyclo-penta[b]quinoxaline	0	0	0	0.037	0	0.18
48.3	methyl 2-(3,4-dimeth-oxyphenyl)acetate	0	0	0	0.023	0	0.076
19.9	2-methoxy-5-methylphenol	0.035	0	0	0	0.082	0
22.2	2-methoxy-benzeneethanol	0.024	0	0	0	0	0
23.8	2-methoxy-4-vinylphenol	0.047	0	0	0	0	0
24.0	methylpento	0.047	0	0	0	0	0

	pyranoside					
24.3	2-methoxy-4-propylphenol	0.065	0	0	0	0.78	0
24.5	2-methoxy-4-(2-propenyl)phenol	0.045	0	0	0	0	0
25.2	beta-D-methyl ribopyranoside	0.023	0	0	0	0	0
26.0	2,6-dimethoxy-phenol	0.38	0	0	0	0	0
26.5	2-methoxy-4-(methoxymethyl)phenol	0.014	0	0	0	0	0
27.3	2-methoxy-4-(1-propenyl)phenol	0.29	0	0	0	0	0
27.8	vanillin	0.082	0	0	0	0	0
28.0	2,4-dimethoxy-3-methylphenol	0.094	0	0	0	0	0
28.6	dimethyl ester nonanedioic acid	0.018	0	0	0	0	0
29.0	2,3-dihydro-2,2,5-trimethyl benzofuran	0.040	0	0	0	0	0
29.7	ethyl syringol	0.055	0	0	0	0	0
29.8	1-(4-hydroxy-3-methoxyphenyl)-ethanone	0.020	0	0	0	0	0
30.1	Methyl ester, 4-hydroxy-3-methoxy benzoic acid	0.11	0	0	0	0	0
30.8	4-hydroxy-3-methoxy benzeneacetic acid	0.047	0	0	0	0	0

31.3	4-propyl syringol	0.040	0	0	0	0	0
31.6	2,6-dimethoxy-4-(2-propenyl)phenol	0.073	0	0	0	0	0
33.0	trans-4-propenylsyringol	0.27	0	0	0	0	0
33.8	methyl ester, hexadecanoic acid	0.11	0.038	0	0	0	0
34.8	coniferyl aldehyde	0.052	0	0	0	0	0
36.1	1-(4-hydroxy-3,5-dimethoxy-phenyl)ethanone	0.044	0	0	0	0	0
36.8	4-hydroxy-3,5-dimethoxy benzoic acid, hydrazide	0.27	0	0	0	0	0
36.8	syringylacet one	0.075	0	0	0	0	0
37.9	Methyl ester, 9,12-octadeca-dienoic acid	0.032	0	0	0	0	0
39.2	dihydrosyrin genine	0.036	0	0	0	0	0
41.4	3,5-dimethoxy-4-hydroxy-cinnamaldehyde	0.029	0	0	0	0	0
19.4	1,2-dimethoxy-benzene	0	0.015	0	0	0	0
21.7	1,2-dimethoxy -4-methyl-benzene	0	0.008	0	0	0	0
24.5	1,2,3-trimethoxy-benzene	0	0.044	0	0	0	0
25.5	4-ethenyl-1,2-dimethoxy-	0	0.041	0	0	0	0

benzene

26.0	1,2-dimethoxy-4-(2-propenyl)benzene	0	0.012	0	0	0	0
26.5	1,2,3-trimethoxy-5-methylbenzene	0	0.020	0	0	0	0
27.5	3-methyl-3-(1-naphthyl)-1-butene	0	0.008	0	0	0	0
27.7	methyl cis-isoeugenol	0	0.008	0	0	0	0
28.0	3,4-dimethoxyphenethyl alcohol	0	0.018	0	0	0	0
28.7	1,2-dimethoxy-4-(1-propenyl)-phenol	0	0.14	0	0	0	0
29.4	4,5-dimethoxy-2-(2-propenyl)-phenol	0	0.062	0	0	0	0
29.9	3,4-dimethoxy benzaldehyde	0	0.16	0	0	0	0
30.8	4-(dimethoxymethyl)-1,2-dimethoxybenzene	0	0.054	0	0	0	0
31.9	3,4,5-trimethoxybenzyl methyl ether	0	0.052	0	0	0	0
32.2	methyl ester, 3,4-dimethoxy benzoic acid	0	0.10	0	0	0	0
32.5	1,2,3-tri-methoxy-5-(2-propenyl)-benzene	0	0.16	0	0	0	0
32.8	3,4,5-trimethoxy benzaldehyde	0	0.078	0	0	0	0

33.2	3-(4-methoxy-phenyl)-1-phenyl 2-propen-1-one	0	0.13	0	0	0	0
34.1	1-hydroxy-2-(methoxy-carbonyl)-5-methylene-cycloheptan-3-one	0	0.096	0	0	0	0
34.9	2-(3,4-di-methoxy-phenyl)tetrahydrofuran	0	0.18	0	0	0	0
35.0	methyl ester, 3,4,5-trimethoxy benzoic acid	0	0.22	0	0	0	0
38.0	1,2,3,4-tetramethoxy-5-(2-propenyl) benzene propen-1-one	0	0.21	0	0	0	0
38.5	methyl ester, 3-(3,4-dimethoxy-phenyl) 2-propenoic acid	0	0.027	0	0	0	0
4.4	2-(2-hydroxy-propoxy)-1-propanol	0	0	0	0	0.010	0
4.6	butanoic acid methyl ester	0	0	0	0	0.017	0
5.0	5,5-dimethyl-1,3-hexadiene	0	0	0	0	0.016	0
9.1	1-isobutyliden-3-methyl-cyclopentane	0	0	0	0	0.054	0
9.2	2,4-dimethyl-cyclopentanol	0	0	0	0	0.021	0
10.1	2,5-dimethyl-2-	0	0	0	0	0.017	0

	hexene						
10.5	3-methyl-cyclohexanone	0	0	0	0	0.022	0
10.6	1,2-exoxyhexane	0	0	0	0	0.012	0
10.8	2-vinylpenta-3,4-dien-2-ol	0	0	0	0	0.014	0
10.9	2,6-dimethyl-1-heptane	0	0	0	0	0.022	0
12.0	2-isobutyl-6-methyl-1-heptene	0	0	0	0	0.042	0
12.6	1-hexanol	0	0	0	0	0.023	0
13.1	2,6-dimethyl-1-heptene	0	0	0	0	0.015	0
13.8	3,4-dimethyl-1-hexene	0	0	0	0	0.022	0
15.2	2,3,6-trimethyldecane	0	0	0	0	0.026	0
15.4	3-methyl-1-hexene	0	0	0	0	0.017	0
15.6	1-cyclohexyl-nonene	0	0	0	0	0.033	0
16.0	2-(1-methyl-2-oxo-propyl)cyclohexanone	0	0	0	0	0.025	0
16.2	3,5-dimethyl-cyclohexanol	0	0	0	0	0.056	0
16.6	5-methyl-2-(1-methyl-ethyl)cyclohexanol	0	0	0	0	0.084	0
16.9	3,4,4-trimethyl-2-pentene	0	0	0	0	0.025	0
17.7	3-methyl-1-	0	0	0	0	0.16	0

	pentene						
17.9	2-methoxyphenol	0	0	0	0	0.070	0
18.2	1-methyl-2-(4-methylpentyl)-cyclopentane	0	0	0	0	0.066	0
18.4	hexylcyclopentane	0	0	0	0	0.056	0
19.1	3-methyl-cyclopentanol	0	0	0	0	0.089	0
19.6	1,2,3,4-tetramethyl-cyclobutene	0	0	0	0	0.061	0
21.0	7,7-dimethyl-bicyclooctan-2-one	0	0	0	0	0.091	0
21.8	3-methyl-3-(1-methyl-ethenyl)cyclohexanone	0	0	0	0	0.078	0
21.9	3,3-dimethyl-1-hexene	0	0	0	0	0.027	0
22.1	4-propylphenol	0	0	0	0	0.025	0
22.2	3-tert-butyl-2-cyclohexen-1-one	0	0	0	0	0.024	0
22.5	2,4,6-trimethylphenol	0	0	0	0	0.016	0
22.7	2-hydroxy-5-methoxybenzaldehyde	0	0	0	0	0.042	0
22.9	4-methyl-2-propylphenol	0	0	0	0	0.022	0
24.1	1-methoxy-1,2,3,4,5,-pentamethyl-1,3-cyclo-pentadiene	0	0	0	0	0.023	0
24.4	1,4-dimethoxy-2,5-	0	0	0	0	0.072	0

	dimethyl-benzene						
24.5	4-ethyl-2-propylphenol	0	0	0	0	0.089	0
24.7	acetophenone	0	0	0	0	0.092	0
26.2	endo-7-hydroxy-8,8-dimethyl-bicyclo-[4.3.0]non-1(9)-en-2-one	0	0	0	0	0.18	0
26.5	1,2-dimethoxy-4-n-propyl-benzene	0	0	0	0	0.32	0
26.7	2-(1,2-epoxy-cycloheptyl)-1-pentene	0	0	0	0	0.42	0
27.2	1,5-heptadiyne	0	0	0	0	0.068	0
27.7	1,4-epoxy-2-exo-ethoxycarbonyl-3-methylene-5-cyclohexene	0	0	0	0	0.073	0
28.0	methyl-9-oxo-8-oxabicyclonona-1(6), 2-diene-2-carboxylate	0	0	0	0	0.072	0
28.2	2-(phenyl-ethynyl)phenol	0	0	0	0	0.093	0
28.8	3-tertbutyl-4-hydroxyanisole	0	0	0	0	0.058	0
30.5	2-cyclohexyl-4-phenyl-1-buten-3-yne	0	0	0	0	0.23	0
31.0	4-methylstibene oxide	0	0	0	0	0.18	0
31.6	2-methyl-3-(methoxy-	0	0	0	0	0.048	0

	carbonyl)-4,5,6,7-tetrahydrobenzofuran						
32.1	syringyl aldehyde	0	0	0	0	0.12	0
32.4	1,2,3,4,9,10-hexahydro-9,10-exo-epoxy-1,4-exo-methano-anthracene	0	0	0	0	0.059	0
32.5	veratryl acetate	0	0	0	0	0.051	0
32.8	1,4-dimethyl-7-methoxy-2,3-dihydroindene	0	0	0	0	0.057	0
32.9	6-beta-methyl-2-propyl-delta-1-bicyclo-[440]decen-8-alpha-ol	0	0	0	0	0.061	0
33.0	trans-isomyristicin	0	0	0	0	0.055	0
33.4	3-phenyl-2,1-benisoxazole	0	0	0	0	0.039	0
34.6	hexadecanoic acid, methyl ester	0	0	0	0	0.053	0
35.5	3-(3,4-di-methoxyphenyl)-1-propionic acid	0	0	0	0	0.040	0
36.4	6-cyclobut-1-enyl-spiro[2,4]hept-4-ene	0	0	0	0	0.026	0
38.4	1-octen-3-yne	0	0	0	0	0.052	0

Table S2.14. GPC results for products from consecutive 3 h runs with organosolv poplar lignin as substrate and the same $Cu_{20}PMO$ catalyst in MeOH/DMC at 300 °C.

GPC Parameters	M_n	M_w	PDI
1st run	330	460	1.4
2nd run	370	530	1.4
3rd run	370	550	1.5
4th run	320	500	1.5
5th run	320	490	1.5

Table S2.15. Yield of products (%) and unconverted anisole substrate for catalysis runs[a] with water or long reaction time in sc-MeOH. All values are reported as calculated % of product mixture. Reaction temperature was 300 °C.

Compound	3 h[b]	+H$_2$O 3 h[c]	48 h[d]
anisole	78.8±3.2	68.9±2.2	1.05
benzene	13.5±2.6	16.8±0.8	26.4
cyclohexane	0.9±0.3	1.5±0.2	40.4
cyclohexanol	0.7±0.1	0.8±0.1	0.00
dimethylcyclohexane	0.0±0	0.0±0	0.51
methylanisole	2.9±0.5	3.9±0.5	17.5
methylcyclohexane	0.0±0	0.0±0	3.10
methylcyclohexanol	0.4±0.2	0.5±0.1	0.57
phenol	0.0±0	0.0±0	0.39
toluene	0.0±0	0.0±0	0.29
conversion (%)	21.2±3.2	31.1±2.2	99.6
mass balance (%)[e]	97.3±2.8	92.4±0.4	90.2

[a]All reactions were conducted with CuPMO calcined at 600 °C and ~2 mmol of anisole. [b]Average of 5 experiments, each run for 3 h. [c]Average of 3 experiments with 1 mmol added H$_2$O, each for 3 h. [d] Same conditions as the first column but with a reaction time of 48 h. [e]Mass balance is relative to the amount of anisole quantified by GC-FID analysis of the stock solution.

Table S2.16. Yields of products and unconverted anisole substrate for catalysis runs with magnesium or sodium nitrate salts in sc-MeOH.[a] All values are reported as % of product mixture calculated based on GC-FID areas and ECN.

Cation (in ppm)[b]	16 (Mg)[c]	97 (Mg)[c]	202 (Mg)[c]	11 (Na)[d]	103 (Na)[d]	201 (Na)[d]
nitrate (in ppm)[e]	80[c]	492[c]	1031[c]	31[d]	277[d]	542[d]
Products						
anisole	86.7	93.9	92.1	86.1	88.0	90.6
benzene	7.41	5.91	3.45	6.76	5.34	4.33
cyclohexane	0.51	0.37	0.20	0.37	0.20	0.13
cyclohexanol	0.38	0.66	0.54	0.55	0.58	0.60
methylanisole	2.27	1.58	0.91	1.47	0.76	0.47
methylcyclohexanol	0.15	0.41	0.37	0.45	0.42	0.37
xylenol	0.00	0.00	0.00	0.00	0.00	0.00

[a]All reactions were conducted for 3 h at 300 °C with CuPMO calcined at 600 °C. [b]ppm = mg cation /L of solvent. [c]Mg(NO$_3$)$_2$·6H$_2$O. [d]NaNO$_3$ as the additive. [e]ppm = mg nitrate /L of solvent.

Table S2.17. Yields of products and unconverted anisole substrate for catalysis runs with sodium phosphate (NaH_2PO_4) in sc-MeOH.[a] All values are reported as % of product mixture calculated based on GC-FID areas and ECN.

phosphate (ppm)[b]	43	302	620
Products			
anisole	81.9	82.9	81.3
benzene	10.4	11.3	11.4
cyclohexane	0.75	0.61	0.60
cyclohexanol	0.60	0.54	0.59
methylanisole	2.58	1.91	1.76
methylcyclohexanol	0.42	0.39	0.36

[a]All reactions were conducted for 3 h in 3.0 mL MeOH at 300 °C with CuPMO calcined at 600 °C. [b]ppm = mg $H_2PO_4^-$ /L of solvent

Table S2.18. Yields of products and unconverted phenol substrate for catalysis runs. All values are reported as % of product mixture calculated based on GC-FID areas and ECN. Reaction temperature was 300 °C.

Compound	3 h[a]	48 h
2-benzylphenol	0.14±0.05	0.34
anisole	6.61±0.22	2.82
benzene	0.52±0.02	2.52
cyclohexane	0.37±0.03	4.67
cyclohexanol	25.8±3.6	0.00
dimethylcyclohexane	0.65±0.09	18.4
dimethylcyclohexanol	1.16±0.11	3.97
methylanisole	0.26±0.03	5.96
methylcyclohexane	0.17±0.01	36.6
methylcyclohexanol	25.3±2.5	9.52
o-cresol	9.79±1.41	0.41
p-cresol	0.12±0.09	0.73
phenol	3.12±1.11	2.57
toluene	0.00±0	1.15
xylenol	3.46±0.37	0.00
conversion (%)	96.9±1.1	97.4
mass balance (%)	77.3±8.1	89.4

[a]average of 4 experiments. All reactions were conducted with CuPMO calcined at 600 °C. The '#' corresponds to entry number. The reaction times are in the top row. Mass balance is relative to the amount of phenol quantified by GC-FID analysis of the stock solution.

Tables S2.19.1-S2.19.3 Yields of products and unconverted anisole substrate for catalysis runs with different chloride concentrations in sc-MeOH. All values are reported as % of product mixture calculated based on GC-FID peak areas calibrated with Effective Carbon Numbers (ECNs). All reactions were conducted for 3 h at 300 °C in sc-MeOH with CuPMO calcined at 600 °C. The "0" corresponds to reactions without additives. Initial anisole for "0" entry = 2225 µmol

Table S2.19.1 (A) entries: $MgCl_2 \cdot 6H_2O$ as the chloride source. (D) entry; catalyst recalcined at 600 °C after one use with 109 ppm Cl. Initial anisole ~2 mmol in each case.

Cl added (in ppm)[a]	0	16 (A)	109 (A)	224 (A)	109 (D)
Products		% yield			
anisole	78.8±3.2	90.4±1.6	97.1±2.8	97.2±0.9	95.9±0.5
benzene	13.5±2.6	5.2±1.0	0.3±0.1	0.00±0	0.05±0.1
cyclohexane	0.92±0.3	0.3±0.1	0.00±0	0.00±0	0.00±0
cyclohexanol	0.70±0.1	0.4±0	0.00±0	0.00±0	0.00±0
methyl anisole	2.91±0.5	1.5±0.3	0.00±0	0.00±0	0.00±0
methyl cyclohexanol	0.46±0.2	0.39±0	0.00±0	0.00±0	0.00±0
xylenol	0.00±0	0.00±0	0.05±0.1	0.00±0	0.26±0.1
conversion (%)	21.2±3.2	9.6±1.6	3.0±2.8	2.8±0.9	4.1±0.5
mass balance (%)	97.3±2.8	97.7±0.5	97.4±2.7	97.2±0.9	96.2±0.4

[a] ppm = mg chloride /L of solvent

Table S2.19.2 (B) = NaCl as the chloride source

Cl added (in ppm)[a]	10 (B)	107 (B)	208 (B)
Products		% yield	
anisole	89.4±0.6	97.7±1.7	98.6±2.2
benzene	7.0±0.3	0.38±0	0.00±0
cyclohexane	0.36±0	0.00±0	0.00±0
cyclohexanol	0.59±0	0.00±0	0.00±0
methyl anisole	1.52±0	0.00±0	0.00±0
methyl cyclohexanol	0.38±0	0.00±0	0.00±0
xylenol	0.00±0	0.00±0	0.00±0
conversion (%)	10.6±0.6	2.3±1.8	1.4±2.2
mass balance (%)	99.2±0.3	101.2±1.8	98.6±2.2

[a] ppm = mg chloride /L of solvent

Table S2.19.3 (C) = CCl$_4$ as the chloride source

Cl added (in ppm)[a]	16 (C)	87 (C)	178 (C)
Products		% yield	
anisole	91.0±3.7	97.6±1.2	97.0±0.9
benzene	5.1±0.6	0.5±0	0.00±0
cyclohexane	0.26±0	0.00±0	0.00±0
cyclohexanol	0.44±0	0.00±0	0.00±0
methyl anisole	1.4±0.2	0.08±0	0.00±0
methyl cyclohexanol	0.35±0	0.00±0	0.00±0
xylenol	0.00±0	0.00±0	0.34±0.1
conversion (%)	9.0±3.7	2.4±1.2	3.1±0.9
mass balance (%)	98.6±2.9	98.2±1.3	97.3±0.9

[a] ppm = mg chloride /L of solvent

117

Tables S2.20.1-S2.20.3 Yields of products (%) and unconverted benzyl phenyl ether (BPE) for catalysis runs with different chloride concentrations in sc-MeOH for CuPMO pretreatment.[a] All values are reported as % of product mixture calculated from GC-FID areas and ECN. All reactions were conducted at 300 °C.

Table S2.20.1 Product yields (%) from the 2 h reaction of BPE with CuPMO pretreated in sc-MeOH for 3 or 72 h. Initial benzyl phenyl ether = 1188 µmol

Pretreatment time / ppm Cl added	3 h[a]	72 h[a]
Products		
anisole	13.6±2.0	11.0±1.3
benzene	0.37±0.05	0.82±0.73
benzyl phenyl ether	0.83±0.03	0.82±0.15
cyclohexane	0.61±0.09	0.58±0.01
cyclohexanol	30.0±9.8	31.8±19.0
dimethylcyclohexanol	0.80±1.13	0.88±0.47
methylcyclohexane	0.40±0.09	0.35±0.07
methylcyclohexanol	28.8±0.1	17.3±7.7
o-cresol	3.34±1.2	4.35±2.0
phenol	4.65±1.29	4.98±3.14
toluene	88.4±2.3	80.9±6.8
xylenol	0.98±0.52	1.24±0.23
dimer	0.64±0.19	5.09±1.31
mass balance (%)	87.5±4.3	83.0±12.7
conversion (%)	99.2±0.03	99.2±0.2

Table S2.20.2 Product yields (%) from the 2 h reaction of BPE with CuPMO pretreated in sc-MeOH for 3 h with chloride added. Initial benzyl phenyl ether = 1184 µmol

Pretreatment time / ppm Cl added	3 h[a] / 15	3 h[a] / 111	3 h[a] / 1022
Products			
anisole	12.2±0.8	2.26±0.06	1.05±0.07
benzene	0.36±0	1.10±0.03	1.67±0.12
benzyl phenyl ether	0.00±0	25.9±0.7	39.4±0.9
cyclohexanol	6.23±0.87	0.00±0	0.00±0
dimethylcyclohexanol	0.96±0.06	2.63±0.07	4.37±0.31
methylcyclohexanol	7.14±1.10	0.00±0	0.00±0
o-cresol	15.5±3.7	7.76±0.22	4.64±0.33
phenol	17.5±1.8	15.0±0.4	13.6±1.0
toluene	91.2±6.5	55.6±1.6	35.3±2.5
xylenol	7.52±0.32	5.18±0.15	2.96±0.21
trimethylphenol	0.46±0	1.54±0.04	0.82±0.06
dimer	5.54±0.37	14.3±0.4	11.7±0.8
mass balance (%)	85.1±1.6	85.6±2.4	83.4±2.2
conversion (%)	100±0	74.2±0.7	60.6±0.9

Table S2.20.3 Product yields (%) from the 2 h reaction of BPE with CuPMO pretreated in sc-MeOH for 72 h with added chloride. Initial benzyl phenyl ether = 1184 µmol

Pretreatment time / ppm Cl added	72 h[a] / 15[b]	72 h[a] / 111[b]	72 h[a] / 1022[b]
Products			
anisole	5.13±0.14	0.55±0.04	0.33±0.03
benzene	0.27±0.01	1.69±0.12	1.47±0.12
benzyl phenyl ether	0.00±0	34.6±2.4	62.4±5.19
cyclohexanol	4.58±0.13	0.00±0	0.00±0
dimethylcyclohexanol	0.00±0	2.53±0.18	1.49±0.12
methylcyclohexanol	0.44±0.01	0.00±0	0.00±0
o-cresol	11.9±0.3	7.11±0.50	3.81±0.32
phenol	59.3±1.7	28.3±2.0	10.1±0.84
toluene	88.9±2.5	52.6±3.7	25.0±2.08
xylenol	0.99±0.03	0.64±0.04	0.15±0.01
dimer	1.93±0.05	6.29±0.73	7.36±0.61
mass balance (%)	87.7±2.4	87.6±6.4	90.9±7.6
conversion (%)	100±0	65.4±2.4	37.6±5.2

[a]sc-MeOH pretreatment. All entries are an average of 2 runs. All reactions were conducted for 2 h with $Cu_{20}PMO$ calcined at 600 °C and pretreated by heating in sc-MeOH at 300 °C for specified time periods. All chloride was added as $MgCl_2·6H_2O$ (ppm $Cl^- = $ mg Cl^- /L of solvent). The label 'dimer' corresponds to compounds which could not be identified but showed m/z over 180. Mass balance is relative to the amount of benzyl phenyl ether observed by GC-FID area of the stock solution.

Table S2.21. Yields of products (%) and unconverted benzyl phenyl ether (BPE) for catalysis runs treated in sc-MeOH for 6 h with organosolv poplar lignin (OPL) and either recalcined at 600 °C or washed with MeOH. All values are reported as % of product mixture calculated from GC-FID areas and ECN. All reactions were conducted at 300 °C. Initial benzyl phenyl ether = 1299 µmol

Run/ pretreatment	6 h OPL + 600 °C[a,b]	6 h OPL + wash[c]
Products		
anisole	3.01±1.27	0.70±0.07
benzene	0.52±0.05	0.65±0.04
benzyl phenyl ether	12.8±1.3	42.3±2.7
dimethylcyclohexanol	0.49±0.05	0.45±0.01
o-cresol	6.97±0.52	3.42±0.48
phenol	11.0±1.5	15.9±1.3
toluene	57.0±0.9	26.6±1.3
xylenol	3.19±0.37	0.51±0.09
trimethylphenol	0.80±0.18	0.00±0
dimer	6.19±1.44	8.21±1.66
mass balance (%)	60.4±1.8	74.6±6.0
conversion (%)	87.2±1.3	57.7±2.7

[a]recalcined for 18 h. [b]average of 3 experiments. [c]average of 2 experiments. All reactions were conducted for 2 h. The label 'dimer' corresponds to compounds which could not be identified but showed m/z over 180. Mass balance is relative to the amount of benzyl phenyl ether observed by GC-FID area of the stock solution.

Table S2.22. Gas phase products after various catalysis runs with CuPMO in sc-MeOH at 300 °C. Substrates and conditions are listed below the table. All values are reported as mmol calculated from GC-TCD areas and standard calibration curves.[a]

Expt	PhOH[b]	An[b]	An[b,c]	sc-MeOH[d]	sc-MeOH[e]	BPE[d,f]	BPE[e,f]	OPL[g]	An[b,h]	An[b,i]	BPE[f,h]	BPE[f,i]
products (in mmol)												
H_2	15.4 ±2.3	14.7 ±1.0	16.7 ±0.2	20.6 ±0.5	18.4	26.2 ±0.6	23.8 ±1.3	8.36 ±0.2	6.18	7.46	7.63	3.07
CO	3.7 ±0.4	3.1 ±0.4	3.6 ±0.1	1.8 ±0.9	0.35	2.55 ±0.02	2.57 ±0.3	0.83 ±0.1	1.09	0.74	0.61	0.40
CH_4	1.2 ±0.2	1.5 ±0.3	1.97± 0.04	0.66 ±0.2	0.46	0.66 ±0.01	0.61 ±0.04	1.15 ±0.1	0.50	0.28	0.23	0.17
CO_2	2.2 ±0.4	1.7 ±0.2	1.9 ±0.1	1.4 ±1.2	0.79	1.5 ±0.1	0.85 ±0.1	5.3 ±1.6	1.92	0.40	0.72	0.25
Volumes (in L)												
Meas.	0.51 ±0.01	0.55 ±0.02	0.56 ±0.00	0.50 ±0.03	0.50	0.48 ±0.01	0.50 ±0.01	0.33 ±0.02	0.26	0.15	0.17	0.10
Calc.	0.52 ±0.07	0.47 ±0.03	0.54 ±0.01	0.60 ±0.04	0.49	0.75 ±0.02	0.61 ±0.18	0.35 ±0.04	0.22	0.21	0.22	0.09

All values are averages of individual experiments performed in at least duplicate. [a]PhOH = phenol, An = anisole, BPE = benzyl phenol ether, OPL = organosolv poplar lignin. [b]Reaction time = 3 h. [c]Added H_2O (1 mmole). [d]Catalyst treated in sc-MeOH for 3 h. [e]Catalyst treated in sc-MeOH for 72 h. [f]Reaction time = 2 h. [g]Reaction time = 6 h. [h]Catalyst pretreated by reaction with OPL for 6 h then recalcined at 600 °C. [i]Catalyst pretreated by reaction with OPL for 6 h then washed with MeOH.

Chapter 3. Alcohol Condensation using Porous Metal Oxides

3.1. Abstract

Improvement of processes that utilize renewable feedstocks to produce chemicals ordinarily derived from fossil carbon feedstocks is paramount to creating environmentally sustainable chemical and fuel industries. Catalytic conversion of biorefinery-derived ethanol via the Guerbet condensation has the potential to serve such a purpose. In this chapter, marked selectivity changes in the ethanol condensation over a copper-doped porous metal oxide catalyst upon a single exposure to ppm quantities of a soluble chloride source are examined. Without this modification, ethyl acetate is the major product, with the others being n-butanol (principally) plus some 1-hexanol, butyl acetate, and ethyl butanoate. In summary, a single exposure to chloride increases activity and, more importantly, dramatically changes selectivity to give n-butanol and 1-hexanol as the largest products. X-ray diffraction and basicity measurements pre- and post-reaction were used to examine how chloride alters the properties of this Earth-abundant catalyst prepared by calcining a Cu-doped Mg/Al hydrotalcite.

3.2. Introduction

3.2.1. The Guerbet Condensation

The Guerbet condensation of ethanol (EtOH) is an established pathway to the production of n-butanol (n-BuOH) and higher alcohols[1] that are industrially useful chemicals.[2,3] Marcel Guerbet described this condensation reaction over a century ago.[4] However, as noted in a recent review by Galadima and Muraza,[5] poor selectivity in catalytic systems have hindered industrial applications. Thus, improvements in catalytic systems must be made for the Guerbet reaction to play a role in a future sustainable bio-based chemical and/or fuel industry.

The Guerbet reaction involves dehydrogenation of an alcohol to an aldehyde, followed by an aldol condensation and dehydration to give an α,β-unsaturated aldehyde. Hydrogenation of the α,β-unsaturated aldehyde gives the longer chain alcohol. For instance, EtOH is dehydrogenated to form acetaldehyde. Acetaldehyde is deprotonated under sufficiently basic conditions (pKa = 13.57 at 25 °C), and this intermediate undergoes an aldol condensation to form crotonaldehyde (Scheme 3.1). Crotonaldehyde is then hydrogenated to form the higher alcohol, n-BuOH (Scheme 3.1).[1,6,7] The product, n-BuOH, may also undergo further Guerbet chemistry with another n-BuOH leading to branched alcohols (2-ethyl-hexanol) and linear alcohols (1-octanol) or with EtOH leading to 2-ethyl-butanol and 1-hexanol. These so-called Guerbet alcohols have potential applications, for example as fuels, however, a more selective product stream would be needed to circumvent energy intensive separations.
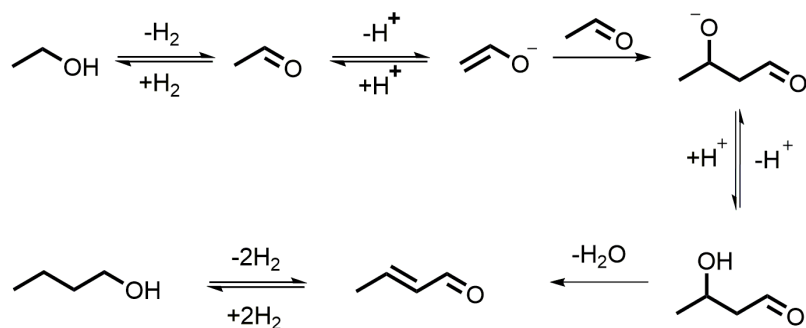
Scheme 3.1. Plausible pathway for the catalytic conversion of EtOH to n-BuOH with transition metal doped PMOs.[1,6,7] Reproduced with permission from *ACS Sustainable Chem. Eng.* **2018**, 6, 15119−15126. Copyright 2018 American Chemical Society.

Some EtOH is likely present as ethoxide under basic conditions in this reaction. The acetaldehyde formed from ethanol dehydrogenation may react with ethoxide to form the hemiacetal 1-ethoxyethan-1-ol (Scheme 3.2). Dehydrogenation of the hemiacetal with a metal catalyst forms ethyl acetate (Scheme 3.2). Another side reaction in the Guerbet condensation of EtOH which results in ethyl acetate is the Tishchenko reaction, where two molecules of acetaldehyde disproportionate in the presence of an alkoxide. The Tishchenko reaction is a crucial industrial process for ethyl acetate production.[8]
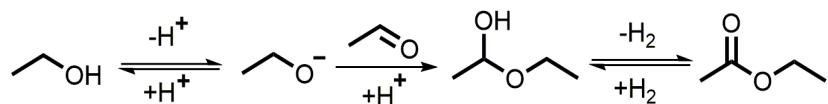
Scheme 3.2. Pathway for the conversion of EtOH to EtOAc showing plausible intermediates. Reproduced with permission from *ACS Sustainable Chem. Eng.* **2018**, 6, 15119−15126. Copyright 2018 American Chemical Society.

The intermediates produced by dehydrogenation of ethanol (acetaldehyde) and aldol condensation of ethanol with acetaldehyde (crotonaldehyde) may undergo reactions which lead to various organic esters. The primary product of Guerbet condensation of ethanol, n-butanol, can itself undergo further condensation or transesterification reactions. These reactions lead to poor selectivity to a single compound in Guerbet condensation systems.[5]

123

3.2.2. Potential for Bio-renewable Alcohols and Esters

Gasoline constitutes most of the transportation energy consumption in the United States. The environmental and economic costs of extensive fossil fuel usage led to the establishment of the Renewable Fuel Standard (RFS) Program[9] as part of a mission to facilitate energy independence and security as well as ensure that transportation fuels contain renewable components that would reduce greenhouse gas (GHG) emissions. The RFS program requirements have in part driven research into the production of lignocellulose-based biofuels, including "second generation" or cellulosic ethanol. Ethanol (EtOH) constitutes the largest portion of biofuels produced in the US and globally.[10]

Fuel EtOH production has continued to rise with approximately 1×10^6 barrels (1.6 $\times 10^8$ liters) produced per day in the United States currently.[11] EtOH is typically mixed with gasoline to produce E10 gasoline (10 % EtOH by volume) which results in increased octane number and combustion efficiency.[12-14] Although most gasoline in the US contains EtOH, the high water solubility and corrosiveness of the aforementioned presents challenges in fuel transport and engine structural integrity.[15] In a recent report to the U.S. Senate, the U.S. Government Accountability Office found that the RFS program is unlikely to meet the current GHG emissions reduction goals for 2022 due to the investment required to overcome domestic fuel transport and storage issues of ethanol blended gasoline.[16]

Butanol (n-BuOH) produced from bio-ethanol would be a potential alternative fuel with favorable characteristics including higher energy density (Figure 3.1) and lower water solubility than EtOH.[14] Furthermore, a recent evaluation of n-butanol, isobutanol, ethanol, methanol, and acetone-gasoline fuel blends in spark-ignition engines showed that the butanol blends provided the greatest GHG emissions reduction amongst the blends evaluated.[17]

These characteristics make butanol an attractive advanced biofuel to help reduce light duty vehicle GHG emissions.
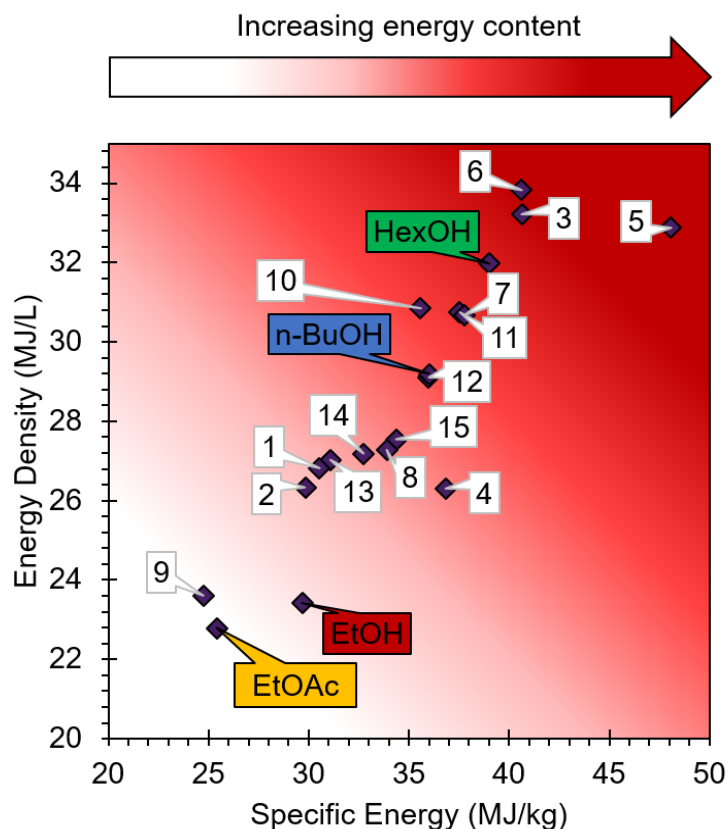
Figure 3.1. Energy density (MJ/L) and specific energy (MJ/kg) of ethanol and ethanol condensation products calculated using NIST condensed phase thermochemical data.[18] EtOAc = ethyl acetate, EtOH = ethanol, n-BuOH = n-butanol, HexOH = 1-hexanol. Numbered entries are minor products from $Cu_{20}PMO$ reaction: 1 = ethyl butanoate, 2 = butyl acetate, 3 = 1-octanol, 4 = diethyl ether, 5 = heptane, 6 = 2-ethyl-1-hexanol, 7 = 2-pentanol, 8 = 2-butanone, 9 = butanoic acid, 10 = ethyl octanoate, 11 = 3-hexanone, 12 = 2-pentanone, 13 = butyl butanoate, 14 = 1,1-diethoxyethane, 15 = butyraldehyde. Reproduced with permission from *ACS Sustainable Chem. Eng.* **2018**, 6, 15119−15126. Copyright 2018 American Chemical Society.

Ethanol coupling mixtures (primarily n-butanol and derivative Guerbet alcohols) were evaluated by Olarte et. al and show similar research and motor octane numbers as gasoline.[19] The selectivity for Guerbet condensation of ethanol discussed in the previous section may not be an issue since combustion fuels are typically mixtures. Examination of

the relative energy content of typical ethanol condensation products from transition metal doped porous metal oxide catalysis shows that these compounds are up to 30% more energy dense that EtOH (Figure 3.1). Combustion of one kg of EtOH would only yield 80 % of the energy obtained from the equivalent n-butanol combustion and 74 % from 1-hexanol combustion. Improvements in selectivity for Guerbet condensation catalytic systems can focus solely on reducing ethyl acetate production if bio-fuel production is the objective.

Our society is striving to transition domestic light duty transportation away from combustion engines. The potential chemical feedstock use of n-BuOH must be surveyed to assess the long-term viability of its production via a biomass based chemical process. The hydroformylation of propylene is the dominant industrial process for production of 1-butanol.[20] Other processes include carbonylation of propylene and biomass fermentation with various *Clostridium* bacteria. The former uses one of the most crucial fossil carbon resources.   The latter uses cellulose for the so-called Acetone-Butanol-Ethanol (ABE) fermentation. This fermentation process has garnered renewed attention as research interest in biomass based chemical production has increased.[15] The primary application for n-butanol is for surface coatings such as wood varnishes.[20] Butanol is either used to solubilize the rest of the coating's components or as a reagent in the production of those components. For example, butyl acrylate is a chemical produced from n-butanol that's used in latex paints. Two common flavors and fragrances, butyl acetate and butyl butyrate, are produced from transesterification reactions of n-butanol and are typically used in fruit flavor mixtures.[21]

The characteristic by-products in the Guerbet condensation reaction, longer chain alcohols and esters, have industrial uses as solvents, plasticizers, flavors, and chemical precursors.[8,21,22] The ability to tailor the product selectivity of a process provides alternative pathways for ethanol upgrading.[23,24] A high selectivity for a single product in Guerbet

126

condensation reactions is beneficial for industrial implementation to avoid the high energy costs associated with separations.[25] The production of higher carbon count alcohols (butanol, hexanol, and octanol) and esters (butyl acetate and ethyl butanoate) from bio-renewable ethanol is a promising path towards advanced biofuels and/or biochemicals. Improvement in selectivity of the Guerbet condensation and tunability of product streams are vital in creating an economically sustainable process.

3.2.3. Catalysts for the Guerbet Condensation

Marcel Guerbet described the reactions of ethyl, isobutyl, and isopentyl alcohols with their sodium alkoxide derivatives at the end of the 19th century.[4] He observed that at elevated temperatures (>200°C), condensation of the C_2, C_4, and C_5 alcohols occurred resulting in limited amounts of C_4, C_8, and C_{10} alcohols respectively. Since this discovery various homogeneous[26] and heterogenous[6] catalysts for the Guerbet condensation of alcohols have been researched.[1] Homogeneous Group 7, 8, and 9 transition metal catalyst systems have shown 90-99% selectivity for n-BuOH at relatively mild conditions 78-100°C with a base additive.[27-29] While homogeneous catalysts offer superior selectivity there are some issues associated with their use in Guerbet reactions.[1] The use of homogeneous bases and metal catalysts require additional purification steps to separate the products from the catalysts. Furthermore, reactor materials that are stable to base at elevated temperature are necessary for an industrial scale process. One of the benefits to using heterogenous catalysts is facile separation of the product stream from the catalyst. Transition metal doped porous metal oxides (PMOs) derived by calcining doped Mg^{2+}/Al^{3+} hydrotalcites are among some of the most active heterogeneous catalysts for the Guerbet reaction.[23,24,30-34] However, ethyl acetate (EtOAc) is a major byproduct of the ethanol condensation catalyzed by such PMOs.[33]

127

Although, it is a useful solvent, EtOAc is less energy dense (i.e. lower specific energy) than EtOH or n-BuOH and is not of great interest as a fuel additive.[8]

As described in Chapter 2, Cu-doped PMOs derived from the calcination of Cu-doped 3/1 Mg^{2+}/Al^{3+} hydrotalcites are effective catalysts for the reductive disassembly of lignin and of lignocellulose in supercritical methanol (sc-MeOH). It has also been shown that Cu-doped PMOs can disassemble lignin in supercritical ethanol (sc-EtOH).[35] Recently, similar CuPMOs have seen application in the Guerbet reaction. For example, Sun et al achieved good EtOH conversions and n-BuOH yields using Cu_xNi_y-PMOs.[36] The authors also examined Cu_{20}PMO, but found that it was as selective for EtOAc as it was for n-BuOH. Remarkably, we found that adding small quantities of chloride salts to the EtOH increases Cu_{20}PMO activity and, more importantly, improves the selectivity of the product stream toward n-BuOH and C_4+ products.[37] The present chapter describes studies on the nature of chloride-modified Cu_{20}PMO catalyst and how structural changes alter the product distribution.

3.3. Results and Discussion

Studies were conducted in closed 10 mL mini-reactors constructed from Swagelok junctions to which the substrate (typically 2.5 mL 100 % ethanol), the calcined catalyst (typically 100 mg), and an internal standard (20 µL decane) were added. The sealed reactors were placed in a preheated calibrated oven (in most cases at 320 °C), for a specific time period, after which these were removed from the oven and rapidly cooled. The reactor was then opened (caution, these are generally under pressure), and the solution was removed for analysis. The solution components were identified by gas chromatography with mass spectrometric detection (GC-MS) and analyzed quantitatively by gas chromatography with

flame ionization detection (GC-FID). Analysis techniques are described in more detail in the Experimental Methods section. Temporal catalysis experiments involved preparing a set of identically loaded mini-reactors that were placed together in the calibrated oven and individually removed at specific time periods. Unless otherwise stated, the catalyst in each case was the Cu-doped porous metal oxide ($Cu_{20}PMO$) prepared by 600 °C calcination of a 3:1 Mg^{2+}/Al^{3+} hydrotalcite (HTC) having 20% of the Mg^{2+} replaced by Cu^{2+}.

3.3.1. Increasing n-Butanol Selectivity over Porous Metal Oxides

The effects of small amounts of chloride impurities in lignin substrates (or added separately in the 10-1000 ppm range) on $Cu_{20}PMO$ activity were discussed in Chapter 2. We attributed those effects to chloride-induced sintering and poisoning of surface metallic Cu sites. The research described in this chapter was originally initiated to evaluate the impact of added chloride salts on the dehydrogenation and condensation reactions over $Cu_{20}PMO$ with a simple substrate. We initially proposed that the chloride induced sintering of Cu(0) nanoparticles would decrease overall catalyst basicity and hinder EtOH conversion. An increase in the size of the Cu(0) nanoparticles means there are on average more Cu-Cu bonds and less Cu-O bonds in the catalyst. This was shown by Dr. Zachary Jones in the Cu K-edge extended X-ray absorption fine structure of $Cu_{20}PMO$ reacted with sc-MeOH. An increase in the peak for Cu-Cu bonds and concurrent decrease in the peak for Cu-O bonds was observed and shown to be from the formation of calculated 2 nm Cu(0) nanoparticles.[38] These Brønsted Acid-Base Metal-Oxide pairs likely act as sites of EtOH deprotonation to form chemisorbed ethoxide.[39] Therefore, we hypothesized decreased EtOH conversion and increased aldol condensation products due to chloride poisoning of $Cu_{20}PMO$.

Figure 3.2 compares the results of two such catalysis experiments, one being the reaction of pure EtOH (2.5 mL 200 proof) at 320 °C for 6 h with $Cu_{20}PMO$ (100 mg), the other being the same conditions except a small amount of magnesium chloride was added (0.3 mg $MgCl_2 \cdot 6H_2O$ per 1 mL of EtOH). In the absence of this additive, EtOH conversion was 43% but this increased to 59% with the added $MgCl_2 \cdot 6H_2O$ (Figure 3.2). More importantly, the product distributions changed (yields calculated considering the reaction stoichiometry). Without chloride, the principal products, as analyzed by GC-FID, were EtOAc (16%) and n-BuOH (10%), while identified secondary products were ethyl butanoate (3%) and butyl acetate (2%), consistent with related studies by Sun et al.[36] The selectivity for conversion of EtOH to EtOAc was 45% while that for n-butanol was 29%. The mass balance for this experiment was 93%. A list of all products with their respective amounts is shown in Appendix B Table S3.1.

For the reaction carried out with added 140 ppm Cl⁻, the increased conversion was accompanied by a remarkable selectivity change. The yield of n-butanol increased to 28% (53% selectivity) while that of ethyl acetate decreased to 5% (8% selectivity). After n-BuOH, the most prominent product was 1-hexanol (13% selectivity), while ethyl butanoate and butyl acetate were observed in yields of ~2% each (Table 3.1). The production of n-butanol corresponds to a space time yield of 748 g_{n-BuOH} kg_{cat}^{-1} h^{-1}, which is slightly higher than that observed by Sun et al using Cu and Ni doped PMOs.[36] The mass balance for this experiment was 94%. These experiments show a single exposure of $Cu_{20}PMO$ to ppm Cl⁻ quantities, in amounts similar to experiments shown in Chapter 2, increased overall EtOH conversion and markedly increased n-BuOH selectivity.
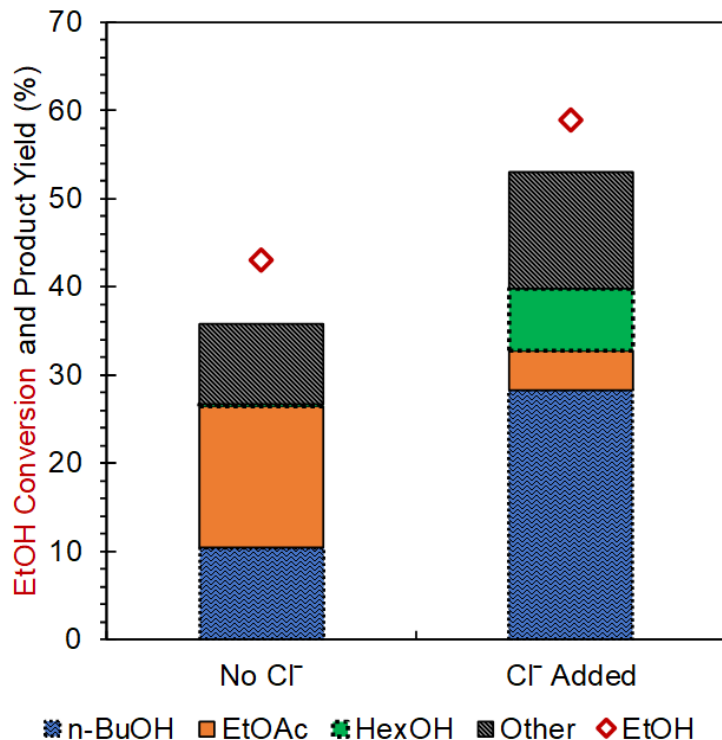
Figure 3.2. Product yield (%) and ethanol conversion (%, red diamonds) after reaction of ethanol with $Cu_{20}PMO$ for 6 h at 320 °C. Catalyst loading was 5 wt. % (100 mg). 'Cl⁻ Added' corresponds to EtOH with $MgCl_2 \cdot 6H_2O$ added (~140 ppm Cl⁻). "Other" products included 2-ethyl-1-butanol, ethyl butanoate, butyl acetate, and other C_{4+} compounds (see Tables 3.1 & Appendix B Table S3.1). Reproduced with permission from *ACS Sustainable Chem. Eng.* **2018**, 6, 15119−15126. Copyright 2018 American Chemical Society.

The EtOH conversion and reaction mass balance for reactions with $Cu_{20}PMO$ for 6 h at 320 °C were affected by the initial volume of EtOH (Table 3.1). EtOH conversion decreased when initial volume was increased from 1.5-2.5 mL, for reaction without any added Cl⁻. Ethanol conversion was 58 % for 1.5 mL EtOH loading presumably due to higher catalyst loading (~8%). The lowest ethanol conversion (43 %) was observed for 2.5 mL EtOH loading. This trend in conversion was not as pronounced for reactions with 140 ppm Cl⁻. EtOH conversion decreased from 65 % to 59 % for 1.5 mL versus an initial volume of 2 and 2.5 mL (Figure 3.3). The product distribution was largely unchanged for reactions with 140 ppm Cl⁻.

Table 3.1. Key products from reaction with $Cu_{20}PMO$ for 6 h at 320 °C data in Appendix B Table S3.1 reported as percent yield. Catalyst loading was approximately 8, 6, and 5 wt. % (100 mg) for 1.5,2, and 2.5 mL EtOH respectively. 'Cl$^-$ Added' corresponds to EtOH with $MgCl_2 \cdot 6H_2O$ added (~140 ppm Cl$^-$).

Compound	Initial V_{EtOH} (mL)					
	1.5 (Cl)	2 (Cl)	2.5 (Cl)	1.5	2	2.5
EtOH Conv.	65	59	59	59	57	43
n-BuOH	29	28	28	12	12	10
EtOAc	5	5	5	14	15	16
Bu(=O)OEt	3	3	2	4	4	3
BuOAc	3	3	2	3	3	2
HexOH	7	6	7	1	0	0
2-EtBuOH	2	2	2	0	0	0
Others (~1 % each)[a]	7	6	7	5	5	4
Mass Balance	80	82	93	92	93	94

[a] Compounds included in 'Others' are listed in Appendix B Table S3.1. n-BuOH = n-butanol, EtOAc = ethyl acetate, Bu(=O)OEt = ethyl butanoate, BuOAc = butyl acetate, HexOH = 1-hexanol, 2-EtBuOH = 2-ethyl-1-butanol. Reproduced with permission from *ACS Sustainable Chem. Eng.* **2018**, 6, 15119−15126. Copyright 2018 American Chemical Society.
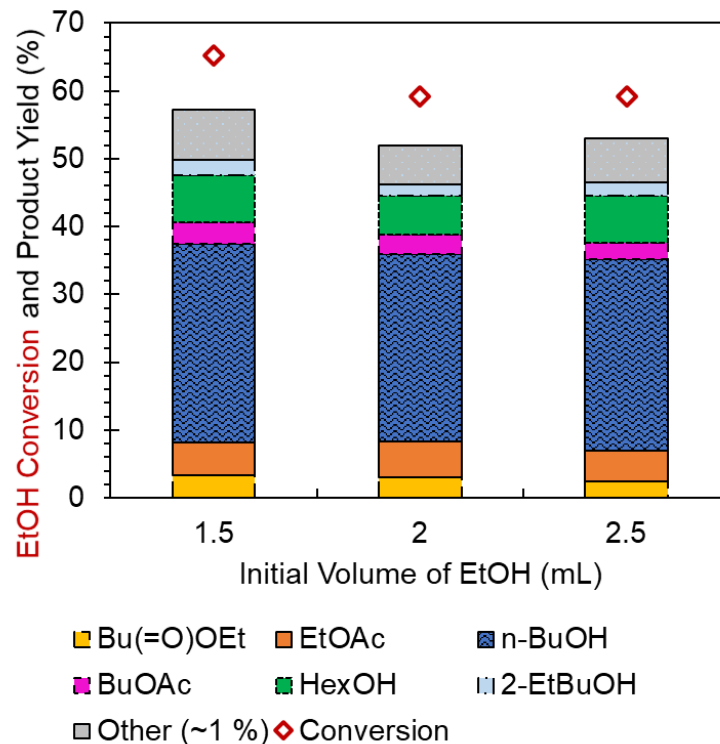
Figure 3.3. Product yield (bars) and ethanol conversion (red rhombi) as a function of initial volume (V_{EtOH}) of ethanol in the 10-mL mini-reactors. Conditions: 100 % EtOH, 100 mg $Cu_{20}PMO$ catalyst, 140 ppm Cl- (added as $MgCl_2 \cdot 6H_2O$). The compounds included in 'Others (~1 %)' can be found in Appendix B Table S3.1. Reaction T = 320 °C, Reaction time = 6 h. Reproduced with permission from *ACS Sustainable Chem. Eng.* **2018**, 6, 15119−15126. Copyright 2018 American Chemical Society.

Notably, similar increases in catalyst activity and n-BuOH selectivity were also observed when CCl_4 (150 ppm Cl⁻) was instead added as a chloride source (Figure 3.4). Given that copper has been shown to catalyze the hydrodechlorination of chlorocarbons under reducing conditions[40] it was my hypothesis that the same reaction would occur under these reaction conditions to produce chloride ions. Since the effect of adding this chlorocarbon on the catalytic reactivity and selectivity indeed was essentially the same as that of adding an inorganic chloride salt, this hypothesis appears to be validated. Reaction of EtOH to which $Mg(NO_3)_2$ had been added (~50 ppm Mg^{2+}) with $Cu_{20}PMO$ for 6 h at 320 °C gave a product distribution nearly identical to that seen in the absence of any additive

133

(Figure 3.4). Thus, we can conclude that it is chloride, not magnesium, that is causing the increased activity and changes in selectivity toward ethanol oligomerization.
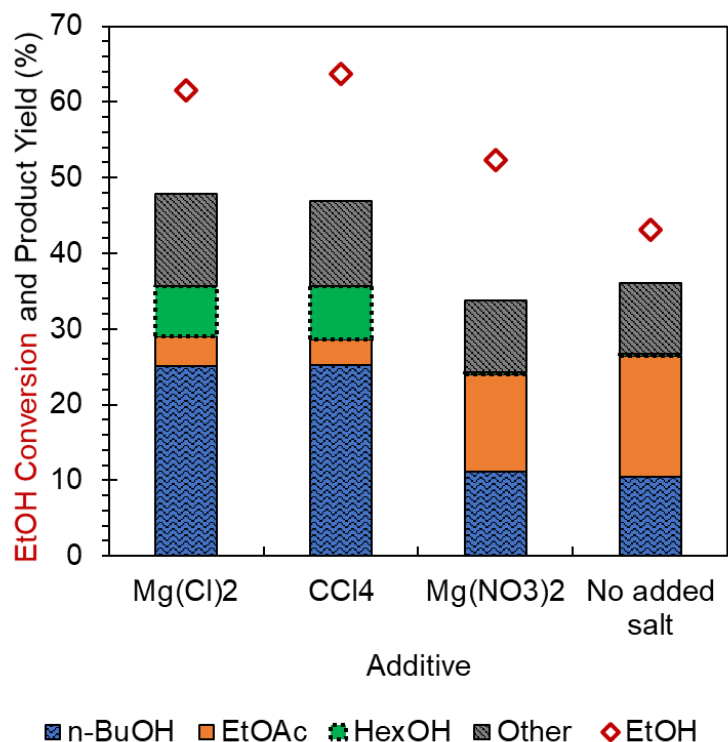
Figure 3.4. Comparison of product yields (bars) and ethanol conversion (red rhombus) with $Cu_{20}PMO$ and different additives. Reaction conditions: 2.5 mL, 100 mg $Cu_{20}PMO$, T= 320 °C, 6 h reaction time. $MgCl_2$= 140 ppm Cl^- and 48 ppm Mg^{2+} added as $MgCl_2 \cdot 6H_2O$, CCl_4 = 150 ppm Cl^-, $Mg(NO_3)_2$ = 50 ppm Mg^{2+}. Reproduced with permission from *ACS Sustainable Chem. Eng*. **2018**, 6, 15119−15126. Copyright 2018 American Chemical Society.

Ethanol from a biorefinery fermentation process can easily be distilled to give 95 % EtOH, or hydrous ethanol. An azeotropic distillation (typically using benzene) with molecular sieves to absorb water is required to obtain 100 % EtOH, or anhydrous ethanol. In this context, it is economically beneficial to use hydrous (95 %) ethanol for a biorefinery process. However, when 95% EtOH (190 proof) was the substrate, conversion under the standard conditions (100 mg $Cu_{20}PMO$, 6 h reaction at 320 °C) dropped to ~32% with

EtOAc remaining the principal product (Figure 3.5). The addition of Cl⁻ (140 ppm in the form of $MgCl_2 \cdot 6H_2O$) increased conversion to ~39%; the n-BuOH yield (10%) unfortunately remained low. Previous work with Guerbet condensation implied that the addition of molecular sieves to the reactor may improve selectivity. In our case, the addition of dried 3 Å molecular sieves (20 wt%) to the batch reactor did not improve EtOH conversion or n-BuOH selectivity (Figure 3.5). The reason for the decreased conversion in 95 % ethanol compared to 100 % ethanol is unknown. One molecule of water is produced in the reaction for every molecule of n-Butanol produced so it seemed that water does not decrease conversion in reactions in 100 % EtOH.
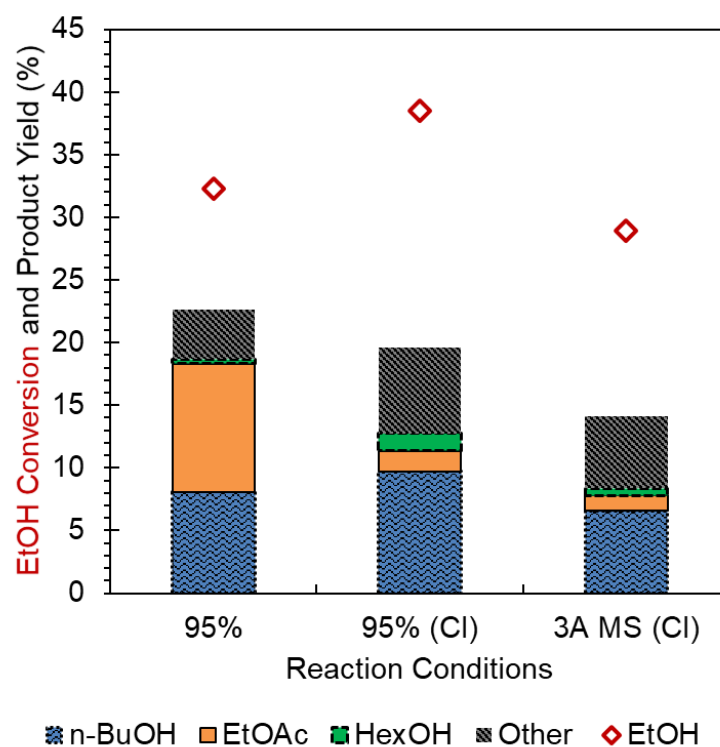
Figure 3.5. Ethanol conversion (red diamonds) and product yields (bars) for reactions of 95% EtOH (2.5 mL) with Cu₂₀PMO (100 mg) for 6 h at 320 °C. Left column: substrate only. Middle: 95% EtOH containing 140 ppm Cl⁻ added as $MgCl_2 \cdot 6H_2O$. Right: same conditions as middle but with 330 mg 3Å MS (20 wt % 3 Å molecular sieves) added to reactor. Reproduced with permission from *ACS Sustainable Chem. Eng.* **2018**, 6, 15119−15126. Copyright 2018 American Chemical Society.

Figure 3.6 illustrates the effects of varying the Cl⁻ concentration in the EtOH substrate solution over the range from 0 to 630 ppm Cl⁻. The reactors contained $Cu_{20}PMO$ catalyst (100 mg) and EtOH containing chloride from $MgCl_2 \cdot 6H_2O$. At the lower chloride concentrations (72-297 ppm), ethanol conversion was ~60% with the selectivity toward n-butanol (~55%) and hexanol (~15%) highest for the runs at 140 and 297 ppm Cl⁻. At higher chloride concentrations (464 and 630 ppm Cl⁻), the conversion decreased although the net selectivity toward n-BuOH remained similar (~51%).
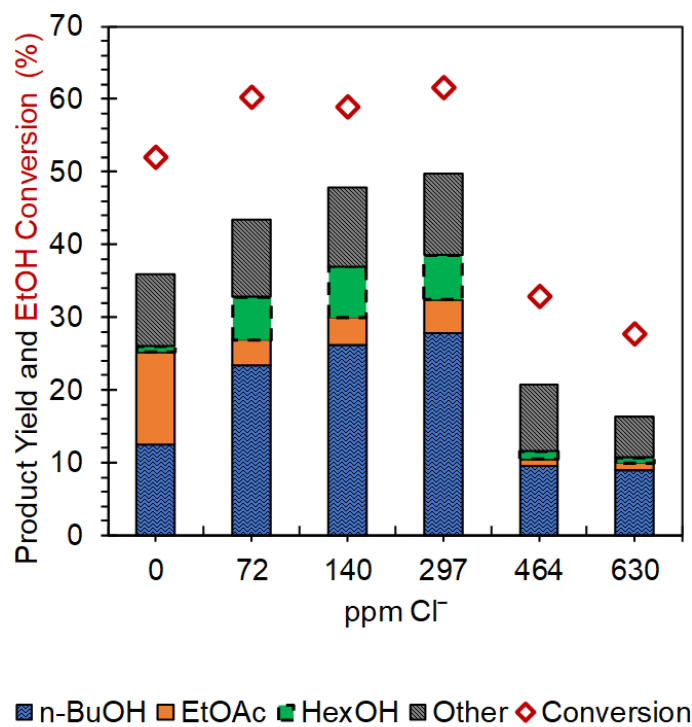
Figure 3.6. Product yield (%), ethanol conversion (%), and product distribution as a function of added chloride (ppm Cl⁻) in the reaction with $Cu_{20}PMO$ for 6 hours at 320 °C. $MgCl_2 \cdot 6H_2O$ was the chloride source. The yields of butanol, ethyl acetate, and hexanol are depicted as blue, orange, and green, respectively. 'Other', depicted as gray, corresponds primarily to butyl acetate and ethyl butanoate. Red diamonds represent EtOH conversion. These data are the averages of two independent experiments (Appendix Table S3.3). Reproduced with permission from *ACS Sustainable Chem. Eng.* **2018**, 6, 15119−15126. Copyright 2018 American Chemical Society.

The stability of the catalyst modified by a single exposure to chloride was evaluated in the following manner. The first catalytic run was conducted with $Cu_{20}PMO$ for 6 h at 320 °C with 100% EtOH containing 140 ppm chloride as the substrate. The subsequent 17 runs used the same catalyst recovered in each case by removing the reaction solution for analysis, drying the catalyst in the reactor in vacuo, and reintroducing fresh EtOH as substrate without any added chloride salt. Substrate conversion, ethanol conversion, and n-BuOH selectivity remained high and relatively consistent (Figure 3.7 and Appendix B Table S3.4.1-3.4.3), although with some unexplained variations. Each point on Figure 3.7 represents the average of 2 experiments. For all reactions, the EtOH conversion was between 41-59 % and the n-BuOH yield was between 18-26 %. Furthermore, the HexOH yield was between 3-6 %, EtOAc yield was between 1-3 %, and the yield of other products was between 5-8 %. The composition of the other products was primarily butyl acetate, ethyl butanoate, 2-ethyl-1-butanol, diethyl ether, and 1-octanol. Thus, catalyst modification by chloride during the initial run appeared permanent and was not washed away in subsequent reactions with ethanol containing no added chloride.
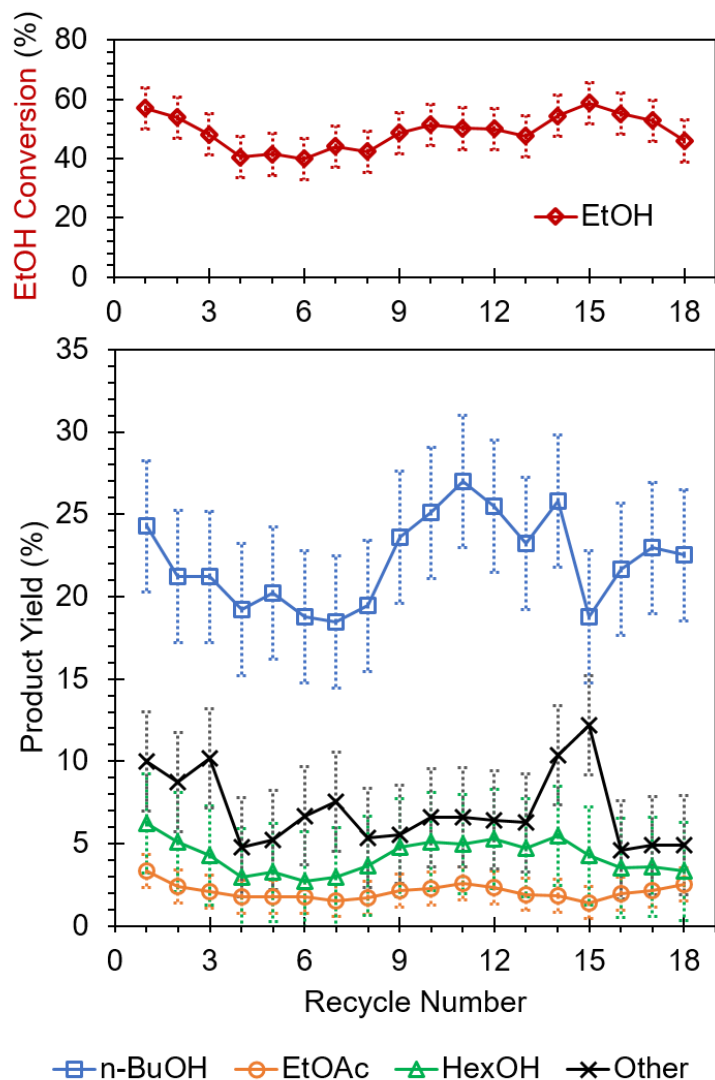
Figure 3.7. Product yield and ethanol conversion (%) as a function of reaction cycle number. For the first run, the substrate was 100% EtOH (2.5 mL) containing 140 ppm Cl⁻. For subsequent recycles, it was 100% EtOH with no added chloride. Markers represent mean values of duplicate experiments run in parallel; Y-axis error bars represent one standard deviation from the mean. Other products included butyl acetate, ethyl butanoate, 1-octanol. Reproduced with permission from *ACS Sustainable Chem. Eng.* **2018**, 6, 15119−15126. Copyright 2018 American Chemical Society.

In contrast, when a sequence of seven batch reactor runs was carried out with fresh 100 % EtOH containing 140 ppm Cl⁻ in each run, the activity of the Cu_{20}PMO catalyst decreased over the first four successive runs until it was about 1/3 of that seen for the first

one (Figure 3.8 & Appendix B Table S3.5). The n-BuOH yield was only 3 times higher than EtOAc yield after the fourth consecutive reaction. The activity and selectivity for sequential runs with chloride-free EtOH and recovered $Cu_{20}PMO$ (Figure 3.9) remained consistent with the results shown in Figure 3.2 (40-50% EtOH conversion, product yields: ~15% ethyl acetate and ~10% butanol (Appendix B Table S3.6).
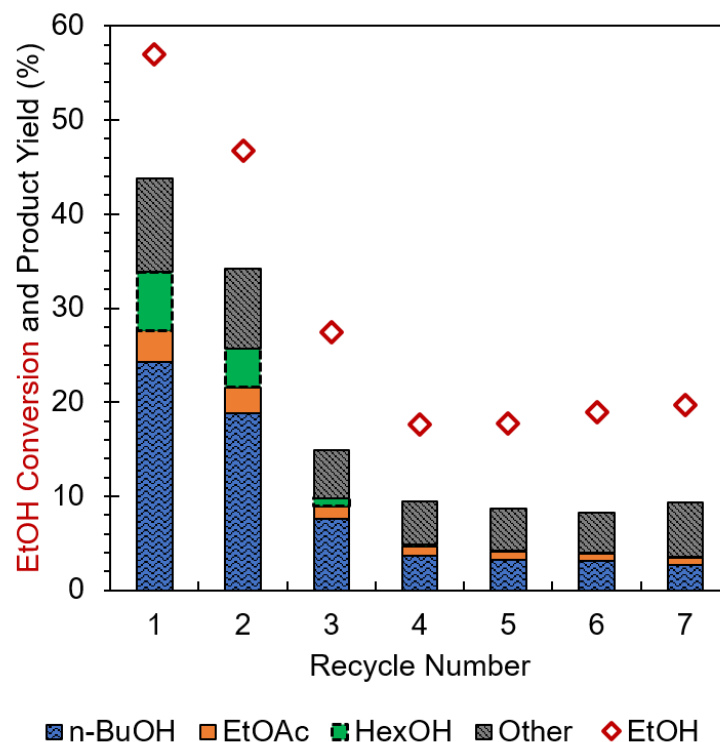
Figure 3.8. Product yield (bars) and ethanol conversion (red rhombi) of consecutive Guerbet reactions with 100 % EtOH containing 140 ppm Cl^- (added as $MgCl_2 \cdot 6H_2O$) and reused $Cu_{20}PMO$ catalyst. Reaction conditions: 2.5 mL anhydrous EtOH, 100 mg $Cu_{20}PMO$, T = 320 °C, 6 h reaction time for each run. Reproduced with permission from *ACS Sustainable Chem. Eng*. **2018**, 6, 15119−15126. Copyright 2018 American Chemical Society.
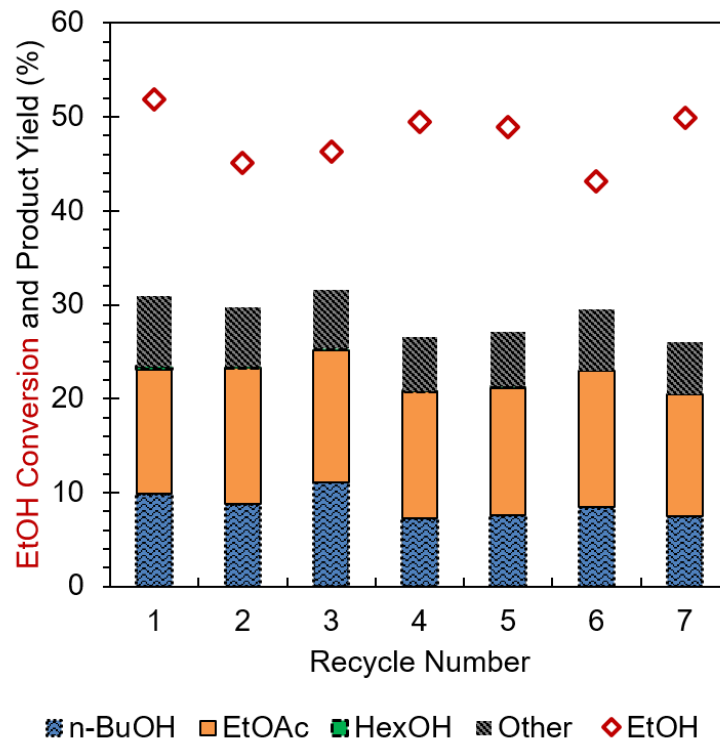
Figure 3.9. Product yield (bars) and ethanol conversion (red diamonds) of consecutive Guerbet reactions with 100 % EtOH and reused $Cu_{20}PMO$ catalyst. Reaction conditions: 2.5 mL anhydrous EtOH, 100 mg $Cu_{20}PMO$, T = 320 °C, 6 h reaction time for each run. Reproduced with permission from *ACS Sustainable Chem. Eng.* **2018**, 6, 15119−15126. Copyright 2018 American Chemical Society.

Higher catalyst loading gave, as expected, higher net conversion for a fixed 6 h reaction time (Figure 3.10). However, there were only modest effects on the selectivity. The highest n-BuOH selectivity (59%) was seen with 50 mg of $Cu_{20}PMO$, but nearly the same selectivity (55 %) was seen with catalyst loadings of 75 and 100 mg. Since n-BuOH also undergoes condensation reactions, as conversion for EtOH increased, conversion for its product n-BuOH increased. This results in higher yields for products like butyl acetate and ethyl butanoate and lower yields of n-BuOH. Thus, increased catalyst loading results in lower selectivity for n-BuOH due to higher selectivity for $C_{6}+$ products. In these experiments, the Cu:Cl ratio increases as less catalyst is used. Therefore, the reaction with

50 mg of $Cu_{20}PMO$ is comparable to reaction with 100 mg of $Cu_{20}PMO$ with 280 ppm Cl^-.

The '297 ppm Cl^- result in Figure 3.6 has higher ethanol conversion and product yields than

the '50 mg catalyst' result in Figure 3.10. This indicates that the decrease in activity

observed upon decreasing catalyst weight is not due to higher chloride concentration relative

to $Cu_{20}PMO$ mass.
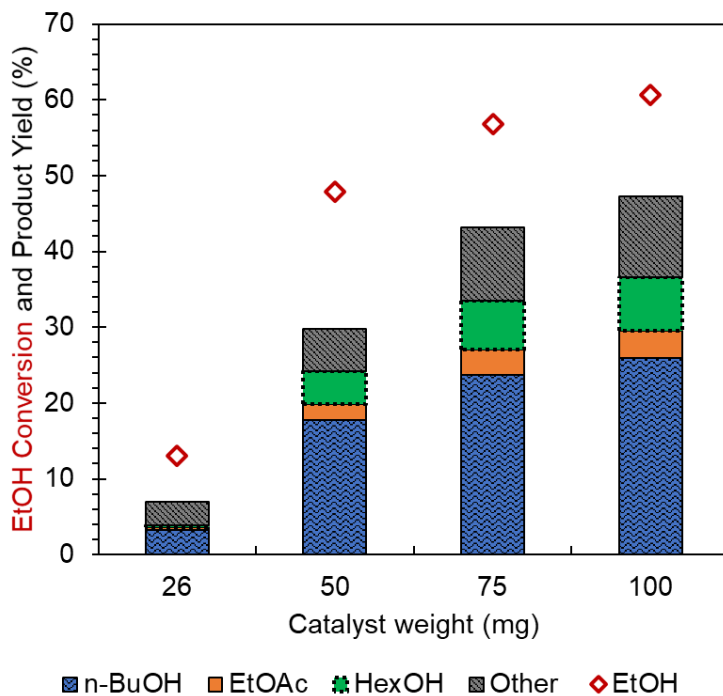
Figure 3.10. Product yield and ethanol conversion (%) as a function of catalyst loading. Reaction of 2.5 mL of ethanol (140 ppm Cl^-) with $Cu_{20}PMO$ for 6 h at 320 °C. Other products are mainly butyl acetate and ethyl butanoate. Reproduced with permission from *ACS Sustainable Chem. Eng.* **2018**, 6, 15119−15126. Copyright 2018 American Chemical Society.

Multiple reactors were loaded with 2 mL of ethanol containing 140 ppm Cl^-, placed

into the furnace (300 or 320 °C) and removed after reaction times between 1-8 hours to

examine the product yield/substrate conversion over time. Figure 3.11 (Appendix B Table

S3.7) shows a time course with 50 mg $Cu_{20}PMO$ and 2 mL of ethanol (140 ppm Cl^-) at 320

°C. The highest selectivity toward n-BuOH occurred at low conversion. A 29 % yield of

butanol was obtained after 6 h at 320 °C and 26 % at 300 °C. Figure 3.12 (Appendix B Table S3.8) shows a time course with 100 mg $Cu_{20}PMO$ and 2 mL of ethanol (140 ppm Cl^-) at 300 °C. The selectivity toward n-BuOH for 300 °C and 320 °C were within experimental uncertainty of one another. The 8 h run at 300 °C (Figure 3.12) had only 2% greater EtOH conversion than the 6 h run but did not lead to a higher net n-BuOH yield owing to secondary reactions of n-BuOH to form C_6+ products (Appendix B Table S3.8), the majority of which are 1-hexanol, ethyl butanoate, butyl acetate, and 2-ethyl-1-butanol.
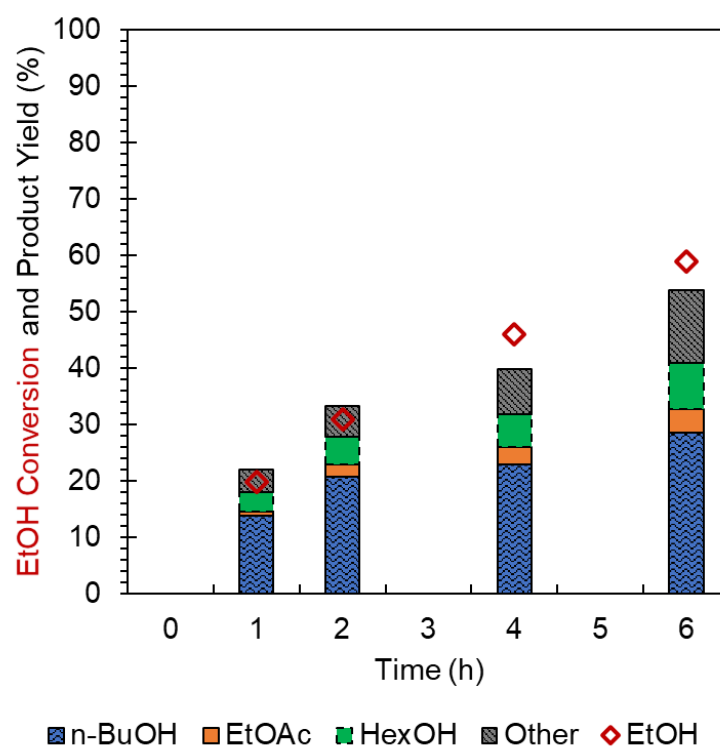
Figure 3.11. Ethanol conversion (red diamonds) and Product yields (bars) versus reaction time (h) from the reaction of 2 mL of 100% EtOH with 140 ppm Cl^- (added as $MgCl_2 \cdot 6H_2O$) and 50 mg of $Cu_{20}PMO$ at 320 °C. Other products include ethyl butanoate, butyl acetate, 2-ethyl-1-butanol, and 1-octanol and other C_6+ compounds like those shown in Appendix B Table S3.1. Reproduced with permission from *ACS Sustainable Chem. Eng.* **2018**, 6, 15119−15126. Copyright 2018 American Chemical Society.

The comparison between the 6 and 8 h reactions at 300 °C indicates that the theoretical maximum n-BuOH yield under these batch reactor conditions is ~30 %. Therefore, the only

way to improve the selectivity for n-BuOH over chloride treated $Cu_{20}PMO$ is to remove it as it is generated. In our laboratory, this was not possible, however a future biorefinery process could potentially be done using a flow reactor system.
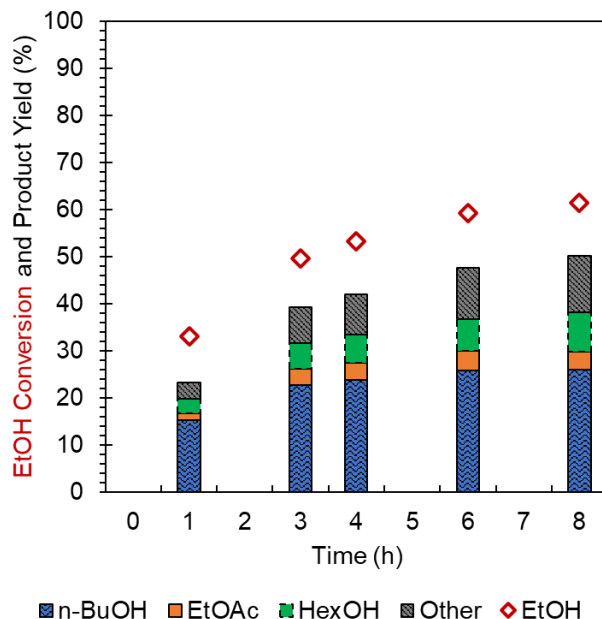
Figure 3.12. Ethanol conversion (red diamonds) and Product yields (bars) versus reaction time (h) from the reaction of 2 mL of 100% EtOH with 140 ppm Cl^- (added as $MgCl_2\cdot6H_2O$) and 100 mg of $Cu_{20}PMO$ at 300 °C. Other products include ethyl butanoate, butyl acetate, 2-ethyl-1-butanol, and 1-octanol and other C6+ compounds like those shown in Appendix B Table S3.1.

3.3.2. Changes in Catalyst Characteristics

In order to gain insight into chloride-induced structural changes, we examined the X-ray diffraction (XRD) patterns of the post-reaction catalysts from the experiment shown in Figure 3.6 (Figure 3.13). Reference patterns can be found in Figures 3.14 & 3.15. As seen previously,[30-36] calcination transforms $Cu_{20}HTC$ to an amorphous $Cu_{20}PMO$. The XRD pattern for freshly calcined $Cu_{20}PMO$ (trace A, Figure 3.13) shows only broad Bragg reflections at 36°, 43°, and 63° 2Θ consistent with some MgO domains. After reaction with ethanol for 6 h at 320 °C (trace B), new reflections at 11°, 22°, 35°, 39°, 60°, and 61° are

143

seen that suggest restoration of a hydrotalcite-like structure, possibly due to H_2O formation as a byproduct of the ethanol condensation (Scheme 3.1). An alternative assignment for the reflections at 35° and 39° would be to CuO domains, while reflections at 36°, 42°, 51°, 62° and 73° correspond to Cu_2O; however, these overlap with the broad reflections for MgO domains noted above.
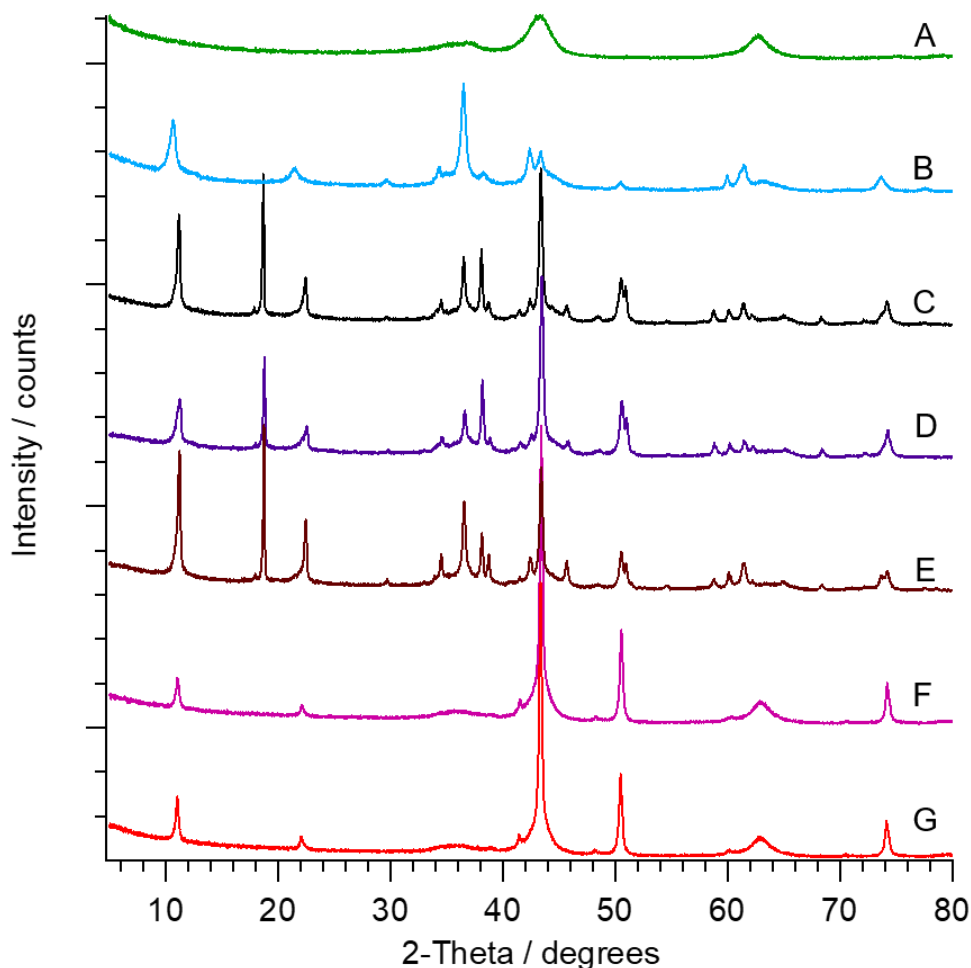
Figure 3.13. XRD of $Cu_{20}PMO$ catalysts after calcination at 600° (A, green) and after reaction with EtOH at 320 °C for 6 h (in descending order) under the following conditions: (B) no chloride, (C) 72 ppm Cl⁻, (D) 140 ppm Cl⁻, (E) 297 ppm Cl⁻, (F) 464 ppm Cl⁻ and (G) 630 ppm Cl⁻. All data analysis was done using Malvern Panalytical HighScore Software with two structural databases; Inorganic Crystal Structure Database and Powder Diffraction Files.

XRD analysis of the solid catalyst after a catalytic run carried out with 72 ppm Cl^- in EtOH (trace C) suggested the presence of a $Mg(OH)_2$ (brucite) phase according to reflections at 19° and 38°. However, there is considerable overlap between reflections characteristic of Mg/Al layered double hydroxides and of $Mg(OH)_2$. It is likely that gibbsite, $Al(OH)_3$ and/or $Al(O)OH$, are also formed in the presence of brucite, $Mg(OH)_2$. However, not all the Bragg reflections for Al-containing phases were observed. The reflections at 35° and 39° are assigned to CuO as are the reflections at 51°, 59°, and 69° characteristic of this solid. The large reflection at 44°, overlapping reflection at 51°, and reflection at 74° correspond to metallic Cu(0). This is consistent with the XRD analyses from Chapter 2 where $Cu_{20}PMO$ treated with organosolv poplar lignin or chloride exhibited Bragg reflections for Cu(0). The formation of copper nanoparticles has been previously observed for $Cu_{20}PMO$ in the reaction of bio-oil sugar fractions in supercritical alcohols using transmission electron microscopy (TEM).[41] Additionally, Sun et al observed spherical metal nanoparticles by TEM for Cu_xNi_yPMO after the Guerbet reaction of ethanol.[36]

The XRD pattern for the recovered catalyst after runs with ethanol containing 140 ppm Cl^- (trace D) or 297 ppm Cl^- (trace E) were nearly identical. However, the recovered catalyst after runs at higher chloride concentrations (464 or 630 ppm Cl) displayed much larger reflections at 44°, 51°, and 74° corresponding to more Cu metal domains (traces F & G) as compared to lower chloride concentrations. The broad reflections for MgO are also still observed as well as ones at 11° and 22°. Clearly, increased chloride concentration resulted in increased Cu sintering.
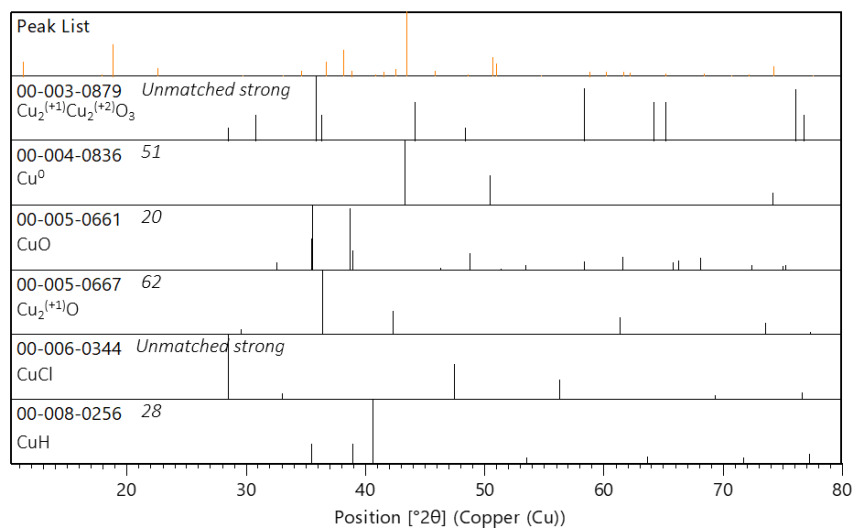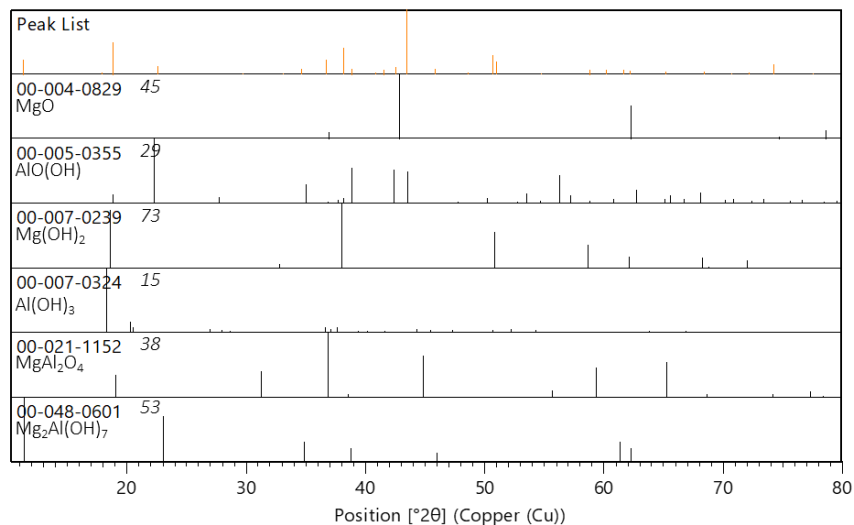
Figure 3.14. XRD patterns from Inorganic Crystal Structure Database and Powder Diffraction Files. The peak list is from $Cu_{20}PMO$ reacted with EtOH containing 140 ppm Cl⁻ for 6 h shown in Figure 3.13. The reference patterns pertaining to potential Cu-containing solids are shown. Each reference is labeled by its identifier number (XX-XXX-XXXX), the chemical composition, and match score (italicized). 'Unmatched strong' means the highest intensity lines of reference do not match highest intensity lines of sample. The highest score for a phase is 100.

146

Figure 3.15. XRD reference patterns from Inorganic Crystal Structure Database and Powder Diffraction Files. The peak list is $Cu_{20}PMO$ reacted with EtOH containing 140 ppm Cl^- for 6 h shown in Figure 3.13. Each reference is labeled by its identifier number and the chemical composition. The reference patterns pertain to potential Mg and Al-containing solids. Each reference is labeled by its identifier number (XX-XXX-XXXX), the chemical composition, and match score (italicized).

The metallic Cu crystallite domain sizes can be roughly estimated from the full width at half maximum (FWHM) of the Bragg reflection at 44° 2Θ using the Scherer equation, Particle Size = 0.9λ / ($L \cos \Theta$).[42] In this equation 0.9 is the shape factor, λ is the X-ray instrument wavelength (Cu Kα =1.5405 Å), L is the FWHM of the peak, and Θ is the Bragg angle. This calculation was done in the X'PERT HighScore Software Package. Typically all reflections corresponding to a crystallite should be used for such estimates; however, overlaps of some reflections made this impractical. Accordingly, the Cu domain size was estimated from the traces shown in Figure 3.13 to be 25 nm for the catalyst after runs at 140 and 297 ppm Cl^- and 24 nm after the run at 72 ppm Cl^-. A larger Cu crystallite size (29 nm)

was found after runs at higher chloride concentration (464 or 630 ppm). In contrast the XRD pattern for the $Cu_{20}PMO$ recovered after reaction with EtOH containing no chloride gave only a very small reflection at 44° too weak to extract a meaningful crystallite size approximation (Figure 3.13). Notably, the XRD pattern (Figure 3.16) of the recovered catalyst after a single run with added chloride followed by 17 successive runs with ethanol alone, as detailed above, appears remarkably similar to that observed in Figure 3.13 after only a single run with the 140 ppm Cl^-. However, according to the full-width half maximum (FWHM) at 44° 2Θ, the estimated Cu domain size increased to 27 nm, which is 3 nm larger than $Cu_{20}PMO$ after a single run. Another major difference is the disappearance of the Bragg reflections at 11°, 22°, and 35° which were attributed to a hydrotalcite-like structure. Perhaps repeated exposure to supercritical EtOH destroys this reformed long-range order.
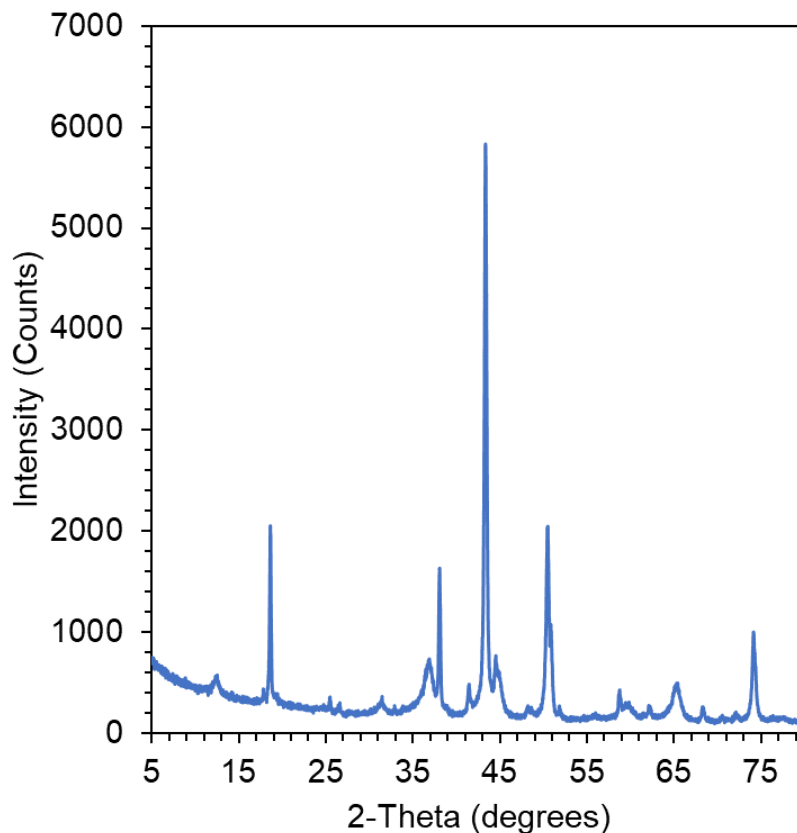
Figure 3.16. XRD pattern of $Cu_{20}PMO$ catalyst recovered after 18 runs with 100% EtOH, the first containing 140 ppm Cl^- (added as $MgCl_2 \cdot 6H_2O$) but with no added Cl^- for runs 2-18. Conditions: 2.5 mL anhydrous EtOH, 100 mg $Cu_{20}PMO$, T = 320 °C, 6 h reaction for each run.

Water may contribute to Cu metal sintering. After reaction with 95% EtOH containing 140 ppm Cl^-, the Cu domain size calculated from the XRD was 33 nm (Figure 3.17). The XRD patterns for $Cu_{20}PMO$ recovered after 7 consecutive reactions with 100 % ethanol show that layered double hydroxide structure indicated by 11°, 22°, 60°, 61° largely disappeared (Figure 3.18). The same observation was made for $Cu_{20}PMO$ after 18 consecutive 6 h reactions shown in Figure 3.16. In both cases the reflections at 19° and 38° assigned as $Mg(OH)_2$ are present. In an earlier study with bioethanol, Marcu et. al showed that the addition of water to CuPMOs decreases catalytic activity.[31] The rationale for this

149

observation was that Lewis base O^{2-} sites are transformed into ^-OH sites in the presence of water. This may be the reason 95 % EtOH did not give high conversion like 100 % EtOH.
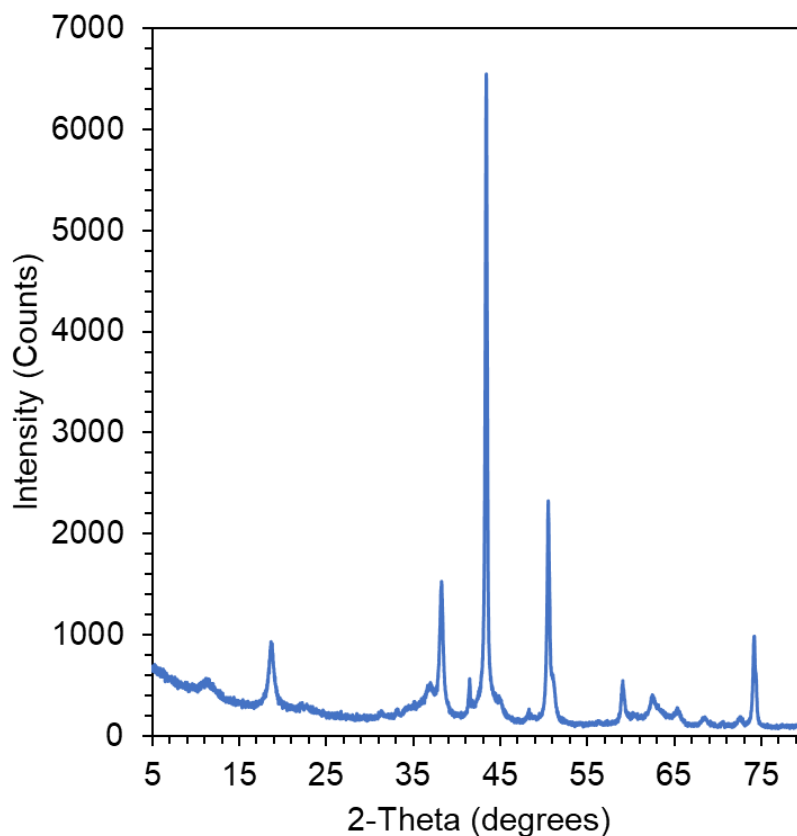
Figure 3.17. XRD pattern of $Cu_{20}PMO$ after a single run with 95% EtOH containing chloride (140 ppm added as $MgCl_2 \cdot 6H_2O$). Reaction conditions: 2.5 mL, 100 mg $Cu_{20}PMO$, T = 320 °C, 6 h reaction time.
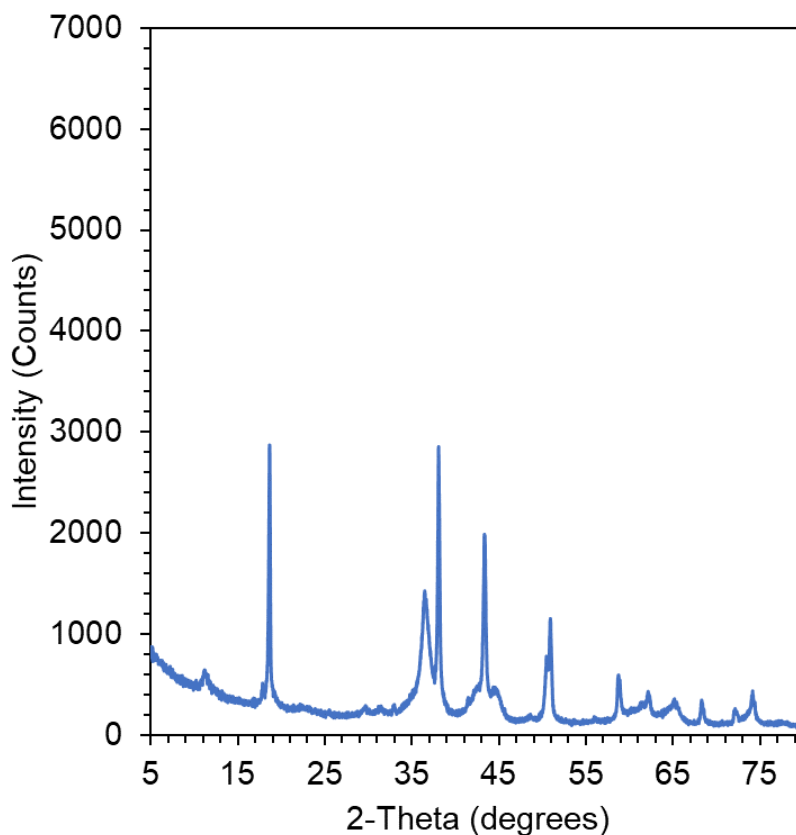
Figure 3.18. XRD pattern of $Cu_{20}PMO$ recovered after 7 consecutive reactions with 100% EtOH containing 140 ppm Cl^- added as $MgCl_2 \cdot 6H_2O$. Reaction conditions: 2.5 mL anhydrous EtOH, 100 mg $Cu_{20}PMO$, T = 320 °C, 6 h reaction time for each run.

In summary, ppm quantities of Cl^- result in the formation of mixed phase catalysts that are more ordered when compared to calcined catalyst. The Bragg reflections indicate that Cu(0), CuO, and Cu_2O may all be present after reaction with EtOH containing 72-297 ppm Cl^- Furthermore, Bragg reflections which can be assigned as a hydrotalcite-like phase are present. It is unlikely that the $Cu_{20}PMO$ is reforming $Cu_{20}HTC$ however layering of brucite and gibbsite may lead to similar reflections. Formation of H_2O as indicated in Scheme 3.1 may contribute to rehydration of the PMO to this hydrotalcite-like phase.[43]

BET measurements for various catalyst samples are summarized in Table 3.2. Notably, the BET surface area for catalyst calcined at 600°C shown in Chapter 2 Table 2.6

was 166 m^2/g with a smaller pore volume (0.6 cm^3/g) and larger pore size (12.7 nm). These N_2 adsorption results highlight the differences between different catalyst batches. The surface area of freshly calcined $Cu_{20}PMO$ (137 m^2 g^{-1}) did not change significantly after a single 6 h run at 320 °C with EtOH alone but decreased by almost 50 % after 7 successive runs (77 m^2 g^{-1}). After reaction with EtOH containing 72 ppm Cl^- there was a 30 % decrease in the surface area to 101 m^2 g^{-1}. In every case $Cu_{20}PMO$ that had reacted with EtOH containing chloride exhibited decreased surface areas even after single runs (97 m^2 g^{-1} with 140 ppm chloride). The is consistent with the XRD observations of Cu nanoparticle formation. As nanoparticle size increases the overall catalyst surface area decreases.

Table 3.2. N_2 adsorption analysis of $Cu_{20}PMO$ catalysts before and after reaction with EtOH. [a]reaction with 2.5 mL of 100 % EtOH at 320 °C for 6 h. [b] after 7 consecutive runs with 2.5 mL of 100 % EtOH at 320 °C for 6 h with no chloride added.

Sample Conditions	BET surface area (m^2/g)	pore volume (cm^3/g)	pore size (nm)
Calcined 600°C	135	0.70	10.5
No chloride[a]	137	0.45	6.1
72 ppm Cl^- [a]	101	0.41	7.4
140 ppm Cl^- [a]	97	0.47	8.2
267 ppm Cl^- [a]	67	0.36	9.6
464 ppm Cl^- [a]	69	0.55	13.9
630 ppm Cl^- [a]	84	0.62	12.7
No chloride[a,b]	77	0.43	9.9

The ATR-infrared spectrum (4,000-1,000 cm^{-1}) was recorded for each $Cu_{20}PMO$ sample for which XRD patterns are shown in Figure 3.13. The spectrum of freshly calcined catalyst displays only broad, weak bands at ~3,400 cm^{-1} and ~1500 cm^{-1} that may represent

surface water and carbonate, respectively (Figure 3.19). The IR spectra recorded after 6 h reactions with ethanol at 320 °C containing different chloride concentrations show distinct changes. In each case, the IR spectrum shows an enhanced broad band at ~3600 cm^{-1} corresponding to surface water and weaker but sharper bands at 2950, 2900 and 2850 cm^{-1} consistent with C-H stretches, indicating that organic molecules remain on the catalyst surface even after subjection to a vacuum for several days. Two stronger bands at ~1575 and ~1411 cm^{-1} are also apparent. These do not represent interstitial water since the H-O-H bending vibrations typically are seen at ~1640 cm^{-1} for hydrotalcites[44] and ~1630 cm^{-1} for brucite.[45] Carbonate shows bands at 1365/1400 cm^{-1} in hydrotalcites,[46] at 1515 cm^{-1} for brucite,[47] and at 1520 and 1430 cm^{-1} for aluminum hydroxy carbonate.[48] A better fit is acetate, which displays bands at 1554 and 1428 cm^{-1} on a ZnO surface.[49] If acetate remains on the surface of the catalyst this may be a source of the mass balance loss. Since we did not observe decreases in catalytic activity we did not treat the catalyst in any way between recycles.
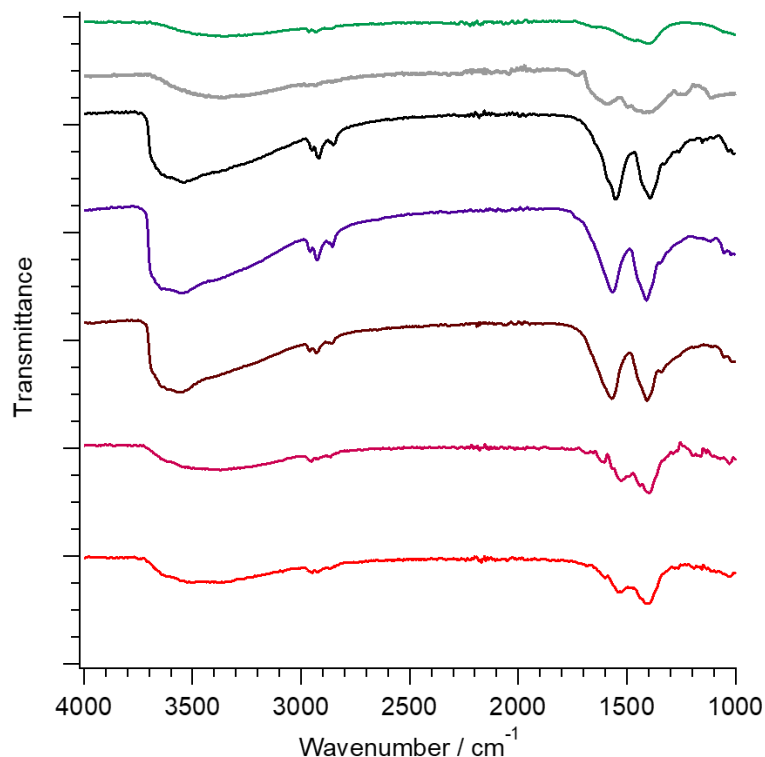
Figure 3.19. ATR-IR spectrum of $Cu_{20}PMO$ catalysts after calcination at 600°C (top, green) and in descending order; after reaction with 100 % EtOH containing respectively 0 ppm Cl⁻ ,72 ppm Cl⁻, 140 ppm Cl⁻, 297 ppm Cl⁻, 464 ppm Cl⁻, and 630 ppm Cl⁻. Conditions: 2.5 mL of EtOH, 100 mg of $Cu_{20}PMO$, T = 320 °C, 6 h reaction time for each run.

PMO basicity is a characteristic that has been correlated with ethanol condensation selectivity and activity.[30] The first step toward EtOAc or n-BuOH is ethanol dehydrogenation to acetaldehyde. The formation of n-BuOH depends on deprotonation of acetaldehyde to form an enolate that condenses with another acetaldehyde molecule to form the C_4 chain (Scheme 3.1). EtOAc formation depends on the reaction of acetaldehyde with ethoxide to form the hemiacetal that undergoes dehydrogenation (Scheme 3.2). Since, acetaldehyde is several orders of magnitude more acidic than is ethanol,[50] we postulated that chloride modification of the $Cu_{20}PMO$ may reduce the surface basicity of the catalyst. To test this possibility, catalyst basicities were evaluated using the Hammett indicator method.[51] The Hammett function (H₋) describes the ability of a solid to ionize weak acid indicators.

154

The H$_-$ of the solid is considered to lie between the pKa of an indicator it can ionize and the indicator it cannot.

Table 3.3. Hammett basicity values (H$_-$) of calcined Cu$_{20}$PMO catalysts before and after reaction with EtOH at 320 °C for 6 h.

Sample conditions	Base strength	Total basicity (mmol/g)
calcined 600°C	10.1 < H$_-$ < 15	1.07 ± 0.10
no chloride	10.1 < H$_-$ < 15	1.34 ± 0.26
140 ppm Cl$^-$	9.3 < H$_-$ < 10.1	1.90 ± 0.20

Table 3.3 summarizes the H$_-$ values determined in this manner for a freshly calcined sample of Cu$_{20}$PMO and of samples recovered after 6 h reactions with EtOH at 320 °C. Of the latter, the catalyst recovered from the run with added chloride displays the lower H$_-$ value, consistent with the above hypothesis. Notably, the same material displayed a greater number of base sites as determined by titration with benzoic acid.

3.4. Conclusions

Improvement of processes that utilize renewable feedstocks to produce chemicals ordinarily derived from fossil carbon feedstocks is paramount to creating environmentally sustainable chemical and fuel industries. Catalytic conversion of biorefinery-derived ethanol via the Guerbet condensation has the potential to serve such a purpose. We have shown that the addition of relatively small quantities of chloride modifies the activity and selectivity of the products generated via the Guerbet reaction of ethanol with Cu-doped PMO catalysts at 320 °C. Thus, although halogens are known poisons for Cu catalysts,[52,53] added Cl$^-$ in this case increases overall reactivity toward ethanol condensation to n-butanol and its derivatives and suppresses formation of ethyl acetate, the predominant product under these conditions in the absence of such catalyst modification. Reaction in the presence of added chloride

155

mediates two key changes in these catalysts, the formation of copper nanoparticles on the surface and decreased surface basicity. The latter change may be key to the shift in product selectivity from EtOAc to n-BuOH and related condensation products. These results show that specific adsorbates like chloride can be useful in tuning the selectivity of mixed phase catalysts for reactions such as the Guerbet condensation of ethanol.

The enhancement in selectivity and conversion for ethanol condensation as catalyzed by mixed metal oxide catalysts realized in this study constitutes an important advance towards the production of n-butanol from renewable feedstocks. BuOH is both a valuable chemical precursor and a superior fuel additive, and its production from the biomass-derived precursor ethanol could enhance the economic viability and sustainability of bio-refineries.

3.5. Experimental Methods for Alcohol Condensation Reactions

3.5.1. Materials

Anhydrous (100 %, 200 proof) and hydrous ethanol (95%, 190 proof) were used as received from Fischer Scientific. Molecular sieves (type 3 Å 8−12 mesh beads) were purchased from Fischer Scientific and dried for 6 hours at 300°C. Magnesium chloride hexahydrate, carbon tetrachloride, magnesium nitrate hexahydrate were purchased from Sigma Aldrich and used as received.

3.5.2. Preparation of Porous Metal Oxide Catalysts

The PMO catalyst was prepared by calcination of the copper-doped hydrotalcite prepared by coprecipitation. In short, a solution of Cu^{2+}, Mg^{2+}, and Al^{3+} nitrates with the cationic stoichiometric ratio 0.6/2.4/1.0 were slowly added to aqueous Na_2CO_3 at 60 °C

while keeping pH between 8 and 10 using aqueous NaOH. The resulting light blue slurry was stirred for 3 days at 60 °C, cooled, and filtered. The resulting solid was resuspended in aqueous Na_2CO_3 for 1 day at room temperature, then washed copiously with deionized water, and dried in vacuo. Catalyst composition was verified by ICP-AES using a ThermoiCAP 6300 ICP equipped with a 6000 K Ar plasma and confirmed that 20% of the dications in the resulting 3/1 hydrotalcite were Cu^{2+}. These materials have been designated as $Cu_{20}HTCs$. Calcination of the $Cu_{20}HTC$ for 18 h at 600 °C gave the $Cu_{20}PMOs$ used as catalysts.

3.5.3. Reaction Procedures

Studies were conducted in closed 10 mL mini-reactors constructed from Swagelok junctions to which were added the substrate (typically 2.5 mL 100 % ethanol), the calcined catalyst (typically 100 mg), and an internal standard (20 µL decane). The sealed reactors were placed in a preheated calibrated oven (in most cases at 320 °C), for a specific time period, after which these were removed from the oven and rapidly cooled. The reactor was then opened (caution, these are generally under pressure), and the solution was removed for analysis. For recycle experiments, after the solution was removed, reactor with the catalyst was dried overnight for 18 h. For reactions with inorganic salt or chlorocarbon additives, a 100 mL EtOH stock solution was made.

3.5.4. Product Analysis

Compounds were identified using GC-MS, Hewlett Packard 5890, and quantified via GC-FID, Agilent 6890N (G1530N), using the Effective Carbon Number (ECN) methodology.[56,57] Liquids were analyzed using an Agilent 6890N (G1530N) gas chromatograph equipped with a flame ionization detector (FID) and 30 m × 0.25 mm

Agilent DB-5 Column (0.25 μm (5%-phenyl)-methylpolysiloxane lining). The inlet temperature was 200 °C with a split ratio of 80:1 and helium carrier gas at 27 mL/min flow rate. One μL of the filtered liquid mixture was injected. The column temperature was held at 70 °C for 2 minutes, then ramped to 250 °C at 12 °C/min where it was held for 2 minutes. The FID was set at 250 °C with a 30 mL/min H_2 flow rate and 350 mL/min air flow rate.

Response factors (rfs) for each compound were calculated (eq. 1) using the experimentally determined rf for n-decane, as well as the ECN of n-decane and the analyte (eq. 2).[54,55] The rf$_{analyte}$ and integrated peak area from the GC-FID chromatogram were used to calculate the concentration of the analyte (eq. 3). The n-decane is the internal standard (20 μL, 103 μmol) and does not react under these conditions. To account for in solvent/reactant volume change and material loss from human error, eq. 4 is used to correlate the theoretical amount of n-decane added (103 μmol) to the amount observed in a chromatogram.

(1)

$$ECN_{analyte} = \sum Aliphatic\ C + Aromatic\ C + (0.95 \times Olefinic\ C) + (0 \times Carbonyl\ C)$$
$$+ (-1 \times Ether\ O) + (-0.5 \times Primary\ Alcohol\ O) + (-0.75 \times Secondary\ Alcohol\ O)$$
$$+ (-1.25 \times Esters)$$

$$rf_{analyte} = rf_{decane} \frac{ECN_{analyte}}{ECN_{decane}}$$

(2)

$$[Analyte] = \frac{Peak\ Area_{analyte}}{rf_{analyte}}$$

(3)

$$\mu mol_{analyte} = [Analyte] \frac{Decane_{theoretical}}{Decane_{observed}}$$

(4)

158

Peaks in the FID chromatogram were identified using standards or GC-MS. For GC-MS, a Shimadzu GC-2010 QP2010, equipped with a 60×0.25 mm $\times 0.25$ µm Agilent DB-5 Column (0.25 µm (5%-phenyl)-methylpolysiloxane lining). The injector temperature was set at 250 °C. Samples were diluted in methanol. The temperature was held at 40 °C for 10 minutes and increased at 10 °C/min to 280 °C. The MS detector is kept at 285 °C with a solvent cutoff of 2.00 minutes to avoid oversaturation.

Yield for each product was calculated according to eq. 5, where SF is the stoichiometric factor (e.g. 2 moles of EtOH are required to form 1 mole of n-butanol), $mol_{product}$ is the amount of product detected, and $mol\ EtOH_{initial}$ is the amount of EtOH initially added to the reactor according to Sun et. al.[36]

$$Yield\ (\%) = \frac{SF\ x\ mol_{product}}{mol\ EtOH_{initial}} \times 100$$

(5)

Percent conversion was calculated according to eq. 6. where $mol\ EtOH_{converted}$ equals $mol\ EtOH_{initial} - mol\ EtOH_{unreacted}$ and $mol\ EtOH_{unreacted}$ is the EtOH found to remain after the reaction. Mass balance (MB) was calculated according to eq. 7.

$$Conversion\ (\%) = \frac{mol\ EtOH_{converted}}{mol\ EtOH_{\ initial}} \times 100$$

(6)

$$MB\ (\%) = \frac{\sum(SF\ x\ mol_{products}) + mol\ EtOH_{unreacted}}{mol\ EtOH_{initial}} \times 100$$

(7)

3.5.5. Catalyst Analysis

The ppb-ppm range standard solutions were prepared either by dissolving a known amount of metal nitrate hydrates in nanopure water (18 MΩ) with 5% HNO_3 or by dilution

of Fluka Analytical TraceCERT 1000 ppm standard metal solutions in 5% HNO_3. The catalyst samples were prepared by digesting a known mass in concentrated HNO_3 ($\geq$69%, Fluka Analytical TraceSELECT) for 24 h and diluting with nanopore water. Each value is the average of three duplicate measurements from the same sample. For $Cu_{20}HTC$, the observed ppm for Cu, Mg, Al were 37.8, 58.2, and 26.2 respectively leading to a Cu/Mg/Al mole ratio of 0.6:2.5:1 with the ideal ratio being 0.6:2.4:1.

PMO catalysts were characterized by powder XRD, BET surface area analysis, and ATR-IR. Powder XRD was performed on a Panalytical Empyrean Diffractometer, with Cu Kα radiation (λ= 1.5405980 Å) in a zero-background sample holder. Infrared spectra were collected on a Bruker ALPHA FTIR instrument with diamond ATR module. Surface area, pore volume, and pore size was measured using a MicroMeritics TriStar Porosimeter. Approximately 100 mg of catalyst sample was degassed under N_2 overnight at 200 °C after which the adsorption isotherm data was collected. Attenuated total reflectance infrared (ATR-IR) spectra were collected on a Bruker ALPHA FT- IR instrument equipped with a diamond ATR module.

The Hammett basicity values (H_-) for several solid catalysts were evaluated using the indicator method.[51] The indicators used were neutral red (pKa = 6.8), bromothymol blue (pKa = 7.2), phenolphthalein (pKa = 9.3), nile blue (pKa = 10.1), and 2,4-dinitroaniline (pKa = 15). The H_- of a solid lies between the pKa of an indicator it can ionize and one it cannot, as observed visually. The total surface basicities (mmol/g) of the same solids were determined by titrating a 25 mg sample suspended in 2 mL of methanol with neutral red indicator by a 0.01 M benzoic acid solution in methanol.

3.6. Acknowledgements

3.7. References

1. Gabriëls, D.; Hernández, W. Y.; Sels, B.; Van Der Voort, P.; Verberckmoes, A. Review of Catalytic Systems and Thermodynamics for the Guerbet Condensation Reaction and Challenges for Biomass Valorization. *Catal. Sci. Technol.* **2015**, *5*, 3876–3902

2. Angelici, C.; Weckhuysen, B. M.; Bruijnincx, P. C. A. Chemocatalytic Conversion of Ethanol into Butadiene and Other Bulk Chemicals. *ChemSusChem* **2013**, *6* (9), 1595–1614.

3. Falbe, J.; Bahrman, H.; Lipps, W.; Mayer, D.; Frey, G. D. Aliphatic Alcohols. In *Ullmann's Encycl. Ind. Chem.*; **2013**

4. Guerbet, M. - Action des alcools éthylique, isobutylique, isoamylique, sur leurs dérivés sodés. *C. R. Hebd. Séances Acad. Sci*, **1899**, 1002−1004

5. Galadima, A.; Muraza, O. Catalytic Upgrading of Bioethanol to Fuel Grade Biobutanol: A Review. *Ind. Eng. Chem. Res.* **2015**, *54* (29), 7181–7194

6. Kozlowski, J. T.; Davis, R. J. Heterogeneous Catalysts for the Guerbet Coupling of Alcohols. *ACS Catal.* **2013**, *3* (7), 1588–1600

7. Veibel, S.; Nielsen, J. I. On the Mechanism of the Guerbet Reaction. *Tetrahedron* **1967**, *23* (4), 1723–1733

8. Riemenschneider, W.; Bolt, H. M. Organic Esters. In *Ullmann's Encycl. Ind. Chem.*; **2012**

9. U.S. Environmental Protection Agency, Renewable Fuel Standard Program: Standards for 2018 and Biomass-Based Diesel Volume for 2019, *Fed Regist.* **2017**, 82 (237), 58486-58527

10. BP. *BP Statistical Review of World Energy 2017*; **2017**

11. U. S. Energy Information Administration, *April Monthly Energy Review*, **2019**

12. Agarwal, A. K. Biofuels (Alcohols and Biodiesel) Applications as Fuels for Internal Combustion Engines. *Prog. Energy Combust. Sci.* **2007**, *33* (3), 233–271

13. U.S. Environmental Protection Agency, Partial Grant of Clean Air Act Waiver Application Submitted by Growth Energy To Increase the Allowable Ethanol Content of Gasoline to 15 Percent, *Fed Regist.* **2011**, 76 (17), 4662–4683

14. Alleman, T. L.; McCormick, R. L.; Yanowitz, J. Properties of Ethanol Fuel Blends Made with Natural Gasoline. *Energy and Fuels* **2015**, *29* (8), 5095–5102.

15. Jin, C.; Yao, M.; Liu, H.; Lee, C. F. F.; Ji, J. Progress in the Production and Application of N-Butanol as a Biofuel. *Renew. Sustain. Energy Rev.* **2011**, *15* (8), 4080–4106

16. U.S. GAO, *RFS Program Unlikely to Meet Its Targets for Reducing Greenhouse Gas Emissions*, GAO-17-94 (Washington, D.C.: November 2016)

17. Elfasakhany, A. Investigations on Performance and Pollutant Emissions of Spark-Ignition Engines Fueled with N-Butanol–, Isobutanol–, Ethanol–, Methanol–, and Acetone–gasoline Blends: A Comparative Study. *Renew. Sustain. Energy Rev.* **2017**, *71*, 404–413

18. *NIST Chemistry WebBook, NIST Standard Reference Database Number 69*; Linstrom, P. J., Mallard, W. G., Eds.; National Institute of Standards and Technology, Gaithersburg MD, 20899, 2017

19. Olarte, M. V; Albrecht, K. O.; Bays, J. T.; Polikarpov, E.; Maddi, B.; Linehan, J. C.; Hagan, M. J. O.; Gaspar, D. J.; Northwest, P.; Box, P. O. Autoignition and Select Properties of Low Sample Volume Thermochemical Mixtures from Renewable Sources. *Fuel* **2019**, *238*, 493–506

20. Hahn, H.-D.; Dambkes, G.; Rupprich, N.; Bahl, H.; Frey, G. D. Butanols. In *Ullmann's Encyclopedia of Industrial Chemistry*; **2013**

21. Panten, J.; Surburg, H. Flavors and Fragrances, 2. Aliphatic Compounds. In *Ullmann's Encycl. Ind. Chem.*; **2015**

22. Bahrmann, H.; Hahn, H. D.; Mayer, D.; Frey, G. D. 2-Ethylhexanol. In *Ullmann's Encycl. Ind. Chem.*; **2013**

23. Di Cosimo, J. I.; Díez, V. K.; Xu, M.; Iglesia, E.; Apesteguía, C. R. Structure and Surface and Catalytic Properties of Mg-Al Basic Oxides. *J. Catal.* **1998**, *178* (2), 499–510

24. Leon, M.; Diaz, E.; Ordonez, S. Ethanol Catalytic Condensation over Mg-Al Mixed Oxides Derived from Hydrotalcites. *Catal. Today* **2011**, *164* (1), 436–442

25. de Haan, A. B; Bosch, H. *Industrial Separation Processes. Fundamentals*. Berlin, Boston: De Gruyter, **2013**.

26. Aitchison, H.; Wingad, R. L.; Wass, D. F. Homogeneous Ethanol to Butanol Catalysis—Guerbet Renewed. *ACS Catal.* **2016**, 7125–7132

27. Fu, S.; Shao, Z.; Wang, Y.; Liu, Q. Manganese-Catalyzed Upgrading of Ethanol into 1 - Butanol. *J. Am. Chem. Soc.* **2017**, *139*, 11941–11948

28. Wingad, R. L.; Gates, P. J.; Street, S. T. G.; Wass, D. F. Catalytic Conversion of Ethanol to N-Butanol Using Ruthenium P-N Ligand Complexes. *ACS Catal.* **2015**, *5* (10), 5822–5826

29. Chakraborty, S.; Piszel, P. E.; Hayes, C. E.; Baker, R. T.; Jones, W. D. Highly Selective Formation of N-Butanol from Ethanol through the Guerbet Process: A Tandem Catalytic Approach. *J. Am. Chem. Soc.* **2015**, *137* (45), 14264–14267

30. Di Cosimo, J. I.; Apesteguıa, C. R.; Ginés, M. J. L.; Iglesia, E. Structural Requirements and Reaction Pathways in Condensation Reactions of Alcohols on MgyAlOx Catalysts. *J. Catal.* **2000**, *190* (2), 261–275.

31. Marcu, I. C.; Tichit, D.; Fajula, F.; Tanchoux, N. Catalytic Valorization of Bioethanol over Cu-Mg-Al Mixed Oxide Catalysts. *Catal. Today* **2009**, *147* (3–4), 231–238.

32. León, M.; Díaz, E.; Vega, A.; Ordóñez, S.; Auroux, A. Consequences of the Iron-Aluminium Exchange on the Performance of Hydrotalcite-Derived Mixed Oxides for Ethanol Condensation. *Appl. Catal. B Environ.* **2011**, *102* (3–4), 590–599.

33. Marcu, I. C.; Tanchoux, N.; Fajula, F.; Tichit, D. Catalytic Conversion of Ethanol into Butanol over M-Mg-Al Mixed Oxide Catalysts (M = Pd, Ag, Mn, Fe, Cu, Sm, Yb) Obtained from LDH Precursors. *Catal. Letters* **2013**, *143* (1), 23–30.

34. Bravo-Suárez, J. J.; Subramaniam, B.; Chaudhari, R. V. Vapor-Phase Methanol and Ethanol Coupling Reactions on CuMgAl Mixed Metal Oxides. *Appl. Catal. A Gen.* **2013**, *455*, 234–246

164

35. Huang, X.; Korányi, T. I.; Boot, M. D.; Hensen, E. J. M. Catalytic Depolymerization of Lignin in Supercritical Ethanol. *ChemSusChem* **2014**, *7* (8), 2276–2288

36. Sun, Z.; Couto Vasconcelos, A.; Bottari, G.; Stuart, M. C. A.; Bonura, G.; Cannilla, C.; Frusteri, F.; Barta, K. Efficient Catalytic Conversion of Ethanol to 1-Butanol via the Guerbet Reaction over Copper- and Nickel-Doped Porous. *ACS Sustain. Chem. Eng.* **2016**, *5* (2), 1738–1746

37. Barrett, J. A.; Jones, Z. R.; Stickelmaier, C.; Schopp, N.; Ford, P. C. A Pinch of Salt Improves N-Butanol Selectivity in the Guerbet Condensation of Ethanol over Cu-Doped Mg/Al Oxides. *ACS Sustain. Chem. Eng.* **2018**, *6*, 15119–15126

38. Jones, Z. R., Doctoral Dissertation, "Elucidating Structure-Activity Relationships through X-ray Absorption Fine Structure Analyses: from Site-Isolated Systems, to Nanoclusters, and to Supported Nanoparticle Catalysts", University of California-Santa Barbara, **2019**

39. Hanukovich, S.; Dang, A.; Christopher, P. Influence of Metal Oxide Support Acid Sites on Cu-Catalyzed Nonoxidative Dehydrogenation of Ethanol to Acetaldehyde. *ACS Catal.* **2019**, 9, 3537–3550

40. Huang, C. C.; Lo, S. L.; Lien, H. L. Zero-Valent Copper Nanoparticles for Effective Dechlorination of Dichloromethane Using Sodium Borohydride as a Reductant. *Chem. Eng. J.* **2012**, 203, 95–100.

41. Yin, W.; Venderbosch, R. H.; Bottari, G.; Krawzcyk, K. K.; Barta, K.; Heeres, H. J. Catalytic Upgrading of Sugar Fractions from Pyrolysis Oils in Supercritical Mono-Alcohols over Cu Doped Porous Metal Oxide. *Appl. Catal. B Environ.* **2015**, *166–167*, 56–65

42. Patterson, A. L. The Scherrer Formula for X-Ray Particle Size Determination. *Phys. Rev.* **1939**, *56* (10), 978–982

43. Angelescu, E.; Pavel, O. D.; Bîrjega, R.; Florea, M.; Zăvoianu, R. The Impact of The "memory Effect" on the Catalytic Activity of Mg/Al; Mg,Zn/Al; Mg/Al,Ga Hydrotalcite-like Compounds Used as Catalysts for Cycloxene Epoxidation. *Appl. Catal. A Gen.* **2008**, *341* (1–2), 50–57.

44. Kloprogge, T.; Frost, R. L.; Al-, M. Infrared and Raman Study of Interlayer Anions CO_3^{2-}, NO_3^-, SO_4^{2-} and ClO_4^- in Mg/Al-Hydrotalcite. *Am. Mineral.* **2002**, *87* (3), 623–629.

45. Frost, R. L.; Kloprogge, J. T. Infrared Emission Spectroscopic Study of Brucite. *Spectrochim. Acta - Part A Mol. Biomol. Spectrosc.* **1999**, *55* (11), 2195–2205.

46. Hernandez-Moreno, M. J.; Ulibarri, M. A.; Rendon, J. L.; Serna, C. J. IR Characteristics of Hydrotalcite-like Compounds. *Phys. Chem. Miner.* **1985**, *12* (1), 34–38.

47. Loring, J. S.; Thompson, C. J.; Zhang, C.; Wang, Z.; Schaef, H. T.; Rosso, K. M. In Situ Infrared Spectroscopic Study of Brucite Carbonation in Dry to Water-Saturated Supercritical Carbon Dioxide. *J. Phys. Chem. A* **2012**, *116* (19), 4768–4777.

48. Su, C.; Suarez, D. L. In Situ Infrared Speciation of Absorbed Carbonate on Aluminum and Iron Oxides. *Clays and Clay Miner.* **1997**, *45*, 814–825.

49. Kandare, E.; Hossenlopp, J. M. Thermal Degradation of Acetate-Intercalated Hydroxy Double and Layered Hydroxy Salts. *Inorg. Chem.* **2006**, *45* (9), 3766–3773

50. Serjeant, E. P.; Dempsey, B. Ionisation Constants of Organic Acids in Aqueous Solution. In *IUPAC chemical data series*; Pergamon Press: Oxford; New York, 1979; p 989

51. Busca, G. Bases and Basic Materials in Chemical and Environmental Processes. Liquid versus Solid Basicity. *Chem. Rev.* **2010**, *110* (4), 2217–2249

52. Argyle, M.; Bartholomew, C. Heterogeneous Catalyst Deactivation and Regeneration: A Review. *Catalysts* **2015**, *5* (1), 145–269.

53. Twigg, M. V.; Spencer, M. S. Deactivation of Supported Copper Metal Catalysts for Hydrogenation Reactions. *Appl. Catal. A Gen.* **2001**, *212* (1–2), 161–174

54. Scanlon, J. T.; Willis, D. E. Calculation of Flame Ionization Detector Relative Response Factors Using the Effective Carbon Number Concept. *J. Chromatogr. Sci.* **1985**, *23* (8), 333–340.

55. Jorgensen, A. D.; Picel, K. C.; Stamoudis, V. C. Prediction of Gas Chromatography Flame Ionization Detector Response Factors from Molecular Structures. *Anal. Chem.* **1990**, *62* (7), 683–689

3.8. Appendix B. Supporting Information for Chapter 3

Abbreviations adapted from IUPAC nomenclature.

Bu(=O)OH = butanoic acid

n-BuOH = *n*-butanol

Bu(=O) = 2-butanone

BuOAc = butyl acetate

Bu(=O)OBu = butyl butanoate

n-Bu(=O)H = *n*-butyraldehyde

Et(OEt)$_2$ = 1,1-diethoxyethane

EtOEt = diethyl ether

EtOH = ethanol

EtOAc = ethyl acetate

Bu(=O)OEt = ethyl butanoate

2-EtBuOH = 2-ethyl-1-butanol

2-EtHexOH = 2-ethyl-1-hexanol

Oct(=O)OEt = ethyl octanoate

Hept = heptane

HexOH = 1-hexanol

Hex(=O) = 3-hexanone

OctOH = 1-octanol

PentOH = 2-pentanol

Pent(=O) = 2-pentanone

Table S3.1. Products from the reaction of different volumes of pure EtOH with $Cu_{20}PMO$ (100 mg calcined at 600 °C) with and without added Cl^- (140 ppm added as $MgCl_2 \cdot 6H_2O$). Conditions: 320 °C for 6 h in 10 mL minireactors. Values are reported in µmol.

	Initial V_{EtOH} (mL)					
	1.5 (Cl)	2 (Cl)	2.5 (Cl)	1.5	2	2.5
methanol	0	0	0	0	0	0
ethanol	8943	13985	17445	10635	14688	24368
heptane	62	66	77	76	105	95
ethyl acetate	617	900	964	1742	2516	3426
n-butanol	3765	4737	6055	1485	2011	2233
2-pentanone	0	0	3	0	0	0
butenol	0	0	0	0	0	0
butyraldehyde	0	0	0	0	0	0
2-ethyl-1-hexanal	0	0	0	3	0	0
ethoxybutane	0	6	13	11	13	12
2-pentanol	35	36	35	73	100	59
ether	0	0	150	0	29	35
2-butanone	36	49	40	207	270	222
1,1-diethoxyethane	0	0	0	0	0	0
3-Hexanone	11	9	13	17	22	28
butanoic acid	42	47	34	103	141	116
ethyl butanoate	289	343	341	337	447	432
butyl acetate	275	326	337	257	362	335
2-ethyl-1-butanol	193	196	280	26	28	24
hexenol	0	0	7	9	12	10
hexenol	0	5	15	0	0	0
1-hexanol	585	653	993	47	36	42
2-ethylbutyl acetate	115	112	106	28	36	20
butyl butanoate	0	0	0	0	0	0
ethyl hexanoate	39	39	56	10	12	6
hexyl acetate	47	48	66	10	9	7
2-ethyl-1-hexanol	46	40	65	0	0	0
1-octanol	51	59	110	0	0	0
butyl hexanoate	36	30	36	0	0	0
ethyl octanoate	10	8	12	0	0	0
sum of products	14704	17785	22700	9839	13542	15331
Mass Balance[a]	92	93	94	80	82	93
conversion (%)	65	59	59	59	57	43
STY[b]	465	585	748	183	248	276
TON[c]	65	79	99	59	76	72
TOF (h^{-1})[d]	11	13	17	10	13	12

[a]Mass balance is calculated based on the initial amount of ethanol analyzed by GC-FID. [b] Space time yield of n-BuOH in grams produced per kg of catalyst per h. [c]Turnover number in moles EtOH converted per mole of Cu in the catalyst. [d]Turnover frequency in TON per h.

Table S3.2.1-S3.2.3 Catalyst screening with 3 mL of EtOH (140 ppm Cl⁻). All values reported in percent unless otherwise noted. * = no chloride. [H] = reduced under hydrogen.

Table S3.2.2. Reactions with Cu-doped PMO catalyst at 310 °C.

Catalyst (Rxn Temp in °C)	Cu_{20} (310)	Cu_{20} (310) *
EtOH Conv.	51	33
n-BuOH Yield	21	12
EtOAc Yield	2	15
HexOH Yield	6	1
Other Yield	15	8
Mass balance	93	101
STY (g/kg*h)	669	375
TON	103	67
TOF ($\times 10^{-3}$ s^{-1})	4.76	3.10

Table S3.2.2 Catalyst screening with 3 mL of EtOH (140 ppm Cl⁻). Reactions with Cu/Ni-doped PMO catalyst at 310 and 320 °C.

Catalyst (Rxn Temp in °C)	Cu$_{10}$Ni$_{10}$ (310)	Cu$_{10}$Ni$_{10}$ (320) [H]	Cu$_{10}$Ni$_{10}$ (320) [H]	Cu$_{20}$Ni$_{20}$ (310)
EtOH Conv.	40	61	63	37
n-BuOH Yield	26	28	29	27
EtOAc Yield	1	1	1	1
HexOH Yield	8	8	9	8
Other Yield	11	8	8	7
Mass balance	105	83	83	105
STY (g/kg*h)	824	737	757	856
TON	78	98	103	81
TOF ($\times$ 10^{-3} s^{-1})	3.62	4.54	4.75	3.75

Table S3.2.3 Catalyst screening with 3 mL of EtOH (140 ppm Cl⁻). Reactions with Cu or Ni/Ga-doped PMO catalyst at 310°C.

Catalyst (Rxn Temp in °C)	$Ni_{24}Ga_{43}$ (310)	$Cu_{20}Ga_{10}$ (310)
EtOH Conv.	13	46
n-BuOH Yield	1	21
EtOAc Yield	1	3
HexOH Yield	1	4
Other Yield	4	6
Mass balance	92	89
STY (g/kg*h)	41	683
TON	30	94
TOF ($\times 10^{-3}$ s⁻¹)	1.37	4.37

[a] Compounds included in 'Others' are listed in Table S3.1.

Table S3.3. Products from the reaction of pure EtOH with $Cu_{20}PMO$ (100 mg calcined at 600 °C) with a range of added Cl^- (0 to 630 ppm added as $MgCl_2 \cdot 6H_2O$). Conditions: 320 °C for 6 h. Values are reported as percent yield. Averages shown in Figure 3.6.

	ppm Cl^-					
	0	72	140	297	464	630
EtOH Conv.	51	57	59	60	32	31
n-BuOH	13	22	26	29	13	11
EtOAc	12	3	4	5	1	1
HexOH	1	6	7	6	2	1
Other	10	11	11	12	6	6
Mass Balance	85	85	89	91	89	88
EtOH Conv.	53	63	59	63	33	24
n-BuOH	12	25	26	26	6	7
EtOAc	13	4	4	5	1	1
HexOH	0	6	7	6	1	1
Other	10	10	11	11	13	5
Mass Balance	83	81	89	85	87	89

Table S3.4.1-3.4.3. Consecutive reactions with 100 % EtOH using the same $Cu_{20}PMO$ catalyst (100 mg initially). Run #1 = 140 ppm chloride (added as $MgCl_2 \cdot 6H_2O$). Run #2 to #18 = no added chloride. Conditions for each run: 2.5 mL anhydrous EtOH, T = 320 °C, 6 h reaction. All values reported in percent yield. '' = sample mean, '+' = maximum observed value, '-' = minimum observed value for 3-5 duplicate runs. Approximately 89 mg of catalyst was recovered after run #18.

Rxn #	1			2			3			4			5			6		
%	$\bar{x}$	+	-	$\bar{x}$	+	-	$\bar{x}$	+	-	$\bar{x}$	+	-	$\bar{x}$	+	-	$\bar{x}$	+	-
EtOH Conversion	57	60	51	54	57	51	48	53	43	40	45	36	41	45	38	40	45	35
EtOAc	3	4	2	2	3	2	2	3	2	2	2	2	2	2	2	2	2	1
n-BuOH	24	27	21	21	22	20	21	24	18	19	22	17	20	23	18	19	23	15
HexOH	6	7	5	5	5	5	4	5	3	3	4	2	3	4	3	3	4	2
Other	10	13	6	9	12	6	10	14	6	5	6	3	5	7	4	7	10	3
Mass Balance	87	90	85	84	86	81	90	92	87	88	89	87	89	89	89	90	92	88

Table S3.4.2. Consecutive reactions (#7-12) with 100 % EtOH using the same $Cu_{20}PMO$ catalyst (100 mg initially).

Rxn #	7			8			9			10			11			12		
%	$\bar{x}$	+	-	$\bar{x}$	+	-	$\bar{x}$	+	-	$\bar{x}$	+	-	$\bar{x}$	+	-	$\bar{x}$	+	-
EtOH Conversion	44	46	42	42	48	37	49	51	46	51	55	48	50	54	47	50	52	48
EtOAc	2	2	2	2	2	1	2	2	2	2	3	2	3	3	2	2	2	2
n-BuOH	18	23	14	19	21	18	24	25	2	25	27	23	27	27	27	25	27	24
HexOH	3	4	2	4	4	3	5	5	4	5	5	5	5	5	5	5	6	5
Other	8	12	3	5	7	4	6	6	5	7	8	5	7	8	5	6	7	6
Mass Balance	86	88	84	88	90	86	87	88	87	88	88	88	91	94	88	90	88	87

174

Table S3.4.3. Consecutive reactions (#13-18) with 100 % EtOH using the same $Cu_{20}PMO$ catalyst (100 mg initially).

Rxn #	13			14			15			16			17			18		
%	$\bar{x}$	+	-	$\bar{x}$	+	-	$\bar{x}$	+	-	$\bar{x}$	+	-	$\bar{x}$	+	-	$\bar{x}$	+	-
EtOH Conversion	**48**	49	46	**54**	57	52	**59**	62	56	**55**	58	52	**53**	54	52	**46**	48	44
EtOAc	**2**	2	2	**2**	2	2	**1**	2	1	**2**	2	2	**2**	3	2	**2**	3	2
n-BuOH	**23**	25	22	**26**	26	25	**19**	22	16	**22**	24	19	**23**	24	22	**23**	23	22
HexOH	**5**	5	4	**5**	6	5	**4**	5	3	**4**	4	3	**4**	4	3	**3**	3	3
Other	**6**	7	6	**10**	13	8	**12**	16	8	**5**	6	4	**5**	6	4	**5**	6	4
Mass Balance	**89**	89	88	**89**	92	86	**78**	89	67	**77**	83	70	**81**	82	80	**87**	88	87

Table S3.5. Consecutive Guerbet reactions with 100 % EtOH and reused $Cu_{20}PMO$ catalyst. Each run contained 140 ppm chloride (added as $MgCl_2\cdot6H_2O$) in the ethanol. Reaction conditions: 2.5 mL anhydrous EtOH, 100 mg $Cu_{20}PMO$, T = 320 °C, 6 h reaction time for each run. All values reported in percent yield. Approximately 92 mg of catalyst was recovered after the reaction due to losses during product filtration.

Rxn #	1	2	3	4	5	6	7
EtOH conversion	57	47	27	18	18	19	20
n-BuOH	24	19	8	4	3	3	3
EtOAc	3	3	1	1	1	1	1
HexOH	6	4	1	0	0	0	0
Other	10	9	5	5	4	4	6
Mass Balance	87	87	87	92	91	89	90

Table S3.6. Consecutive Guerbet reactions with 100 % EtOH and reused $Cu_{20}PMO$ catalyst. Reaction conditions: 2.5 mL anhydrous EtOH, 100 mg $Cu_{20}PMO$, T = 320 °C, 6 h reaction time for each run. All values reported in percent yield. Approximately 90 mg of catalyst was recovered after the reaction due to loss during product filtration.

Rxn #	1	2	3	4	5	6	7
EtOH conversion	52	45	46	49	49	43	50
n-BuOH	10	9	11	7	8	8	7
EtOAc	13	15	14	14	14	15	13
Other	8	6	6	6	6	7	5
Mass Balance	79	85	85	77	78	86	76

Table S3.7. Temporal product distribution from Guerbet reaction with 100 % EtOH and $Cu_{20}PMO$ catalyst. All runs contain 140 ppm chloride (added as $MgCl_2 \cdot 6H_2O$) in the ethanol. Reaction conditions: 2.0 mL anhydrous EtOH, 50 mg $Cu_{20}PMO$, T = 320 °C, 6 h reaction time. All values reported in percent yield. Each time point represents individual experiments conducted concurrently.

Rxn Time (h)	1	2	4	6
EtOH conversion	20	31	46	59
n-BuOH	14	21	23	29
EtOAc	1	2	3	4
HexOH	3	5	6	8
Other	4	5	8	13
Mass Balance	102	102	94	95

Table S3.8. Temporal product distribution from Guerbet reaction with 100 % EtOH and $Cu_{20}PMO$ catalyst. All runs contain 140 ppm chloride (added as $MgCl_2 \cdot 6H_2O$) in the ethanol. Reaction conditions: 2.0 mL anhydrous EtOH, 100 mg $Cu_{20}PMO$, T = 300 °C, 6 h reaction time. All values reported in percent yield. Each time point represents individual experiments conducted concurrently.

Rxn Time (h)	1	3	4	6	8
EtOH conversion	33	50	53	59	61
n-BuOH	15	23	24	26	26
EtOAc	1	3	4	4	4
HexOH	3	5	6	7	8
Other	4	8	9	11	12
Mass Balance	90	90	89	88	89

Part 2. Mechanistic Study of Hydrogen Peroxide Triggered Carbon Monoxide Release from a Manganese Tricarbonyl Complex

Chapter 4. Kinetics and Reaction Mechanism of Hydrogen Peroxide with *fac*-Mn(CO)₃(Br)(bpCO₂H)

4.1. Abstract

Carbon monoxide (CO) release from the water-soluble manganese (I) tricarbonyl complex, fac-Mn(CO)$_3$(Br)(bpCO$_2$H) **A**, where bpCO$_2$H is 2,2'-bipyridine-4,4'-dicarboxylic acid, can be photochemically initiated or chemically initiated by reaction with hydrogen peroxide (H$_2$O$_2$). Metal carbonyl compounds have potential applications as carbon monoxide delivery, anti-microbial, and anti-tumoral therapeutics. Hydrogen peroxide reactions with Mn(I) carbonyl complexes have been previously reported; however, the reaction mechanisms are unknown. Elucidating such mechanisms is crucial to understanding how such compounds can be efficiently utilized as therapeutics. This chapter will focus on studies on the kinetics and plausible mechanisms of the reaction between complex **A** and hydrogen peroxide. In aqueous phosphate buffer solution at pH 7.4, the manganese tricarbonyl substrate of interest fac-Mn(CO)$_3$(Br)(bpCO$_2$H) is indefinitely stable. The addition of excess H$_2$O$_2$ to such solutions resulted in the consumption of **A** with concurrent production of CO, CO$_2$, and O$_2$. The resulting changes in the optical absorption spectra were used to examine the reaction kinetics as a function of solution variables including reactant concentrations, temperature and pH.

4.2. Introduction

4.2.1. Toxicity and Benefits of Carbon Monoxide

Carbon monoxide (CO) is a diatomic molecule that is widely known for its toxicity, which is largely attributed to the high binding affinity of CO to hemoglobin.[1] The formation of carboxyhemoglobin hinders the ability of this protein to transport oxygen throughout the cardiovascular system. Additionally, CO binds other heme proteins such as cytochrome C oxidase, and by doing so hinders cellular respiration. Inhibition of cytochrome C oxidase activity could also result in the partial reduction of O_2 to reactive oxygen species (ROS) instead of water. However, the binding affinity of CO to hemoglobin is about 220 times higher than the binding affinity to cytochrome C oxidase, thus carboxyhemoglobin formation is possibly a cytoprotective measure against CO's more toxic effects.[2]

Although CO is a toxic molecule, it is endogenously generated in mammalian cells. Physiological production of CO is almost entirely from heme catabolism by heme oxygenase (HO) enzymes. In this process free heme is converted to Fe(II), biliverdin, and CO. Endogenous production of CO is associated with various physiological benefits such as anti-inflammatory, anti-microbial, and anti-proliferation effects.[3] In addition, deficiency in endogenous CO production is associated various disease states including sepsis, diabetes, and vascular inflammation. Despite the body of literature that describes the biological importance of CO, the mechanism of its physiological actions are not well understood.

4.2.2. Carbon Monoxide Releasing Molecules and Hydrogen Peroxide

To harness the beneficial effects of CO and to evade inhalation toxicity, researchers have focused on developing carbon monoxide releasing molecules (CORMs). These CORMs are designed to only release CO under an external stimulus like heat, light, enzymatic actions, or chemical reaction. Photo-initiated carbon monoxide releasing molecules (PhotoCORMs) are typically metal carbonyl complexes. Various metal carbonyl based CORMs, mainly using Group 6-9 transition metals, have been studied for photochemically triggered CO release.[1] There are several examples of Mn(I) photoCORMs that include the tricarbonyl motif $Mn(CO)_3(L)2X$.[4] Recent work has reported the release of CO from Mn(I) photoCORMs by external addition of H_2O_2 or by endogenously produced cellular H_2O_2.[5-7] Hydrogen peroxide triggered CORM activation for targeted CO delivery to physiological sites has potential therapeutic applications in tumor chemotherapy[8,9] and in treating other sites of inflammation such as those infected with antibiotic resistant bacteria.[10,11]

It is generally recognized that hypoxic tumors tend to have hydrogen peroxide concentrations significantly higher than normal tissues.[12] In addition to these higher steady state hydrogen peroxide concentrations, tumor microenvironments are typically slightly acidic and hypoxic and have lower catalase activity. The lower catalase activity is likely to be a main contributing factor to the higher intracellular H_2O_2 concentration in tumors. These features have prompted research on the applications of Fenton or Fenton-like reactions in tumor chemotherapy.[13] Another ubiquitous enzyme family that affects H_2O_2 cellular levels is peroxiredoxins.[14] Although the exact roles that H_2O_2 plays in growth, proliferation and

180

migration of cancer cells are complex,[15] the abnormal H_2O_2 concentrations in tumors provide strategies for cancer chemotherapy.[16,17]

In this context, He et al recently proposed that carbon monoxide (CO) can be delivered to tumor cells via the reaction of manganese carbonyl complexes with endogenous H_2O_2.[6,18] Similar H_2O_2 activation of metal carbonyl CORMs has been noted with other tissues subject to oxidative stress.[7,19] Poole et. al observed hydroxyl radical production (using 3'-(p-hydroxyphenyl) fluorescein as a probe) when $[Mn(CO)_3(tpa-\kappa^3N)]^+Br^-$ as irradiated with 365 nm light in an aqueous solution containing 300 µM H_2O_2.[7] The authors also observed that the CO-depleted complex produced similar amounts of hydroxyl radical without irradiation.[7] However, no hydroxyl radical was detected when this PhotoCORM was allowed to react the same concentration of H_2O_2 in the dark. Lo Iacono et al. demonstrated that CO release from $Ru(CO)_3Cl(glycinate)$ uncouples mitochondrial respiration by accelerating pyruvate/malate oxygen consumption but decelerating ADP oxygen consumption (through ADP phosphorylation).[20] Recent work on a Mn(I)-carbonyl complex bearing a dansyl fluorophore showed that CO-release can be triggered either by light irradiation or by reaction with H_2O_2.[5] The authors reported an apparent first order rate constant (0.3 s^{-1}) for CO release with H_2O_2 in pH 7.4 phosphate buffered saline. This rate constant was determined by an exponential fit of the emission of the complex at 514 nm (excited at 365 nm) over time. A six-line EPR spectrum of the photolyzed solution (405 nm) was obtained and indicated a paramagnetic Mn(II) product.[5] The authors also reported CO-release from photolysis at 405 nm with an 8 mW cm^{-2} irradiation source. The Mn(I) carbonyl complex exhibited cytotoxicity towards hepatic cell lines (LX-2 and HepaRG) in the 100 µM range.[5] Although the therapeutic applications of H_2O_2 reaction with Mn(I) and

181

other low valent metal carbonyls are well established, the chemical mechanisms have not been defined.

While it is not surprising that CO would dissociate from such complexes once the metal is oxidized, many fundamental mechanistic questions arise. For example: Is the first step a one electron, outer sphere electron transfer reaction? Since H_2O_2 is both an oxidant and a reductant—does this initial step involve oxidation or reduction of the metal center? Alternatively, is the first step an inner sphere process, where a peroxide species displaces a ligand on the metal center? Since H_2O_2 is partially dissociated at physiological pH – is the active species H_2O_2 or HO_2^-? What are the reaction products beyond the qualitative observation of CO release? What plausible reaction intermediates are formed? The present kinetics investigation of the reaction of H_2O_2 with fac-Mn(CO)$_3$(Br)(bpCO$_2$H) (bpCO$_2$H = 2,2'-bipyridine-4,4'-dicarboxylic acid) was initiated with the goals of addressing these questions.

4.3. Results and Discussion

4.3.1. Photolysis of fac-Mn(CO)$_3$(Br)(bpCO$_2$H)

The photo-initiated release of carbon monoxide (CO) from Mn(I) tricarbonyl complexes has been extensively studied.[4] Many Mn(I) based photoCORMs are photoactive in the UV and visible region (300-500 nm). For instance, Motterlini and coworkers found at least three CO were released from irradiation of the tetracarbonyl manganese complex, [Mn(CO)$_4${S$_2$CNMe(CH$_2$CO$_2$H)}].[21] The UV-visible spectra of fac-Mn(CO)$_3$(Br)(bpCO$_2$H) (**A**), (structure shown in Scheme 4.1) shows a distinct metal to ligand charge transfer

(MLCT) peak (λ_{max} = 408 nm, ε = 3.31× 10^3 M^{-1} cm^{-1}). Irradiation of complex **A** with 365 nm light in pH 7.4 phosphate buffer resulted in depletion of the MLCT absorbance.

fac-Mn(CO)$_3$(Br)(bpCO$_2$H)
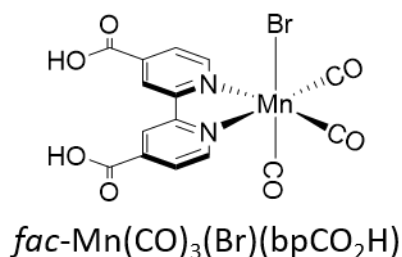
Scheme 4.1. Chemical structure of facial tricarbonylbromido-2,2'-bipyridine-4,4'-dicarboxylic acid manganese (I), denoted as **A**.

The samples were photolyzed in a 1-cm pathlength cuvette sealed with a septum screw cap and having an internal volume of ~5 mL. The temporal absorbance changes at the MLCT band maximum (408 nm, ε = 3.31× 10^3 M^{-1} cm^{-1}) were used to calculate the number of molecules reacted. The measured power of the light source was used to determine the number of incident photons and absorbance of **A** at 365 nm was used to determine the numbers of photons absorbed. A plot of the molecules reacted versus the photons absorbed gave a slope equal to the quantum yield (efficiency) for the depletion of **A**. The quantum yields for the depletion of **A** (ϕ_{MLCT}) were almost identical in aerobic (0.22) and in anaerobic solutions (0.24) (Figure 4.1 & 4.2).
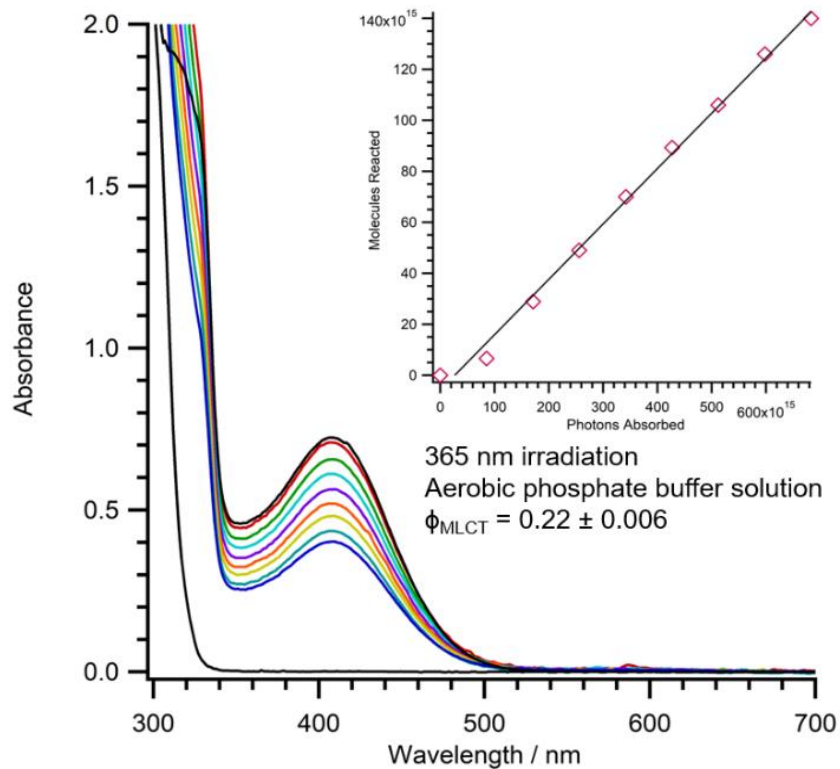
Figure 4.1. UV-visible spectral changes resulting from the irradiation of 220 µM **A** with 365 nm light (23 mW) in aerobic 0.118 M phosphate buffer solution (pH = 7.4) at 25°C. *Inset*: Quantum yield measurement: $\phi_{MLCT} = 0.22 \pm 0.006$. Measured CO is shown in Table 4.1.
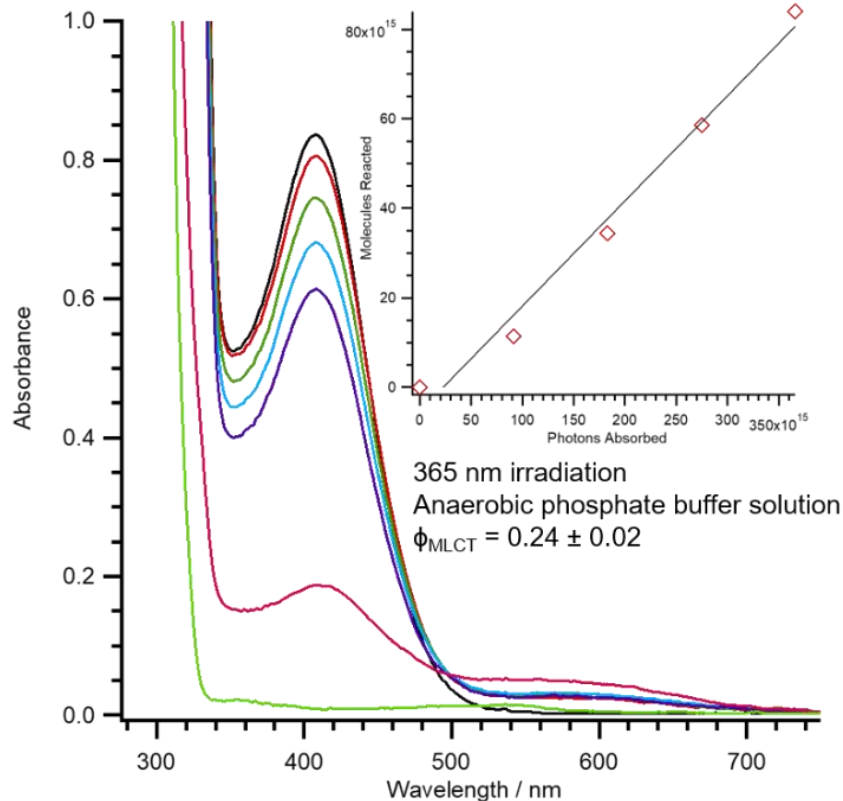
Figure 4.2. UV-visible spectral changes resulting from irradiation of 250 µM **A** with 365 nm light (23 mW) in anaerobic 0.118 M phosphate buffer solution (pH = 7.4) at 25°C. *Inset*: Quantum yield measurement: $\phi_{MLCT} = 0.24 \pm 0.02$. Measured CO is shown in Table 4.1.

The carbon monoxide released upon photolysis of **A** was measured by gas chromatography with thermal conductivity detection (GC-TCD). The headspace of the completely photolyzed solutions of **A** were sampled using a gastight Hamilton syringe. The moles of CO released upon complete photolysis was then calculated from the GC-TCD signal using a calibration curve (Appendix C Figure S4.1) by taking into account the cell volume (5 mL), the solution volume (2.4 mL), injection aliquot (100 µL) and the CO solubility in water.[22] Under anaerobic conditions, the CO release from **A** was nearly quantitative after complete photolysis, generating 2.8 moles CO per mole of **A** reacted; however, under aerobic conditions, only 1.9 moles of CO were detected per mole of **A** consumed.

185

Table 4.1. GC-TCD headspace analysis, for CO measurements, from 365 nm photolysis of **A** in aerobic and anerobic conditions shown in Figures 4.1 and 4.2.

Conditions	Calculated moles of A reacted[a]	Moles of CO measured from 100 μL injection	CO peak area	Calculated moles of CO in headspace[b]	Moles CO per moles A
Aerobic	5.25×10^{-7}	3.61×10^{-8}	223	9.75×10^{-7}	1.9
Anaerobic	6.06×10^{-7}	6.33×10^{-8}	391	1.71×10^{-6}	2.8

The final absorbance after exhaustive photolysis was 0.001. [a]calculated from initial absorbance at 408 nm, $\varepsilon = 3.31 \times 10^3$ M^{-1} cm^{-1}, and 2.4 mL solution volume. [b]calculated from peak area, slope from calibration curve, see Appendix C Figure S4.1 (1.62×10^{-10} moles CO/area), and headspace volume (2.6 mL).

In summary, the GC-TCD experiments show that after complete photolysis in aerobic aqueous conditions only 2 of the 3 possible CO molecules from *fac*-Mn(CO)$_3$(Br)(bpCO$_2$H) were detected. Carbon dioxide (CO$_2$) is likely another product; however, this was not measured. In contrast, all the CO from *fac*-Mn(CO)$_3$(Br)(bpCO$_2$H) was released after complete photolysis in anaerobic aqueous conditions.

4.3.2. Products of *fac*-Mn(CO)$_3$(Br)(bpCO$_2$H) Reaction with H$_2$O$_2$

As noted above H$_2$O$_2$ initiates release of CO from Mn(I) tricarbonyl complexes.[5,6] A similar result would be expected for the water soluble complex *fac*-Mn(CO)$_3$(Br)(bpCO$_2$H) (**A**). In phosphate buffered solution at near-neutral pH, the carboxylates of **A** are deprotonated, given the experimentally determined pKa values for the carboxylic acids of 2.25 and 2.6.[23] Upon addition of H$_2$O$_2$, yellow color due to the MLCT band of **A**, is bleached, while bubbles are visually noted to form on the sides of the cuvette. Figure 4.3 shows the temporal UV-visible spectral changes upon preparing a pH 7.4 solution of **A** (150 μM) and H$_2$O$_2$ (32 mM). The initial spectrum, shown in red, displays the MLCT band at 408 nm and two ligand centered π-π* transitions (300 nm and 220 nm) characteristic of the

bpCO₂H ligand. Absorbances of all three decrease over time, and after 66 minutes ~50 % of

A remained (blue, Figure 4.3).
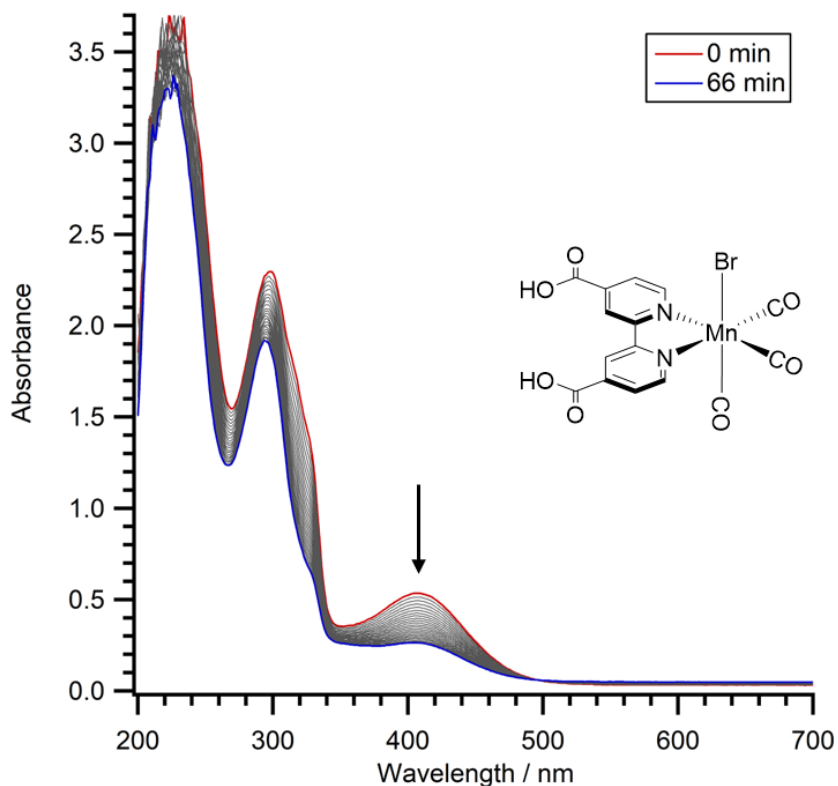
Figure 4.3. Temporal UV-visible spectral changes for the reaction of 150 µM **A** and 32 mM H_2O_2 at 37 °C in 0.118 M phosphate buffered solution (pH = 7.4). The time interval for recording each spectrum is 3 minutes. The red spectrum is the initial and the blue spectrum is after reaction for 66 minutes. 408 nm = MLCT, 220 nm and 300 nm = π-π*.

Figure 4.4 shows the infrared spectral changes from 2200-1800 cm⁻¹ of a DMSO solution initially 18.5 mM **A** and 185 mM H_2O_2 and containing 5% aqueous phosphate buffer solution at room temperature (23°C). There are three v_{CO} bands at 2023, 1933, and 1920 cm⁻¹ which are consistent with literature spectrum of **A**.[24] After 100 minutes the absorbances of these bands decreased 25 %, presumably as the carbonyls dissociated from the manganese (I) complex due to the reaction with H_2O_2. No new v_{CO} bands were observed.

This result is consistent with the UV-visible spectral changes. The IR experiment indirectly shows CO release from complex **A** via the decreased CO stretching frequencies.
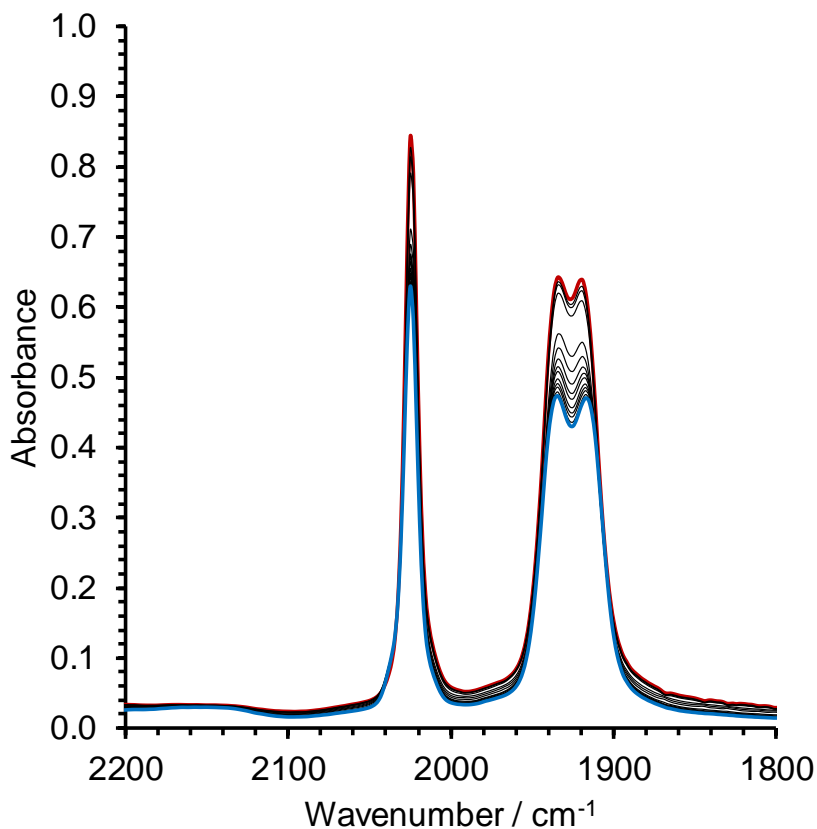
Figure 4.4. Temporal infrared spectral changes of a DMSO solution of **A** (18.5 mM) and H_2O_2 (185 mM) and 5% aqueous phosphate buffer at 25°C. The time interval for the first four spectra is 5 minutes. The gap represents 20 minutes of no data collection and the next spectra was then recorded 45 minutes after starting the reaction. Spectra after this were recorded every 5 minutes. The initial spectrum is shown in red and the final spectrum (100 minutes) is shown in blue.

The gaseous products were measured alongside the temporal absorption changes in Figure 4.5. The concentration of **A** was calculated using the absorbance at 408 nm and the molar absorptivity coefficient, $\varepsilon = 3.31 \times 10^3$ M^{-1} cm^{-1}. The solution volume (2.32 mL) was used to calculate the moles of **A** reacted. Thus, the moles of **A** reacted can be compared to the moles of gas released over time, as measured by GC-TCD. The CO gas release data as a

function of the reaction time are shown in Table 4.2.1. After 1 h reaction with H_2O_2 the MLCT band at 408 nm decreased 50 %, which was calculated as 73 µM decrease (from the 146 µM initial concentration) based on the assumption that any products or intermediates absorb at or near baseline at this wavelength. At this point, the CO production observed was only 1.1 mole per mole of complex **A** reacted. GC-TCD analysis after reaction for 3 h showed 1.7 moles of CO per mole of complex **A** reacted (Table 4.2.1). After 5 h only 1 % of the absorbance at 408 nm remains while the amount of CO produced was 2.3 moles per mole of **A** (Table 4.2.1). After complete reaction of **A** with H_2O_2 (18 h), the CO release was 2.2 mole per mole of **A** consumed.

Since any CO_2 released would be trapped as bicarbonate in such solutions, analysis for CO_2 required acidification of the solution after the reaction is completed. Accordingly, 1 mL of 3 M H_3PO_4 was added through the cuvette septum and the gas phase analyzed by GC-TCD. This procedure demonstrated that 0.5 moles of CO_2 were produced per mole of **A** reacted after complete reaction with H_2O_2 (Table 4.2.2). The baseline CO_2 in the solution was determined by the addition of 1 mL 3 M H_3PO_4 to a 150 µM solution of **A** without H_2O_2. No spectral changes were observed for this solution over 24 hours. These experiments show that, upon reaction of **A** with H_2O_2, at least one reaction pathway presumably leads to the oxidation of a metal-carbonyl ligand to CO_2. Although earlier studies reported CO release from similar Mn(I) tricarbonyls as triggered by H_2O_2,[5,6] CO was the only gaseous product reported in those examples.

189
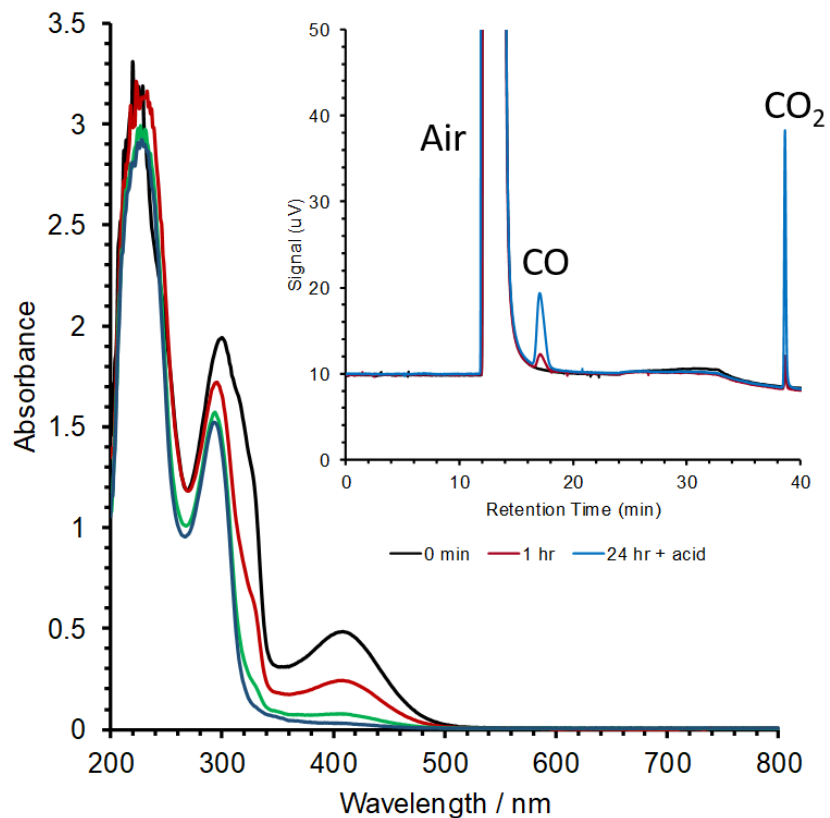
Figure 4.5. UV-visible spectral changes of 146 µM **A** from reaction with 32 mM H_2O_2 at 37°C in 0.118 M phosphate buffer solution (pH = 7.4). Black = optical spectrum before H_2O_2 addition, red = 1 hour after addition, green = 3 hours after addition, and blue = 5 hours after addition. *Inset*: Gas chromatograms of 200 µL headspace sample, black = before H_2O_2 addition, red = for 1 h reaction, and blue = 24 h reaction after the addition of 1 mL 3 M H_3PO_4.

Table 4.2.1 GC-TCD headspace analysis (for CO) for the reaction of 146 µM **A** and 32 mM H_2O_2 at 37 °C in 0.118 M phosphate buffered solution (pH = 7.4) shown in Figure 4.5. *headspace sample after 24 h and 1 mL 3 M H_3PO_4 addition.

Time (h)	Moles of **A** reacted[a]	Moles of CO[b]	CO peak area	Moles of CO in headspace[c]	Moles CO per moles **A**
1	1.69×10^{-7}	1.07×10^{-8}	66	1.85×10^{-7}	1.09
3	2.86×10^{-7}	2.85×10^{-8}	176	4.93×10^{-7}	1.72
5	3.39×10^{-7}	4.42×10^{-8}	273	7.64×10^{-7}	2.25
23	3.39×10^{-7}	4.32×10^{-8}	266	7.45×10^{-7}	2.20
24*	3.39×10^{-7}	6.90×10^{-8}	426	8.46×10^{-7}	2.50

The final absorbance after 24 h was 0.031. The internal volume of the cuvette was 5.57 mL [a]calculated from initial absorbance at 408 nm, $\varepsilon = 3.31 \times 10^3$ M^{-1} cm^{-1}, and 2.32 mL solution volume. [b]from 200 µL injection [c]calculated from peak area, slope from calibration curve, see Appendix C Figure S4.1 (1.62×10^{-10} moles CO/area), and headspace volume (3.25 mL).

Table 4.2.2 GC-TCD headspace analysis (for CO_2) for the reaction of 146 µM **A** and 32 mM H_2O_2 at 37 °C in 0.118 M phosphate buffered solution (pH = 7.4) *headspace sample after 24 h and 1 mL 3 M H_3PO_4 addition shown in Figure 4.5.

Time (h)	Moles of **A** reacted[a]	Moles of CO_2[b]	CO_2 peak area	Moles of CO_2 in headspace[c]	Moles CO_2 per moles **A**
24*	3.39×10^{-7}	2.15×10^{-8}	155	1.67×10^{-7}	0.49

The final absorbance after 24 h was 0.031. The internal volume of the cuvette was 5.57 mL [a]calculated from initial absorbance at 408 nm, $\varepsilon = 3.31 \times 10^3$ M^{-1} cm^{-1}, and 3.32 mL solution volume. [b]measured from 200 µL injection [c]calculated from peak area, slope from calibration curve, (1.39×10^{-10} moles CO/area), and headspace volume (2.25 mL). Baseline CO_2 was measured using a control sample that had **A** and H_3PO_4, but no H_2O_2.

When a more concentrated solution of **A** (2 mM) in 0.118 M phosphate buffer was reacted with 32 mM H_2O_2, a white precipitate was observed. Inductively Couple Plasma Optical Emission Spectroscopy (ICP-OES) of this precipitate showed that this white solid contained manganese and phosphorous in a 1.45 molar ratio. The theoretical molecular formula for a manganese phosphate salt consistent with this composition would be

$Mn_3(PO_4)_2$. Jin et. al synthesized a $Mn_3(PO_4)_2 \cdot 3H_2O$ as a water oxidation catalyst and characterized it by X-ray diffraction.[25] The solid product we obtained is not a well ordered material, however, the Bragg reflections observed in our XRD pattern (Figure 4.6) are consistent with those observed by Jin and coworkers for $Mn_3(PO_4)_2 \cdot 3H_2O$.[25] Thus, the XRD analysis and ICP results indicate that $Mn_3(PO_4)_2$ is produced from the reaction of 2 mM **A** with 32 mM H_2O_2 in 0.118 M phosphate buffer.
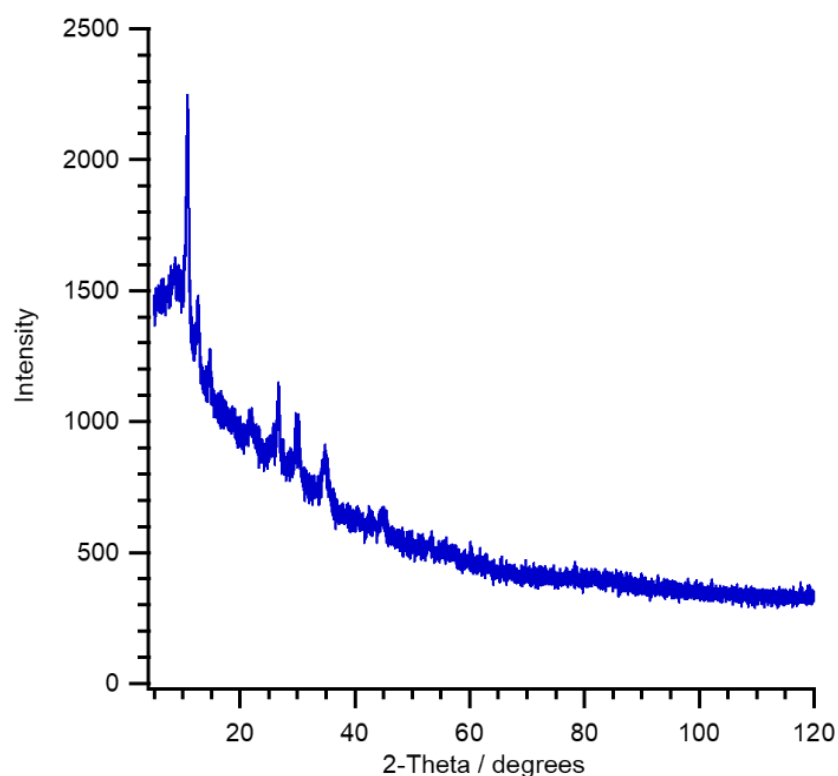
Figure 4.6. X-ray diffraction pattern of the white solid precipitate collected from the reaction of 2 mM **A** with 32 mM H_2O_2 at 25 °C in 0.118 M phosphate buffer solution at pH 7.4. Performed on a Panalytical Empyrean diffractometer, with Cu Kα radiation (λ = 1.5405980 Å) in a zero-background sample holder.

The ^{1}H NMR spectra of 2 mM **A** in 0.118 phosphate buffered D_2O before and after 32 mM H_2O_2 was added are shown in Figure 4.7. Low spin Mn(I) is diamagnetic and hence clear resolution of the three peaks at 7.97, 8.70, and 9.36 ppm corresponding to the three [1]H

environments on the coordinated bpCO$_2$H of **A** are observed (Figure 4.7, spectrum 1). The resonances at -0.16, 0.48, 1.60, and 2.75 ppm correspond to an internal standard 3-(trimethylsilyl)propane-1-sulfonic acid (DSS). The large broad peak at 4.79 ppm is from H$_2$O, since hydrogen phosphate salts were added to the D$_2$O. Immediately after the addition of 32 mM H$_2$O$_2$ (Figure 4.7, spectrum 2), all NMR peak intensities decreased and broadened. After 1 h the peaks for the bpCO$_2$H ligand are barely visible (Figure 4.7, spectrum 3). A similar spectrum was obtained after 2 h (Figure 4.7, spectrum 4). There were no additional features observed when the ^{1}H NMR spectra were collected between 80 to -80 ppm.   The broadening of the NMR peaks indirectly indicates the formation of a paramagnetic manganese species. Electron Paramagnetic Resonance (EPR) spectroscopy experiments were performed to attempt to directly observe the formation of a paramagnetic Mn species.
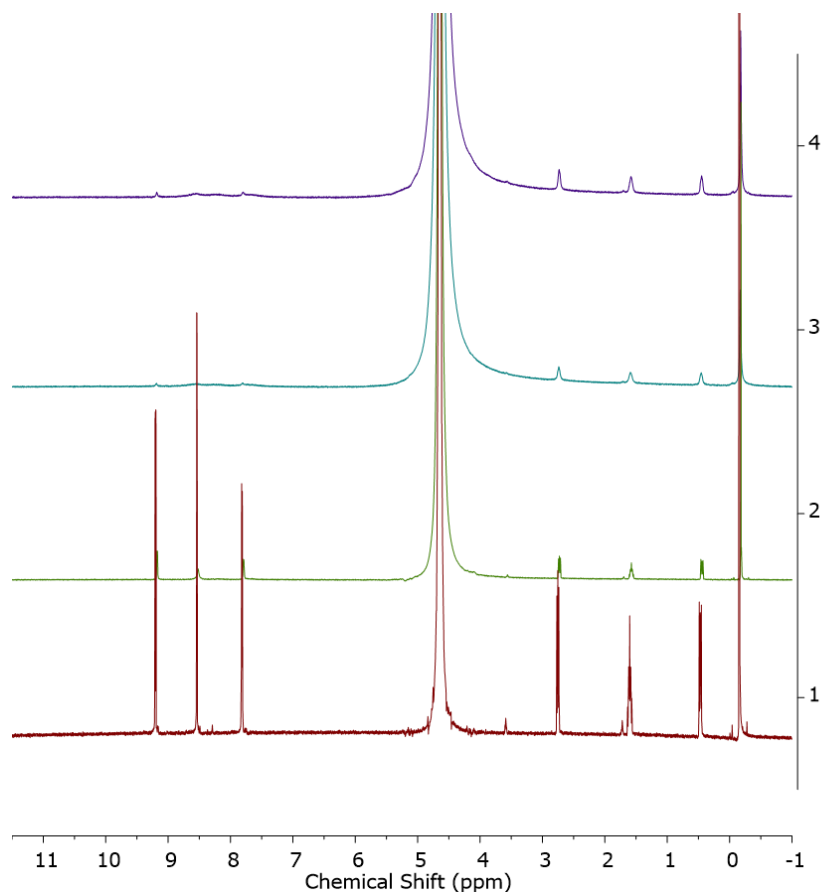
Figure 4.7. ^1H NMR spectra of 2 mM **A** in pH 7.4 D_2O/H_2O 0.118 M phosphate buffer solution (spectrum 1), after 32 mM H_2O_2 was added (spectrum 2), reacted for 1 h (spectrum 3), and reacted for 2 h (spectrum 4) at 25 °C. $bpCO_2H$ = 7.97, 8.70, and 9.36 ppm, DSS (internal standard) = -0.16, 0.48, 1.60, and 2.75 ppm, H_2O = 4.79 ppm

In situ X-band electron paramagnetic resonance (EPR) spectroscopy experiments were conducted on 150 µM **A** samples dissolved in 0.118 M phosphate buffered solution. A capillary tube was used to limit the sample volume as water strongly absorbs in the microwave region. In each case the first derivative of the absorbance spectrum is shown. The X-band EPR spectrum at 298 K of 150 µM **A** shows no signal, which is consistent with diamagnetic low spin Mn(I) (Figure 4.8). The X-band EPR spectrum of 150 µM **A** and 32 mM H_2O_2 after reacting for 42 min at 298 K showed no discernable signal either (Figure 4.9).

194
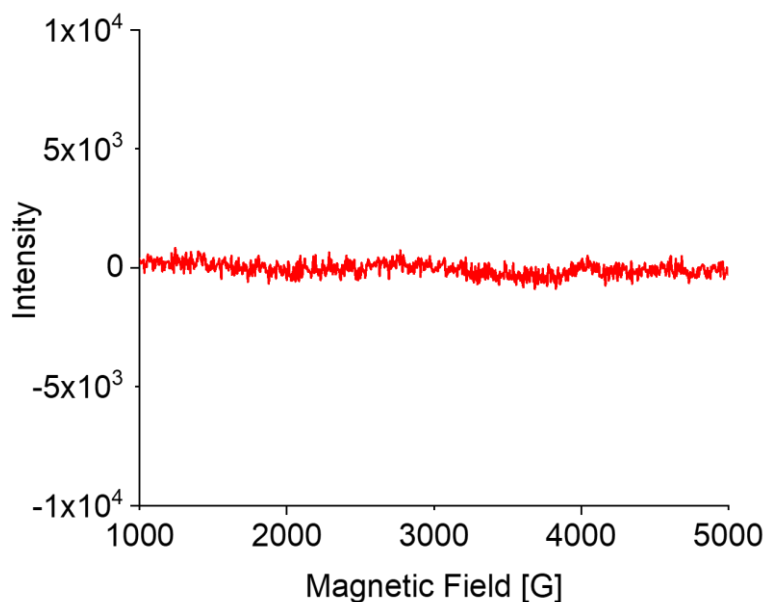
Figure 4.8. X-Band EPR spectrum of 150 µM **A**, taken at 298 K in 0.118 M phosphate buffer solution.
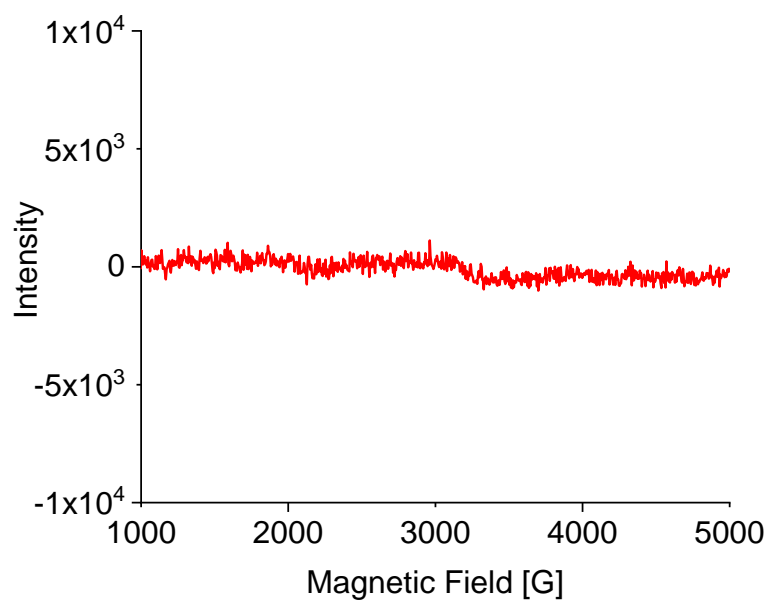
Figure 4.9. X-Band EPR spectrum of 150 µM **A** and 32 mM H_2O_2 after 42 min reaction, taken at 298K in 0.118 M phosphate buffer solution.

A signal was evident after 5 h reaction of 150 µM **A** and 32 mM H_2O_2 (Figure 4.10).

This signal may correspond to a species with a delocalized unpaired spin. A Mn(VI), low

spin Mn (IV), and low spin Mn(II) could all result in the observed signal as a singlet. However, this signal cannot be definitively assigned to a Mn species as the likelihood of observing a small signal from some introduced impurity is high due to the EPR instrument's sensitivity. Additionally, an EPR spectrum was obtained at 100 K after carefully freezing the capillary insert, which appears to have a similar singlet signal (Figure 4.11). After collecting these spectra, EPR experiments in acetonitrile were performed to avoid the problems with high water content.
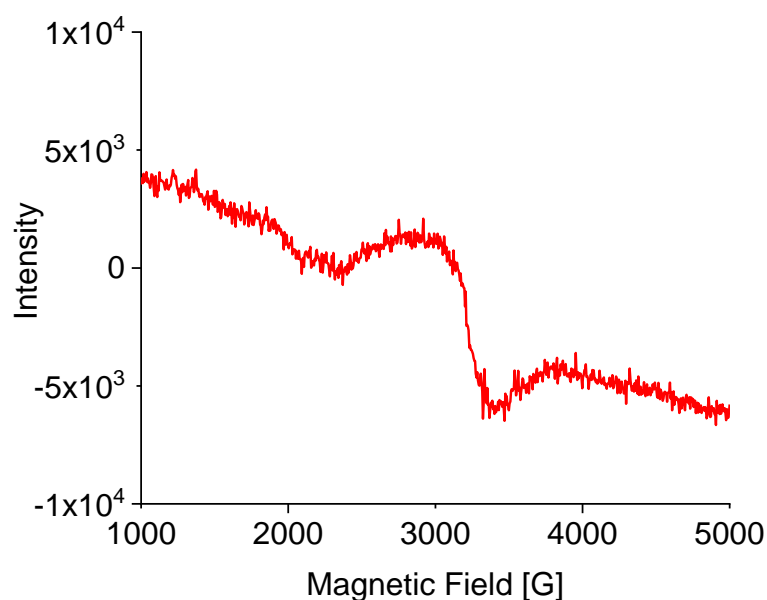
Figure 4.10. X-Band EPR spectrum of 150 µM **A** and 32 mM H_2O_2 after 5 h reaction, taken at 298 K in 0.118 M phosphate buffer solution.
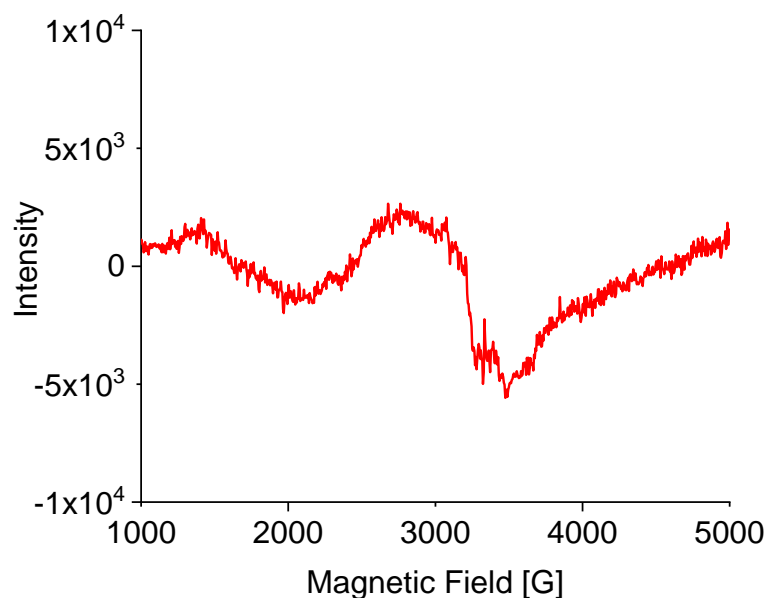
Figure 4.11. X-Band EPR spectrum of 150 µM **A** and 32 mM H_2O_2 after 5 h reaction, taken at 100 K in 0.118 M phosphate buffer solution.

Figure 4.12 highlights some of the X-band EPR spectra obtained in acetonitrile. Spectrum **A** (blue) shows there is no signal from 32 mM H_2O_2 and spectrum **B** (red) shows there is a small singlet signal for 150 µM *fac*-Mn(CO)$_3$(Br)(bpCO$_2$H) in acetonitrile. A six-line pattern is present in spectrum **C** (black) with a calculated g = 2.0038. This pattern is consistent with a paramagnetic high spin Mn(II) species. Notably, Schiller et. al observed a six-line pattern for the photolysis product and H_2O_2 reacted product of a Mn(I) 5-(dimethylamino)-N,N-bis(pyridin-2-ylmethyl) naphthalene-1-sulfonamide complex in 1:1 DMSO/water.[5] Mascharak et. al also observed a six-line pattern for a Mn(II) photoproduct after the photolysis of a Mn(Imdansyl)(CO)$_3$(phen)](CF$_3$SO$_3$).[26] Thus, the EPR results in acetonitrile indicate Mn(I) is oxidized to Mn(II) in the reaction with H_2O_2.

The UV-visible spectrum in acetonitrile has a MLCT λ_{max} at 459 nm and a shoulder centered at 364 nm. The MLCT band is 51 nm red-shifted from the 408 nm MLCT λ_{max}

197

observed in phosphate buffered solution. Tignor and coworkers previously observed a MLCT λ_{max} for **A** in 5% acidic H_2O/MeCN at 459 nm which was blue-shifted to 417 nm in 5% basic H_2O/MeCN.[27] This was likely due to the carboxylic acid groups of bpCO$_2$H being protonated in 5% acidic H_2O/MeCN and deprotonated in 5% basic H_2O/MeCN.[27] Furthermore, this shift is consistent with the solvato-chromatic behavior often observed for the MLCT bands of Group 7 metal carbonyl complexes.[28,29] The reaction of **A** with 32 mM H_2O_2 in acetonitrile is considerably slower than in phosphate buffered solution (Figure 4.13). After 81 minutes only a 16% absorbance decrease in the MLCT band at 459 nm was observed.
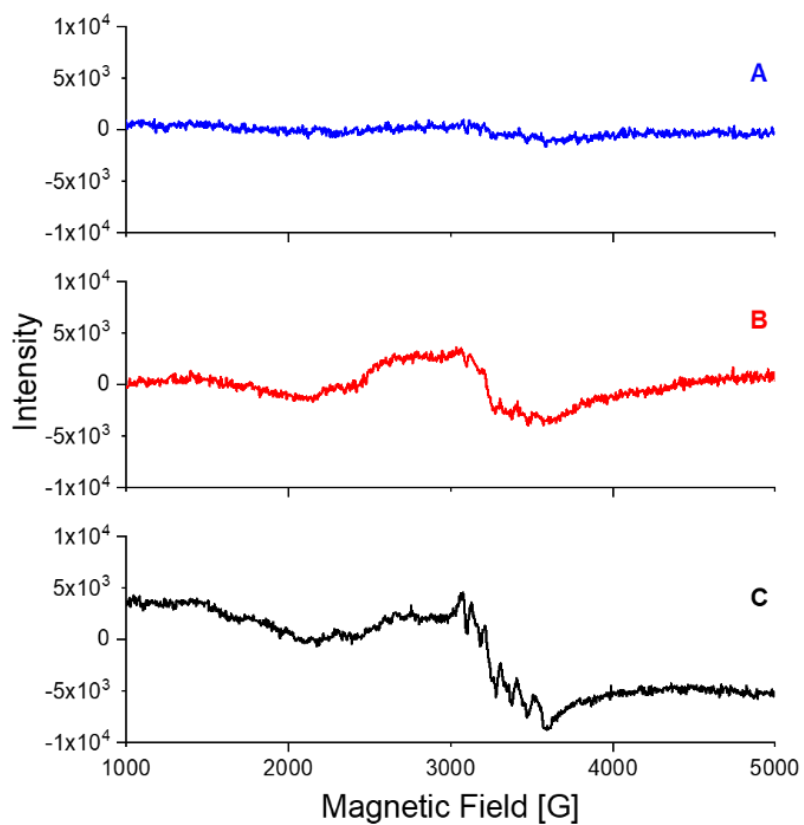
Figure 4.12. X-Band EPR spectra obtained in acetonitrile at 100 K. *Spectrum A* (blue) = 32 mM H_2O_2, *Spectrum B* (red) = 150 µM *fac*-Mn(CO)$_3$(Br)(bpCO$_2$H), and *Spectrum C* (black) = 150 µM *fac*-Mn(CO)$_3$(Br)(bpCO$_2$H) and 32 mM H_2O_2 after 81 min reaction at 25°C.
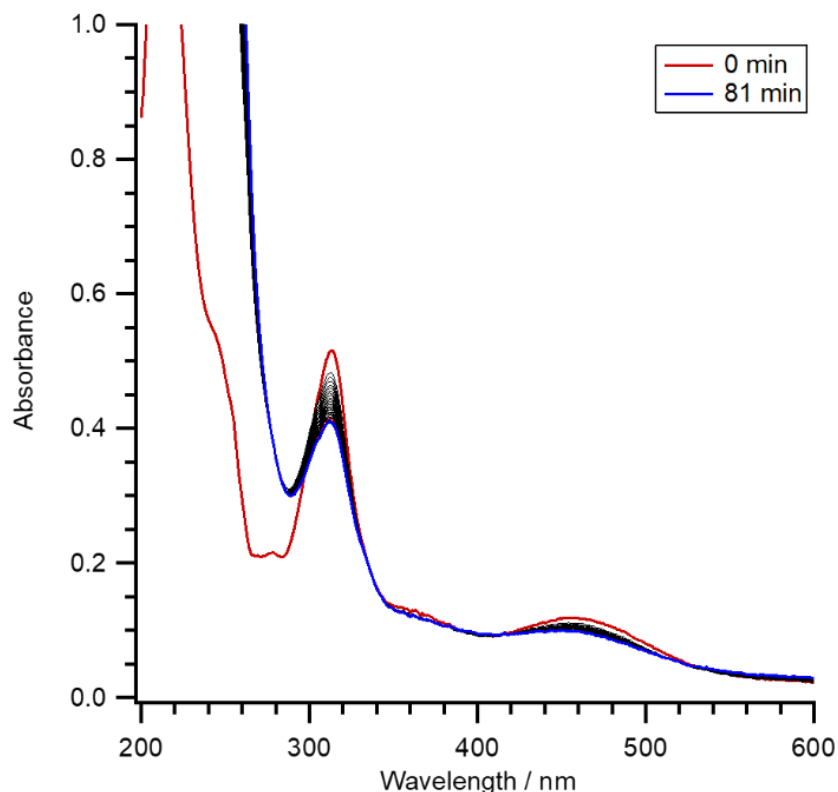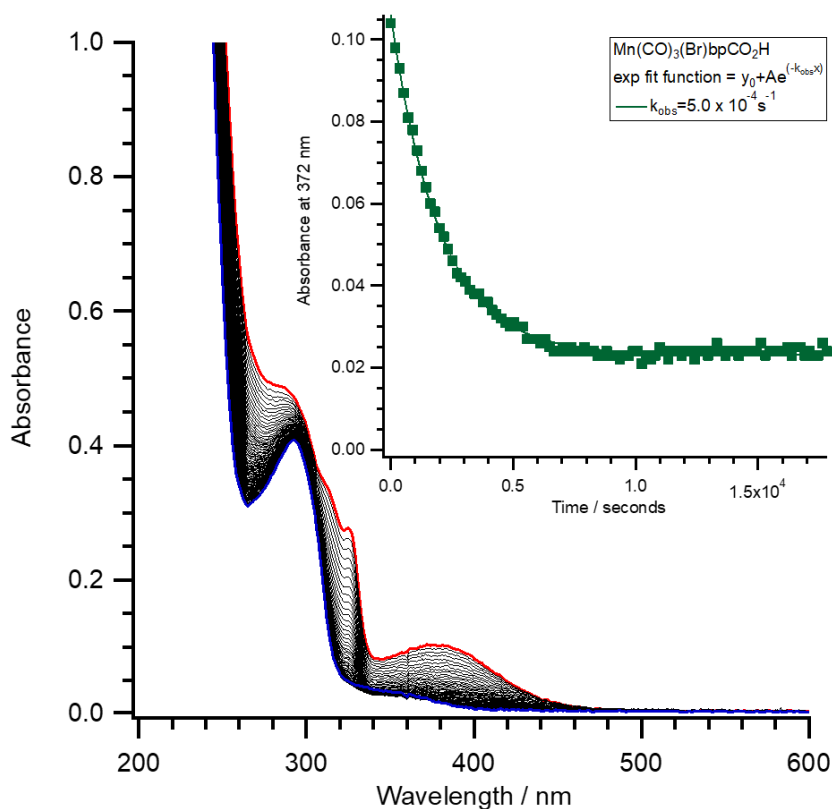
Figure 4.13. Temporal UV-visible spectral changes for the reaction of 100 µM **A** and 32 mM H_2O_2 at 37 °C in acetonitrile. The red spectrum is the initial and the blue spectrum is after reaction for 81 minutes. 459 nm = MLCT, 310 nm = π-π*.

In summary, the UV-Visible and IR spectral changes show that **A** is consumed in the reaction with H_2O_2. The GC-TCD measurements indicate that CO apparently does not immediately dissociate from the resulting intermediates, since only 1.1 mole of CO was measured per mole of **A** reacted after 1 h. However, the headspace analysis of the gas released after complete reaction (24 hours) and adding 3 M H_3PO_4 show that 2.5 moles of CO and 0.5 moles of CO_2 are produced per mole of **A**. The XRD analysis of the solid precipitate and ^1H NMR spectra from reaction of 32 mM H_2O_2 with 2 mM **A**, indicate that a Mn(II) product is formed. Furthermore, this observation is corroborated by 100 K EPR spectrum of 150 µM **A** with 32 mM H_2O_2, that showed a six-line pattern.

4.3.3. Ligand Substitution lability on *fac*-Mn(CO)₃Br(bpCO₂H)

The lability of the bromide ligand was examined by various experiments to understand how this might play a role in the reaction of **A** with H_2O_2. Cowan et. al proposed that the bromide ligand is labile in water and forms the aqua analog of **A**.[23] They attributed the large shift in the MLCT band in 75% water/ 25% acetonitrile mixtures to Br ligand displacement.[23] Additionally, in 50% water/50% acetonitrile mixtures the authors observed a difference between the absorbance spectrum of freshly prepared and 3 h old solutions. As noted above, it is more likely that the large shift in the MLCT band is due to solvato-chromatic effects and to deprotonation of the bpCO₂H ligand. The latter conclusion would be consistent with UV-visible spectral observations of **A** by Tignor and coworkers in acidic or basic 5 % water/acetonitrile.[27]

My experiments show the MLCT band shifted to 372 nm in 50% phosphate buffer/50% acetonitrile immediately and was stable at 37 °C (Figure 4.14). When 32 mM H_2O_2 was added to this solution, an absorption decrease comparable to 100 % aqueous phosphate buffer solution was observed (Figure 4.15). Based on literature precedence, the bromide ligand is still attached to complex **A**. One plausible reaction pathway would be substitution of a peroxide species for the bromide on **A** to form either *fac*-Mn(CO)₃(H₂O₂)(bpCO₂H) or *fac*-Mn(CO)₃(HO₂)(bpCO₂H). If this were the case, exchanging the bromide for a different ligand should alter the observed reaction rates.
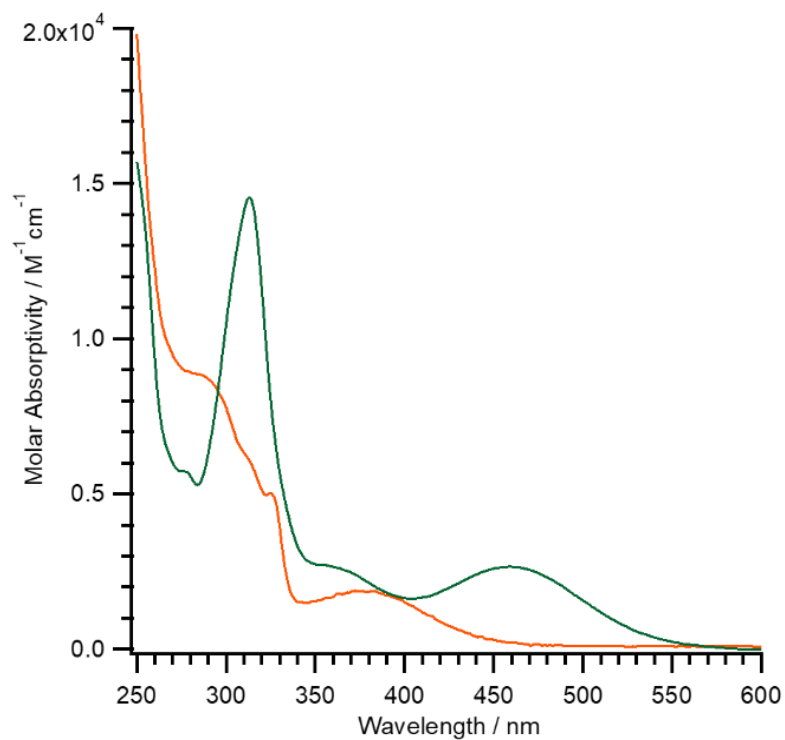
Figure 4.14. UV-Visible absorption spectra of 100 µM **A** in acetonitrile (green) and immediately after addition of 0.118 M phosphate buffered solution (orange) to give a 50% acetonitrile/50 % 0.118 M phosphate buffer solution. The large blue-shift is proposed to be due to combined solvato-chromatic effect and deprotonation of $bpCO_2H$ ligand on **A**.

Figure 4.15. Temporal UV-visible spectral changes for the reaction of 100 µM **A** and 32 mM H_2O_2 at 37°C in 50% phosphate buffer/50% acetonitrile. The red spectrum is the initial and the blue spectrum is after reaction for 5 h. $k_{obs} = 5.0 \times 10^{-4}$ s^{-1}.

The trifluoromethanesulfonate (OTf, triflate) complex *fac*-Mn(CO)$_3$(OTf)(bpCO$_2$H), denoted as **B**, was synthesized, and the reaction with H_2O_2 examined (Figure 4.16). Since complex **B** has the more weakly bound triflate ligand, it should be more substitution labile than is complex **A**. Complex **B** has a very similar optical spectra to **A**; however, upon addition of 32 mM H_2O_2, the MLCT absorbance decreases 4 times faster than observed for analogous experiment with **A** (Figure 4.17) under otherwise identical conditions. This result suggests that ligand substitution is a plausible pathway for the reaction between H_2O_2 and *fac*-Mn(CO)$_3$(X)(bpCO$_2$H). These experiments also suggest that complexes **A** and **B** retain their -Br and -OTf ligands when dissolved in solution in contrast to the conclusions by

203

Cowan et al.[23] However, an alternative explanation would be that complex **B** is more easily oxidized than is complex **A** and, consequently, would display an increased reaction rate constant for an electron transfer reaction with H_2O_2.[30] However, either conclusion would imply that both the bromido and triflato complexes stay intact in solution.
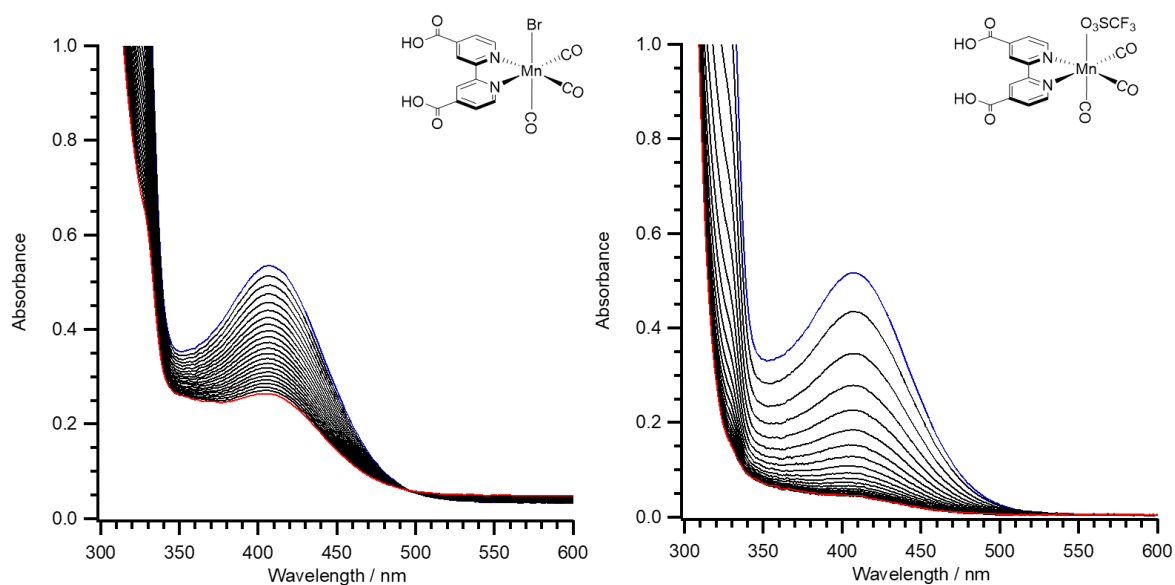
Figure 4.16. Temporal UV-visible spectral changes for the reaction of 150 µM **A** (*left*) and **B** (*right*) with 32 mM H_2O_2 at 37 °C in 0.118 M phosphate buffer solution (pH = 7.4). The blue spectrum is the initial and the red spectrum is after reaction for 66 minutes. 372 nm = MLCT band, $k_{obs} = 5.0 \times 10^{-4}$ s^{-1}.
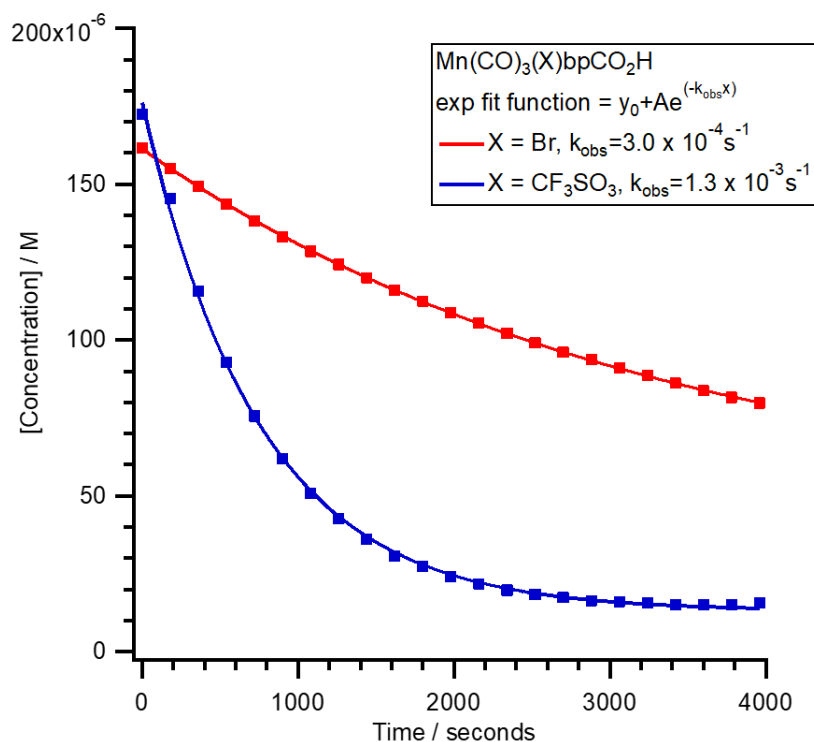
Figure 4.17. Concentration of **A** (red) and **B** (blue) over time from reaction with 32 mM H_2O_2 at 37 °C in 0.118 M phosphate buffer solution (pH = 7.4). Extinction coefficients of 3.3×10^3 M^{-1} cm^{-1} for **A** and of 3.0×10^3 M^{-1} cm^{-1} for **B** were used to calculate the concentrations. The lines show the exponential fit of these absorbance data which gave the respective rate constants. k_{obs} for **A** = 3.0×10^{-4} s^{-1} and k_{obs} for **B** = 1.3×10^{-3} s^{-1}.

In another experiment, excess sodium triflate (32 mM) was added to the reaction of 32 mM H_2O_2 with 70 µM **A**. The observed reaction rate of complex **A** disappearance was 2.5 times faster when 32 mM sodium triflate was present (Figure 4.18). This result was unexpected since the $^-$OTf salt is a very weak base.
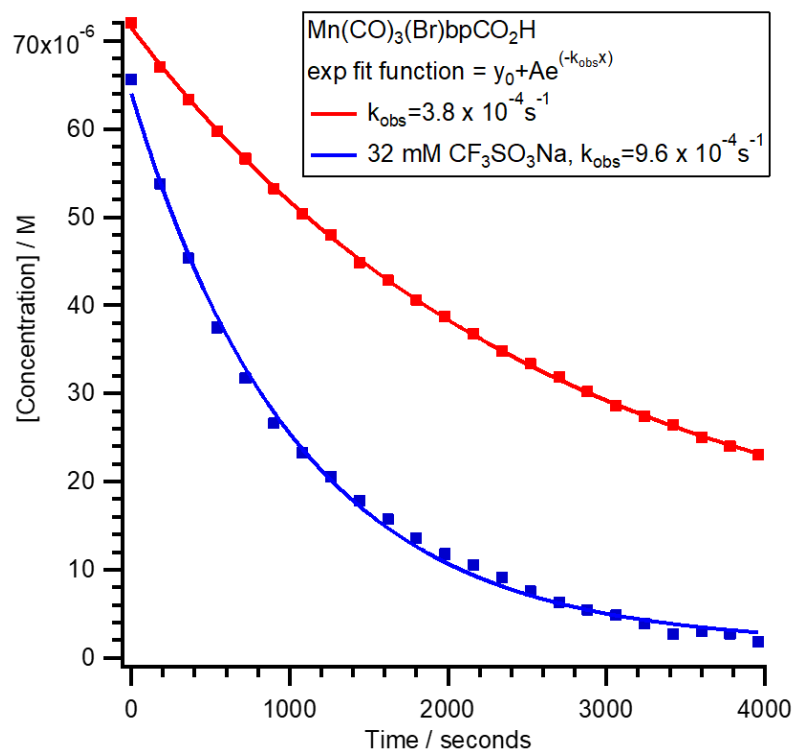
Figure 4.18. Concentration of complex **A** over time from reaction with 32 mM H_2O_2 at 37 °C in 0.118 M phosphate buffer solution (pH = 7.4) with (*blue*) and without 32 mM NaOTf (*red*). Extinction coefficient of 3.3×10^3 M^{-1} cm^{-1} for **A** used to determine concentration. The lines show the exponential fit of these absorbance data which gave the respective rate constants. (blue) $k_{obs} = 9.6 \times 10^{-4}$ s^{-1} and (red) k_{obs} for **B** = 3.8×10^{-4} s^{-1}.

Additionally, the ligand substitution mechanism hypothesis was evaluated by adding pyridine to the solution. The pyridine solutions were prepared in 0.118 M phosphate buffer and the solution pH was measured at 7.4. The addition of 32 mM pyridine to a solution of 70 μM **A** in phosphate buffer resulted in an overall increase in absorbance of the MLCT band with a corresponding modest shift of the λ_{max} from 408 nm to 401 nm (Figure 4.19). Concurrently, the π-π* absorbance at 298 increased 17 %. The spectrum stopped changing after 100 minutes, and there was no further change in the spectrum when the solution was left overnight (approximately 15 hours). These observations suggest that the pyridine substitutes for the bromide, since pyridine (a π-acceptor ligand) should have a different

206

electronic effect than bromide (a π-donor ligand) on the Mn d-orbitals. For simplicity, complex that was substituted with pyridine will be denoted as **C**.
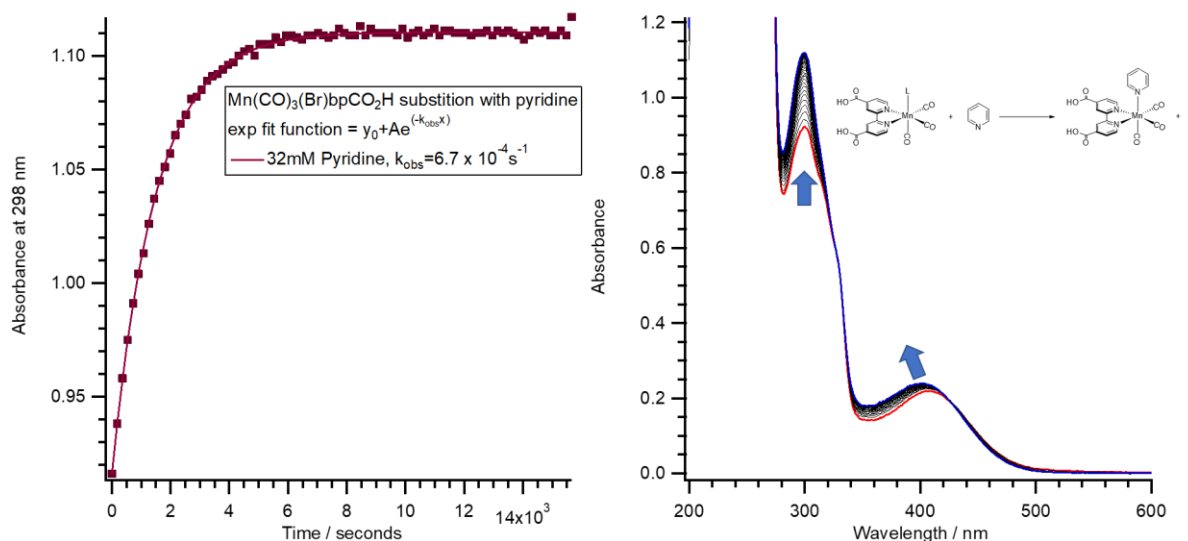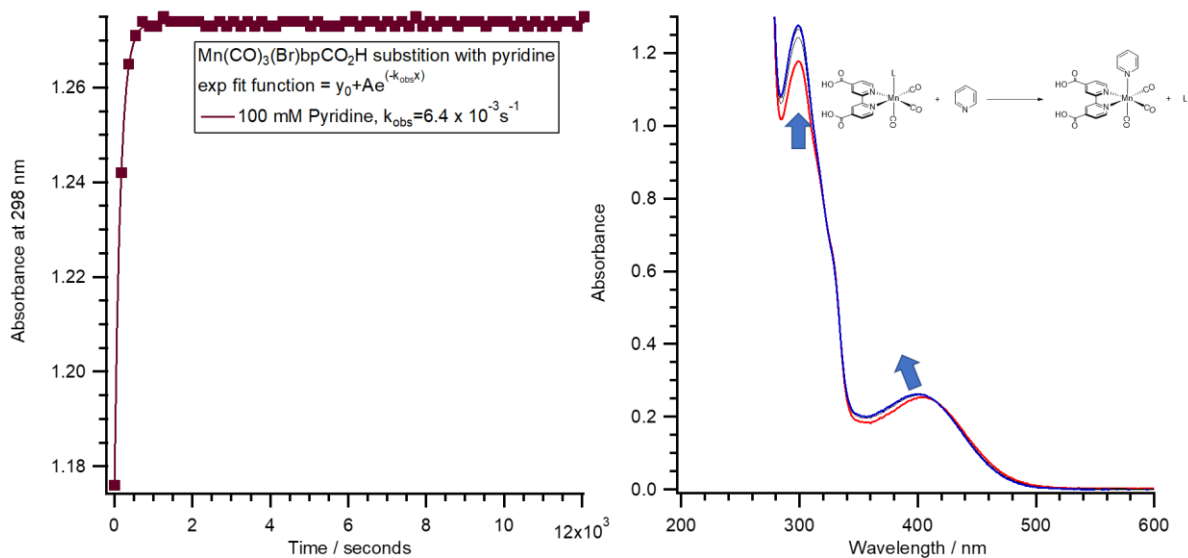

Figure 4.19. Temporal change in absorbance at 298 nm (*left*) and temporal UV-visible spectral changes (*right*) of 70 μM **A** from the addition of 32 mM pyridine at 25 °C in 0.118 M phosphate buffer solution (pH = 7.4). The red spectrum is the initial and the blue spectrum is after reaction for 4.4 h. An exponential fit of these absorbance changes gave k_{obs} = 6.7×10^{-4} s^{-1}.

The rate of the pyridine reaction with **A** (k_{obs} = 6.7×10^{-4} s^{-1} for 32 mM pyridine) proved to be similar to the rate of the redox reactions with H_2O_2 shown in Figure 4.17. Notably, the rate of the pyridine substitution of **A** with 100 mM pyridine (Figure 4.20) was ~10 times faster than that with 32 mM pyridine (Figure 4.19). However, only three data points were collected under the former conditions before the absorbance stopped changing, so the only valid conclusion is that the rate of the pyridine reaction is concentration dependent. After the solution mixture sat overnight (~15 h) there was no change in the absorbance. Hydrogen peroxide was then directly added to the solution without isolating the complex **C** in order to evaluate the effect of forming a putative pyridine complex on the rate of oxidation.

207

Figure 4.20. Temporal change in absorbance at 298 nm (*left*) and temporal UV-visible spectral changes (*right*) of 70 µM **A** from the addition of 100 mM pyridine at 25 °C in 0.118 M phosphate buffer solution (pH = 7.4). The red spectrum is the initial and the blue spectrum is after reaction for 3.3 h. An exponential fit of these absorbance changes gave k_{obs} = 6.4 × 10^{-3} s^{-1}.

Figure 4.21 is a comparison between the rate of disappearance for complex **C** and the rate of disappearance for complex **A** upon reaction with 32 mM H_2O_2 at pH 7.4 and 25 °C. The observed rate of disappearance for complex **A** is double the rate for complex **C**. Thus, it appears that pyridine substitution and/or the presence of pyridine in the solution inhibited the depletion reaction with H_2O_2. This result would be consistent with a mechanism for the reaction between *fac*-Mn(CO)$_3$(X)(bpCO$_2$H) and H_2O_2 initially proceeding by ligand substitution.
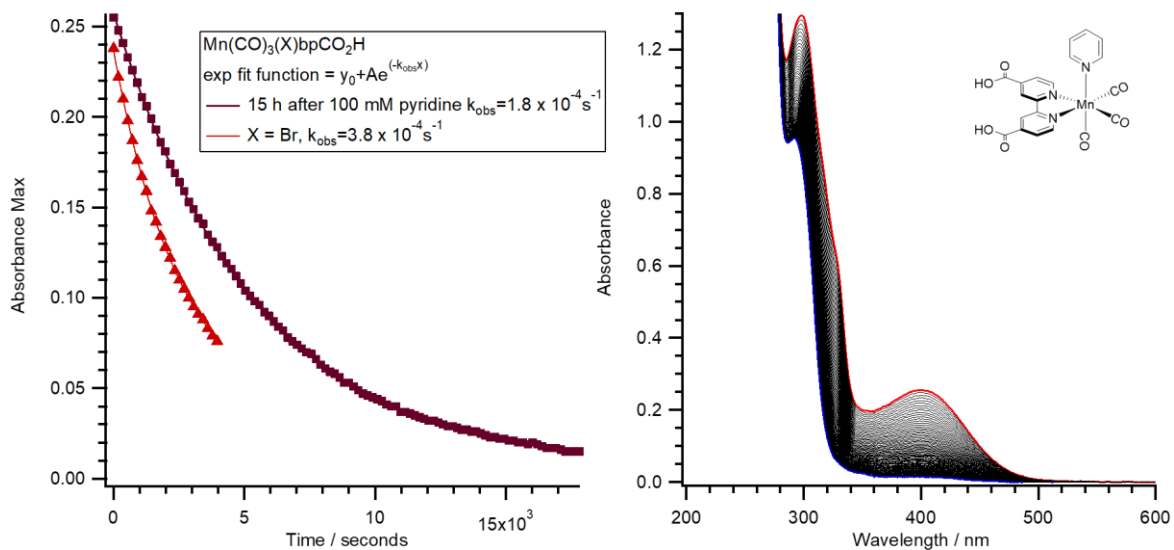
Figure 4.21. Temporal change in absorbance at λ_{max} (**A** = 408 nm, **C** = 400 nm) (*left*) and temporal UV-visible spectral changes (*right*) of 70 µM **C** from reaction with 32 mM H_2O_2 at 25°C in 0.118 M phosphate buffer solution (pH = 7.4). Initial pyridine concentration was 100 mM. The red spectrum is the initial and the blue spectrum is after reaction for 5 h. An exponential fit of these absorbance changes gave $k_{obs} = 1.8 \times 10^{-4}$ s^{-1}.

4.3.4. Reaction Kinetics of *fac*-Mn(CO)$_3$(Br)(bpCO$_2$H) with H$_2$O$_2$

Kinetics were evaluated using the initial rate method owing to the likelihood that this reaction proceeds by a sequence of steps. The first 5% change in the MLCT band of **A** was used to calculate the initial rates (d[**A**]/dt)$_{initial}$), and the responses of these rates to the solution variables were used to determine the rate law. The value of (d[**A**]/dt)$_{initial}$ under pseudo-first order conditions (excess H_2O_2) is directly proportional to [**A**]$_{initial}$ at each pH studied, as shown in Table 4.3. Thus, the initial rate is equal to the product of **[A]** and the observed rate constant (k_{obs}) (eq. 1).

$$\left(\frac{d[A]}{dt}\right)_{initial} = Initial\ rate = k_{obs}[A]_{initial}$$

(1)

Table 4.3. Selected results from reaction of *fac*-Mn(CO)$_3$(Br)(bpCO$_2$H) **A** with H$_2$O$_2$ showing that the initial reaction rate under pseudo-first order conditions is proportional to [**A**]$_{initial}$ and to [H$_2$O$_2$]$_{total}$.

entry	pH	[A]$_{initial}$ (µM)	Stdev	[H$_2$O$_2$] (mM)	- Initial rate ($\times 10^{-7}$ M/s)	Stdev	k_{obs} (s^{-1})
1	6.1	174	3.3	15.8	0.78	0.19	0.0045
2	6.1	171	2.8	31.5	1.35	0.12	0.0079
3	6.1	92	5.1	31.5	0.72	0.06	0.0078
4	7.4	73	0.42	15.8	0.68	0.13	0.0009
5	7.4	74	3.0	31.5	1.08	0.15	0.0015
6	7.4	147	12.6	31.5	2.25	0.40	0.0015
7	8.0	167	-	31.5	5.09	-	0.030
8	8.0	39	5.5	31.5	1.11	0.14	0.029

k_{obs} = (-initial rate)/ [**A**]$_{initial}$

A plot of k_{obs} vs. [H$_2$O$_2$]$_{total}$ at pH 7.4, where [H$_2$O$_2$]$_{total}$ represents the total concentration of hydroperoxide species initially present in the solution, also proved to be linear as shown in Figure 4.22 (eq. 2). Thus, k_{obs} is proportional to [H$_2$O$_2$], as shown in eq. 2, and -d[A]/dt = k' [A][H$_2$O$_2$].

$$k_{obs} = \frac{Initial\ rate}{[A]} = k'\,[H_2O_2]_{total} \qquad\qquad (2)$$
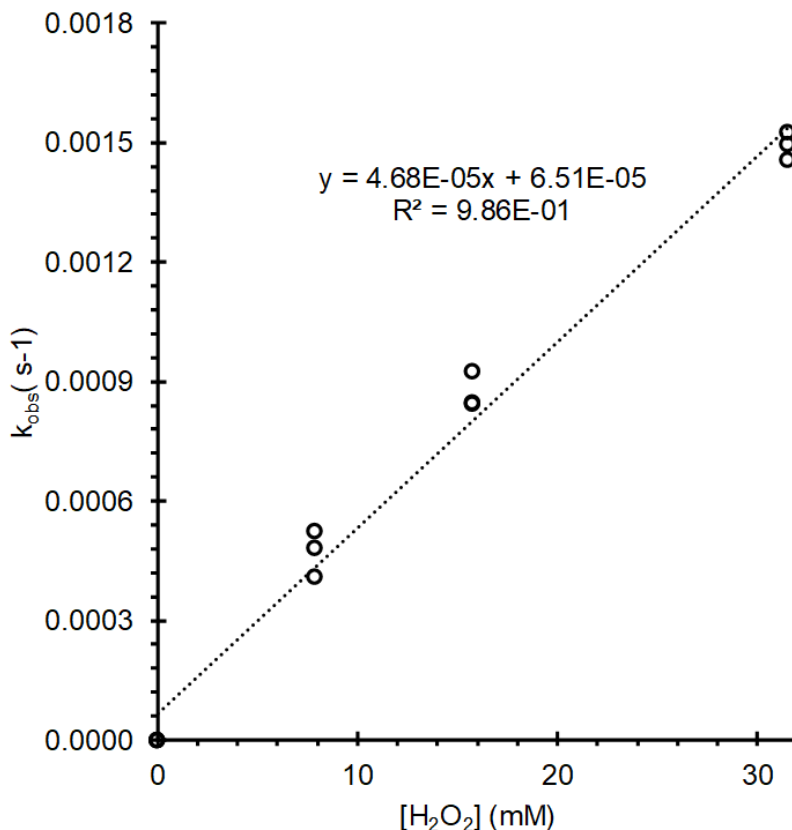
Figure 4.22. Plot of k_{obs} (s^{-1}) vs. [H$_2$O$_2$]$_{total}$ in 0.118 M phosphate buffer solution at pH 7.4. The initial rate is the measured rate of disappearance of **A** using its MLCT absorbance at 408 nm. All experiments were done between 34-147 µM **A** and at 37°C. Each point represents a single, independent experiment.

The effects of reaction temperature on the reaction rates were examined to determine the Gibbs free energy, enthalpy and entropy of activation (eq. 3). Figure 4.23 shows the plot of initial rate of **A** disappearance versus [H$_2$O$_2$] in mM. The slope of the lines in Figure 4.24 is the k′ and the second order reaction rate constant was calculated using [**A**]$_{initial}$. The Eyring-Polanyi equation (eq. 4) was used to relate the reaction rate constant (k) to the Gibbs energy of activation. The frequency that the transition state reacts to form products is defined by k_b/h, where k_b is Boltzmann's constant and h is the Planck constant. The gas constant (R) in J mol^{-1} K^{-1} and absolute reaction temperature (T) in K are used in this calculation.

$$\Delta G^{\ddagger} = \Delta H^{\ddagger} - T\Delta S^{\ddagger} \qquad (3)$$

$$k = \frac{k_B T}{h} e^{\frac{-\Delta G^{\ddagger}}{RT}} \qquad (4)$$

The Eyring-Polanyi equation can also be written as shown eq. 5. The Gibbs energy can be calculated using equation 6 by taking the experimentally determined rate constant (k) at a specific reaction temperature (T).

$$\ln(k) = \ln\left(\frac{k_B T}{h}\right) - \frac{\Delta G^{\ddagger}}{RT} \qquad (5)$$

$$\Delta G^{\ddagger} = -RT \times \ln\left(\frac{k}{\frac{k_B T}{h}}\right) = -RT(\ln(k) - \ln(\frac{k_B T}{h})) \qquad (6)$$

The activation enthalpy ($\Delta H^{\ddagger}$) and entropy ($\Delta S^{\ddagger}$) can be determined by rewriting the Eyring-Polanyi equation as follows (eq. 7) and then using the relationship between the Gibbs free energy and enthalpy/entropy (eqs. 8 & 9).

$$\frac{k}{T} = \frac{k_B}{h} e^{\frac{-\Delta G^{\ddagger}}{RT}} \qquad (7)$$

$$\frac{k}{T} = \frac{k_B}{h} e^{\frac{-\Delta H^{\ddagger}}{RT}} e^{\frac{\Delta S^{\ddagger}}{R}} \qquad (8)$$

$$\ln\left(\frac{k}{T}\right) = \frac{-\Delta H^{\ddagger}}{R}\frac{1}{T} + \ln\frac{k_B}{h} + \frac{\Delta S^{\ddagger}}{R} \qquad (9)$$

The Eyring plot of ln (k/T) vs. 1/T (Figure 4.24) gives a slope (m) that is used to calculate $\Delta H^{\ddagger}$ (eq. 10). The experimental uncertainty is calculated as the product of the determined $\Delta H^{\ddagger}$ and the standard deviation in ln (k).

$$m = \frac{-\Delta H^{\ddagger}}{R} \qquad \text{(10)}$$

$$-\Delta H^{\ddagger} = -11187 \times 8.314\, J\, mol^{-1}K^{-1} = -93\, \pm 12\, kJ\, mol^{-1}K^{-1}$$

The y-intercept (b) is used to calculate $\Delta S^{\ddagger}$ (eq. 11 & 12). The experimental uncertainty is calculated as the product of the determined $\Delta S^{\ddagger}$ and 3 times the standard deviation in ln (k).

$$b = \ln\left(\frac{k_b}{h}\right) + \frac{\Delta S^{\ddagger}}{R} \qquad \text{(11)}$$

$$\Delta S^{\ddagger} = R \times \left(b - \ln\left(\frac{k_b}{h}\right)\right) \qquad \text{(12)}$$

$$\Delta S^{\ddagger} = 8.314\, J\, mol^{-1}K^{-1} \times (27.332 - 23.76) = 29.7\, \pm 11.5\, J\, mol^{-1}K^{-1}$$

213
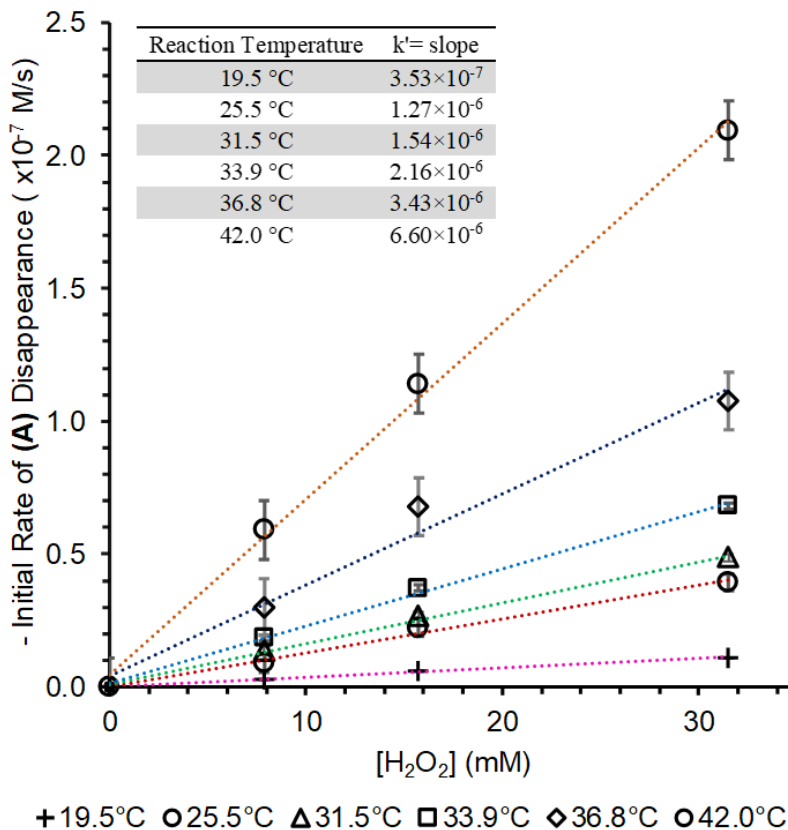
Figure 4.23. Temperature dependence for initial rate of **A** disappearance (10^{-7} M/s) versus [H_2O_2] in mM between reaction temperature 19.5 and 42.0 °C in 0.118 M phosphate buffered solution. The slope for each line = k' at a specific reaction temperature. Second order rate constant (k) determined by dividing by the [**A**]$_{initial}$.
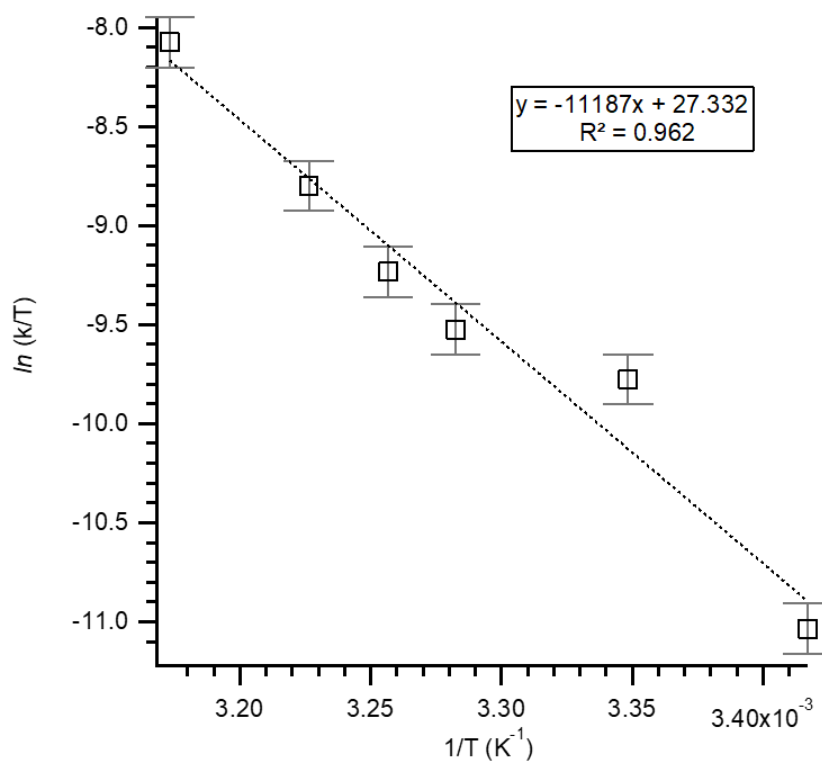
Figure 4.24. Eyring-Polanyi plot of ln(k/T) vs. 1/T where k was determined from the slope of the linear fit for data shown in Figure 4.23 for the initial rate of **A** decrease via the reactions of 70 µM [**A**]$_{initial}$ with 8 to 32 mM H_2O_2 between reaction temperature 19.5 and 42.0°C in 0.118 M phosphate buffer solution shown in Figure 4.24.

Alternatively, the rate constant observed at a given temperature and the determined activation enthalpy can be related to the entropy. In this way, the error associated with extrapolating the Eyring plot can be visualized. Table 4.4 below shows the calculations of $\Delta G^{\ddagger}$ and $\Delta S^{\ddagger}$. The general trend shows that $\Delta G^{\ddagger}$ decreases with increasing reaction temperature, except for 25.5 °C which is attributed to random error. The values of $\Delta S^{\pm}$ so calculated agree with the extrapolated value reported above.

Table 4.4. Data for the rate constant temperature dependence shown in Figure 4.23 and 4.24. Calculation of Gibbs free energies and entropies of activation.

k ($\times 10^{-2}$, M^{-1} s^{-1}, 2nd order)	T (K)	k_bT/h	$\Delta G^{\ddagger}$ (kJ mol^{-1})	$\Delta S^{\ddagger}$ (J mol^{-1} K^{-1})
0.47	292.65	6.10×10^{12}	84.7	28.5
1.70	298.65	6.22×10^{12}	83.3	32.6
2.22	304.65	6.35×10^{12}	84.3	28.6
3.00	307.05	6.40×10^{12}	84.2	28.6
4.67	309.95	6.46×10^{12}	83.9	29.4
9.81	315.15	6.57×10^{12}	83.4	30.5

Standard deviation for $\Delta G^{\ddagger} = \pm 11$ kJ mol^{-1} and $\Delta S^{\ddagger} = \pm 11.5$ J mol^{-1} K^{-1}. $\Delta H^{\ddagger} = 93$ kJ mol^{-1}.

The reaction kinetics were also studied as a function of pH to evaluate if the conjugate base of hydrogen peroxide, the hydroperoxyl anion (HOO$^-$), plays a role. Notably, the initial rate of **A** disappearance increased as the reaction pH increased (Figure 4.25). This behavior has been previously observed by Salem and coworkers with Mn(III) Schiff base complexes.[31,32] Salem et. al proposed that a Mn(OOH) species is formed initially.[31] Figure 4.25 clearly shows that reaction of **A** with H_2O_2 can be described by a pH independent pathway dominant at the lower pH values studied (6.1-7.0) and a second pathway that is markedly pH sensitive, becoming a major contributor to the reaction rate above pH 7. Given that hydrogen peroxide is a relatively weak acid (eq. 13) and that the solutions are relatively stable at these pH values before adding H_2O_2, we conclude that the marked rate acceleration at higher pH is due to enhanced reactivity of the hydroperoxyl anion HOO$^-$ (eq. 14) relative to that of H_2O_2 itself.

$$H_2O_2 \rightleftharpoons HOO^- + H^+ \quad K_a(H_2O_2) = 1.8 \times 10^{-12} M \qquad \textbf{(13)}$$
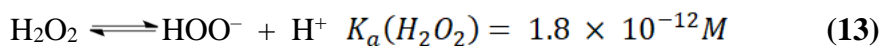
$$Initial\ rate = k_1[H_2O_2][A] + k_2[HOO^-][A] \qquad \textbf{(14)}$$
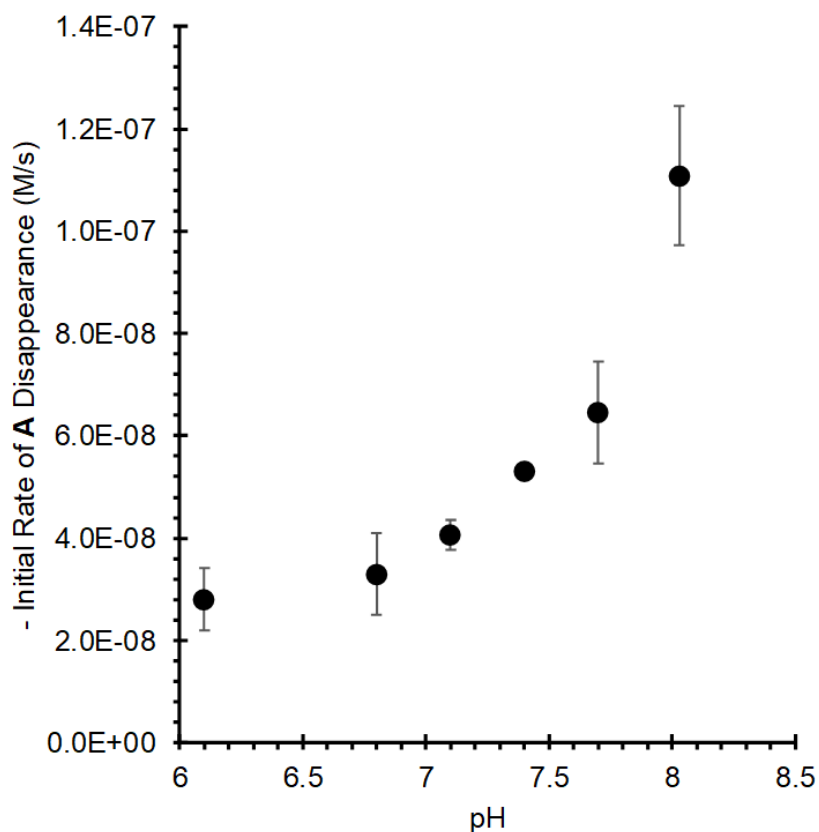
Figure 4.25. Plot of -Initial Rate (M/s) vs. pH. The initial rate is the measured rate of disappearance of **A** using its MLCT absorbance at 408 nm. All experiments were done with 40 µM [**A**]$_{initial}$ and 32 mM H_2O_2 at 37 °C in 0.118 M phosphate buffer solution. Each point is an average of 3-5 experiments, except pH 7.4. The y-axis error bars represent the sample standard deviation from the mean.

The total concentration of hydrogen peroxide, [H_2O_2]$_{total}$, was calculated based on dilution of 10.4 M H_2O_2, which was determined by iodometry of a Certified ACS grade Fischer Scientific 30 % w/v H_2O_2 bottle. The hydrogen peroxide in the buffered solution is present as H_2O_2 and HOO$^-$ (eq. 15), where this equilibrium constant expression (eq. 16) can represent [HOO$^-$] in equation 17, which leads to the relationship shown in equation 18 for [H_2O_2]$_{total}$.

$$K_a = \frac{[HOO^-][H^+]}{[H_2O_2]} \qquad \text{(15)}$$

$$[HOO^-] = \frac{K_a[H_2O_2]}{[H^+]} \qquad \text{(16)}$$

$$[H_2O_2]_{total} = [H_2O_2] + [HOO^-] \qquad \text{(17)}$$

$$[H_2O_2]_{total} = [H_2O_2] + \frac{K_a[H_2O_2]}{[H^+]} = [H_2O_2]\left(1 + \frac{K_a}{[H^+]}\right) \qquad \text{(18)}$$

The H_2O_2 present in buffered solution decreases relative to the conjugate base, HOO^- (equation 19 with decreased $[H^+]$ (increased pH).

$$[H_2O_2] = \frac{[H_2O_2]_{total}}{1 + K_a[H^+]^{-1}} = [H_2O_2]_{total}\frac{[H^+]}{[H^+] + K_a} \qquad \text{(19)}$$

therefore, can be written entirely in terms of the pH, K_a, and the initially added $[H_2O_2]_{total}$ (eq. 20).

$$[HOO^-] = \frac{K_a}{[H^+] + K_a} \times [H_2O_2]_{total} \qquad \text{(20)}$$

Combining eqs. 2 and 14 gives equation 21.

$$k_{obs} = k_1[H_2O_2] + k_2[HOO^-] \qquad \text{(21)}$$

which now can be rewritten as:

$$k_{obs} = \left(\frac{k_1[H^+] + k_2K_a}{[H^+] + K_a}\right)[H_2O_2]_{total} \qquad \text{(22)}$$

When the solution pH is much smaller than the pKa , i.e. when $[H^+] \gg K_a$, then eq. 22 simplifies to;

$$k_{obs} = (k_1 + \frac{k_2 K_a}{[H^+]})[H_2O_2]_{\text{total.}} \qquad (23)$$

Accordingly, a plot of k_{obs} (the initial rate/[A]) vs. $1/[H^+]$ yields a slope (m) equal to $k_2 K_a [H_2O_2]_{\text{total}}$ and a y-intercept (b) equal to $k_1 [H_2O_2]_{\text{total}}$ (Figure 4.26). Given the $[H_2O_2]_{\text{total}}$ = 32 mM and $K_a = 1.8 \times 10^{-12}$ M, the rate constant k_2 for the reaction of HOO$^-$ with **A** is 344 M^{-1} s^{-1}, while the rate constant k_1 for the reaction of H_2O_2 with **A** calculated from this data set is 2.48×10^{-2} M^{-1} s^{-1}. These data imply that hydroperoxyl anion is 13,000 times more reactive than hydrogen peroxide towards **A**.
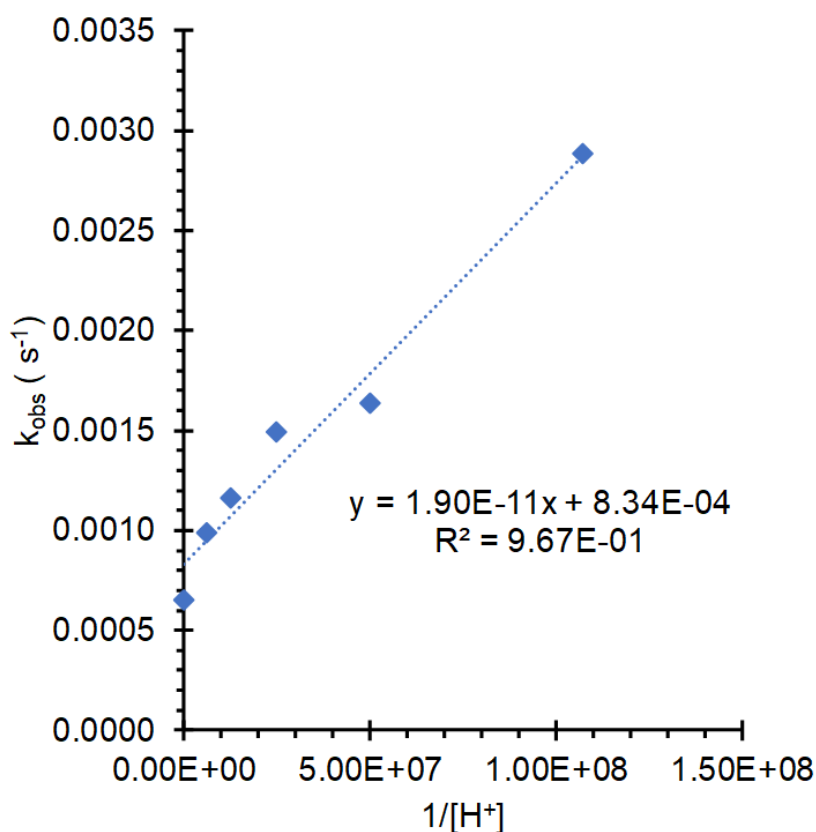
Figure 4.26. Plot of the initial rate/[A] (k$_{obs}$) vs. 1/[H$^+$]. k_{obs} was calculated using the starting concentration of *fac*-Mn(CO)$_3$(Br)(bpCO$_2$H). The proton concentration [H$^+$] was calculated from the measured pH. All points are averages of 3-5 experiments plotted in Figure 4.25. All experiments were done with 40 µM (**A**) and 32 mM H$_2$O$_2$ at 37 °C.

4.3.5. Probing for Hydroxyl Radical Production

Proton coupled one electron reduction of H_2O_2 leads to H_2O and HO·. The production of HO· can be tested using the probe molecule coumarin-3-carboxylic acid (3CCA). It is well established that the reaction of 3CCA with HO· leads to the formation of a fluorescent product, 7-hydroxycoumarin-3-carboxylic acid (7OH3CCA).[33] The rate constant for this reaction is reported as 6.8×10^9 M^{-1} s^{-1} with a conversion factor of 4.7% per mol of HO·.[34] The absorption spectrum for 7OH3CCA is red-shifted compared to 3CCA. Therefore, UV-vis absorption and fluorescence spectroscopy were used to evaluate hydroxyl radical formation in this reaction.

To establish whether this probe performs under our conditions, we first examined the temporal absorption changes of 86 µM 3CCA with 32 mM H_2O_2 and 45 µM $CuCl_2$. Copper(II) complexes have been extensively studied and are known to have catalytic H_2O_2 decomposition activity, and form HO· as an intermediate.[35] The UV-vis spectra on the right of Figure 4.27 show an increase in absorbance at 395 nm simultaneous with a decrease at 290 nm and 320 nm. An isosbestic point is apparent at 340 nm for the first 66 minutes of the reaction. This result indicates that, as expected, HO· is catalytically produced by $CuCl_2$ and hydroxylates 3CCA to form 7OH3CCA. The concentration of 7OH3CCA was 23 µM after 3 h reaction time based on its molar absorptivity coefficient at 395 nm (5×10^3 M^{-1} cm^{-1}).[34] The 7OH3CCA concentration reaches a maximum after 2 h and then decreases, since it is further oxidized by the generated hydroxyl radical.
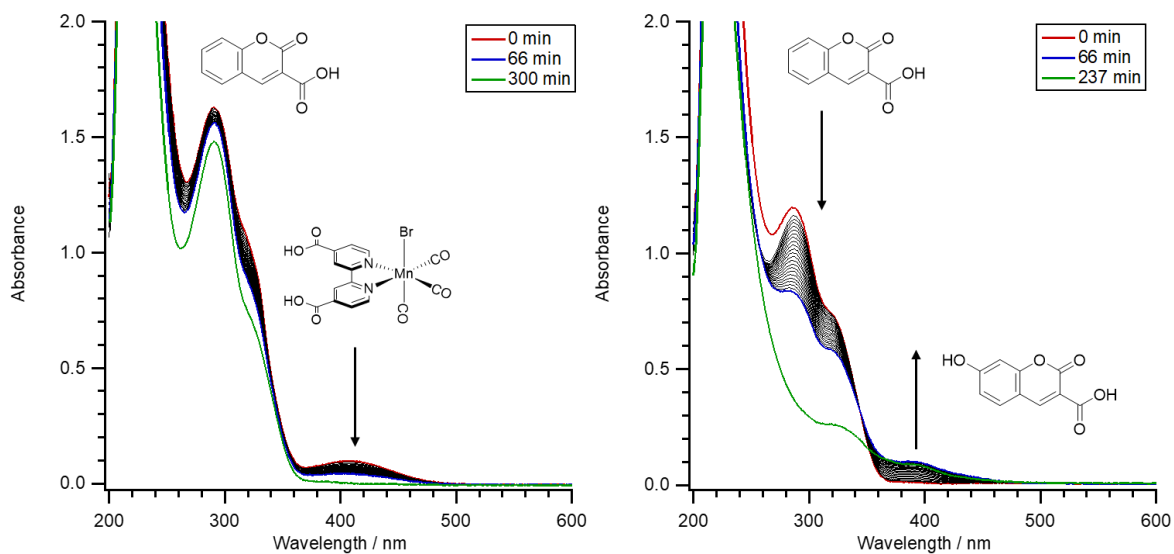
Figure 4.27. Temporal UV-Visible spectral changes of 86 µM coumarin-3-carboxylic acid and 32 mM H_2O_2 with 45 µM **(A)** (left) or 45 µM $CuCl_2$ at 25°C in 0.118 M phosphate buffered solution (pH = 7.4) (right).

The absorption spectra on the left of Figure 4.27 represents the reaction of **A** with H_2O_2 in the presence of 3CCA. The small decreases at 290 nm, 320 nm, and 408 nm are all associated with the disappearance of **A**. Additionally, the spectrum after 300 minutes is consistent with that for unreacted 3CCA, so it would appear that little or no hydroxyl radical is formed in this case. However, if the reaction with **A** formed only stoichiometric amounts of HO· (45 µM based on the [A]$_{initial}$), then only 2.1 µM 7OH3CCA (4.7 % yield) might be expected. Thus, the absorbance increase at 395 nm would only be 0.01, a value too low to quantify. Even so, this result shows **A** does catalytically decomposing H_2O_2 to form HO· via a pathway such as observed with Cu^{2+}.

Fluorescence spectroscopy would be a more sensitive method to determine if hydroxylation of 3CCA occurs during the reaction of H_2O_2 with **A**. Figure 4.28 shows that substantial increase in fluorescence signal (4.2×10^5 counts) was observed for the reaction of 32 mM H_2O_2 and 45 µM $CuCl_2$. The estimate amount of 7OH3CCA produced in this

221

reaction is 40 µM based on UV-Visible absorption changes. The increase in the fluorescence signal (4.2×10^4 counts) from the reaction of **A** with H_2O_2 was only 1/10th that from the $CuCl_2$ reaction with H_2O_2. When this value was corrected for the enhanced fluorescence signal (2.9×10^4 counts) from the control reaction of 3CCA with H_2O_2 alone it appears that at most ~1.3 µM 7OH3CCA is produced from the reaction of 45 µM **A** with 32 mM H_2O_2 Thus it is clear that the reaction of **A** with H_2O_2 does not catalytically produce HO· in the same way as Cu(II). However, this is only 0.7 µM smaller than we would expect from stoichiometric HO· from 45 µM **A**. If the rate constant for the reaction of HO· with **A** is greater than or equal to the rate constant for 3CCA hydroxylation ($k_{HO.} = 6.8 \times 10^9$ M^{-1} s^{-1}), then it may compete with 3CCA when the respective concentrations are similar.

He et. al hypothesized that the observed cytotoxicity of a $Mn(CO)_3(Br)bpy$-MOF was due to the catalytic production of HO· by Fenton-like chemistry.[6] The results shown in Figures 4.27 and 4.28 indicate that **A** does not react with H_2O_2 to produce catalytic quantity of HO· in phosphate buffered solution at 25 °C, in agreement with the conclusion of Tinajero-Trejo et. al regarding the reaction of $[Mn(CO)_3(tpa-\kappa^3N)]^+$ with H_2O_2 kept in the dark.[7]
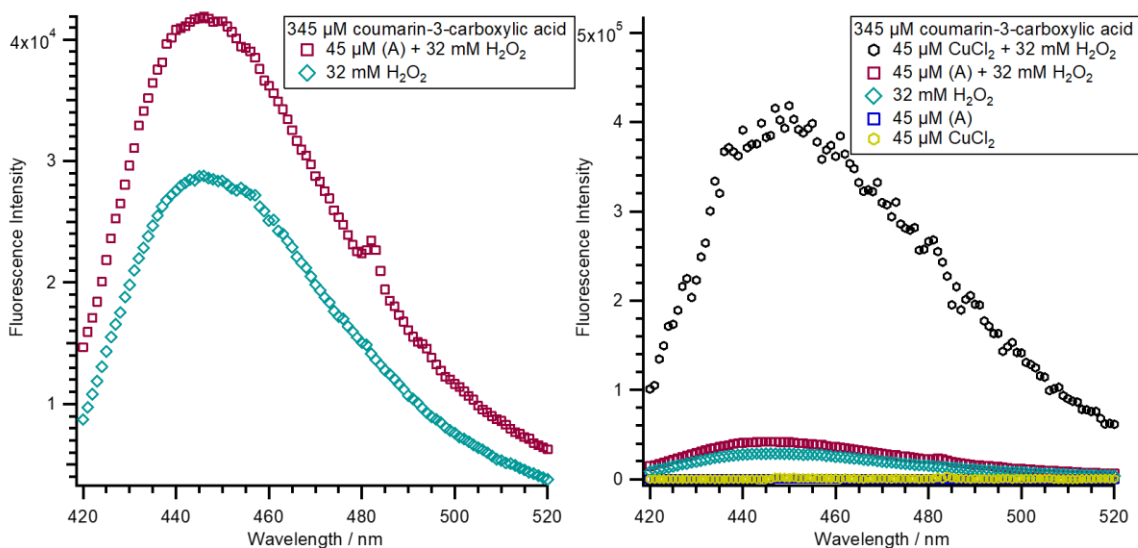
Figure 4.28. Emission spectra of reaction mixtures after 3 hours with 345 µM coumarin-3-carboxylic acid in 0.118 M Phosphate buffered solution at 25 °C under various conditions. black hexagons = 45 µM $CuCl_2$ and 32 mM H_2O_2, red squares = 45 µM **A** and 32 mM H_2O_2, green diamonds = 32 mM H_2O_2, blue squares = 45 µM **A**, and yellow hexagons = 45 µM $CuCl_2$.

4.3.6. Electrochemical Measurement of O_2 Production

Figure 4.29 displaces the cyclic voltammogram (CV) of **A** in deaerated phosphate buffered solution. An irreversible oxidation of **A** was observed at 0.76 V vs saturated calomel electrode (SCE) and an irreversible reduction at -1.11 V at 37 °C. I propose that the irreversible oxidation at 0.76 V corresponds to a single electron oxidation of *fac*-$Mn(CO)_3(Br)(bpCO_2H)$ (**A**). One electron oxidation of Complex **A** would form a low spin d^5 complex which should be stable but may spin crossover to the more substitution labile high spin d^5 configuration. The irreversible reduction at -1.11 V is typical for facial manganese(I) tricarbonyl complexes and is generally accepted as a one electron reduction localized on the π^* orbital of the ligand.[27] Since these waves are irreversible, a reduction potential for these couples cannot be determined accurately. However, the location of the reduction wave is consistent with literature measurements in 95/5 acetonitrile/water (-1.07 V).[24] Walsh and

223

coworkers studied complex **A** for catalytic CO_2 electroreduction and observed the first reduction wave at -1.07 V and a second reduction wave at -1.41 V vs. SCE.[24]
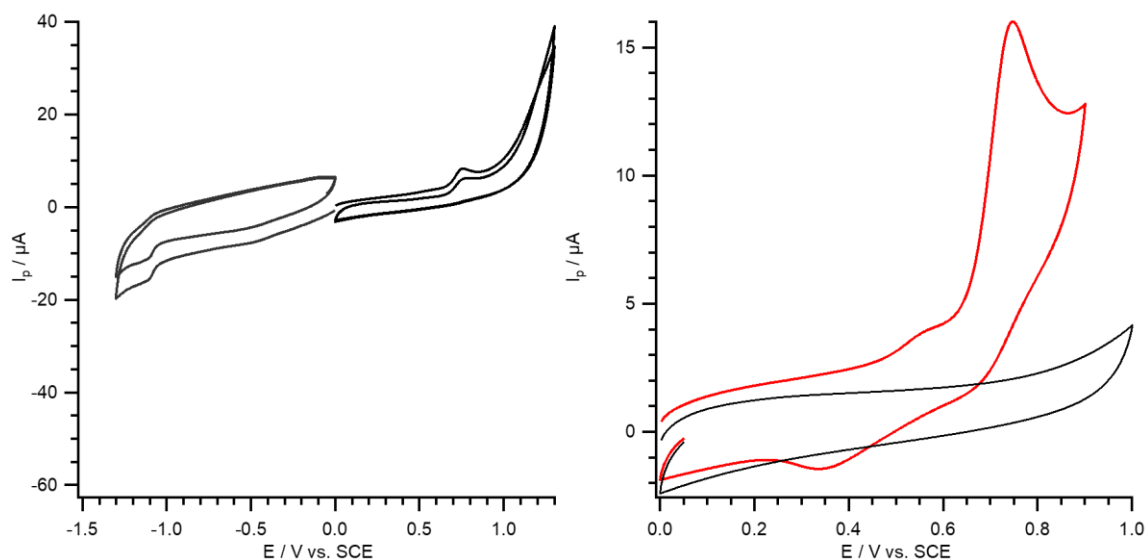

Figure 4.29. Cyclic Voltammogram (CV) of 150 µM **A** in deaerated 0.118 M phosphate buffered solution scanned twice at 20 mV/s from 0 to 1.3 and 0 to -1.6 (*left*). Single CV of 150 µM **A** in deaerated 0.118 M phosphate buffered solution, scanned at 50 mV/s from 0 to 0.85 V (red) and 0.118 M phosphate buffered solution scanned at 50 mV/s from 0 to 1.0 V (black) at 37 °C.

Half reaction reduction potentials are shown in Table 4.5. A qualitative examination of these literature potentials indicates that hydrogen peroxide is thermodynamically capable of oxidizing **A** by one or two electrons if it is assumed that the reduction potential for **A** is -0.76 V vs. SCE. The more positive reduction potential is the oxidizer in the redox reaction. For example, the 1-electron 1-proton reduction of H_2O_2 to form H_2O and HO· at pH 7.0 is 0.08 V vs. SCE which is more positive than the reduction potential for **A**. This qualitative assessment provides some insight on the feasibility of the redox reaction but does not mean these reactions are kinetically favorable.

Table 4.5. Half reactions reduction potentials of various peroxide species. The potentials pertaining to peroxide or oxygen species were taken from taken from Winterbourn[14] or Buettner[36]

Half Reaction	Reduction Potential (V vs. SCE)[a]
$HO\cdot + H^+ + e^- \longrightarrow H_2O$	2.07
$H_2O_2 + 2\ H^+ + 2\ e^- \longrightarrow 2\ H_2O$	1.54
$HOO\cdot + H^+ + e^- \longrightarrow H_2O_2$	0.82
$H_2O_2 + H^+ + e^- \longrightarrow H_2O + HO\cdot$	0.08

[a]Converted from potential vs. standard hydrogen electrode (SHE) measured at pH 7.0.

As mentioned earlier in this chapter, I observed a Mn(II) phosphate salt product by XRD and a Mn(II) species by EPR for the reaction of complex **A** with H_2O_2. The catalytic decomposition of H_2O_2 through disproportionation to H_2O and O_2 has been shown to be catalyzed by Mn(II) salts.[37,38] In this reaction, H_2O_2 is simultaneously oxidized to O_2 and reduced to H_2O.

$$2\ H_2O_2 \longrightarrow 2\ H_2O + O_2$$
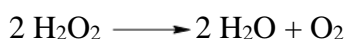
I hypothesized that a Mn(II) intermediate or product in the reaction of complex **A** with H_2O_2 could catalyze this disproportionation and thus result in O_2 formation. Oxygen can be electrochemically reduced to H_2O_2 in aqueous conditions. On a glassy carbon electrode (GCE) this reduction reaction typically occurs around -0.5 V vs. SCE thus a potential window between 0 and -0.85 V is sufficient for qualitatively measuring oxygen.

$$O_2 + 2\ e^- + 2\ H^+ \longrightarrow H_2O_2 \quad \text{(at the electrode surface)}$$
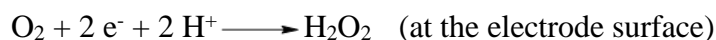
The rate of oxygen formation was first examined using cyclic voltammetry with a macroelectrode (Figure 4.30) at 37 °C in aqueous pH 7.4 phosphate buffer solution. First, a solution of 150 µM **A** was purged with nitrogen to remove atmospheric oxygen. The red cyclic voltammogram in Figure 4.30 shows the current measured with a potential window of

0 to -0.85 V. Only capacitive current from the phosphate buffer is observed and there is no peak, indicating that no O_2 is present in this solution before the addition of 15 mM H_2O_2. The blue cyclic voltammogram in Figure 4.30 was obtained after the addition of 15 mM H_2O_2, and the observed reductive wave reflects trace amount of O_2 added as a consequence of using unpurged hydrogen peroxide solutions. After 5 minutes (green voltammogram), a more well-defined peak with maximum current (I_{max}) around -0.55 V was observed. The peak observed at about -0.55 V corresponds to the 2-electron, 2 proton reduction of O_2 to H_2O_2 on the bare GCE. Based on this experimental setup it can be concluded that the additional O_2 present in the solution is generated during the reaction of H_2O_2 with **A**. The Randles-Sevcik equation was used to calculate $[O_2]$ in the solution based on the observed peak current (I_p) (eq. 24).[39] The charge transfer coefficient (α) was determined to be 0.25 via Tafel analysis.[39] The charge transfer coefficient (α) used to calculate $[O_2]$ in eq. 24 was determined by a Tafel plot (Figure 4.30). The natural logarithm of absolute current measured (*ln* $|I|$) versus the potential (-E /V vs. SCE) for the CV of 150 µM **A** with 15 mM H_2O_2 after 18 minutes was used in the Tafel plot. A linear region between 15 and 50 % of the peak current (Figure 4.31 inset) yields a slope of that is proportional $\alpha F/RT$. In this relationship F is the Faraday constant (96485 s A/mol), R is the gas constant (8.314 J K^{-1} mol^{-1}), and T is the temperature of the measurement (310.15 K). The α is reflective of the transition state in an electrochemical redox reaction. If α is >0.5, the transition state resembles the product more than the reactant and if α is <0.5 the opposite is true.
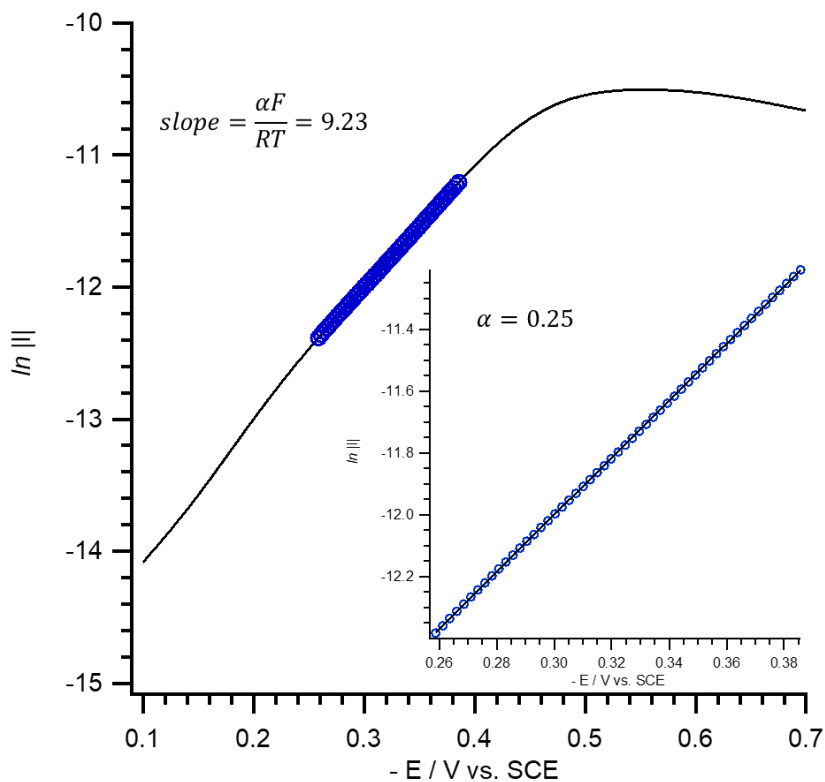
Figure 4.30. Tafel plot for cyclic voltammogram of 150 µM **A** with 15 mM H_2O_2 in deaerated 0.118 M phosphate buffered solution scanned at 50 mV/s from 0 to -0.85 V after 18 minutes at pH 7.4 and 37 °C.

A plot of the peak current versus time yields a slope that describes the change in current as a function of time, dI_p/dt, and thus proportional to the change in O_2 concentration over time, $d[O_2]/dt$, by eq. 25. The rate of oxygen formation calculated from the data in Figure 4.30 was 8.60×10^{-7} M/s. The initial rate of disappearance for 150 µM **A** under similar conditions (16 mM H_2O_2, pH 7.4 and 37 °C) was determined to be 1.2×10^{-7} M/s based on the change in MLCT absorbance of complex **A**. However, there are some inherent disadvantages to using a macroelectrode to quantify oxygen. The measurement itself takes time (50 mV/s scan rate) and the reaction in the bulk occurs on a similar timescale. Furthermore, the current measured on a macroelectrode is sensitive to mass transport as the

size of the diffusion layer changes over the course of the scan. The imprecision of this method is visually apparent by the scatter in the points in Figure 4.31.

$$I_p = n\, 2.99 \times 10^5 \sqrt{\eta + \alpha}\, D^{1/2} A v^{1/2} [O_2]$$

(24)

$$\frac{dI_p}{dt} = n\, 2.99 \times 10^5 \sqrt{\eta + \alpha}\, D^{1/2} A v^{1/2} \frac{d[O_2]}{dt}$$

(25)

$$2.44 \times 10^{-8} \frac{Ampere}{s} = (2\,e^-)(2.99 \times 10^5)\sqrt{0.25}\left(1.9 \times 10^{-9}\frac{m^2}{s}\right)^{\frac{1}{2}}(7.1 \times 10^{-6} m^2)(0.05)^{1/2}\frac{d[O_2]}{dt}$$

$$\frac{d[O_2]}{dt} = rate\ of\ O_2\ formation = 8.60 \times 10^{-4}\frac{mM}{s} = 8.60 \times 10^{-7}\frac{M}{s}$$
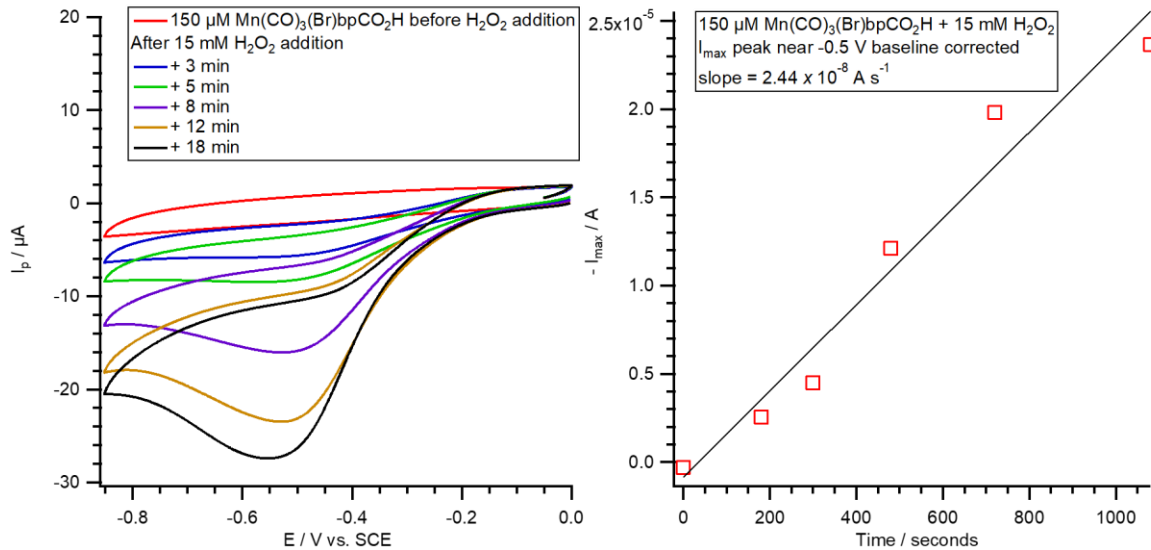
Figure 4.31. *Left*: Cyclic voltammograms of 150 µM **A** with 15 mM H₂O₂ in deaerated 0.118 M phosphate buffered solution scanned at 50 mV/s from 0 to -0.85 V after varying amounts of elapsed reaction time (single scan for each time point). *Right*: Plot of the $-I_p$ for the peak at about -0.55 V versus time in seconds at pH 7.4 and 37 °C.

Thus, the rate of oxygen formation was also quantitatively examined using microelectrode chronoamperometry (Figure 4.32) at 25 °C in aqueous phosphate buffer

solution. For these experiments the potential of the cell was held at -0.8 V vs. SCE. This is to ensure that the electrochemical reduction of O_2 to H_2O_2 is at a steady state. The solution was kept at 25 °C outside of the Faraday cage and then transferred inside to avoid electrical noise from the stir plate. Two key advantages to using a microelectrode are the static diffusion layer due to radial diffusion and the ability to constantly measure current at high time resolution (in this case 1s). These two factors largely eliminate any lag time between the bulk reaction and the electrochemical measurement. First, the current was measured for a solution of 32 mM H_2O_2 over 900 seconds (black Figure 4.32) to obtain a baseline measurement of atmospheric O_2. The temporal current measured for 70 µM **A** and 32 mM H_2O_2 under aerobic conditions (purple, Figure 4.32) shows a higher initial current and a steeper current increase. The observed higher initial current (0-60 seconds, purple Figure 4.32) may be due to rapid formation of O_2 in the initial stages of the reaction. Subtraction of the black and purple traces gives a difference (red) which corresponds to oxygen formation exclusively as a result of the reaction of complex **A** with H_2O_2. The measured current at a set time can be used to calculate $[O_2]$ by eq. 26.[39] The slope of the red trace gives the change in measured current (dI_p) as a function of time (dt). This value was used to calculate the rate of O_2 formation using eq. 27. In this relationship, the number of electrons transferred is 2, F is the Faraday constant (96485 s A/mol), D is the diffusion coefficient of O_2 (1.9×10^{-9} m^2 s^{-1})[40], and r is the experimentally determined radius of the carbon fiber microelectrode (4.6 µm). The rate of oxygen formation calculated from the data in Figure 4.32 was 1.09×10^{-7} M/s. The initial rate of disappearance for 70 µM **A** under similar conditions (32 mM H_2O_2, pH 7.4, and 25.5 °C) was 0.4×10^{-7} M/s based on the change in MLCT absorbance of complex **A**.

$$I_p = 4\,n\,F\,D\,r[O_2]$$

(26)

$$\frac{dI_p}{dt} = 4\,n\,F\,D\,r\,\frac{d[O_2]}{dt}$$

(27)

$$7.35 \times 10^{-13}\,\frac{Ampere}{s} = (4)\,(2)\,(96485\,\frac{s\,A}{mol})\,(1.9 \times 10^{-9}\,\frac{m^2}{s})(4.6 \times 10^{-6}m)\,\frac{d[O_2]}{dt}$$

$$\frac{d[O_2]}{dt} = rate\ of\ O_2\ formation = 1.09 \times 10^{-4}\,\frac{mM}{s} = 1.09 \times 10^{-7}\,\frac{M}{s}$$
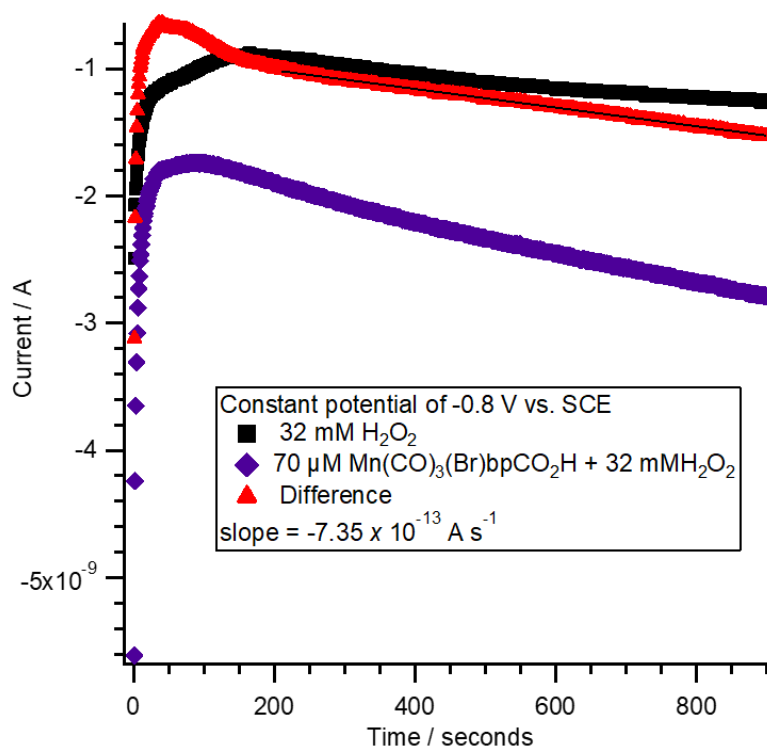
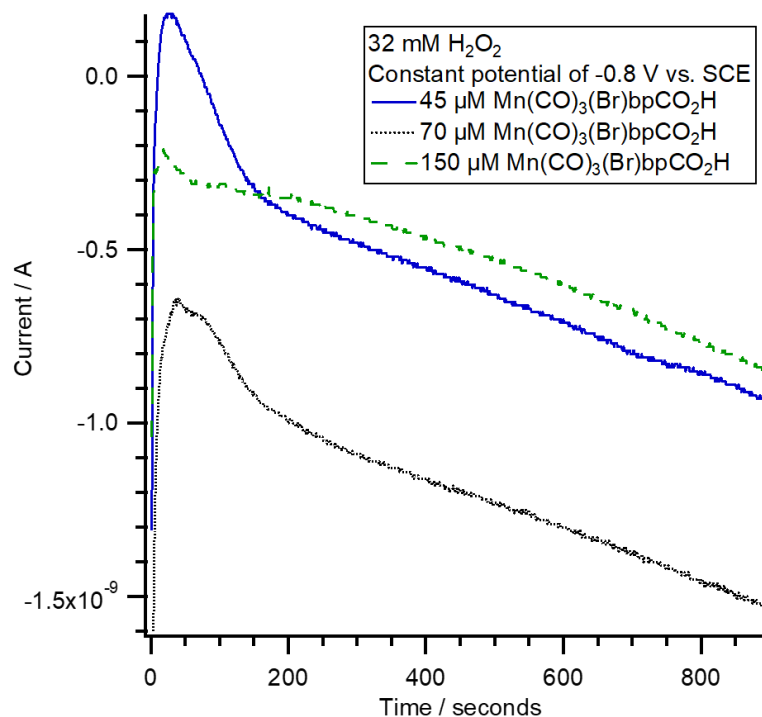**Figure 4.32.** Chronoamperometry for reaction of 70 µM **A** with 32 mM H_2O_2 at 25 °C in 0.118 M phosphate buffered solution. The cell is held at a constant potential of -0.8 V. Black = only 32 mM H_2O_2, purple = 70 µM **A** with 32 mM H_2O_2, and red = the difference between black and purple. The linear fit of the red data set gave the slope -7.35 × 10^{-13} A/s.

The rate of O_2 formation determined by microelectrode chronoamperometry (70 µM

A, 32 mM H_2O_2, pH 7.4, and 25 °C) was 2.8 times faster compared to the rate of initial

depletion of **A** under similar conditions (73 µM **A**, 32 mM H_2O_2, pH 7.4, and 25.5 °C). The

catalytic disproportionation of H_2O_2 should be second order with respect to $[H_2O_2]$ and zero

order with respect to complex **A**. The rate of O_2 formation was examined as a function of the

concentration of **A** as shown in Figure 4.33. When the reaction of 45 and 150 µM **A** with 32

mM H_2O_2 at 25 °C in phosphate buffered solution were compared to 70 µM **A**, it was found

that the change in measured current from 200 seconds to 900 seconds was the same. The

difference between these three measurements was in the initial 0-200 seconds of the

measurement.

Figure 4.33. Chronoamperometry for reaction of 45-150 µM **A** with 32 mM H_2O_2 at 25 °C in 0.118 M phosphate buffered solution. The cell is held at a constant potential of -0.8 V. Blue line = 45 µM **A** with slope 7.12×10^{-13} A/s, dotted black line = 70 µM **A** with slope 7.35×10^{-13} A/s, Dotted green = 150 µM **A** with slope 7.64×10^{-13} A/s.

These electrochemical experiments illustrate that O_2 is formed from the reaction of **A**

with H_2O_2. This is presumably via the catalytic decomposition of H_2O_2 which has been

231

demonstrated by non-metal carbonyl Mn(II), Mn(III), and Mn(IV) complexes in the literature.[41]

4.3.7. Proposed Reaction Mechanisms

Mechanism studies of H_2O_2 reactions of Mn(II)-(IV) (non-carbonyl) complexes with have been previously reported.[41-43] For example, Salem et al. proposed that a ligand substitution is the first step in the reaction of Mn(II) Schiff base complexes with H_2O_2.[42] Manganese(IV)-oxide complexes have been shown to perform triflic acid (HOTf) assisted O-atom transfers to alkenes by an outer sphere electron transfer followed by an $O^{\cdot-}$ transfer.[44] However, to my knowledge, there have been no quantitative mechanistic investigations of the H_2O_2 reaction with Mn(I) carbonyl complexes in the literature. In this section, plausible mechanisms for the latter reaction will be discussed as well as how the experimental data supports or opposes them.

One such plausible reaction pathway is initiated by an outer sphere electron transfer (Scheme 4.2). The one-electron oxidation of **A** would form the Mn(II) species **A1**. Concurrently, H_2O_2 would be reduced to HO^- and $HO\cdot$. Complex **A1** is postulated to be a d^5 Mn(II) species that would be expected to readily undergo substitution of the carbonyl ligands, resulting in Mn^{2+}, 3 CO, and $bpCO_2^-$ as products, although it is possible that the $Mn(II)(bpCO_2^-)$ unit may stay intact. The $HO\cdot$ radical has several likely pathways. Aside from water, H_2O_2 is the highest concentration reactant in solution, and under these conditions, it is probable that $HO\cdot$ would react with H_2O_2 to form hydroperoxyl radical $HOO\cdot$ plus H_2O. The rate constant for this second order reaction is 2.7×10^7 M^{-1} s^{-1} as measured by pulse radiolysis experiments.[45] The resulting $HOO\cdot$ radical may react with a carbonyl on **A** to give (formally) a Mn(II) hydroperoxylcarbonyl complex. Protonation of the

hydroperoxylcarbonyl would lead to **A2** and water. Dissociation of CO_2 from **A3** leads to a dicarbonyl Mn(II) species **A4** which will exchange the rest of its ligands with water to give Mn(II), 2 CO, and $bpCO_2^-$. An alternative pathway for the decay of HOO· would be disproportionation to H_2O_2 and O_2 ($k_{dis} = 8.3 \times 10^5$ M^{-1} s^{-1}).[46] However, given that this would be the second order reaction of a low concentration transient intermediate, such disproportionation is unlikely to play a major role in the mechanism. The steps depicted in Scheme 4.2 predict the release of 5 CO's and formation of one CO_2 for every 2 molecules of **A** reacted, 3 COs from dissociation from complex **A1** and 2 COs plus a CO_2 from the dissociation of complex **A4**. This reaction would also be overall second order, first order in **A** and first order in H_2O_2. Presumably some of the HO· generated in the first step may be trappable with a probe such as 3CCA; however, the success of such trapping would depend on the relative concentrations of H_2O_2 and 3CCA and the rate constants of the competing reactions. The rate constants for HO· have been measured by pulse radiolysis of water, where the reaction between 2 HO· molecules is $k_{2HO·} = 1.1 \times 10^{10}$ M^{-1} s^{-1} and with H_2O_2 is $k_{2HO·} = 2.7 \times 10^7$ M^{-1} s^{-1}.[45] Scheme 4.2 also predicts the formation of Mn(II) as was observed, and the resulting Mn^{2+} would be expected to catalyze disproportionation of H_2O_2 to O_2 and H_2O.[37,38] Thus the stoichiometry of Scheme 4.2 agrees with the products observed for this reaction, although the trapping experiments designed to identify the hydroxyl radical intermediate gave, at best, an ambiguous answer. An argument against the mechanism outlined in Scheme 4.2 would be that, if it is assumed that both H_2O_2 and its conjugate base the hydroperoxyl anion react with **A** through the same outer sphere oxidation mechanism, HOO^- should be less, not more, reactive given that H_2O_2 is the better oxidant (higher reduction potential).[47] The standard reduction potential for $HOO^- + H_2O + 2 e^- \rightleftharpoons 3 HO^-$ is

0.88 V and for $H_2O_2 + 2H^+ + 2$ e$^-$ $\rightleftharpoons$ 2 H_2O is 1.78 V vs. standard hydrogen electrode (SHE).[47]
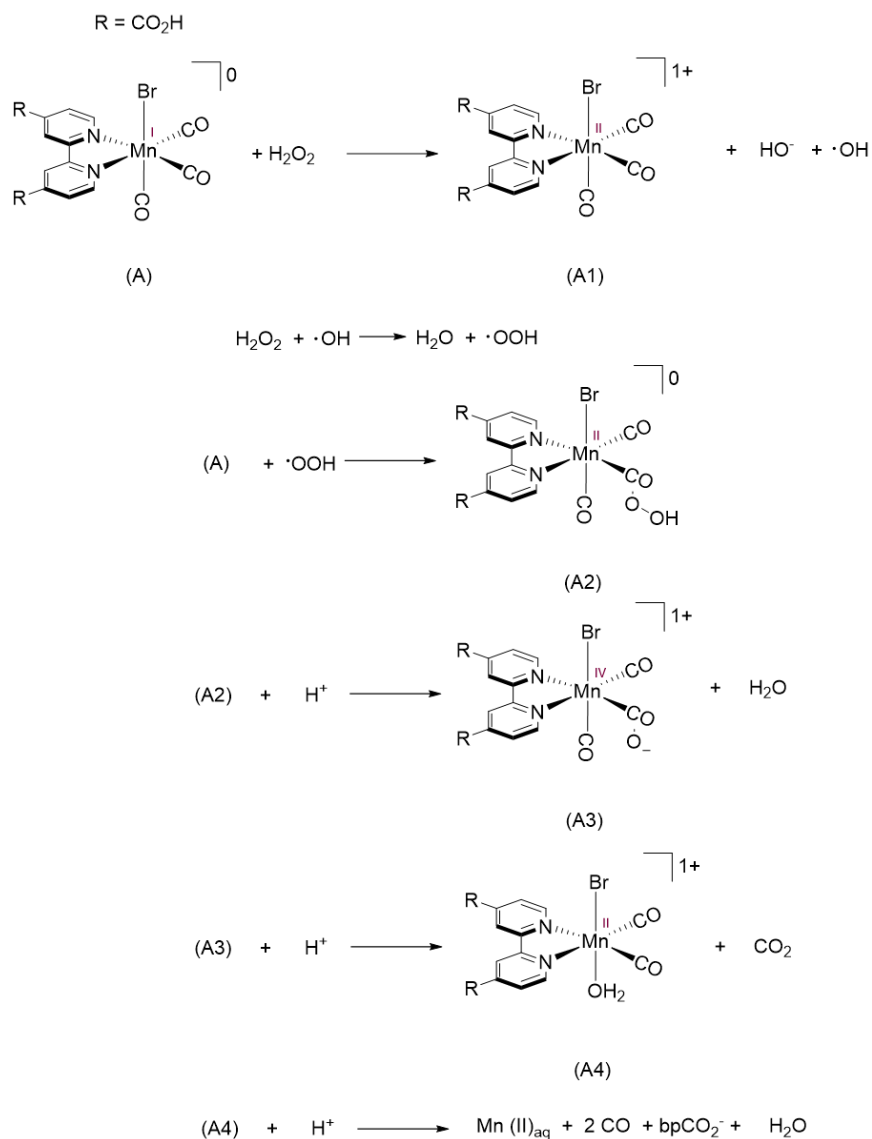
Scheme 4.2. Proposed mechanism for the initial outer sphere electron transfer from **A** to H_2O_2. This reaction pathway assumes hydroxyl radical reacts with hydrogen peroxide to form hydroperoxyl radical. Then HOO· reacts with a carbonyl to give a hydroperoxyl carbonyl complex.

(A5)

(A6)

(A7)
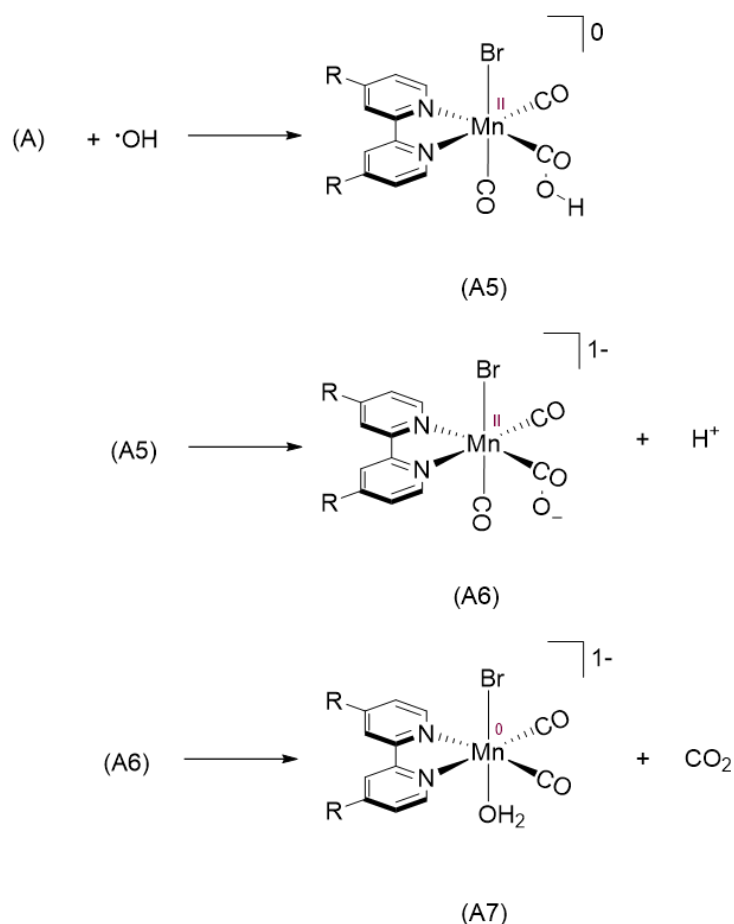
Scheme 4.3. Proposed Mechanism for the initial outer sphere electron transfer from **A** to H_2O_2. This reaction pathway assumes hydroxyl radical reacts with **A** which is unlikely in large excess of H_2O_2

Scheme 4.3 examines another possible fate of the hydroxyl radical if formed by the direct reaction of A with H_2O_2 as in the first step of Scheme 4.2, namely reaction of HO· with a carbonyl on **A** to form a hydroxy carbonyl species **A5**. We consider this reaction is less likely than trapping by H_2O_2, since the latter is 200 times more concentrated than **A**. Deprotonation of the hydroxy carbonyl would give **A6,** which can dissociate CO_2 to form a d^7 Mn(0) species **A7**. This species should readily exchange at least some ligands with water due to the Jahn-Teller distortion of low spin d^7 complexes. The net products from this hypothetical sequence would be 2 CO, 1 CO_2, and Mn(0), which would be oxidized by

H$_2$O$_2$. Notably we would expect to see the same gas composition (5 CO's: 1 CO$_2$ per 2 equivalents **A**) as Scheme 4.2.

Another plausible reaction pathway would be an inner sphere redox reaction beginning with ligand substitution (Scheme 4.4). The substitution of bromide on **A** would give a hydroperoxyl Mn(I) species **A8** as well as a proton and the displaced ligand. Inner sphere electron transfer from the Mn to the hydroperoxyl group in **A8** could lead to hydroxide (HO$^-$) via heterolytic cleavage and a Mn(III)O complex **A9**. We would expect 3 CO, bpCO$_2$H, and a Mn(III) product. This Mn(III) product could further react with H$_2$O$_2$ to form HOO· and Mn(II). While unlikely, the inner sphere electron transfer on **A8** results in homolytic cleavage of the O-O bond, the products would be **A10** and HO·. Either of these radicals could react with a carbonyl as shown in Schemes 4.1 and 4.2. Therefore we might expect the same gas products in both cases, 5 CO and 1 CO$_2$ per 2 molecules of **A**. The reaction rate increased as pH increased, which is expected if associative ligand substitution is the initial reaction pathway since HOO$^-$ is a better nucleophile. Furthermore, we would expect the OTf complex **B** to react faster and the pyridine complex **C** to react slower. The results shown in Figure 4.17 and Figure 4.21 confirm the expectations for reaction with **B** and **C** and therefore support a substitution reaction mechanism.
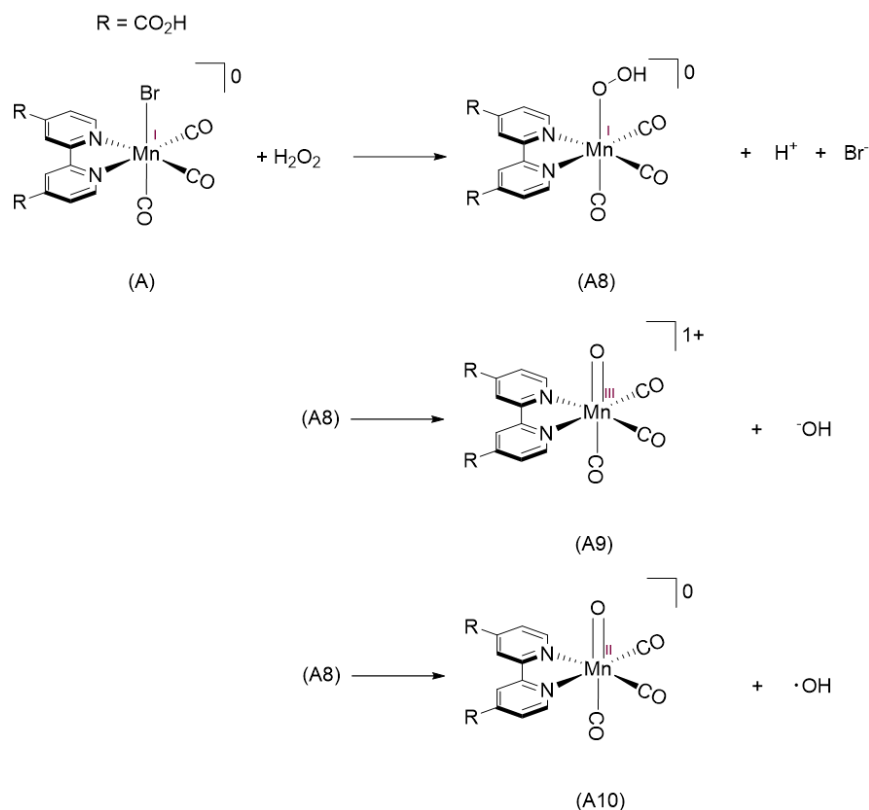
Scheme 4.4. Proposed Mechanism for the initial outer sphere electron transfer from **A** to H_2O_2.

All three scenarios predict the reaction stoichiometry, so the product ratios do not differentiate between these proposed mechanisms. However, many of the experiments suggest a substitution mechanism rather than an outer sphere redox pathway. The ligand substitution mechanism is supported by the increased reaction rate at higher pH, increased rate for the triflate complex **B**, and the decreased rate for the pyridine complex. The UV-vis and fluorescence data for 3CCA hydroxylation imply that little or no free HO· is formed. The bulk of evidence supports the substitution initiated sequence suggested by Scheme 4.4. However, it is unlikely that this reaction proceeds via a single reaction pathway, especially if HO· and HOO· are involved. The electrochemically measured O_2 formation supports a Mn(II) product as catalytic disproportionation of H_2O_2 to H_2O and O_2 is known to occur over

Mn(II). However, this is a secondary consequence of the oxidation of **A** to Mn^{2+} and does not discriminate between the outer and inner sphere redox mechanisms.

4.4. Conclusions

4.4.1. Experimental Summary

The experimental data strongly argues in favor of an inner sphere pathway for the reaction of **A** with H_2O_2. The 365 nm photolysis experiments indicate that there is a difference in the photochemical reaction in aerobic versus anaerobic aqueous media. Near-quantitative CO release (2.8 molecules of CO per molecule of **A** depleted) was observed in anaerobic conditions, but only 1.9 molecules of CO per molecule of **A** depleted were observed in aerobic conditions. Presumably 1 molecule of CO_2 is released per molecule of **A** depleted. The IR and UV-visible spectral changes show that **A** is consumed in its reaction with H_2O_2. Furthermore, ~2.5 molecules of CO and 0.5 molecules of CO_2 per molecule of **A** consumed were measured by GC-TCD after complete reaction (24 hours followed by 3 M H_3PO_4 addition). From the XRD analysis of the white precipitate, ^1H NMR spectra, and EPR spectra it can be inferred that **A** is oxidized from Mn(I) to Mn(II) in the reaction with H_2O_2. The increased observed rate constant for the reaction of H_2O_2 with *fac*-Mn(CO)$_3$(OTf)(bpCO$_2$H) and the decreased observed rate constant for *fac*-Mn(CO)$_3$(C$_5$H$_5$N)(bpCO$_2$H) suggest the reaction proceeds via a ligand substitution, inner sphere pathway. The reaction was shown to be first order in both **A** and H_2O_2 and a second order rate constant of 4.67×10^{-2} M^{-1} s^{-1} was determined at 37 °C. The enthalpy of activation ($\Delta H^\ddagger$) was 93 ± 12 kJ/mol and entropy ($\Delta S^\ddagger$) was 30 ± 12 J/mol. The positive entropy of activation suggests a dissociative mechanism where the rate determining step is the breaking

of a chemical bond. The marked increase in reaction rate as pH was increased for the reaction of **A** with H_2O_2 suggests that hydroperoxide anion, HOO^-, also plays a major role even at pH 7.4. UV-visible and fluorescence spectroscopy with 3CCA showed little or no catalytic $HO\cdot$ production from H_2O_2 reaction with **A**, however stoichiometric $HO\cdot$ production could not be eliminated with these experiments. Electrochemical measurements revealed that O_2 is produced on the same timeframe as **A** is consumed with H_2O_2.

4.4.2. Broader Implications

Since the experimentally determined 2nd order rate constant for the aforementioned reaction was 4.7×10^{-2} M^{-1} s^{-1} and intracellular H_2O_2 is in the nM-µM range, this reaction is unlikely to cause peroxide radical triggered physiological effects.[15] Poole and coworkers observed $HO\cdot$ production from 365 nm irradiation of a Mn(I) carbonyl but none without irradiation.[7] Furthermore, there was little or no $HO\cdot$ detected from the reaction of **A** with H_2O_2; therefore, it is unlikely that Mn(I) carbonyls will undergo Fenton-like reactions with H_2O_2 unless irradiated with light. The anticancer and antimicrobial effects of Mn(I) tricarbonyl complexes like **A** is potentially caused by the released CO's interaction with haem-containing proteins crucial to cellular respiration.[48] The CO binding of essential haem-containing enzymes like cytochrome C oxidase could result in the incomplete reduction of O_2 to H_2O and thus the generation of reactive oxygen species. Furthermore, the co-depleted CORM may result in cytotoxicity from reactions with various cellular components.[3] While complex **A** (or its products) does not appear to catalytically produce $HO\cdot$, intercellular CO release in the 100-300 µM range would likely have a substantial impact on cellular respiration and thus the generation of reactive oxygen species.[10] Both H_2O_2 and light are effective triggers for CO (and CO_2) release from **A**. However, the biological effects of **A** and

similar Mn(I) tricarbonyls are presumably due to downstream effects of the released CO and metal ion, rather than Fenton-like catalysis[49] by the CORM.

4.5. Future Work

More research is necessary to understand the reaction pathways of Mn(I) carbonyls with H_2O_2 before they can effectively be used as therapeutics. Gas release profiles and kinetic characterization of all complexes are crucial to our understanding in the efficient therapeutic usage and observed effects of CORMs.[2] In this chapter the characterization of products and the kinetics gave insight on the reaction of **A** with H_2O_2 and how this may be applied therapeutically. Further research to identify intermediates may aid in the mechanistic understanding of this reaction. Time-resolved infrared spectroscopy studies may facilitate the observation of a metal hydroperoxyl carbonyl or carboxyl intermediate. Spectroelectrochemical infrared experiments could also facilitate the comparison electrochemical oxidized and chemically oxidized *fac*-Mn(CO)$_3$(Br)(bpCO$_2$H) intermediates and products. Spin trapping of any produced radicals may facilitate differentiation between proposed reaction pathways. For instance, the comparison between photochemically produced radicals and radicals generated from chemical/electrochemical oxidation may identify intermediates that could help to eliminate reaction pathways. Selective detection of HOO· over HO· may also help in the evaluation of the reaction mechanism. Furthermore, these experiments do not examine where the origin of the O-atom on the CO_2 molecule. Experiments with isotopically labeled hydrogen peroxide, water, or oxygen may help to elucidate the reaction pathways.

4.6. Experimental Methods

4.6.1. Materials

Bromopentacarbonylmanganese(I) (98 %) was purchased from Strem Chemicals. Silver trifluoromethanesulfonate (≥99 %) was purchased from Sigma-Aldrich. 4,4'-dicarboxy-2,2'-bipyridine (98 %) and phosphoric acid (85 %) were purchased from Fischer Scientific. Toluene, methanol, diethyl ether, dichloromethane, acetonitrile and tetrahydrofuran were purchased from Fischer Scientific, dried with 3Å molecular sieves, and stored in an Argon glovebox. Dimethyl sulfoxide, dibasic sodium phosphate, and monobasic potassium phosphate were purchased from Fischer Scientific. H_2O_2 (30%, Certified ACS) was purchased from Fischer Scientific and titrated using the iodometric method to determine a concentration of 10.4 M. In all cases diluted solutions were made using 18 MΩ·cm resistivity deionized water. All deuterated solvents were purchased from Cambridge Isotope Laboratories. Carbon monoxide, carbon dioxide, nitrogen, argon, and helium gas cylinders were purchased from Praxair.

4.6.2. Syntheses

The *fac*-Mn(CO)$_3$(Br)(bpCO$_2$H) complex (**A**) was synthesized using literature methods.[24] A methanol solution of L (4,4'-dicarboxy-2,2'-bipyridine) was added to a toluene solution of bromopentacarbonylmanganese(I) and refluxed 2 hours under an argon atmosphere. The color of the solution changes from orange to red after an hour and precipitates a red solid when stored at 10 °C overnight. The crude product was washed with cold diethyl ether and dichloromethane. The bright red powder was analyzed by ^{1}H NMR, IR, UV-Vis and CHN analysis to ensure purity. ^{1}H-NMR (500 MHz, DMSO-d$_6$): δ (ppm)

8.10 (d, 2H), 9.04 (s, 2H), 9.40 (d, 2H). ^{1}H-NMR (500 MHz, D_2O): δ (ppm) 7.97 (d, 2H), 8.70 (s, 2H), 9.36 (d, 2H) (Appendix C Figure S4.2). FTIR (95:5 $DMSO/H_2O$) 2023, 1933, 1920 cm^{-1}. Calculated CHN analysis for $C_{15}H_8BrMnN_2O_7 \cdot H_2O$: C, 37.45; H, 2.10; N, 5.82. Found: C, 37.04; H, 2.34; N, 4.95. The NMR, IR, and UV-vis spectra observed were consistent with Cowan et al.[24]

fac-$Mn(CO)_3(OTf)(bpCO_2H)$ was synthesized by triflate exchange of **A**. Complex **A** 0.195 mmol (90.1 mg) was dissolved in 100 mL of dry THF. Approximately 51 mg of Ag(OTf) was dissolved in 3 mL of dry THF and added dropwise to the solution of **A**. The solution changed from a transparent orange-red to cloudy yellow immediately and was stirred for 2 hours. The mixture was centrifuged to remove the AgBr solid and concentrated by rotary evaporation. The solution was slowly added to 30 mL of diethyl ether and centrifuged to obtain the solid. The solid yellow powder was dried in vacuo and used as is. ^{19}F-NMR spectra indicated the *fac*-$Mn(CO)_3(OTf)(bpCO_2H)$ was successfully made. ^{1}H-NMR (400 MHz, DMSO-d_6): δ (ppm) 8.92 (s, 2H), 8.85 (s, 2H), 7.91(s, 2H) (Appendix C S4.3). ^{19}F-NMR (400 MHz, DMSO-d_6): δ (ppm) -77.79 (Appendix C S4.4).

4.6.3. UV-Vis Spectroscopy

The change in absorbance at 408 nm as a function of time was measured using a Shimadzu UV-2401PC Spectrophotometer. This absorbance corresponds to a MLCT of the *fac*-$Mn(CO)_3(Br)(bpCO_2H)$ complex and is used to determine its rate of disappearance. The initial rates were determined by linear regression of the first 5 % decrease in absorbance. All stock solutions are made in 0.118 M aqueous phosphate buffer. A 50-200 µL aliquot of a 1.9 mM *fac*-$Mn(CO)_3(Br)(bpCO_2H)$ stock solution and 2100-2250 µL aliquot of 0.118 M aqueous phosphate buffered solution were added to a cuvette and allowed to acclimate in the

UV-Vis cell holder for 15 minutes. Then, a 20 µL aliquot of H_2O_2 stock solution was added to give a final concentration of 8, 16, or 32 mM H_2O_2 in the cuvette depending on the desired conditions.

4.6.4. Gas Chromatography

Carbon monoxide and carbon dioxide release from $Mn(CO)_3(Br)(bpCO_2H)$ were quantified using an Agilent 6890N (G1530N) Gas Chromatograph System equipped with a thermal conductivity detector (GC-TCD). Chromatographic separation of gases was done with a Sigma-Aldrich Carboxen-1006 Capillary Column (30 m × 0.32 mm with average thickness 15 µm). Samples were obtained from a using a gas tight syringe to sample the headspace of a screw-top septum quartz cuvette and injected into the inlet in splitless mode. The inlet pressure and temperature were 0.05 bar and 225 °C. The carrier gas, helium, was set at a constant flow rate of 1 mL/min. The column temperature was held at 35 °C for 20 minutes, then ramped to 250°C at 10 °C/min where it was held for 25 minutes. The thermal conductivity detector was set at 230 °C with a 12 mL/min reference flow rate and 7 mL/min He makeup flow rate. Gas phase products (CO and CO_2) were quantified by comparison to calibration curves generated using a Schlenk Flask filled with a known pressure (measured by a mercury monometer) of the gas obtained from a cylinder. Injection volumes were between 10 and 200 µL (10-50 µL for the low CO concentrations on the calibration curve and 200 µL for reaction headspace analysis).

4.6.5. Continuous Photolysis

Photolysis experiments were done using an Oriel 200 W Hg Arc Lamp in an Oriel Housing (model 66033) with an Oriel Light Intensity Controller. The beam was aligned to pass through an 8 cm water-cell to filter out infrared light, a neutral density filter to reduce

the intensity, and an interference filter to isolate 365 nm light. The light was focused to a 5 mm diameter spot, A Uniblitz shutter controlled by a Model SD-1000 Uniblitz Drive was used to control the irradiation time. The solution was irradiated in a septum screw top quartz cuvette (1 cm pathlength).

The quantum yield (Φ) of complex **A** depletion was determined by plotting the number of molecules reacted (N_{mol}) versus the number of photons absorbed (N_{abs}). The number of molecules reacted was calculated from eq.1 using the initial absorbance at an observed wavelength (A_0), absorbance at irradiation time t (A_t), final absorbance after complete photolysis (A_F), initial analyte concentration (C_0), and solution volume (V). The number of photons absorbed were calculated from the incident photon flux (I_0) and the solution absorbance (A) at the irradiation wavelength using eq. 2. The incident photon flux was determined by measuring the power of the focused beam where the cuvette is located with a Coherent Field Max II meter and calculation using eq. 3.

$$N_{mol} = \frac{A_0 - A_t}{A_0 - A_F} \times C_0 \times V$$

(1)

$$N_{abs} = (1 - 10^{-A}) \times I_0 \times t$$

(2)

$$I_O = \frac{P}{E} = \frac{P\lambda}{hc}$$

(3)

For eq. 3 the irradiation wavelength (λ) was 365 nm, the power (P) was measured in Joule/s (Watt), photon energy (E) is in Joule/Einstein at 365 nm, the Planck constant (h), and the speed of light (c).

4.6.6. Infrared Spectroscopy

An infrared cell with CaF_2 windows was used to obtain liquid phase infrared spectra with a Nicolet iS50 FTIR spectrometer. Samples were dissolved in dimethyl sulfoxide. A stock solution of hydrogen peroxide in phosphate buffer was used to observe the temporal changes from the reaction of H_2O_2 with **A**. The solution in the infrared cell was 18 mM $Mn(CO)_3(Br)(bpCO_2H)$ with 185 mM H_2O_2 in 5 % phosphate buffer in DMSO.

4.6.7. EPR Spectroscopy

Perpendicular-mode X-band EPR spectra were collected on a Bruker EMX EPR spectrometer equipped with an Oxford ESR 900 liquid helium cryostat. All EPR samples were measured in quartz tubes. Aqueous samples were measured using a capillary insert to minimize the cross-sectional area of sample. Low temperature samples were frozen in a dry ice/ethanol bath prior to placement in the sample holder.

4.6.8. Fluorescence Spectroscopy

Emission spectra were obtained using a Photon Technology International fluorimeter with an 814 PMT detection system at 1 nm resolution. The excitation and emission slit width were both set to 5 nm. Coumarin-3-carboxylic acid (3-CCA) was used as a probe for hydroxyl radicals where 3-CCA is converted to 7-hydroxy-coumarin-3-carboxylic acid (7-OH-3-CCA) with a 4.7% conversion factor.[34] The emission of 7-OH-3-CCA was recorded from 420-520 nm using a 395 nm excitation wavelength. A 400 µL aliquot of a 2 mM 3-CCA solution, 60 µL aliquot of 1.9 mM $Mn(CO)_3(Br)(bpCO_2H)$ solution, and 1780 µL aliquot of 0.118 mM aqueous phosphate buffered solution were added to a quartz cuvette. Then, a 20 µL aliquot of H_2O_2 stock solution was added to give a final concentration of 32 mM H_2O_2 in the cuvette. The solutions were stirred at 24°C for 3 hours before taking a

fluorescence spectrum. Control reactions were performed without Mn and/or H_2O_2 as well as with $CuCl_2$, which is known to catalyze the Fenton reaction.[35] Absorbance changes were observed on the Shimadzu spectrophotometer with lower 3-CCA concentration (100 µL aliquots).

4.6.9. *Electrochemical Measurements*

A graphite rod counter electrode, SCE (standard calomel) reference electrode, and GCE (glassy carbon) working electrode were used to run a single sweep over the range of 0V to -0.9 V at a scan rate of 0.2-0.5 V s-1 at steps size of 2.4 mV. A Metrohm PGSTAT 128N potentiostat was used for these electrochemical measurements. Chronoamperometry was performed with a graphite rod counter electrode, SCE (standard calomel) reference electrode, and CFME (carbon fiber microelectrode). The constant -0.8 V potential was applied to reduce oxygen generated during the reaction.

4.7. Acknowledgements

4.8. References

1. Marhenke, J.; Trevino, K.; Works, C. The Chemistry , Biology and Design of Photochemical CO Releasing Molecules and the Efforts to Detect CO for Biological Applications. *Coord. Chem. Rev.* **2016**, *306*, 533–543

2. Motterlini, R.; Otterbein, L. E. The Therapeutic Potential of Carbon Monoxide. *Nat. Rev. Drug Discov.* **2010**, *9* (9), 728–743

3. Ling, K.; Men, F.; Wang, W. C.; Zhou, Y. Q.; Zhang, H. W.; Ye, D. W. Carbon Monoxide and Its Controlled Release: Therapeutic Application, Detection, and Development of Carbon Monoxide Releasing Molecules (CORMs). *J. Med. Chem.* **2018**, *61* (7), 2611–2635

4. Simpson, P. V; Schatzschneider, U. Small Signaling Molecules and CO-Releasing Molecules (CORMs) for the Modulation of the Cellular Redox Metabolism. In *Redox Active Therapeutics*; **2016**; pp 311–334

5. Reddy G, U.; Axthelm, J.; Hoffmann, P.; Taye, N.; Gläser, S.; Görls, H.; Hopkins, S. L.; Plass, W.; Neugebauer, U.; Bonnet, S.; Schiller, A.; Co-Registered Molecular Logic Gate with a CO-Releasing Molecule Triggered by Light and Peroxide. *J. Am. Chem. Soc.* **2017**, *139* (14), 4991–4994

6. Jin, Z.; Zhao, P.; Zhang, J.; Yang, T.; Zhou, G. Wang, T.; He, Q. Intelligent Metal Carbonyl Metal – Organic Framework Nanocomplex for Fluorescent Traceable H_2O_2-Triggered CO Delivery. *Chem. A Eur. J.* **2018**, *24*, 11667–11674

7. Tinajero-Trejo, M.; Rana, N.; Nagel, C.; Jesse, H. E.; Smith, T. W.; Wareham, L. K.; Hippler, M.; Schatzschneider, U.; Poole, R. K. Antimicrobial Activity of the Manganese Photoactivated Carbon Monoxide-Releasing Molecule [Mn(CO) $_3$ (Tpa-κ ^{3} *N*)] $^+$

Against a Pathogenic *Escherichia Coli* That Causes Urinary Infections. *Antioxid. Redox Signal.* **2016**, *24* (14), 765–780

8. Kawahara, B.; Ramadoss, S.; Chaudhuri, G.; Janzen, C.; Sen, S. Carbon Monoxide Sensitizes Cisplatin-Resistant Ovarian Cancer Cell Lines toward Cisplatin via Attenuation of Levels of Glutathione and Nuclear Metallothionein. *J. Inorg. Biochem.* **2019**, *191* (June 2018), 29–39.

9. Nemeth, Z.; Csizmadia, E.; Vikstrom, L.; Li, M.; Bisht, K.; Feizi, A.; Otterbein, S.; Zuckerbraun, B.; Costa, D. B.; Paolo, P.; et al. Alterations of Tumor Microenvironment by Carbon Monoxide Impedes Lung Cancer Growth. *Oncotarget* **2016**, *7* (17), 23919–23932

10. Wareham, L. K.; Poole, R. K.; Tinajero-Trejo, M. CO-Releasing Metal Carbonyl Compounds as Antimicrobial Agents in the Post-Antibiotic Era. *J. Biol. Chem.* **2015**, *290* (31), 18999–19007.

11. Klinger-Strobel, M.; Glaser, S.; Makarewicz, O.; Wyrwa, R.; Weisser, J.; Pletz, M. W.; Schiller, A. Bactericidal Effect of a Photoresponsive Carbon Monoxide-Releasing Nonwoven against Staphylococcus Aureus Biofilms. *Antimicrob. Agents Chemother.* **2016**, *60* (7), 4037–4046

12. Szatrowski, T. P.; Nathan, C. F. Production of Large Amounts of Hydrogen Peroxide by Human Tumor Cells. *Cancer Res.* **1991**, *51*, 794–799

13. Tang, Z.; Liu, Y.; He, M.; Bu, W. Chemodynamic Therapy : Tumour Microenvironment-Mediated Fenton and Fenton-like Reactions *Angew. Chem.- Int. Ed.* **2019**, 946–956

14. Winterbourn, C. C. Reconciling the Chemistry and Biology of Reactive Oxygen Species. *Nat. Chem. Biol.* **2008**, *4* (5), 278–286

15. Lennicke, C.; Rahn, J.; Lichtenfels, R.; Wessjohann, L. A.; Seliger, B. Hydrogen Peroxide - Production, Fate and Role in Redox Signaling of Tumor Cells. *Cell Commun. Signal.* **2015**, *13* (1), 1–19

16. Wlassoff, W. a; Albright, C. D.; Sivashinski, M. S.; Ivanova, A.; Appelbaum, J. G.; Salganik, R. I. Hydrogen Peroxide Overproduced in Breast Cancer Cells Can Serve as an Anticancer Prodrug Generating Apoptosis-Stimulating Hydroxyl Radicals under the Effect of Tamoxifen-Ferrocene Conjugate. *J. Pharm. Pharmacol.* **2007**, *59* (11), 1549–1553

17. Ranji-burachaloo, H.; Karimi, F.; Xie, K.; Fu, Q.; Gurr, P. A.; Dunstan, D. E.; Qiao, G. G. MOF-Mediated Destruction of Cancer Using the Cell's Own Hydrogen Peroxide. *ACS Appl. Mater. Interfaces* **2017**, *9*, 33599–33608

18. Jin, Z.; Wen, Y.; Xiong, L.; Yang, T.; Zhao, P.; Tan, L.; Wang, T.; Qian, Z.; Su, B. L.; He, Q. Intratumoral H_2O_2-Triggered Release of CO from a Metal Carbonyl-Based Nanomedicine for Efficient CO Therapy. *Chem. Commun.* **2017**, *53* (40), 5557–5560

19. Fayad-kobeissi, S.; Ratovonantenaina, J.; Dabiré, H.; Louise, J.; Marie, A.; Berdeaux, A.; Dubois-randé, J.; Mann, B. E.; Motterlini, R.; Foresti, R. Vascular and Angiogenic Activities of CORM-401 , an Oxidant-Sensitive CO-Releasing Molecule. *Biochem. Pharmacol.* **2016**, *102*, 64–77

20. Lo Iacono, L.; Boczkowski, J.; Zini, R.; Salouage, I.; Berdeaux, A.; Motterlini, R.; Morin, D. A Carbon Monoxide-Releasing Molecule (CORM-3) Uncouples Mitochondrial Respiration and Modulates the Production of Reactive Oxygen Species. *Free Radic. Biol. Med.* **2011**, *50* (11), 1556–1564

21. Crook, S. H.; Mann, B. E.; Meijer, A. J. H. M.; Adams, H.; Sawle, P.; Scapens, D.; Motterlini, R. [Mn(CO)$_4${S$_2$CNMe(CH$_2$CO$_2$H)}], a New Water-Soluble CO-Releasing Molecule. *Dalt. Trans.* **2011**, *40*, 4230–4235

22. Lorimer, J. W.; Clever, H. L.; Young, C. L. Carbon Monoxide. In *Solubility Data Series*; **1990**; Vol. 43.

23. Walsh, J. J.; Neri, G.; Smith, C. L.; Cowan, A. J. Water-Soluble Manganese Complex for Selective Electrocatalytic CO$_2$ Reduction to CO. *Organometallics*, **2019**, *386*, 1224-1229

24. Walsh, J. J.; Smith, C. L.; Neri, G.; Whitehead, G. F. S.; Robertson, C. M.; Cowan, A. J. Improving the Efficiency of Electrochemical CO $_2$ Reduction Using Immobilized Manganese Complexes. *Faraday Discuss.* **2015**, *183*, 147–160

25. Jin, K.; Park, J.; Lee, J.; Yang, K. D.; Pradhan, G. K.; Sim, U.; Jeong, D.; Jang, H. L.; Park, S.; Kim, D.; et al. Hydrated Manganese(II) Phosphate (Mn$_3$(PO$_4$)$_2$·3H$_2$O) as a Water Oxidation Catalyst. *J. Am. Chem. Soc.* **2014**, *136*, 7435–7443

26. Jimenez, J.; Chakraborty, I.; Dominguez, A.; Martinez-Gonzalez, J.; Sameera, W. M. C.; Mascharak, P. K. A Luminescent Manganese PhotoCORM for CO Delivery to Cellular Targets under the Control of Visible Light. *Inorg. Chem.* **2018**, *57*, 1766–1773

27. Tignor, S. E.; Kuo, H.-Y.; Lee, T. S.; Scholes, G. D.; Bocarsly, A. B. Manganese-Based Catalysts with Varying Ligand Substituents for the Electrochemical Reduction of CO $_2$ to CO. *Organometallics* **2018**, *38* (6), 1292–1299.

28. Niesel, J. Doctoral Dissertation, "CO Release Properties and Biological Activity of Manganese Tricarbonyl Complexes", Ruhr-Universität Bochum, **2012**. Retrieved May 18, 2019 http://www-brs.ub.ruhr-uni-bochum.de/netahtml/HSS/Diss/NieselJohanna/diss.pdf

29. Lo, L. T.; Lai, S.; Yiu, S.; Ko, C. A New Class of Highly Solvatochromic Dicyano Rhenate(I) Diimine Complexes – Synthesis, Photophysics and Photocatalysis. *Chem. Commun.* **2013**, *49*, 2311–2313

30. Marcus, R. A. On the Theory of Oxidation-Reduction Reactions Involving Electron Transfer. I*. *J. Chem. Phys.* **1956**, *24* (5). 966-977

31. Salem, I. A. A Kinetic Approach for the Homogeneous Reaction between N , N′ - Propylenebis (Salicylideneiminato) Manganese (III) Complex and Hydrogen Peroxide in Aqueous Solution, *Polyhedron*, **1994**, *10*, 1547-1551

32. Salem, I. A.; Amer, S. A. Kinetics and Mechanism of the Homogeneous Reaction between Some Manganese (III) -Schiff Base Complexes and Hydrogen per- Oxide in Aqueous and Sodium Dodecyl Sulphate Solutions. *Transit. Met. Chem.* **1995**, *20*, 494–497

33. Newton, G. L.; Milligan, J. R. Fluorescence Detection of Hydroxyl Radicals. *Radiat. Phys. Chem.* **2006**, *75*, 473–478

34. Yamashita, S.; Baldacchino, G.; Maeyama, T.; Muroya, Y.; Lin, M.; Kimura, A.; Murakami, T. Mechanism of Radiation-Induced Reactions in Aqueous Solution of Coumarin-3-Carboxylic Acid : Effects of Concentration , Gas and Additive on Fluorescent Product Yield. *Free Radic. Res.* **2012**, *46* (7), 861–871

35. Goldstein, S.; Meyerstein, D.; Czapski, G. The Fenton Reagents. *Free Radic. Biol. Med.* **1993**, *15*, 435–445

36. Buettner, G. R. The Pecking Order of Free Radicals and Antioxidants: Lipid Peroxidation, a-Tocopherol, and Ascorbate. *Archives of biochemistry and biophysics*. **1993**, pp 535–543

37. Rebelo, L.; Maria, S.; Tavares, F.; Jorge, C.; Terezinha, S.; Nakagaki, S.; Vencato, I.; Bortoluzzi, A. J. Synthesis , Structural Characterization , Catalase-like Function and Epoxidation Activity of a Mononuclear Manganese (II) Complex. *Monatshefte fuer Chemie* **2007**, 269, 22–29.

38. Tikhonov, K. G.; Zastrizhnaya, O. M.; Kozlov, Y. N.; Klimov, V. V. Composition and Catalase Like Activity of Mn (II)– Bicarbonate Complexes. *Biochem. (Moscow)* **2006**, *71* (11), 1270–1277

39. Compton, R. G.; Laborda, E.; Ward, K. R. *Understanding Voltammetry*; IMPERIAL COLLEGE PRESS, **2014**

40. Li, Q. Doctoral Dissertation, "Electrochemical Reduction of Oxygen", Oxford University, UK, **2014**.

41. Yamaguchi, K. S.; Sawyer, D. T. The Redox Chemistry of Manganese(III) and -(IV) Complexes. *Isr. J. Chem.* **1985**, *25*, 164–176

42. Salem, I. A.; El-Maazawi, M.; Zaki, A. B. Kinetics and Mechanisms of Decomposition Reaction of Hydrogen Peroxide in Presence of Metal Complexes. *Int. J. Chem. Kinet.* **2000**, *32* (11), 643–666

43. Saisaha, P.; de Boer, J. W.; Browne, W. R. Mechanisms in Manganese Catalysed Oxidation of Alkenes with H_2O_2. *Chem. Soc. Rev.* **2013**, *42*, 2059–2074

44. Fukuzumi, S. Unified Mechanism of Oxygen Atom Transfer and Hydrogen Atom Transfer Reactions with a Triflic Acid-Bound Nonheme Manganese(IV)–Oxo Complex via Outer-Sphere Electron Transfer. *J. Am. Chem. Soc.* **2019**, *141*, 2614–2622

45. Buxton, G. V; Greenstock, C. L.; Helman, P.; Ross, A. B. Critical Review of Rate Constants for Reactions of Hydrated Electrons , Hydrogen Atoms and Hydroxyl Radicals ($\cdot$ OH/$\cdot$O) in Aqueous Solution. *J. Phys. Chem. Ref. Data* **1988**, *17*, 513

46. Bielski, B. H. J.; Cabelli, D. E.; Arudi, R. L.; Ross, A. B. Reactivity of HO2 / O 2 Radicals in Aqueous Solution. *J. Phys. Chem. Ref. Data* **1985**, *14*, 1041

47. Vanýsek, P. Electrochemical Series. *In CRC Handbook of Chemistry and Physics*, 9nd ed.; Haynes, W. M., Ed.; CRC Press: Boca Raton, **2012**; pp 8-20

48. Wegiel, B.; Gallo, D.; Csizmadia, E.; Harris, C.; Belcher, J.; Vercellotti, G. M.; Penacho, N.; Seth, P.; Sukhatme, V.; Ahmed, A.; Pandolfi, P. P.; Helczynski, L.; Bjartell, A.; Persson, J. L.; Otterbein, L. E. Carbon monoxide expedites metabolic exhaustion to inhibit tumor growth. *Cancer Res.* **2013**, *73* (23), 7009−7021

49. De Laat, J.; Gallard, H. Catalytic Decomposition of Hydrogen Peroxide by Fe (III) in Homogeneous Aqueous Solution : Mechanism and Kinetic Modeling. *Environ. Sci. Technol.* **1999**, *33* (16), 2726–2732

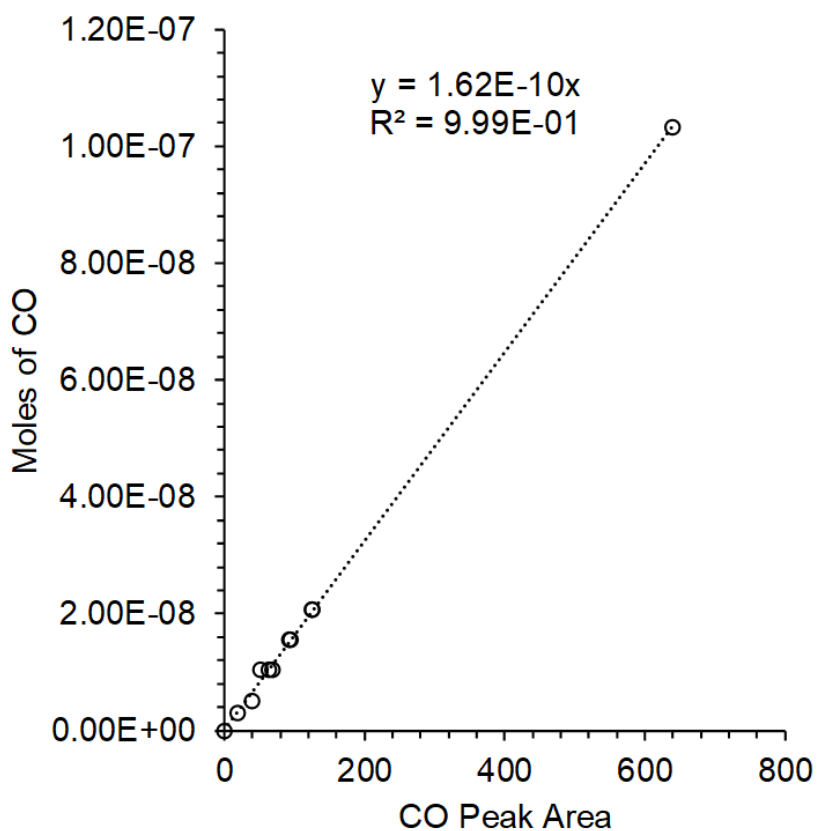## 4.9. Appendix C: Supporting Information for Chapter 4

Figure S4.1. Carbon monoxide calibration curve showing the moles of CO versus CO Peak Area from GC-TCD injections of prepared standards. The moles of CO are calculated for the injection volume (10-150 µL) and the CO partial pressure (0.25 atm). The standard was prepared in a Schlenk flask using a Schlenk line equipped with a Hg manometer
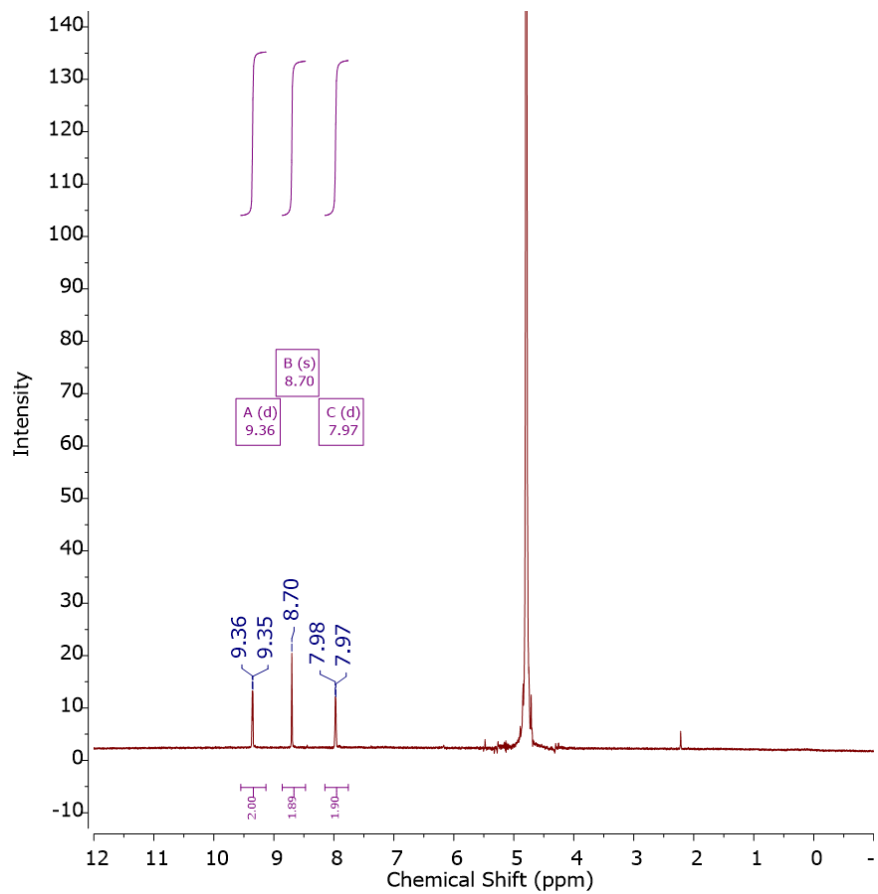
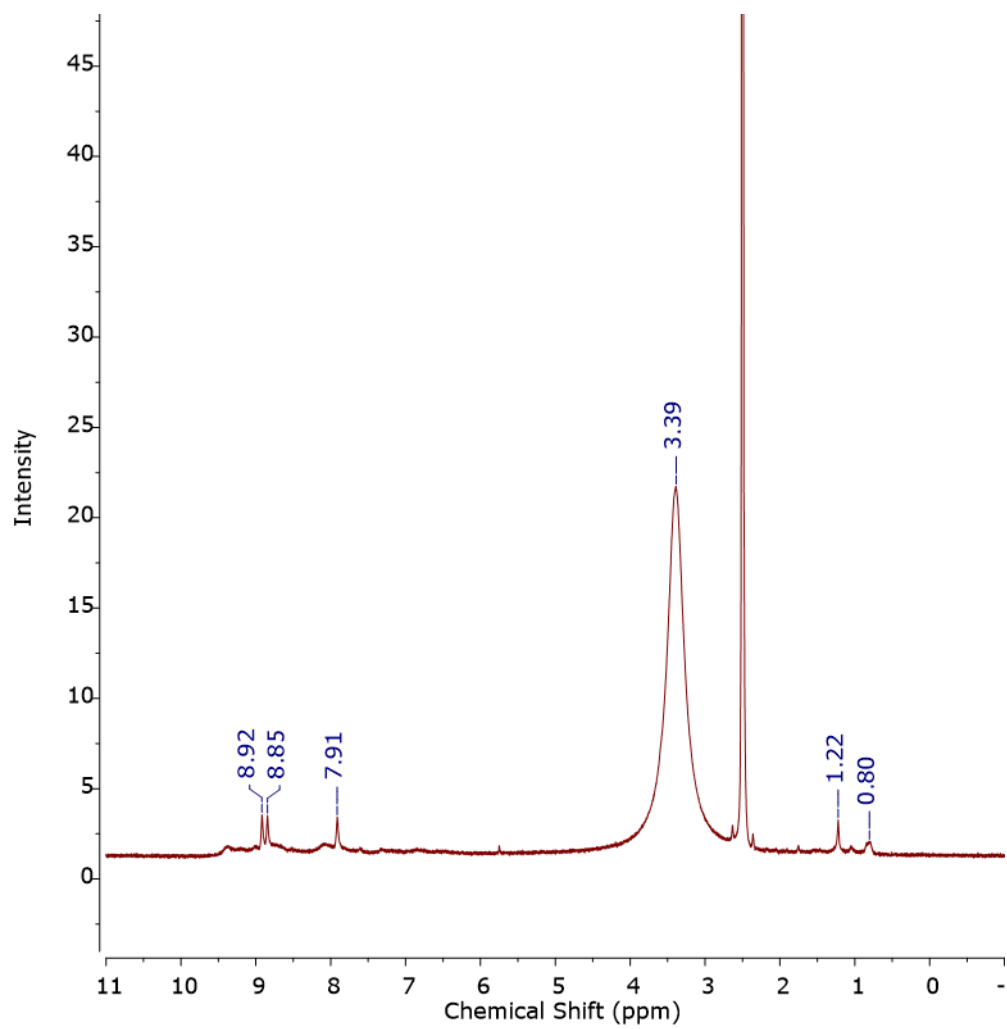**Figure S4.2.** ^{1}H NMR of approximately 20×10^{-4} M **A** in D$_2$O.

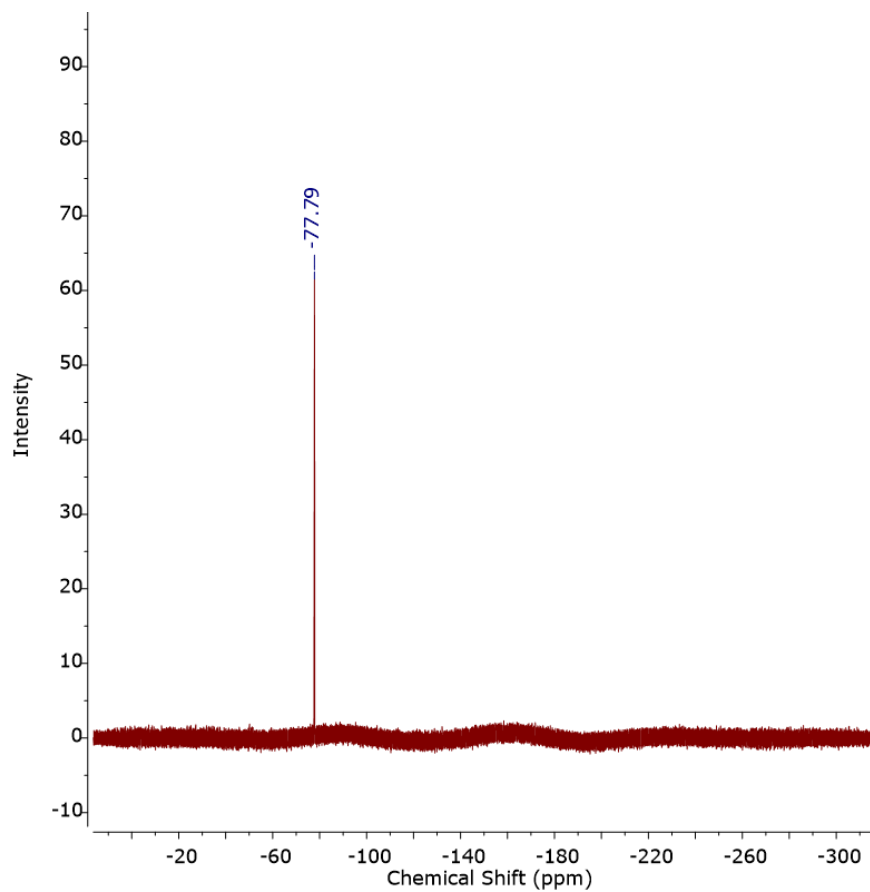**Figure S4.3**. ^{1}H NMR of approximately 20×10^{-4} M **B** in DMSO-d$_6$.

Figure S4.3. ^{19}F NMR of approximately 20×10^{-4} M **B** in DMSO-d$_6$.